

## Matching high voltage pulsed power technologies

**Citation for published version (APA):**

Voeten, S. J. (2013). *Matching high voltage pulsed power technologies*. [Phd Thesis 1 (Research TU/e / Graduation TU/e), Electrical Engineering]. Technische Universiteit Eindhoven. <https://doi.org/10.6100/IR750268>

**DOI:**

[10.6100/IR750268](https://doi.org/10.6100/IR750268)

**Document status and date:**

Published: 01/01/2013

**Document Version:**

Publisher's PDF, also known as Version of Record (includes final page, issue and volume numbers)

**Please check the document version of this publication:**

- A submitted manuscript is the version of the article upon submission and before peer-review. There can be important differences between the submitted version and the official published version of record. People interested in the research are advised to contact the author for the final version of the publication, or visit the DOI to the publisher's website.
- The final author version and the galley proof are versions of the publication after peer review.
- The final published version features the final layout of the paper including the volume, issue and page numbers.

[Link to publication](#)

**General rights**

Copyright and moral rights for the publications made accessible in the public portal are retained by the authors and/or other copyright owners and it is a condition of accessing publications that users recognise and abide by the legal requirements associated with these rights.

- Users may download and print one copy of any publication from the public portal for the purpose of private study or research.
- You may not further distribute the material or use it for any profit-making activity or commercial gain
- You may freely distribute the URL identifying the publication in the public portal.

If the publication is distributed under the terms of Article 25fa of the Dutch Copyright Act, indicated by the "Taverne" license above, please follow below link for the End User Agreement:

[www.tue.nl/taverne](http://www.tue.nl/taverne)

**Take down policy**

If you believe that this document breaches copyright please contact us at:

[openaccess@tue.nl](mailto:openaccess@tue.nl)

providing details and we will investigate your claim.

# Matching High Voltage Pulsed Power Technologies

PROEFSCHRIFT

ter verkrijging van de graad van doctor aan de Technische Universiteit Eindhoven, op gezag van de rector magnificus, prof.dr.ir. C.J. van Duijn, voor een commissie aangewezen door het College voor Promoties in het openbaar te verdedigen op donderdag 10 januari 2013 om 16.00 uur

door

Stefan Johan Voeten

geboren te Nijmegen

Dit proefschrift is goedgekeurd door de promotor:

prof.dr.ir. J.H. Blom

Copromotoren:

dr.ing. A.J.M. Pemen

en

dr.ir. G.J.H. Brussaard

# Contents

---

1	Introduction	5
1.1	High voltage pulsed power applications	5
1.2	High voltage pulse generators	5
1.3	Motivation for this research	8
1.4	Thesis organization	11
2	The Surface Discharge Switch	13
2.1	Introduction	13
2.2	Surface discharge	16
2.2.1	Influence of gas and pressure	20
2.2.2	Influence of dielectric	21
2.3	Experimental setup	23
2.3.1	Pulse source	25
2.3.2	Voltage and current measurement	27
2.3.3	Optical diagnostics	27
2.3.4	D-dot sensors	29
2.3.5	Synchronization of optical and electric measurements	32
2.4	Results	33
2.4.1	Discharges in Air	34
2.4.1.1	Observations with the D-dot sensors	35
2.4.1.1.1	Charging voltage 38 kV	35
2.4.1.1.2	Charging voltage 17 kV	39
2.4.1.2	Analysis of optical observations	40
2.4.2	Discharge in Argon	45
2.4.2.1	Observations with the D-dot sensors	46
2.4.2.1.1	Charging voltage 17 kV	46
2.4.2.2	Analysis of optical observations	48
2.4.3	Helium	51
2.4.3.1	Observations with the D-dot sensors	52
2.4.3.1.1	Charging voltage 17 kV	52
2.4.3.2	Analysis of optical observations	54
2.4.4	Discharges in Air using SrTiO <sub>3</sub>	56
2.4.4.1	Observations with the D-dot sensors	57
2.4.4.1.1	Charging voltage 17 kV	57
2.4.4.2	Analysis of optical observations	59



2.4.5	Switch life time	62
2.5	Conclusions and discussion	64
3	The Parallel Plate Transmission Line Transformer	67
3.1	Introduction	67
3.2	Transmission Line Transformer basics	67
3.3	Parallel Plate Transmission Line Transformer	69
3.4	Simulations of the PPTLT	73
3.4.1	Voltage gain	74
3.4.2	Reflections and mismatch	75
3.4.3	Losses in the dielectric and conductors	76
3.5	Measurements	78
3.5.1	Transient pulse	78
3.5.1.1	4 STAGE PPTLT	80
3.5.1.2	8-STAGE PPTLT	81
3.5.2	Scattering parameters	82
3.6	High voltage application considerations	87
3.6.1	Rotation of the transmission lines	87
3.6.2	Transmission line edges	87
3.6.3	Series stacking of transmission lines	87
3.7	Conclusions	89
4	Comparison of a D-dot sensor and a Capacitive Voltage Divider to measure nanosecond high-voltage pulses	91
4.1	Introduction	91
4.2	The Blumlein topology and its implementation	93
4.3	Blumlein charging circuit	99
4.4	Blumlein voltage sensors	100
4.4.1	Capacitive voltage divider	100
4.4.2	D-dot sensor	102
4.5	Numerical simulation results	104
4.5.1	Capacitive voltage divider	104
4.5.2	D-dot sensor	107
4.5.3	Time delay determination	114
4.6	Measurement results	115
4.6.1	Time delay verification	115
4.6.2	Current sensor measurement	115
4.6.3	Capacitive Voltage Divider (CVD)	116
4.6.4	D-dot sensor	118
4.7	Conclusions	125

5	Measuring the rise time of (high) voltage pulses using autocorrelation	127
5.1	Introduction	127
5.2	Auto-correlation	129
5.2.1	Theoretical description	129
5.2.2	Electric autocorrelator	130
5.2.3	Microwave power detector; GaAs Planar Doped Barrier Diode	132
5.2.4	Characterization of the microwave power detector	134
5.3	Pulse measurement	137
5.4	Practical implementation in a high voltage pulse source	142
5.5	Conclusions	145
6	Application of developed technologies	147
6.1	Surface discharge and plasma research	147
6.2	Accelerator structure	151
7	Conclusions	155
8	Summary	157
9	Samenvatting	159
10	Appendix	161
10.1	Modeling of a laser triggered spark gap	161
10.2	D-dot sensor calibration	165
10.2.1	Model	165
10.2.2	Measurement without discharge	167
10.2.3	Numerical simulation	168
10.2.4	Measurement with discharge	169
10.3	Analysis of optical images	173
10.3.1	Definition of the discharge front	173
10.3.2	Image calibration	173
10.3.3	Absolute size	175
10.3.4	Single Image	175
10.3.5	Limitations of the velocity measurement	178
10.3.6	From $v(x)$ to $x(t)$ and $v(t)$	179
11	Bibliography	182
12	Dankwoord	187
	Curriculum Vitae	193



# 1 Introduction

---

## 1.1 High voltage pulsed power applications

Nanosecond high voltage pulses have numerous applications, one of them the generation of plasmas. Although plasma can be generated in various ways, transient plasma generated by nanosecond pulses perform much better in energy efficiency and processing performance than continuous plasmas and they even can offer new features [1], [2]. From an application perspective, a rapid advance of pulsed power driven transient plasma technology will contribute to improved performance of pulsed corona reactors for air and water purification, and to new methods for the processing of (liquid) fuels to enhance their sustainable uses.

Another intriguing example of the application of pulsed electric fields is the manipulation of biological cells [3], [4]. By applying short intense pulses, the proliferation of cells can be enhanced. This allows new solutions for stimulated wound healing, skin treatment and tissue engineering. Under some circumstances it is even possible to initiate apoptosis (the self termination process of a cell) [5]. The benefit of initiating apoptosis is that the removal of the cell happens in a natural way and therefore causes a minimal burden for the body in which the cell resides. Another effect, when applying lower electric field strengths, is electroporation. In this case the cell membrane becomes porous for a short while. This can be used to introduce medicine or other substances to a cell [4].

Another application that is of particular interest to us, is in particle accelerators. [6–9]. Using DC voltages makes equipment relatively large and the continuous electric field stress makes the components susceptible to breakdown. Using a pulsed electric field has the important advantages that the probability of electrical breakdown is reduced and higher electric fields can be applied.

## 1.2 High voltage pulse generators

The generation of nanosecond high-voltage pulses has two main design concerns. The first one is related to the fact that an electromagnetic pulse of 1 nanosecond has a length, in air or vacuum, of 30 cm. The length of the pulse is of the same order of magnitude as the dimensions of the pulse source, which therefore cannot be analyzed by lumped elements. Designs must be analyzed and optimized by means of distributed models and/or (3D) electromagnetic modeling (preferably in the time domain). The main design criteria are a fast rise time and the optimization of energy transfer to the load. Both have a strong correlation with minimization of reflections and losses.

The second design concern is the switch, which is of major importance. Its switching time determines the fastest possible rise time of the output pulse, and also its impedance must match the pulse forming circuit. An important part of the research in this thesis is therefore devoted to the study of a fast switch. A comprehensive summary of the state of the art of the technology of pulsed power sources and techniques is given by [10].

A commonly used topology for the generation of square (high-) voltage pulses is shown in Figure 1-1. Here the left coaxial transmission line is charged by a DC voltage source through a high impedance. When the switch closes, a pulse is formed with a duration that is equal to twice the transit time of the pulse along the left transmission line. The amplitude of the output pulse is half the DC charging voltage. This pulse can be transferred to a matched load by the right transmission line (with similar characteristic impedance). The advantage of this topology is the relatively good matching of the switch to the transmission lines. Because the switch is incorporated in a matched structure, reflections can be minimized and the rise time of the pulse can be very fast, less than 100 ps. [11].

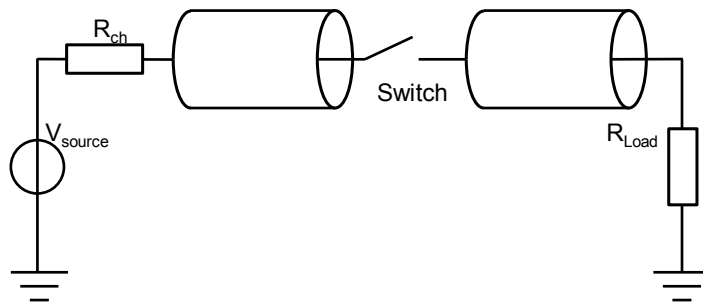


Figure 1-1. Basic transmission line based pulsed power source.

The disadvantage this topology, is that the amplitude of the output pulse is half the charging voltage. This can be overcome by applying a so called Blumlein topology, as shown in Figure 1-2.

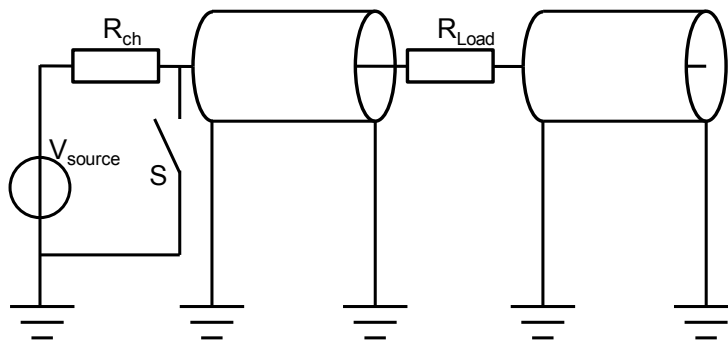


Figure 1-2. Basic Blumlein pulse source.

Two transmission lines of equal length and characteristic impedance are initially charged. By closing the switch, a wave front travels down the left transmission line. Once it reaches the matched load, with twice the impedance of a single transmission line, the wave will reflect such that the total

charging voltage will appear over the load. The duration of the pulse is twice the transit time along the transmission lines. This type of source will be discussed in more detail in chapter 4.

The switch in the circuits described above plays a crucial role in the overall performance of the source. It sets a limit for the maximum attainable rise time and its impedance influences the output voltage. A widely used high voltage switch is the spark gap. It is a simple and robust switch that, when well designed, can be used to generate high-voltage pulses of 200 picoseconds [12]. A brief estimation of the voltage rise time of a spark gap is given in [13]. Lehr and Baum show that the closing time of a spark gap switch is mainly determined by the avalanche phase of the discharge process in the spark gap. Since the breakdown process in a spark gap switch is a stochastic process, unavoidable jitter in the moment of switching will occur. Also, the spark has an inherent inductive behavior limiting the rise time. Still Lehr and Baum come to the conclusion that picoseconds rise times are possible.

At Eindhoven University of Technology, an extremely fast spark gap switch has been developed [14]. The concept of this laser triggered, photoconductive spark gap is shown in Figure 1-3, and has been applied in a pulse circuit as shown in Figure 1-1. By using a high power 200 femtosecond laser pulse a conducting plasma is created almost instantaneous (on a femtosecond time scale) in between the two electrode tips. This allows the generation of high voltage pulses up to 5 kV with measured rise times below 100 ps and jitter between the laser pulse and the electric pulse in the order of 12 picoseconds.

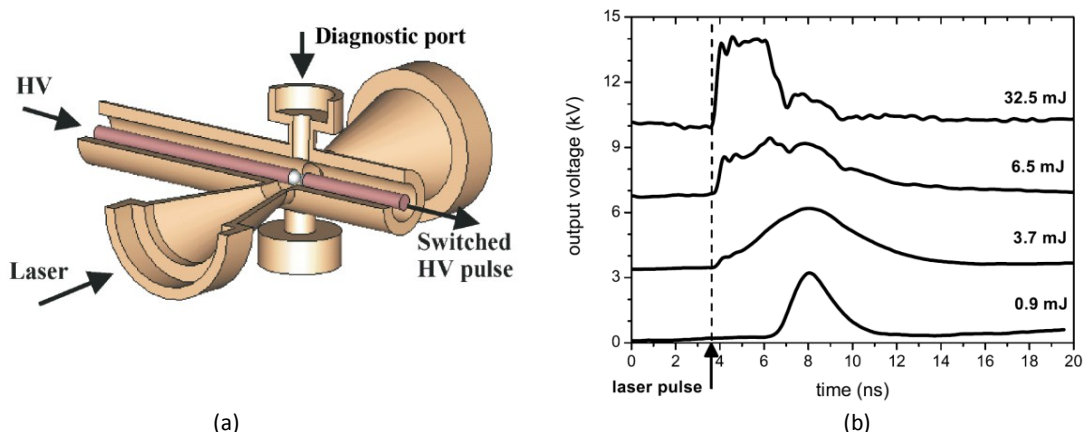


Figure 1-3. (a) The laser switched spark gap studied by J. Hendriks and the output pulses (b) generated with this spark gap. Applied voltage: 4.5 kV, 1 mm gap, atmospheric air.

In the investigations done so far on this switch, the rise time of the pulse was expected to be faster than the bandwidth of the oscilloscope used to measure the pulse. This is confirmed by numerical simulations, described in section 10.1, to find an estimate for the rise time. This motivated us to reproduce the experiments done by Hendriks, and to develop a new method to measure the rise time of very fast high-voltage pulses by an autocorrelation method, chapter 5.

Besides using the breakdown process of gasses or liquids as in spark gaps, semiconductors can also be applied for switching fast high voltage pulses. A very interesting technique was developed at the Ioffe Institute in Saint-Petersburg, Russia. It was first mentioned in 1980 by I.V. Grekhov et. al., in a paper on a high power sub-nanosecond switch [15]. The switch, known as a Drift Step Recovery Diode, DSRD, is a  $p^+nn^+$  silicon diode. By applying a very steep voltage pulse to a reverse biased diode, an electron-hole plasma is formed directly inside the space charge region at the p-n junction allowing the

diode to switch from non-conducting to conducting within hundreds of picoseconds with jitter in the order of 30 ps.

The very low output impedance requirements for the switch that we are aiming for cannot be met by conventional and available techniques. Therefore, in this project we investigate a new option, based on surface discharges along a dielectric.

### 1.3 Motivation for this research

The goal of the research in this thesis is to investigate new techniques to improve short high voltage pulse technology. The system that we study, schematically shown in Figure 1-4, is a pulse source with a single switch at the ‘low voltage’ side. The philosophy of using a single switch is that this inherently reduces jitter with respect to a system with a sequence of switches in series. The single switch approach makes the pulse source more suitable for timing critical applications. By placing the switch at the low voltage side, the requirements applicable to the switch are relaxed. For example the hold off voltage the switch must be able to handle.

Directly following the switch is a transmission line transformer, TLT, whose output is matched to the load. Here we search for an elegant method to amplify the output voltage with minimal pulse distortion and minimal losses due to reflections and mismatch and due to the secondary mode.

To be able to, eventually, make any claim on the performance of a pulse source, its pulses must be measured. With respect to diagnostics our goal is to research two different techniques; differentiating electric field sensors, so called D-dot sensors, and electronic autocorrelation. The D-dot sensors are used to measure the derivative of fast high voltage pulses. By integrating the output of the D-dot sensors the measured high voltage pulse can be recovered. Electronic autocorrelation can be used to measure the Full Width at Half Max, FWHM, of electric pulses with a duration of 10 to 100 picoseconds.

Combining the D-dot sensors and the autocorrelator allows us to accurately measure the FWHM of the very fast (10 to 100 picosecond) risetime of a high voltage pulse.

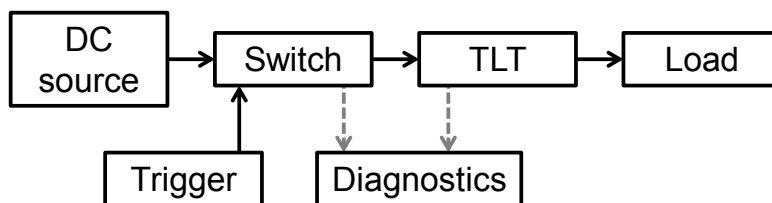


Figure 1-4. Schematic overview of the proposed pulse source.

The conventional technique to generate short, high-voltage pulses is to first create a long pulse. This long pulse can be relatively easily transformed to high voltages. This long, high-voltage pulse is then compressed by a pulse forming network or “cut” by a series of switches to form a short pulse. The appeal of the approach as depicted in Figure 1-4 is based on the fact that first a ‘low’ voltage nanosecond pulse is made which then is amplified. This is more efficient, allows for a smaller pulse source and greatly reduces electromagnetic noise to the environment. Also, the use of a single, low impedance switch allows for good switch timing and jitter control.

The energy for the pulse can be supplied with a pulse forming network, an energy storage line or capacitor. Because we do not study this source here, we make the assumption that such a source will operate at frequencies much lower than those present after the switch. Hence, for generality, it is referred to as a DC source. Important to bear in mind is the fact that in the presented design the charge stored in this source is used to determine the pulse length.

A transmission-line-transformer (TLT), schematically shown in Figure 1-5, will be used to amplify the switch output voltage. The voltage amplification is achieved by the impedance transformation between the input and output impedance. The advantage of such a transformer is the fact that it is constructed of transmission lines giving it a very high bandwidth. F. Davanloo, J.J. Coogan, C.B. Collins et. al. [16], [17] successfully combine a Blumlein and TLT into a high voltage X-ray generator. D.B. Pawelek, P.A.A.F. Wouters et. al., [18], have studied a 10 stage TLT and have shown the applicability of the TLT as a pulse transformer. A TLT allows voltage transformation up to about a factor 10 (due to practical input and output impedance limitations and losses) without disturbing the pulse shape.

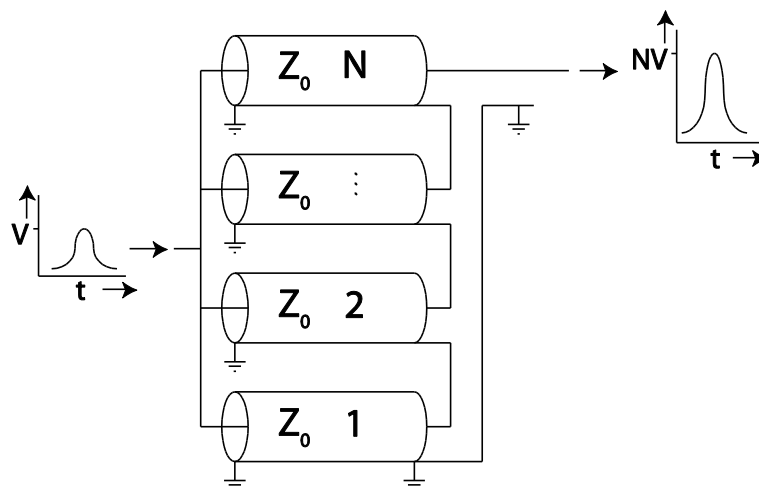


Figure 1-5. Schematic representation of a Transmission Line Transformer. The voltage amplification is achieved through impedance transformation between the input and output impedance.

The TLT has low input impedance. This requires a low impedance switch. The impedance of the TLT, as described in chapter 3, has an input impedance in the order of  $3 \Omega$ . For both the spark gap and the Drift Step Recovery Diode, DSRD, switches this is a very low impedance load. Therefore a surface discharge switch is studied. The advantage of such a switch, with respect to a spark gap or a rail gap switch (see Figure 1-6), [19], is that the discharge can be made to cover a wide area resulting in a low impedance switch.



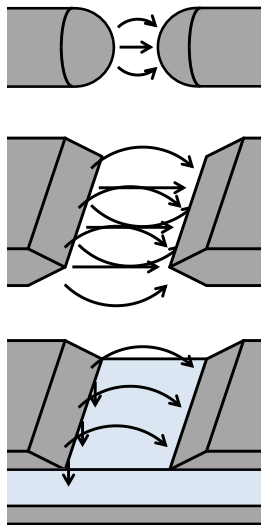


Figure 1-6. (Top) Simplified representation of a spark gap switch. (Center) A rail gap switch; wider than a spark gap but still electric field points from one electrode directly to the other electrode. (Bottom) Surface discharge switch; This switch allows for a strong vertical electric field component enabling better control over the discharge plasma.

Under the right conditions it is believed that the surface discharge can be treated as a conductor which, while sliding over a grounded dielectric, forms a transmission line together with the grounded dielectric. This would allow for good matching with both the source and the load resulting in reduced losses. Finally, a surface discharge allows for very good control over the electric field allowing fast triggering of the switch. Chapter 2 discusses an experimental surface discharge and describes its performance. In the final chapter a conceptual model of triggering such a surface discharge is discussed.

## 1.4 Thesis organization

In this thesis the critical components of the pulse source, shown schematically in Figure 1-4, are studied separately. As discussed previously, the switch is a critical component for the pulse source. The proposed surface discharge switch is studied first in chapter 2. The performance of the switch is greatly influenced by the plasma. A surface discharge by itself contains a lot of fascinating physics and it has been a fruitful research subject for many years. Trying to fully understand the physics of the surface discharge is an entire study by itself. To design an optimal switch, we have chosen a practically oriented approach. Our focus is on the voltage applied over the switch, the current flowing through the switch and optical observation of the plasma growth. The current and voltage give an indication of switching performance and the optical observations show the plasma behavior. These two are combined to determine how the plasma behavior influences the switch performance.

For the amplification of a nanosecond pulse a completely new design for a TLT was made. In this design losses due to the secondary mode and pulse distortion are minimized. This new design is studied in chapter 3. Two different TLTs are simulated and tested. The TLTs are tested at low voltages and different design modifications are opted to make the TLTs suitable for high voltage applications.

To validate the performance of a pulsed source the output pulses must be measured. In chapter 4 we describe electric field sensors. These sensors measure the derivative of the electric field and hence are called D-dot sensors. By numerically integrating the signal, the actual electric field, and thus voltage, can be determined. The small size, and therefore inherently high bandwidth, of these probes make that there is very little intrusion in the high voltage circuit and very low risk of breakdown caused by the probe.

The rise time is an important aspect of the source. Here the high frequency components reside that are used for the broadband applications [12]. In chapter 5 we describe the autocorrelator, a device that can be used to measure the autocorrelate of a pulse. From the autocorrelate, the width of the measured pulse can be determined. By combining the autocorrelator with the D-dot sensors, the rise time of the high voltage pulse could be measured.

Because we study the different components of the pulse source independently, an outlook to possible implementations is given in chapter 6 followed by conclusions and discussion.



## 2 The Surface Discharge Switch

---

### 2.1 Introduction

“It’s the Switch”; the switch plays a crucial role in the generation of very short high-voltage pulses with nanosecond duration and sub-nanosecond rise times. For the applications as described in the introduction, a switch must be able to switch 20 to 50 kV with a rise time in the order of a single nanosecond or less and must have a very low impedance. Also the shot to shot jitter must be extremely small for timing purposes with other devices in the application. The high voltage and low impedance require a switch that can conduct very large currents. In our case, a load voltage of 50 kV with a  $3\ \Omega$  impedance gives an estimate of the peak current in the order of 16 kA.

The most well known high voltage switch for such applications is the spark gap. Its simplicity makes it an often used switch for pulsed high voltage applications. An interesting example of a spark gap, used for sub nanosecond pulses, is investigated by M. Lehr, C. Baum et. al. [13]. They search for a switch with a small gas volume, making the single spark gap switch the preferred choice over the rail gap. They describe a method to reduce the inductance of the spark gap, which they agree is higher than that of a rail gap. A rail gap allows for a reduction of inductance to the level of the inductance of the source circuit.

J. Hendriks studied the performance of a laser switched spark gap, [20]. He uses a TW-level femtosecond laser that generates a conducting plasma in the gap in 200 femtoseconds (almost instantaneously). A very short rise time of the output voltage in the order of 50 picoseconds has been realized, and the jitter between the laser pulse and the output voltage pulse was in the order of 12 picoseconds. The performance of this laser triggered spark gap is extremely good but a practical drawback of this option is the need for a TW femtosecond laser. This introduces a large cost factor and operating a laser system of this caliber is not trivial.

So it is possible to realize a fast spark gap switch with sub nanosecond closing times. But these switches are used for loads with impedances in the order of  $50\ \Omega$ . J. Hendriks used a  $50\ \Omega$  coaxial load, [20], and M. Lehr and C. Baum et. al., [12], also apply a load with a comparable impedance. The load impedance limits the current, and thus the power, the switch has to handle. The Transmission Line Transformer, which will be treated in chapter 3, has a  $3\ \Omega$  input impedance. To be able to feed such a low impedance load, the impedance of the switch must be comparable or lower and the switch must be able to handle the power.

Besides the low load impedance that must be matched, reflections also play a significant role in the design of a switch for our application. On these time scales components must be treated as waveguides. This asks for a switch which is highly integrated with the load. In our case, the switch has to feed a parallel plate transmission line transformer. Aside from impedance matching, the more different the shape between the switch and the input of the transmission line transformer, the more reflections, and thus energy losses, occur.

Another interesting switch, strongly related to the spark gap, is the rail gap switch. A rail gap is in fact nothing more than a very wide spark gap, which is operated so that many parallel sparks are

generated in the wide gap, thereby reducing the impedance of the switch. The geometry of such a rail gap can be very well matched with the input of a planar transmission line transformer. The fact that multiple arcs are present also increases the power handling capabilities.

The initial streamer discharge in such a rail gap switch is described and modeled by Pang Lei, Fengbo Tao et al.[19]. They study the effect of the distance between the streamers. Models and experiments show a large dependence on the rise time of the trigger voltage. When two streamers are very close to each other they can distort each other's electric field such that the electric field of one of the streamers becomes too weak for ionization resulting in its extinction. This illustrates the difficulty of controlling the switching performance of the rail gap. Due to the fact that the main electric field component in the switch is from one electrode directly to the other, the performance of the switch relies on its trigger. If the trigger can create a  $dV/dt$  on the source rail high enough to initiate multiple parallel streamers that can co-exist, multiple arcs can be formed. If the time between the different streamers is too large, the number of streamers is likely to drop and the rail gap loses its advantage.

Jurgen, Salge and Katschinski [21] describe three other techniques that may be potential candidates to fulfill the demands for the switch we are looking for. These technologies are the Multichannel Field Distortion Foil Switch, multichannel Surface Discharge Switch and the Optically Triggered Semiconductor Switch. They study these techniques to supply a pulse to the KALIF pulse generator. This is a 1.5 TW Pulse generator of the Karlsruhe Institute of Technology used for the generation of intense light ion beams. Of the three mentioned switch techniques, they conclude the optically triggered semiconductor switch has the best chance to be suitable for their application. This does however require a laser to trigger the switch and as shown by [Hendriks and Brussaard] a laser can turn out to become the most expensive and complicated component of the switch.

In this thesis we will explore a surface discharge switch. Such a switch can be very well matched and integrated with the planar transmission line transformer. The most important reasons for us to investigate the surface discharge switch are discussed in the following section.

A surface discharge switch is very similar to a rail gap but it has its electrodes on top of a grounded dielectric surface (see Figure 2-1). This gives the surface discharge switch its improved control of the electric field in the gap. In a rail gap the electric field points from one electrode straight to the other. In a surface discharge switch, the electric field has a vertical component towards the grounded plane underneath the dielectric surface. The advantage of this will be explained in more detail in the following sections. This vertical field component can be much larger than the horizontal field component because the distance between the electrode and the grounding plane can be small due to the high dielectric strength of the dielectric material. This advantage of the surface discharge switch will be described in more detail in the following sections. Another benefit comes from the triple points at the edges of the electrodes. These triple points generate field enhancement which is beneficial for the ignition of the plasma. Due to the presence of the dielectric plate, proper matching with a load such as the parallel plate transmission line transformer can be achieved. Essentially, the surface discharge switch (with a homogeneous layer of conducting plasma along the dielectric surface) can be regarded as a parallel plate transmission line with a gap over the full width of the top electrode.

Bergmann, [22], gives, to our knowledge, as one of the first a qualitative description of the development of the surface discharge. He describes the different phases of the discharge and states that a minimum  $dV/dt$  of 1 kV/ns is needed to have multiple parallel arcs.

Trusov, [23], recognizes three different subsequent phases in the development of the discharge in a surface discharge switch; avalanche phase, thermal heating and arc mode. His studies focus on the

second and third phase and he gives a description of the inductance of the arcs over a dielectric surface using mirror charges. Also Buzzi, Doucet, et. al., [24], derive the induction of the multichannel mode phase using mirror charges. They find inductances in the order of single nH's. But the first phase of the discharge has not been described extensively.

Having multiple parallel sparks on a surface discharge switch results in the beneficial low inductance, in the order of nH as described by Buzzy and Doucet et. al., [24], and a very low resistance, Fulker and Fouracre, [25]. The disadvantage of the multichannel mode is that the arcs need time to form. Thermal heating of the electrodes precedes the formation of the arcs. The thermal heating, followed by the high current arcs damages the electrodes which is disadvantageous for the lifetime of the switch. This damage, which can be related to the current in an arc, is expected to decrease with an increase in the number of arcs, and thus a lower current per arc.

Reinovsky gives a descriptive model of the first phase of the surface discharge using a ladder RC network to describe the avalanche and streamer phase [26]. He states that the energy needed for the ionization front must come from the charged dielectric directly behind the discharge front and for long discharge gaps, this energy can no longer be supplied by the electrode. He has shown a relation between the propagation velocity of the streamers and the specific capacitance of the dielectric surface over which the discharge occurs. The larger the dielectric constant, the more charge is needed to reach the electric field strength at the front of the discharge needed for ionization.

Mankowski and Curry describe the effect of different dielectrics and gasses [27], [28]. Most dielectrics Curry uses have a dielectric constant in the order of  $\epsilon_r \approx 3$  which is typically in the region of Teflon, PE, glass fiber and other materials which are often used as isolator or circuit board material in electronics.

In this chapter we describe a parameter study of a surface discharge in a 10 mm wide, 8 mm long gap as shown in Figure 2-1. The goal is to study the effect of gas type, pressure and dielectric constant on the development of the plasma. We try to realize a layer of plasma that is homogeneous, covers as much of the dielectric surface as possible, and forms a good conductive path as fast as possible. The width of the switch is chosen to be 10 mm, which is relatively small, to ensure the power and energy from the pulse source is adequate to form a plasma. Even though the small width of 10 mm of the electrodes, the experimental results are promising; the influence of edge effects at the corners of the electrodes is small enough to still be able to draw conclusions on a surface discharge from the measurements on the plasma behavior of a wider switch.

The load after the surface discharge is set to 50  $\Omega$ . This makes the surface discharge setup a scaled model for a 16 cm wide switch, roughly the width of the TLT input (which will be discussed in chapter 3), and have a load of 3  $\Omega$ .

In the first section we motivate why we chose to develop a surface discharge switch and describe the details of the surface discharge based on available literature. In the second section we describe the setup, pulse source and measurement systems followed by the measurements result and conclusions.

## 2.2 Surface discharge

As discussed in the introduction, a surface discharge is the preferred switch mechanism in our case. Besides its relative simplicity concerning its construction and the materials used, it also has beneficial properties that allow for E-field control in the gap and thereby a control over the development of the surface plasma. Figure 2-1 gives a schematic representation of the surface discharge switch and the electric field at the tip of the discharge. Because the grounding plane is close to the plasma, the vertical electric field component,  $E_y$ , is initially much larger than the horizontal electric field component,  $E_x$ . This is expected to influence the propagation velocity on the plasma allowing the discharge to form over the full width of the switch. The influence of the grounding plane is that the effect of the electric field of the load electrode has a minimal influence on the discharge until the front of the discharge is in close proximity to the load electrode.

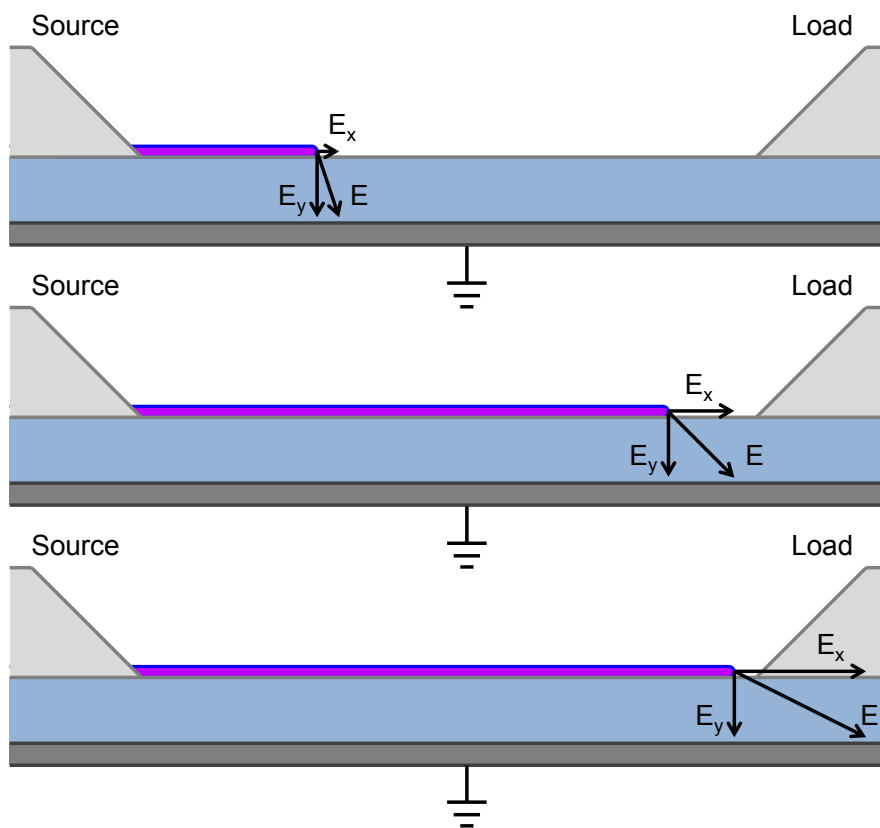


Figure 2-1. Electric field control in a surface discharge. Due to the nearby grounding plane, the E-field at the front of the discharge will obtain a significant forward component once its distance from the load is less than the thickness of the dielectric.

Ignoring field enhancement caused by the sharp edges, the electric field obtains a horizontal,  $E_x$ , component equal to the vertical component  $E_y$  once the front of the discharge is within a distance of the load electrode equal to the thickness of the dielectric. From this moment on, the discharge is expected to accelerate forward. Unfortunately we have not been able to observe this acceleration conclusively.

The closing action of the surface discharge starts once the discharge reaches the load electrode. Bearing this in mind, the advantage of the added electric field control becomes clear; until the plasma makes first contact with the load electrode the switch is still open and the propagation velocity of the plasma does not determine the performance of the switch. This allows for the manipulation of the plasma such that it can be optimized to form a good conductive path as fast as possible once it makes contact with the load electrode. In our setup this formation process can be influenced by changing gas type, pressure and the dielectric underneath the plasma.

Another advantage of the surface discharge is the effect of field enhancement at the tip of the electrodes as shown in Figure 2-2. In Figure 2-2 (a) a triple point is indicated by the black circle. The sharp edge of the high voltage electrode at the dielectric surface causes significant electric field enhancement [29]. Adding a small gap between the high voltage electrode and the dielectric can be used to further enhance the electric field as shown in Figure 2-2 (b). The gap between the high voltage electrode and the grounding plane can now be seen as two capacitances,  $C_{gap}$  and  $C_{diel}$ . The voltage over  $C_{gap}$ ,  $V_{C_{gap}}$ , is equal to

$$V_{C_{gap}} = \frac{C_{diel}}{(C_{gap} + C_{diel})} V_{HV} \quad 2-1$$

With  $V_{HV}$  the voltage on the high voltage electrode. The larger  $C_{diel}$  becomes with respect to  $C_{gap}$  the larger the voltage in the gap becomes. This is beneficial for igniting the plasma because the electric field enhancement allows for plasma ignition at lower voltages.

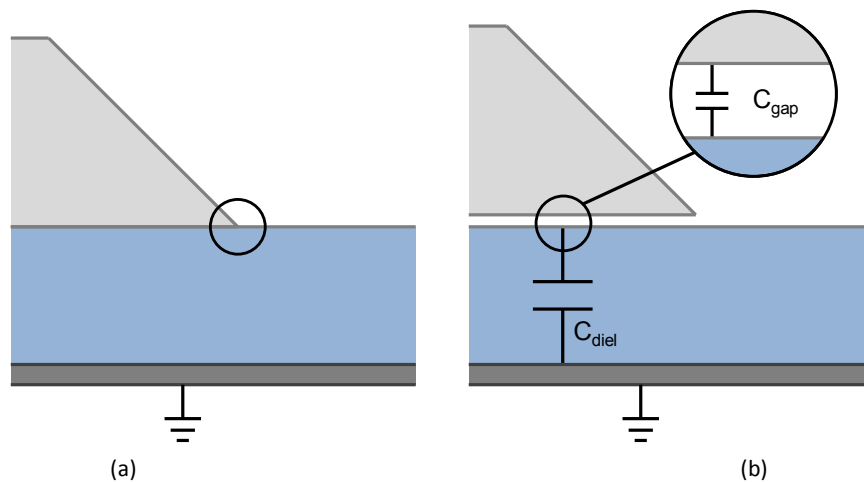


Figure 2-2. (a) The knife edge of the high voltage source and load electrode form a triple point at the dielectric surface causing significant electric field enhancement. (b) A small air gap between the electrode and the dielectric results in field enhancement due to the difference in dielectric constants between gas and dielectric. The higher the dielectric constant of the surface material, the stronger the effect.

The final advantage of the surface discharge switch, with respect to the spark gap, is shown in Figure 2-3. If the plasma covers the entire gap, it can be seen as one of the two conductors of a transmission line with a height  $h$  and width  $d$ . Fast transient signals in a transmission line only cause current in the innermost side of the conductors due to the skin effect [30].



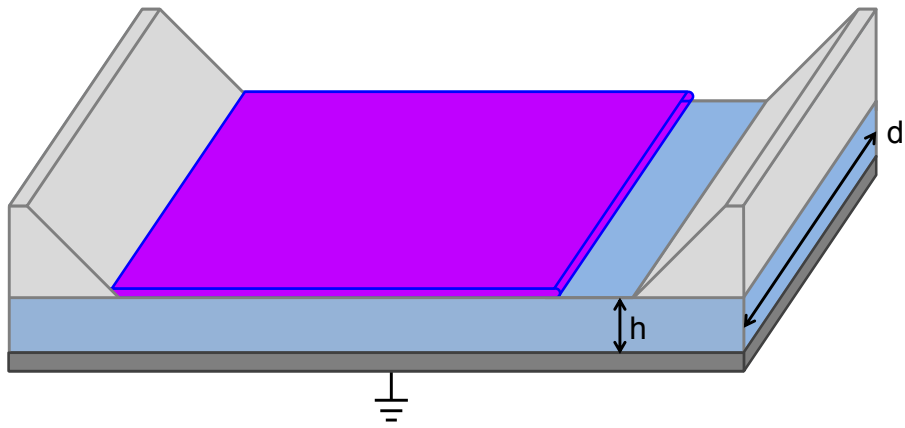


Figure 2-3. The surface discharge forms a transmission line making it less dependent on the thickness of the plasma.

The skin thickness is given by

$$\delta_s = \sqrt{\frac{2}{\omega \mu_0 \mu_r \sigma}}$$

2-2

With  $\sigma$  the conductivity,  $\omega$  the frequency in rad/sec,  $\mu_0$  the magnetic constant and  $\mu_r$  the relative permeability. For aluminum with a conductivity of  $3.56 \cdot 10^7 \text{ S/m}$  at a frequency of 1 MHz,  $\delta_s$  is roughly  $85 \mu\text{m}$ .

To estimate the skin depth in the plasma we first use eq. 2-2. The skin depth as a function of frequency and conductivity is shown in Figure 2-4. As can be seen, it is possible to achieve skin depth below 0.2 mm and even 0.1 mm. This indicates that a surface discharge, if its conductivity is sufficient, could function as a good conductor in a transmission line and thus inflict very little losses.

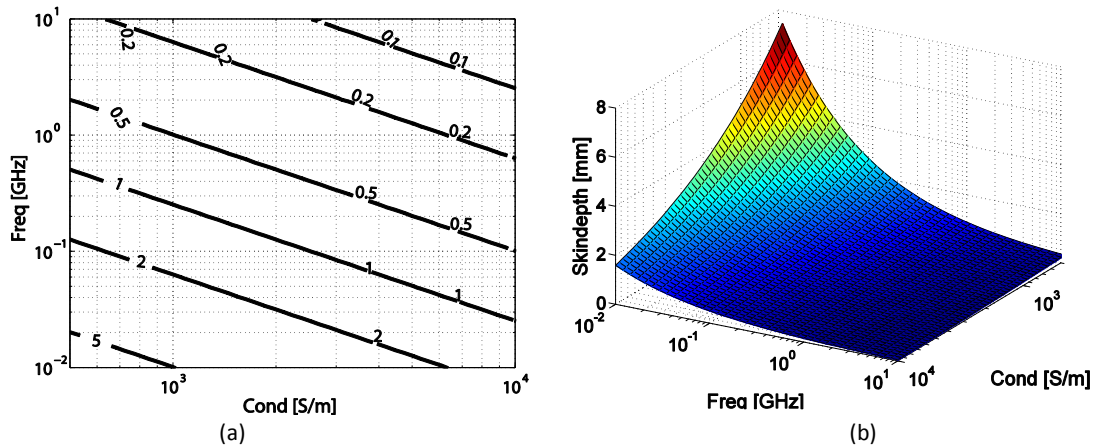


Figure 2-4. (a) Skin depth in [mm] as a function of frequency and conductivity. Used as first estimate for the skin depth in a plasma. (b) Surface plot of the skin depth.

To find a first estimate of the conductivity of the plasma, it is treated as a weakly ionized homogeneous plasma. This allows us to use the Lorentz gas model [31]; a plasma in which only the electron motion is important. When also assuming a constant and uniform electric field and no magnetic field, we find for the DC conductivity of the plasma

$$\sigma_0 = \frac{n_e e^2}{m_e \nu_c}$$

2-3

Here  $n_e$  is the electron density per  $\text{m}^3$ ,  $m_e$  the electron mass in kg,  $e$  the electron charge and  $\nu_c$  the effective constant collision frequency for momentum transfer between the electrons and heavy particles. To give an example we estimate  $\nu_c$  for a Lorentz gas model of a nitrogen plasma at 1000 mBar.  $\nu_c$  is given by

$$\nu_c = \frac{\bar{v}}{\lambda}$$

2-4

With  $\lambda$  the mean free path and  $\bar{v}$  the average velocity of the electrons defined as

$$\bar{v} = \sqrt{\frac{kT_e}{M_e}} \quad 2-5$$

Here  $M_e$  is the mass of the electron.

$\lambda$  is defined as

$$\lambda = \frac{1}{\sigma_{coll}n} \quad 2-6$$

Here  $n$  is the density of the neutral gas and  $\sigma_{coll}$  is the collision cross section. At a pressure of 1 Bar,  $n$  is  $2.5 \cdot 10^{25} \text{ m}^{-3}$ . In a weakly ionized plasma, the degree of ionization ranges from  $10^{-1}$  to  $10^{-6}$ . Based on [32] the total cross section  $\sigma$  for nitrogen at an energy of 0.1 eV is  $5 \cdot 10^{-20} \text{ m}^2$ . This results in a conductivity of  $2 \cdot 10^3 \text{ S/m}$ . The sole purpose of this rough and simple estimation is to show that the conductivity of a plasma could be of the order as shown in Figure 2-4 such that the skin depth can be made small enough to have the plasma function similar to a good conductor making the switch function as a wave guide.

### 2.2.1 Influence of gas and pressure

For a discharge to be a surface discharge, it must slide over the dielectric surface, covering a substantial fraction of the surface and be close to it. Figure 2-5 shows surface discharges in air at different pressures, shown from the side (see also Figure 2-9). These discharges are generated with 17 kV peak charging voltage. At 1000 mBar down to 100 mBar the discharges are on top of the surface. But, not visible in these sideview images, at the higher pressures the discharges forms arcs and thereby do not cover the whole surface. At 50 mBar, the discharge is no longer directly on top of the surface, there is a gap in between the surface and the discharge. At 20 and 10 mBar it is clearly seen that the discharge is even more removed from the surface. In this regime, the discharge has turned into a glow discharge. For our goals, a good surface discharge lies somewhere in the middle, covering a large surface while sliding directly over it.

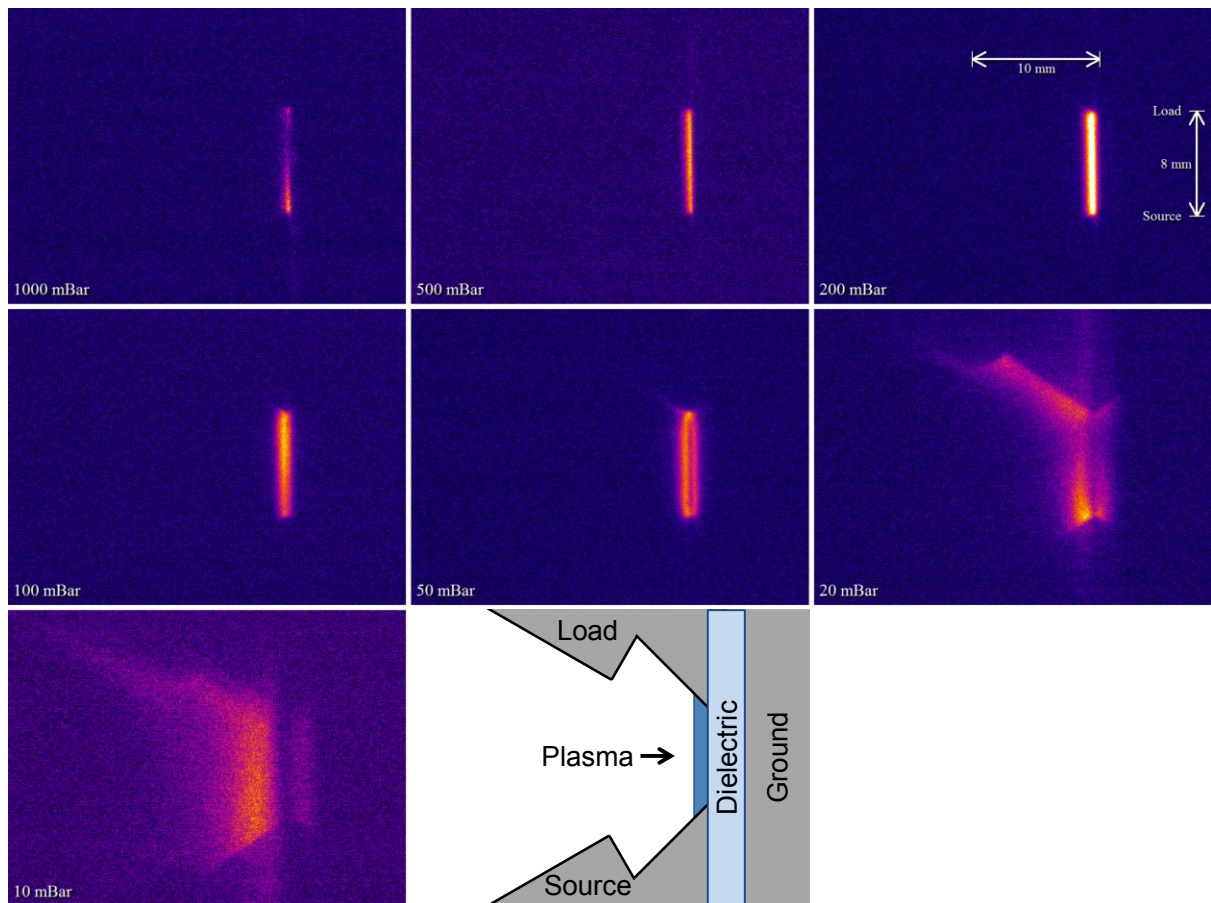


Figure 2-5. Side view of discharges in air with 17 kV charging voltage. Surface discharges are seen at pressures from 100 to 1000 mBar. At 50 mBar and lower pressures, the discharge no longer slides over the surface.

### 2.2.2 Influence of dielectric

Not only the gas and its pressure have a significant influence on the behavior of the discharge in the gap. Also the dielectric and its material properties play a significant role. As mentioned in the introduction, many materials have been studied but all have a relatively low dielectric constant. We study the effect of  $\text{SrTiO}_3$ , with a dielectric constant of the order  $10^3$ , on the performance of the plasma. There are three reasons why the use of a high dielectric constant material could be of interest for a surface discharge switch.

First, as stated by Reinovsky, the plasma has resistance. When the plasma grows, it becomes increasingly difficult to get the electric field, needed for ionization, at the plasma front. To overcome this, the energy must come from the plasma directly behind the discharge front. If Reinovsky is right, this would mean that the energy is mainly delivered to the plasma by the (capacitance) between the surface plasma and the ground plane. Thus more energy will become available for ionization during the development of the surface plasma. An increase of  $\epsilon_r$  gives an increase of this capacitance. Due to the larger capacitance it takes longer to achieve the electric field strength needed for ionization which might slow down the propagation velocity of the plasma.

The second motivation to study high dielectric constants is to influence the closing behavior of the switch. In the measurements above we have seen that closure of the switch starts after the phase in which the plasma crosses the dielectric. Closing of the switch is characterized by the increase of the load voltage and current. The electric field inside the dielectric will influence the electric field in the plasma. If the propagation velocity of the electric field is lowered, more charge can accumulate in the plasma allowing for the faster construction of a conducting path between the electrodes in the final phase when the discharge connects with the load electrode. When increasing the dielectric constant the propagation velocity of the electric field inside the dielectric will decrease according to

$$v = \frac{c}{\sqrt{\epsilon_r}}$$

2-7

The propagation velocity of the plasma varies between the  $1 \cdot 10^6$  and  $8 \cdot 10^6$  m/s depending on gas type and pressure. To achieve a propagation velocity below  $1 \cdot 10^6$  m/s for the electromagnetic field in the dielectric, an  $\epsilon_r$  of 90000 is needed. This is an extreme high value. The highest dielectric constant we could find is that of  $\text{SrTiO}_3$  which is 2000, according to [Robertson]. With such an  $\epsilon_r$   $v$  would become  $6.7 \cdot 10^6$  m/s. This is within the range of the propagation velocities we reach with the plasma. Still, in our case it is unlikely this effect plays a significant role.

The third motivation to study high  $\epsilon_r$  materials shows the advantage of a surface discharge switch over a rail gap switch. Due to the dielectric, which has much better insulating properties than a gas, a grounding plane can be placed close to the high voltage electrodes. This allows for control of the vertical component of the electric field. Whereas with the rail gap, the main electric field component is directed from one electrode directly to the other electrode, here it is possible to have the electric field point vertically downwards. When assuming static electric fields at a dielectric interface we know

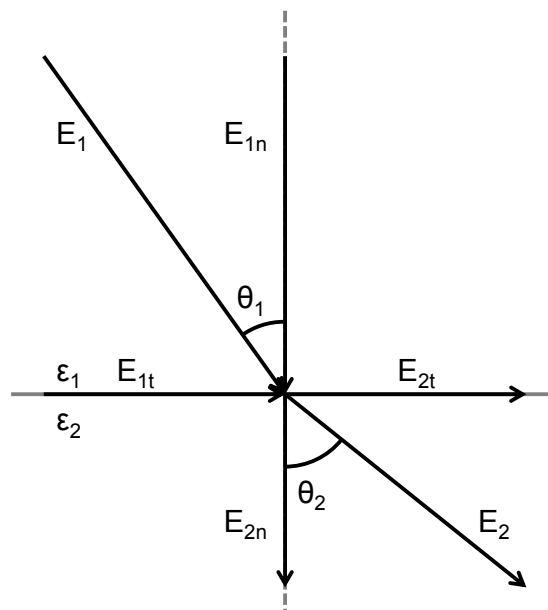


Figure 2-6. Static electric field at a dielectric boundary assuming no surface charge.

$$D_{n1} - D_{n2} = \rho \quad 2-8$$

When we assume no surface charge is present,  $\rho$  is zero and we get

$$E_{t1} = E_{t2} \quad 2-9$$

$$E_{n1} = \epsilon_2 E_{n2} \quad 2-10$$

The normal component of the electric field just above the dielectric surface is larger than the normal component of the electric field in the dielectric surface. And this difference increases with the dielectric constant. The advantage of this effect is that the plasma experiences an electric field mainly pointed downwards. It isn't until the front of the plasma is very close to the load electrode that the horizontal field component becomes dominant and accelerates the plasma towards the load electrode. This effect allows for a better control of plasma propagation and allows for a uniform plasma front to develop.

Finally, as can be seen in Figure 2-7, a larger  $\epsilon_r$  results in a larger electric field in the air gap underneath the electrode. This makes ignition of the plasma easier.

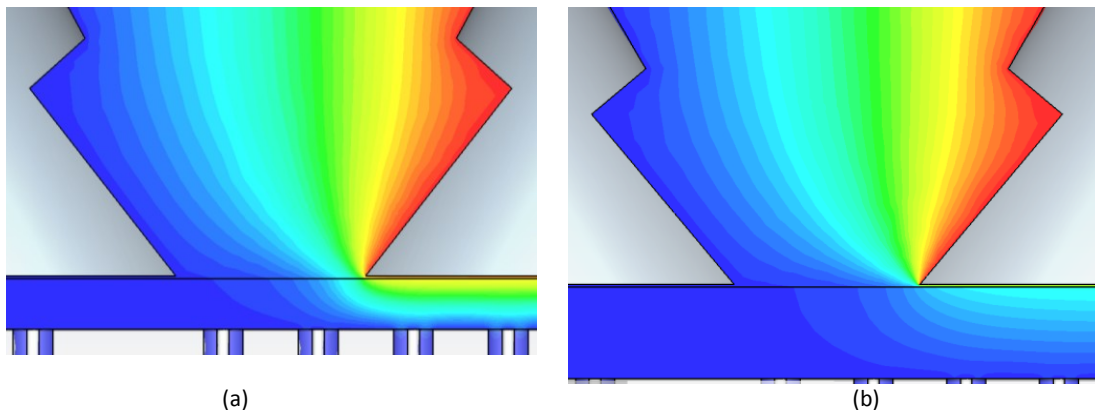


Figure 2-7. Equipotential lines, (a)  $\epsilon_r = 6.7$ , (b)  $\epsilon_r = 100$ . As can be seen, using a higher  $\epsilon_r$  forces a larger voltage drop over the gap in between the source electrode (on the right of both images) and the dielectric, see Figure 2-2b. This significantly enhances the electric field nearby the source electrode and thereby the ignition of the plasma.

## 2.3 Experimental setup

The setup used to study the surface discharge is shown in Figure 2-8. A Megalmpulse high voltage pulse generator, [33], is connected to a 100 meter long coaxial cable. A Pearson 6600 current monitor is placed directly at the output of the pulse source. The output of this current monitor is used as trigger signal for the camera and oscilloscope. The 100 meter cable gives a time delay in the order of 500 ns which is used to compensate for the internal delay of the camera. The output of the coaxial line is terminated with a 50  $\Omega$  HVR linear disk resistor stack in parallel with the switch which itself is connected in series with another 50  $\Omega$  HVR linear disk resistor stack. The entire setup is placed in a

vacuum vessel so different gas types and pressures can be used. The parallel  $50\ \Omega$  resistor ensures the setup is matched with the output of the source in case the switch does not close. This prevents a pulse will be reflected back towards the source. The resistor in series with the switch makes the setup a representative scaled version of a wider switch as will be discussed later in this section and in chapter 3.

The switch input voltage is measured with a North Star PVM 1 voltage probe. The current through the  $50\ \Omega$  load resistor underneath the switch is measured with a Pearson 6600 current monitor.

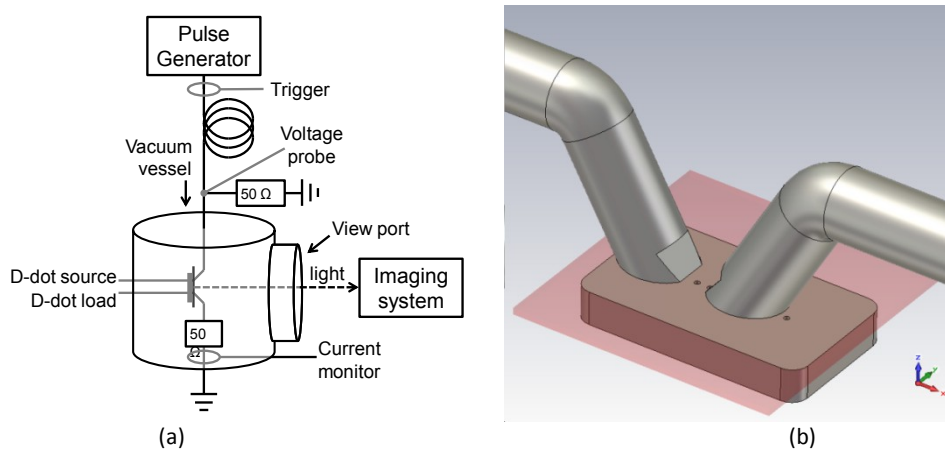


Figure 2-8. (a) Schematic representation of the vacuum vessel, pulse source and imaging system. (b) 3D model of the surface discharge gap. The dielectric plate is shown in transparent red.

The switch is schematically shown in Figure 2-9. Both the source and load electrode are aluminum rods with a diameter of 20 mm. The tips of the electrodes are made of copper-tungsten. The electrodes are placed under an angle of 60 degrees on the surface. The knife edge like tips of the electrodes are under an angle of 50 degrees with the surface and are 10 mm wide. The dielectric is a square plate of 80 x 80 mm with a maximum thickness of 8 mm. The setup is supported by a PEEK construction which gives flexibility in placing the electrodes on the dielectric surface. We have chosen for a 10 mm wide, 8 mm long gap for two reasons; it ensures the power and energy, delivered by the pulse source, is sufficient to achieve adequate levels of ionization and it is optimal for the optical imaging to have a square area to focus on to use as much of the camera CCD area as possible.

A grounding plane is placed underneath the dielectric. In this grounding plane four D-dot sensors are placed of which one directly under the source electrode and one directly under the load electrode. The positions of the D-dot sensors are shown in Figure 2-9.

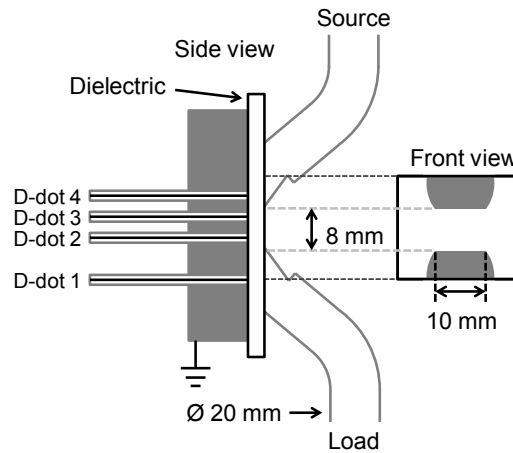


Figure 2-9. Schematic side view of the surfaced discharge setup.

### 2.3.1 Pulse source

The pulse voltage used to generate the plasma in all experiments is shown in Figure 2-10. The main pulse starts just before  $t = 0 \text{ ns}$  and it reaches a peak voltage of 38 kV with a maximum rise time of  $(3.7 \pm 0.1) \cdot 10^{12} \text{ V/s}$ , Figure 2-10 (Right). This rise time is more than sufficient to ignite multiple parallel surface discharges [Bergmann]. The full width at half max, *FWHM*, of the main peak is 15.5 ns and the total duration of the entire pulse is 140 ns.

Around -75 ns, the output of the source rises to 5 kV after which it slowly drops to 4 kV just before the main pulse. This is a characteristic artifact of the pulse source used and could not be prevented. Undesired ignition of the plasma is prevented in all experiments by avoiding experimental parameters where this can occur.

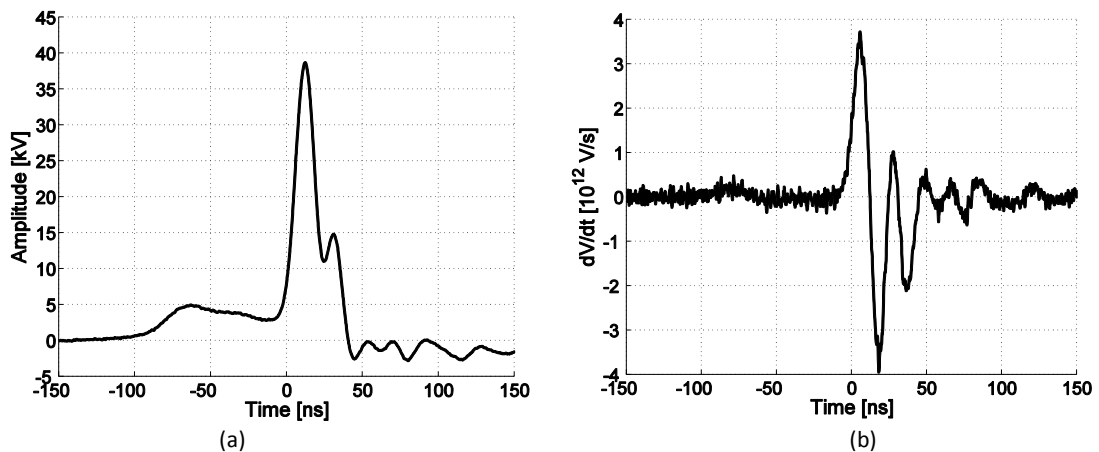


Figure 2-10. (a)  $V_{\text{source}}$  pulse. (b) time derivative of  $V_{\text{source}}$ . The peak values of the time derivative show the source pulse is fast enough to ignite multiple parallel discharges.

If needed, the voltage applied to the surface discharge switch (SDS) can be reduced by splitting off a fraction of the main pulse source at the  $50 \Omega$  HVR matching resistor at the input of the vacuum vessel.

The simplified electric network of the setup is shown in Figure 2-11. Here  $R_1$  and  $R_2$  together are  $50 \Omega$  as is  $R_3$ . With the SDS open, the output of the source is matched with  $50 \Omega$ .



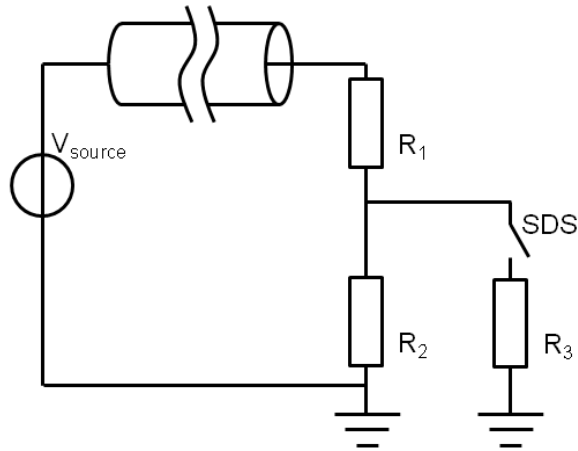


Figure 2-11. Simplified network of the setup.

In this matched case, if the SDS does not close during the pulse, the output power and energy of the source are shown in Figure 2-12. In this case the pulse delivers 420 mJ with a peak power of 30 MW.

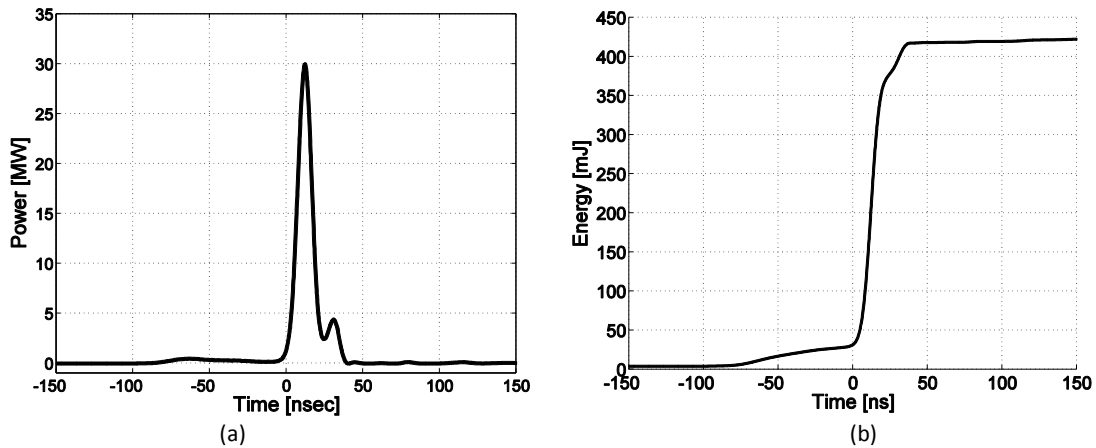


Figure 2-12. Power and energy in the source pulse for a matched load.

When the SDS is closed, the series connection of the SDS and  $R_3$  is in parallel with  $R_2$ . This changes the total impedance  $Z_t$ .

$$Z_t = \frac{(Z_{sw} + R_3)R_2}{(Z_{sw} + R_3) + R_2} + R_1 \quad 2-11$$

For a simple estimation, the SDS impedance,  $Z_{sw}$ , is assumed to be ohmic. The total impedance  $Z_t$  is shown in Figure 2-13 as a function of the SDS impedance  $Z_{sw}$ . If  $R_1$  is larger than  $30 \Omega$ , the total impedance,  $Z_t$ , seen by the pulse source, is larger than  $44 \Omega$ . Even if the SDS is perfectly conducting. Thus the pulse source is reasonably matched for all the experimental conditions.

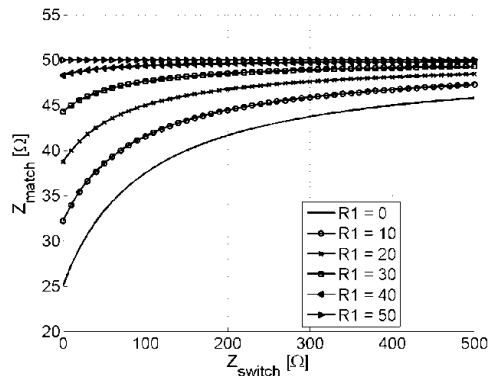


Figure 2-13. Influence of the SDS impedance on the matching with the pulse source.

### 2.3.2 Voltage and current measurement

To measure the voltage over and the current through the SDS we use a North Star PVM 1 probe and the Pearson 6600 current probe respectively. The oscilloscope is a LeCroy WavePro 7300A with a sampling rate of 10 GS/s on each of the 4 channels. The North Star signal is attenuated 10 dB and the Pearson current probe output is attenuated 20 dB using 50 Ω attenuators. The bandwidth of the attenuators used is much larger than the bandwidth of the probes and the oscilloscope.

The 80 MHz bandwidth of the North Star and the 70 MHz bandwidth of the Pearson probe is sufficient to measure a pulse as shown in Figure 2-10. But it is expected that the various development stages of the surface discharge take place on a (sub-) nanosecond timescale. Although the North Star and Pearson probes can follow the signals, details of the discharge behavior might get lost. Figure 2-14 shows the source and load voltage as measured with the North Star and Pearson probes. Here we used air at a pressure of 1000 mBar. The dielectric is 2 mm thick optical glass with an  $\epsilon_r$  of 6.7. To obtain the load voltage, the current, as measured by the Pearson probe, is multiplied with 50 Ω of the load resistor. The resonance, as seen on the load voltage, has a frequency of 650 MHz and is an internal resonance of the Pearson probe. The resonance is suppressed by filtering the signal afterwards.

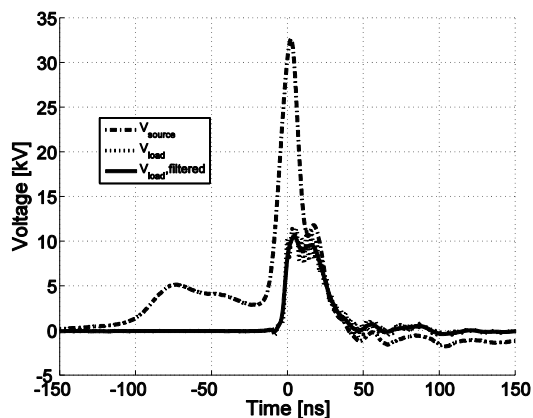


Figure 2-14. Source voltage, unfiltered load voltage and filtered load voltage.

### 2.3.3 Optical diagnostics

A Stanford Computer Optics Digital 4-Picos ICCD camera with a shutter time  $\geq 200$  ps is used to study the plasma development. To minimize the influence of jitter in the trigger system on the velocity

measurement, two images are made of each discharge simultaneously with one camera. The optical setup is shown in Figure 2-15. Both optical paths deliver an image of the discharge to the camera. By changing the path length with respect to each other, a time delay can be created between the two images. Using a total path length difference of 15 +/- 0.5 cm, the discharge images have a time delay of 500 ps +/- 17 ps. The jitter in the trigger system will still affect how well known the moment is at which the images are made. But the time difference between the two images is known with picoseconds accuracy. Making a large series of images of the discharge allows us to get a very clear idea of the discharge development. The two lenses are 3" achromatic lenses with a focal length of 40 cm. the mirrors are silver coated 70 mm diameter elliptical mirrors. The lens on the camera is a Sigma 70-300 F4-5.6 macro-zoom lens.

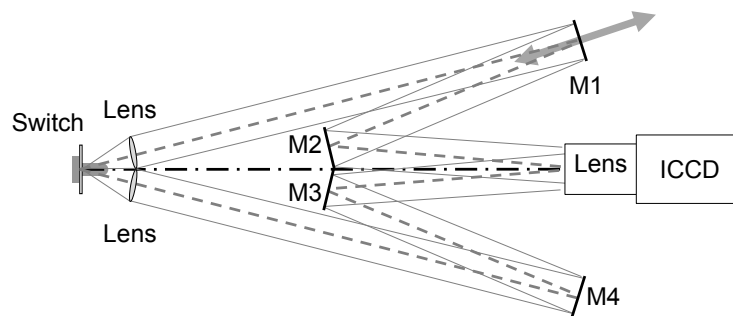


Figure 2-15. Schematic top view of the optical setup used to make 2 images of one discharge with a delay of 500 ps +/- 17 ps in between the images.

Figure 2-16 explains what can be observed from the discharge images. In this figure, the source electrode is shown at the bottom and the load electrode at the top. On the left side the discharge at time  $t_n$  is shown and on the right the same discharge is shown at time  $t_n + 0.5 ns$ . The dotted areas represent the gap of the SDS.  $t_n$  is known with an accuracy determined by the timing accuracy of the imaging system. But the time difference between the two images is determined by the optical setup and is set to 500 ps  $\pm$  17 ps. The discharge propagation velocity is found by measuring the position of the front of the plasma in the two images. Appendix B describes this procedure in more detail.

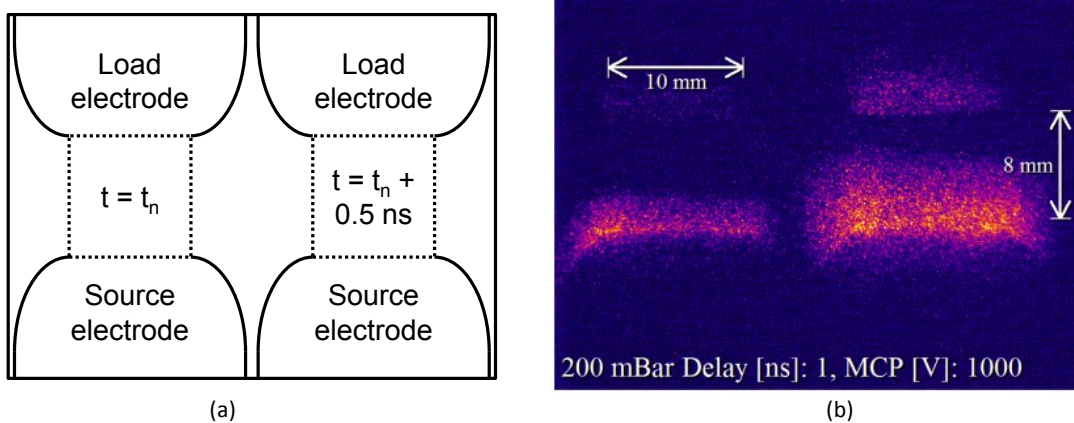


Figure 2-16. (a) Schematic image of a discharge, The left and right image are similar but have a time delay of 500 ps  $\pm$ 17 ps. (b) Example of a discharge image in air at 200 mBar.

### 2.3.4 D-dot sensors

To get a better understanding of the discharge development, additional capacitive sensors are placed in the grounding plane. These D-dot sensors are also used to measure the electric field in the Kumamoto Blumlein Pulsar which is treated in detail in chapter 4. Measuring the voltage with the D-dot sensors has two advantages; the voltage is measured very close to the gap and, due to the small size of the sensors, a higher bandwidth, and thus faster voltage changes, can be measured. Due to the small size and thus large bandwidth of these sensors, they can be treated as ideal differentiators for the frequencies we can measure.

Four D-dot sensors are placed in the grounding plane of the Surface Discharge Switch as shown in Figure 2-9. The sensors consist of RG-405 rigid coax cables that are placed flush into the grounding plane. Sensors 1 and 4 are directly underneath the load and source electrodes respectively. Sensors 2 and 3 are underneath the surface over which the plasma propagates. Sensor 1 and 2 are spaced 8 mm apart. Sensor 2, 3 and 4 are 4 mm apart. Sensor 2 and 3 are both 2 mm from the center of the gap and are each 2 mm from the nearest electrode edge. Figure 2-17 shows the capacitive couplings between the D-dot sensors and the electrodes that play a significant role.

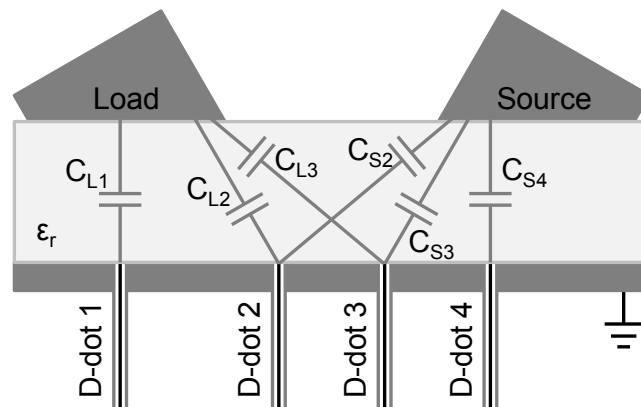


Figure 2-17. The capacitive coupling between the D-dot sensors and the high voltage electrodes.

Here, the use of such sensors is more complicated than with the Kumamoto Blumlein. The time dependent variation of the plasma coverage along the dielectric surface, [34], causes the capacitive coupling between the D-dot sensors and the high voltage electrodes to change. Therefore the current through each capacitance depends on both the change in applied voltage and change in capacitance

$$I = C \frac{dV}{dt} + V \frac{dC}{dt} \quad 2-12$$

Eq. 2-12 is sufficient to obtain the source and load voltage based on the output voltage of D-dot 4 and 1 respectively since their output is only influenced by the electrode directly above them. The capacitive coupling with the other electrode is so small, it can be neglected. The capacitance and the change in capacitance are estimated using numerical simulations and optical images. This is described in appendix A.

D-dot 2 and 3 experience another effect; both the source and the load electrode are close to these D-dot sensors and thus the output of the D-dot sensors is influenced by both, as shown by eq. 2-13.

$$I_x = C_{Sx} \frac{dV_S}{dt} + V_S \frac{dC_{Sx}}{dt} + C_{Lx} \frac{dV_L}{dt} + V_L \frac{dC_{Lx}}{dt} \quad 2-13$$

The D-dot output voltage is determined using

$$V_x = I_x R_x \quad 2-14$$

With  $R_x$  the 50  $\Omega$  impedance of the rigid RG-405 line. Here we use two assumptions; the voltage at the load,  $V_{load}$ , is negligible until the moment the plasma fully covers the gap and the plasma resistance can be neglected. These assumptions allow us to simplify eq. 2-13 to eq. 2-12. Although these assumptions are very crude, they allow for a first estimate of the voltage in the gap and the signals of the different D-dot sensors can be compared with each other. Even if the absolute voltage is not measured correctly, the D-dot sensors do give more insight in the dynamic behavior of the plasma.

Figure 2-18 shows an example of a single shot recording of the D-dot output voltages and the derived source voltage,  $V_{source}$ , and load voltage  $V_{load}$ .

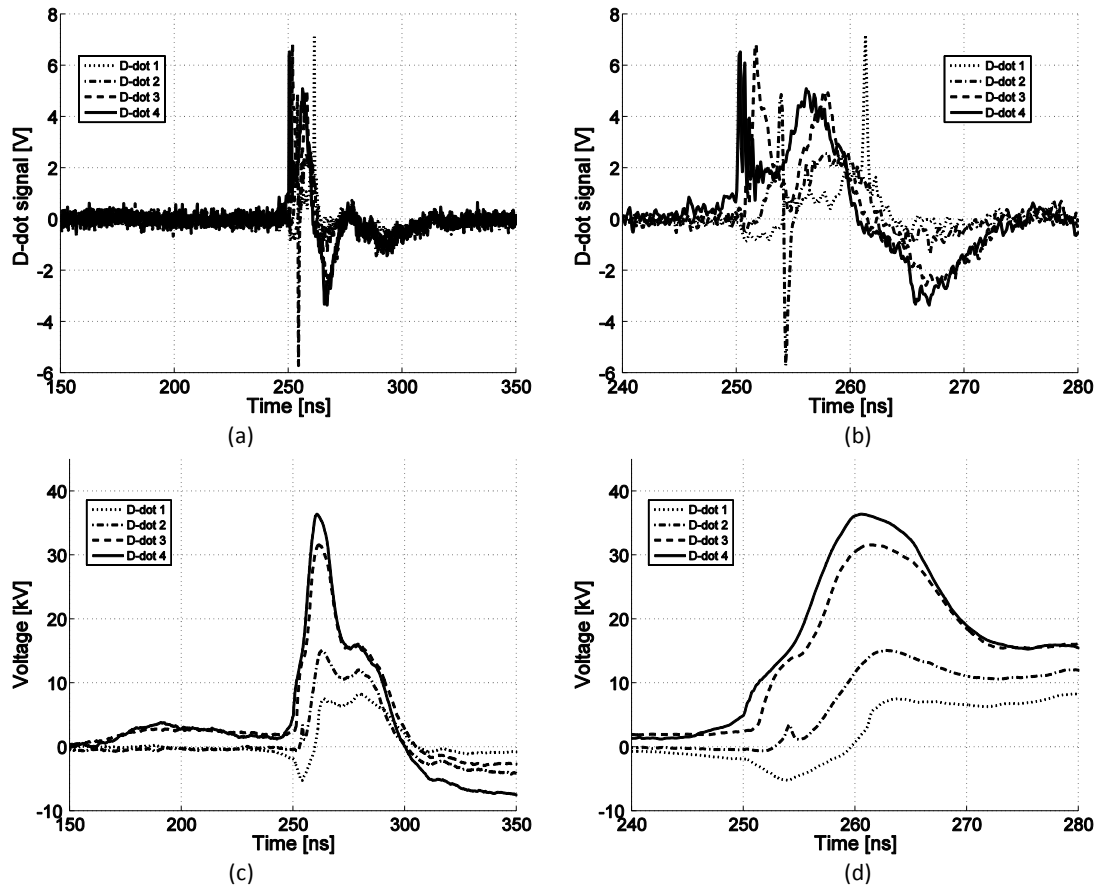


Figure 2-18. Single shot recording of the 4 D-dot sensors. (a)  $V_{D-dot}$ , (b)  $V_{D-dot}$  zoomed view of plasma growth phase. (c) Estimated voltages in the gap based on  $V_{D-dot}$ . (d) Zoomed view of the estimated voltages in the gap.

The valuable information in the D-dot measurement is best shown in Figure 2-18b. Each sensor shows a clear spike at a different moment in time. As we will see later, there seems to be a very strong correlation between the timing of these spikes and the development of the plasma as seen in the optical images. The first spike, D-dot 4, can be related to the ignition of the plasma at the source electrode. This spike can be explained by the fact that the plasma, at the moment of ignition, fills the air gap in between the source electrode and the dielectric (see Figure 2-2b for this air gap). This results in a sudden increase of the capacitance and hence, eq. 2-12, the D-dot current experiences a spike and so does its output voltage. The second and third spike, D-dot 3 and D-dot 2, indicate the passing of the plasma at the respective sensors. The final spike, on D-dot 1, indicates a sudden change in voltage and or capacitance at the load. Striking is the time difference between the spikes measured on D-dot 1 and D-dot 2. This time difference is much larger than the other time differences. Optical images have not shown plasma propagation velocity variations that would explain this difference. It is thought that the pulse at D-dot 1 occurs when the voltage at the load electrode is so high a plasma is formed in between the electrode and the dielectric. This would cause a similar capacitance increase as described with D-dot 4 and explain the measured pulse.

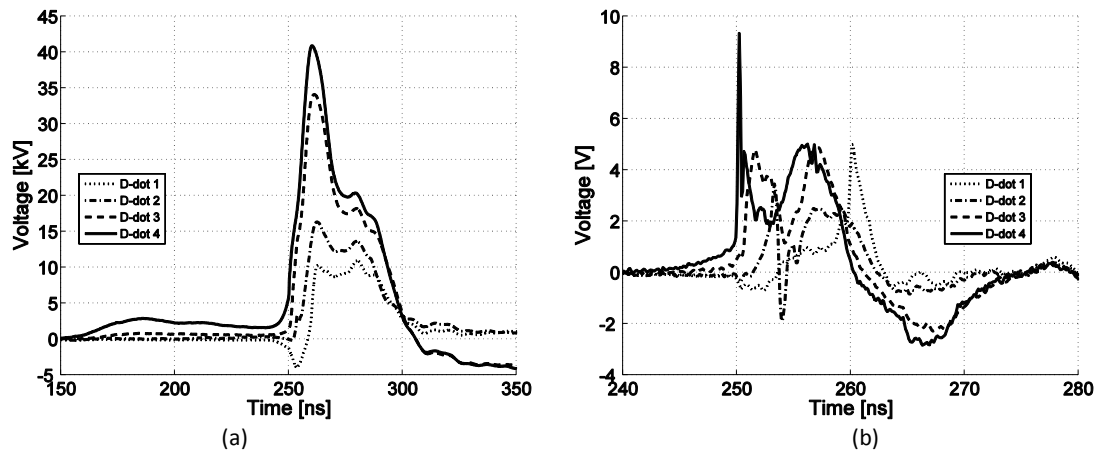


Figure 2-19. 50 shot average of the 4 D-dot sensors. (a) estimated voltages in the gap based on  $V_{D-dot}$ . (b) zoomed view of  $V_{D-dot}$ .

Figure 2-19 shows the average of 50 shots. As can be seen, by averaging a lot of details are lost in the  $V_{D-dot}$  signals. Although the discharge reproduces very well and each shot has the same characteristic, at these time scales the details vary slightly from shot to shot. The added information obtained by the D-dot sensors is in these small details, the very sharp spikes, and they are lost by averaging. Therefore we will treat single shot recordings.

Obtaining a good representation of  $V_{source}$  and  $V_{load}$  based on the D-dot sensors is sensitive to the parameter settings and is not always successful. Still, the D-dot sensors show valuable information of the plasma dynamics. Besides this, the detection of the ignition of the plasma, done with D-dot 4, is used directly to synchronize the electric and optical measurements.

### 2.3.5 Synchronization of optical and electric measurements

To couple the optical images to the voltage measurements in time, we can use two different methods. The first is to take all the cable lengths and equipment delays into account. This works well when also taking the optical delays and the difference in point of measurement into account and when all internal delays of the equipment are known. In our case, the last item could not be fulfilled. The internal delay of the camera is known with an accuracy of  $\pm 10$  ns. Secondly the confirmation signal received from the camera when taking a picture has a minimum width of 7 ns, even when the shutter time is much shorter. This method leaves us with an uncertainty in time of roughly 10 to 15 ns which is too much for our application. The second method uses the D-dot sensors. Here we use the fact that the ignition of the plasma generates a spike on the output of the D-dot sensor directly underneath the source electrode. This is shown in Figure 2-20 for air with a pressure of 1000 mBar and a 38 kV peak charging voltage. The D-dot signal can be compared, and matched in time, with the derivative of the source voltage measurement.

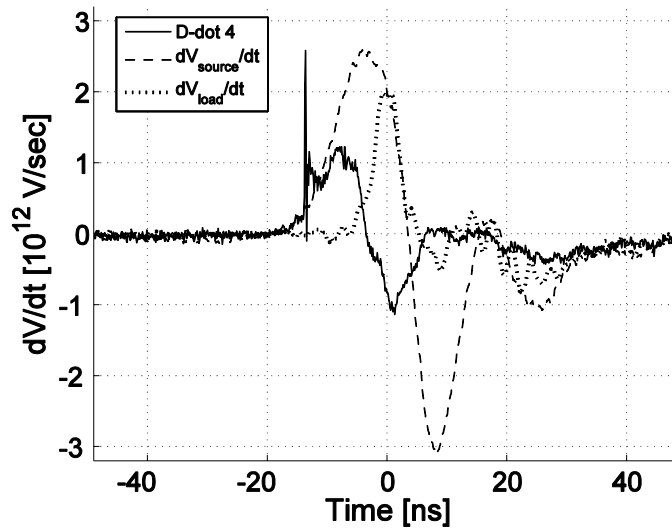


Figure 2-20. Matching the timing of the different time derivatives of the measured voltages. The spike in the D-dot signal indicates the ignition of the discharge.

Here  $V_{D-dot 4}$  has been scaled by a factor of three to fit over  $dV_{source}/dt$ . Up to -13 ns,  $dV_{source}/dt$  and  $V_{D-dot 4}$  overlap nearly perfect. At -13 ns, a spike occurs in  $V_{D-dot 4}$  indicating the ignition of the plasma. This changes the capacitive coupling between the source electrode and the D-dot sensor. At -6 ns  $V_{D-dot 4}$  decreases and  $\dot{V}_{load}$  increases. From this we could estimate that, for the plasma parameters of this example, it takes in the order of 7 ns to form a sufficiently conducting path which allows for the increase of the load voltage. Comparing these results with the optical images gives a good impression of the plasma development.

## 2.4 Results

Here we characterize the quality of the switch by the transferred energy and the rise time of the load voltage. Both these properties are strongly influenced by the behavior of the plasma. To study the plasma behavior and the switch performance, four parameters are varied; gas type and pressure, dielectric constant and charging voltage.

In this section we discuss the effect of these parameters on the plasma behavior and switch performance. To characterize the plasma behavior we study the avalanche velocity and the structure of the plasma.

Three different gasses are selected; air, argon and helium. The latter two are both with a purity of 5.0 ( $\geq 99.999\%$ ). The air used in the experiments is plain simple air from the laboratory and therefore not conditioned except for pressure and temperature ( $21^\circ\text{C} \pm 3^\circ\text{C}$ ). Air is studied because of its abundance and its simplicity in use. Helium and argon are studied because they are inert, are not electro negative like oxygen and for their difference in ionization potential. All experiments are done at pressures that vary from 10 to 1000 mBar. At pressures lower than 100 mBar, a glow discharge occurs at numerous places in the vacuum vessel. For pressures higher than 1000 mBar, the charging voltage is not high enough to initiate a discharge.



## 2.4.1 Discharges in Air

Figure 2-21 shows the voltages at both electrodes for discharges in air at 1000, 500 and 200 mBar.

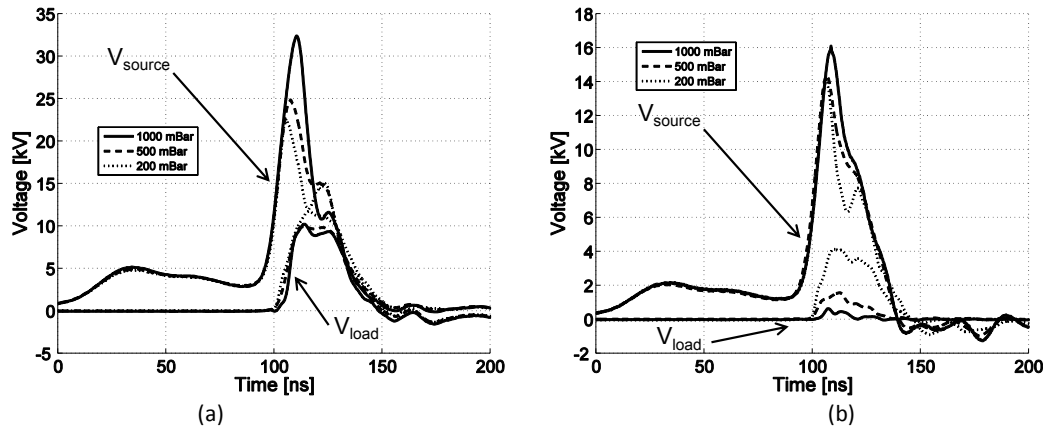


Figure 2-21. (a) Source and load voltage using air, 38 kV peak charging voltage and  $\epsilon_r = 6.7$ . (b) 17 kV peak charging voltage.

Figure 2-21 (a) shows the average of 50 shots using a charging voltage of 38 kV. As discussed, the initial increase in source voltage from around 35 ns, is an artifact of the pulse source. At around 90 ns, the source voltage increases up to the point of inception and the plasma is ignited. After reaching the inception voltage the source voltage drops in roughly 10 ns to somewhere between 1 and 5 kV above the load voltage, depending on the pressure, at around 125 ns. The peak in the source voltage indicates a strong overvoltage, aiding in the formation of the plasma during the plasma inception phase. The overvoltage is lost once the plasma starts to conduct. The voltage difference between  $V_{source}$  and  $V_{load}$ , after 120 ns, can be used as an indication for the conductivity of the plasma.

Using the 17 kV charging voltage, Figure 2-21 (b),  $V_{load}$  is much smaller than  $V_{source}$  and no good conducting plasma is formed. Only when using a pressure of 200 mBar a decent  $V_{load}$  is generated but still roughly half of  $V_{source}$  is lost over the switch. From this voltage drop, combined with a load impedance of 50  $\Omega$ , the plasma impedance could roughly be estimated to be in the order of 50  $\Omega$ .

Nevertheless, a discharge still occurs. But now, only for the 200 mBar case a conducting path is formed. In the 500 and 1000 mBar case, the discharge does not develop to a fully conducting path and  $V_{load}$  is significantly smaller than  $V_{source}$ . The peak power and energy supplied to the load for the different settings is shown in Table 2-1. For both charge voltage settings the 200 mBar setting performs best when it comes to energy transfer and peak power. The maximum  $dV_{load}/dt$  is obtained with 1000 mBar and 38 kV.

Table 2-1. Peak power and energy delivered to the load electrode.

Pressure	[mBar]	1000	500	200	1000	500	200
$V_{\text{charge}}$	[kV]	38	38	38	17	17	17
$P_{\text{peak}}$	[kW]	2110	1980	2770	5	50.5	346
E	[mJ]	44	52	70	0.05	0.7	6.9
Max $dV_{\text{load}}/dt$	[kV/ns]	2.2	1.2	1.3	0.1	0.3	0.7

### 2.4.1.1 Observations with the D-dot sensors

#### 2.4.1.1.1 Charging voltage 38 kV

The voltages as measured by the D-dot voltages are shown in Figure 2-22, Figure 2-23 and Figure 2-24 for 1000, 500 and 200 mBar respectively. In every figure (a) shows the D-dot voltages during the pulse and (b) during plasma ignition. The numerical integration of the D-dot sensor signals results in the estimated voltages as shown in (c) and the zoomed view in (d).

The shape of the voltages as measured with the North Star and Pearson probes is clearly recognized. Besides the good agreement with the North Star and Pearson probes, the D-dot sensors give a more detailed view of the dynamics of the plasma.

The time delay between the spikes of the different D-dot sensors decreases with decreasing pressure. At 1000 mBar the delay between the first and the last peak is in the order of 11 ns. For both 500 and 200 mBar this delay is in the order of 6 ns. As we will see later, this timing agrees very well with the observations made with the optical images. Comparing the timing of these spikes with the maximum  $dV_{\text{load}}/dt$  from Table 2-1 shows a difference. At 1000 mBar the time delay between the spikes is largest but also the maximum  $dV_{\text{load}}/dt$ , which is counter intuitive. This gives a strong reason to believe that, even though the spikes tell something about the plasma dynamics, the timing between the spikes cannot, in this case, be directly correlated to switch closing time.

An interesting detail in the load voltage, which is not observed with the Pearson current probe, is the negative voltage drop just before the load voltage rises. As can be seen this drop starts together with the spike in the source electrode. When a fast pulse occurs on the source electrode, the voltage of the grounding plane is lifted due to the capacitive coupling. The load electrode, which has a much weaker capacitive coupling with the source electrode, remains at the same voltage. Since the grounding plane is the reference potential for the D-dot sensors, D-dot sensor 1 will experience a negative voltage from the load electrode. This pulse is not observed with the Pearson probe because the Pearson probe measures current but, at this moment during the discharge there is no significant current through the load electrode.

Figure 2-23 shows the D-dot signals and the estimated electrode voltages for air at a pressure of 500 mBar. Here the inception voltage is smaller than in the 1000 mBar case. Also with the North Star and the Pearson probes a lower inception voltage, with respect to the 1000 mBar case, is measured.

An interesting detail in Figure 2-23 (d) is the gradual change in the shape of the calculated voltages. Whereas D-dot 4 shows similarities with the North Star measurement, D-dot 1 does this with the Pearson measurement. D-dot 2 shows a lot of similarity with D-dot 1 and D-dot 3 with D-dot 4. The

4 voltage measurements give insight in the voltage drop in the switch as a function of position. In this particular case it gives the impression that the largest voltage drop occurs in the center of the plasma.

For both 1000 and 500 mBar, the calculated voltage from D-dot 4 and 3 are relatively close to each other when taking the integrated offset into account. The same holds for D-dot 1 and 2 on the load side. This gives the impression, that a significant voltage drop is present over the plasma. Now looking at the 200 mBar case, the difference in the shape of the calculated voltages is much smaller. This gives the strong impression of a significant reduction of the plasma impedance.

At a pressure of 200 mBar a striking difference is observed for both the 500 and 1000 mBar case. D-dot 4 shows 2 spikes, instead of 1, spaced roughly 6 ns apart and the first spike is negative in contrast to what we have seen at 1000 and 500 mBar. Also D-dot 2 and 3 show two spikes, spaced 6 ns apart. D-dot 1 shows very small spikes. As we will see in the plasma images, the discharge at 200 mBar is much more glow like. The occurrence of 2 peaks on each D-dot sensor could indicate that multiple processes play a significant role in the formation of the plasma.

For decreasing pressure, the time between the different spikes decreases. The spikes also seem to group together indicating that at lower pressures the formation of good conducting plasma has 2 critical moments whereas at higher pressures the formation is more gradual. The calculated voltages, and the North Star and Pearson measurements support this, the source and load voltages reach similarity much faster at lower pressures, indicating faster formation of conducting plasma.

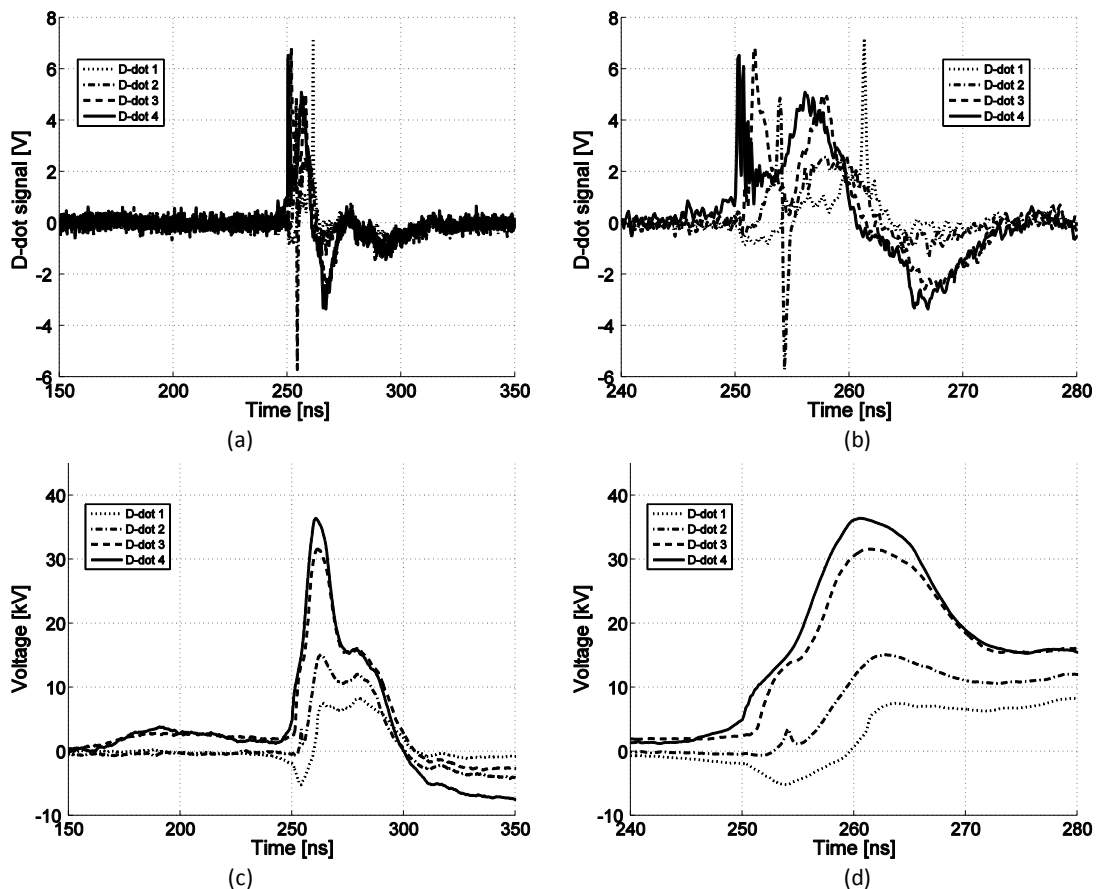


Figure 2-22. 1000 mBar, 38 kV. (a) D-dot voltage, (c) estimated electrode voltages. (b) and (d) respective zoomed views.

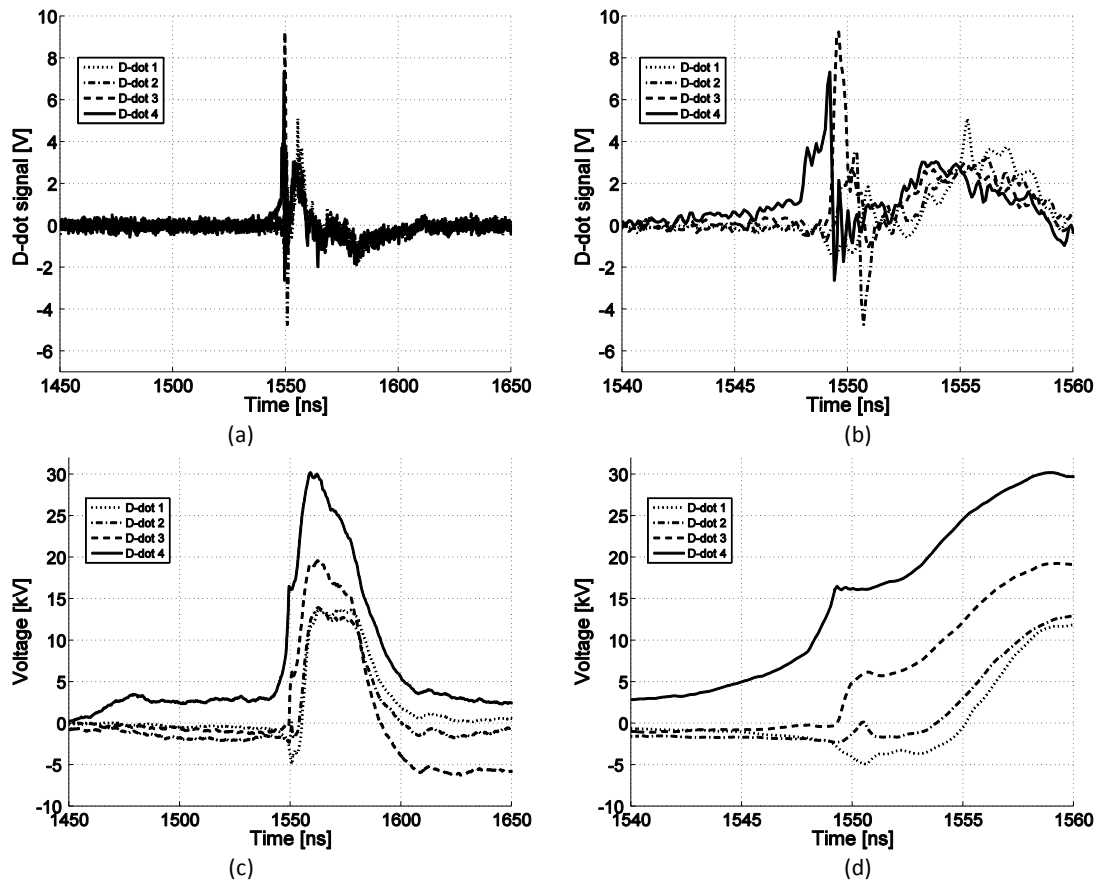


Figure 2-23. 500 mBar, 38 kV. (a) D-dot voltage, (c) estimated electrode voltages. (b) and (d) respective zoomed views.

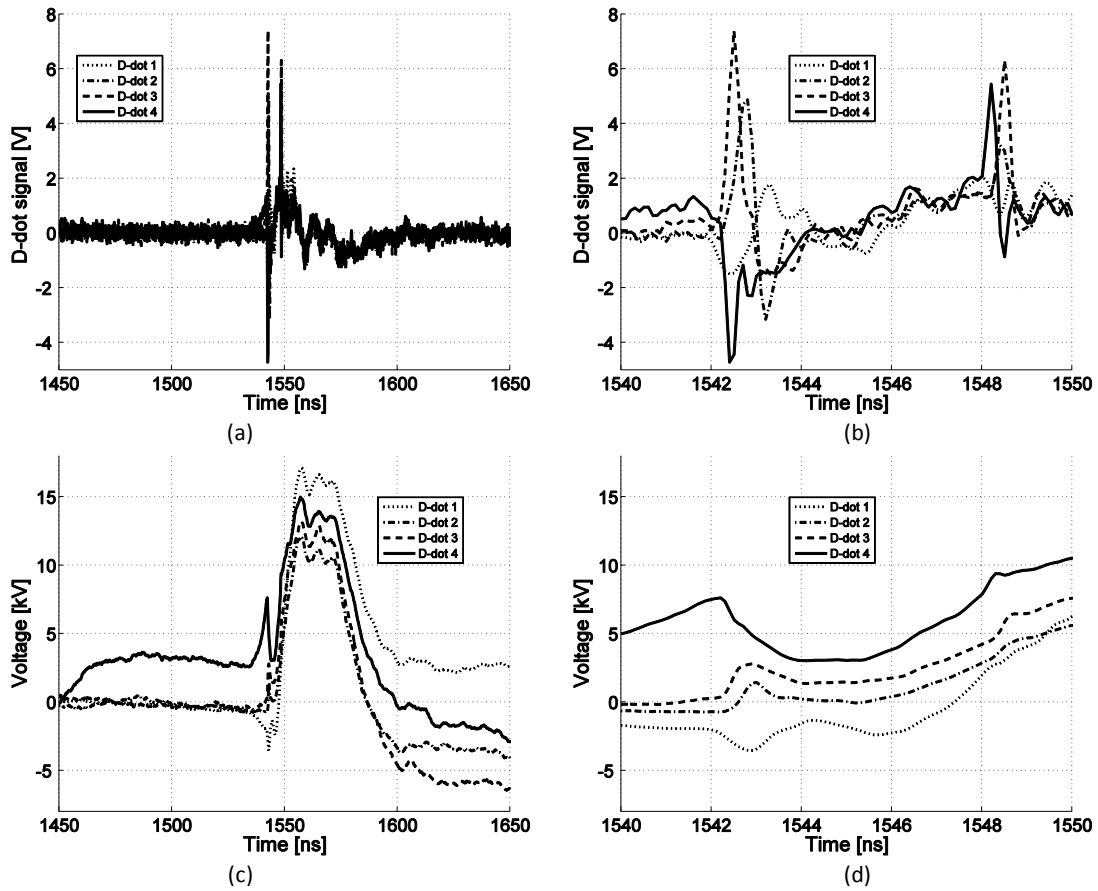


Figure 2-24. 200 mBar, 38 kV. (a) D-dot voltage, (c) estimated electrode voltages. (b) and (d) respective zoomed views.

### 2.4.1.1.2 Charging voltage 17 kV

For the case of 500 and 200 mBar measurements at 17 kV charging voltage were also done with the D-dot sensors and they will be briefly discussed below. The results are shown in Figure 2-26. In the left column are the results for 500 mBar and in the right column for 200 mBar.

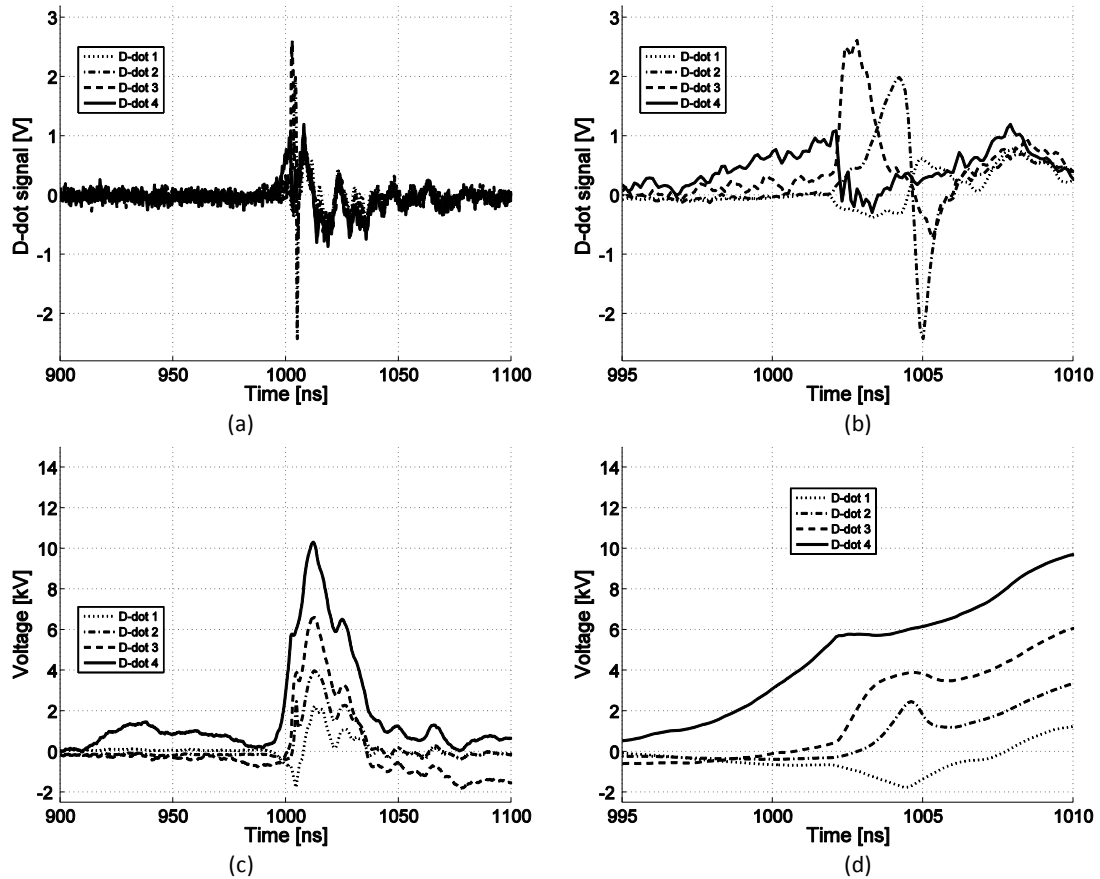


Figure 2-25. 500 mBar, 17 kV. (a) D-dot voltage, (c) estimated electrode voltages. (b) and (d) respective zoomed views.

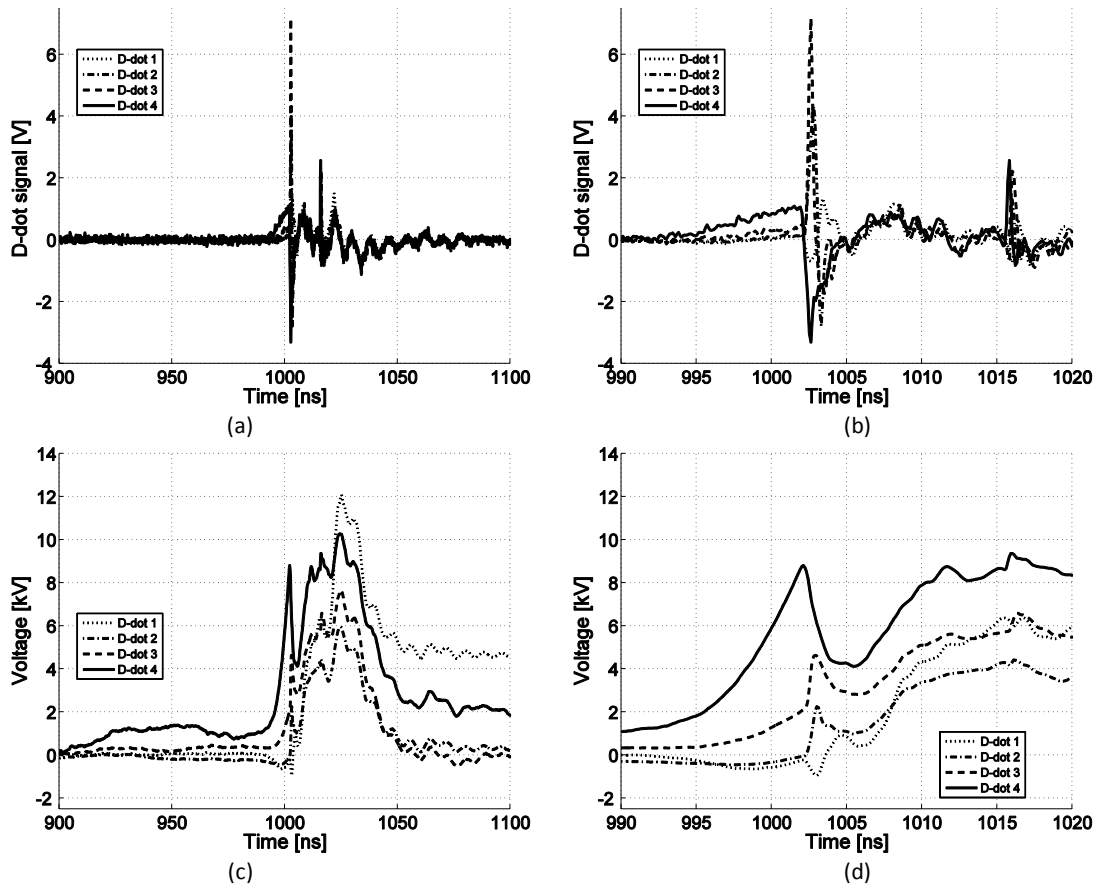


Figure 2-26. 500 mBar, 17 kV. (a) D-dot voltage, (c) estimated electrode voltages. (b) and (d) respective zoomed views.

In Figure 2-21 (b), 500 mBar, the load voltage does not increase very much indicating high plasma impedance. Now looking at Figure 2-26 (a) and (c), no large spike is observed on D-dot 4. Also the duration of the spikes on D-dot 2 and 3 is relatively large. The transients in the electric field in the gap are much less intense and slower than in the case of 38 kV. This could indicate that successful ignition of the plasma, strong enough to obtain low impedance, can be identified with sharp peaks in the D-dot signals.

For 200 mBar, spikes do occur again and in between the spikes, the signals of the D-dot sensors are very similar. As a result, the calculated voltages are also very similar. This can be interpreted as an indication of low plasma impedance.

#### 2.4.1.2 Analysis of optical observations

The optical images of the discharges are used to determine the average propagation velocity of the avalanche, as described in appendix B, and to study the general development of the discharge. The average velocities are shown in Table 2-2. Here  $\sigma_v$  is the standard deviation of the average propagation velocity.

Table 2-2. Average propagation velocities during the avalanche phase.

Pressure	[mBar]	1000	500	200	1000	500	200
$V_{\text{charge}}$	[kV]	38	38	38	17	17	17
$v$	[ $10^6$ m/s]	1.6	3.2	7.0	1.7	2.4	4.7
$\sigma_v$	[ $10^6$ m/s]	0.5	0.8	0.6	0.3	0.3	0.6

A representative selection of the images is shown in Figure 2-27 and Figure 2-28 for 38 and 17 kV charging voltage respectively. The left column shows the images for 1000 mBar, the center and right column show the images for 500 and 200 mBar respectively.

The general development of the plasma, adheres to the description given by H.M. von Bergman in [35] and J.C. Martin in [36]. The development can be observed from the pictures in the following way;

- The voltage at the source electrode, at the bottom of the image, increases causing the plasma to ignite. An avalanche starts at the source electrode and propagates towards the load electrode. In this first phase a clear difference due to pressure is observed. With 1000 mBar, the front of the discharge is the most luminous area. Lowering the pressure, making the discharge more glow like, results in a shift of the most luminous area to the edge of the source electrode. Due to the presence of the grounded dielectric surface, the propagation of the plasma progresses with the same speed over the full width of the source electrode. This shows the benefit of the addition of the grounded dielectric.
- Once the avalanche reaches the load electrode, very bright spots occur. At these hotspots secondary electrons are extracted from the load electrode. The hotspots will be the connection points of the conductive plasma channels at a later stage of the discharge.
- As can be seen in the second row of images, around 5 ns after ignition, the hotspots' optical intensity increases significantly and now a second plasma wave propagates back from the load electrode to the source electrode again. When this wave reaches the source electrode, conductive channels are formed starting from the source electrode. Once these channels are formed, they increase in intensity, indicating an increase in conducted current. The lower the pressure, the more diffuse the formed channels are. For 1000 mBar, the channels are very distinct while for 200 mBar, the channels look like one homogeneous sheet covering the entire discharge gap. This process takes around 10 ns for all three pressure settings. In the final stage of the discharge, around 15 ns after the ignition, the conducting channels increase even further in intensity, forming very bright spots on both the load and source electrode. Finally the channels turn into arcs.



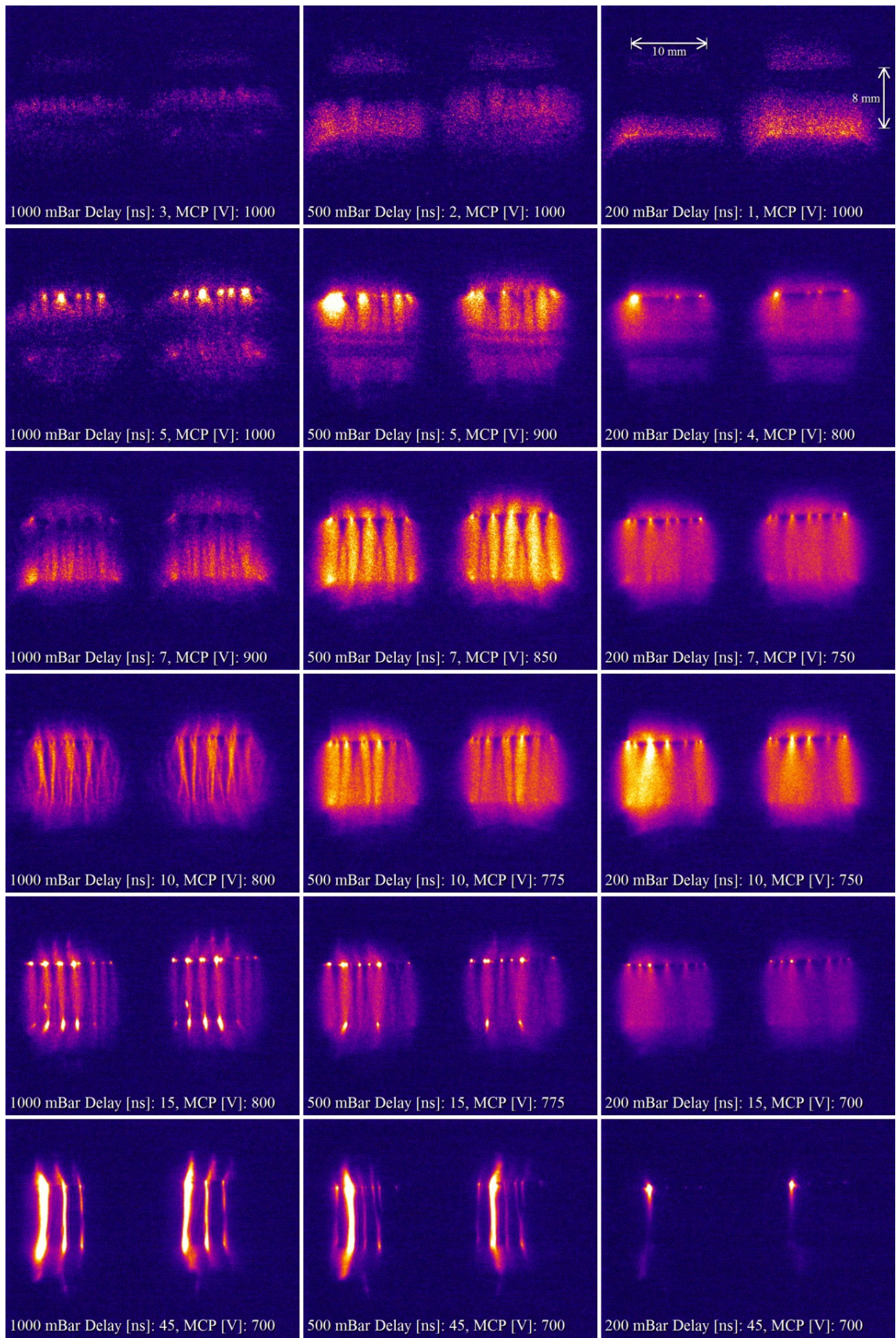


Figure 2-27. Development of the plasma using a peak charging voltage of 38 kV in air.



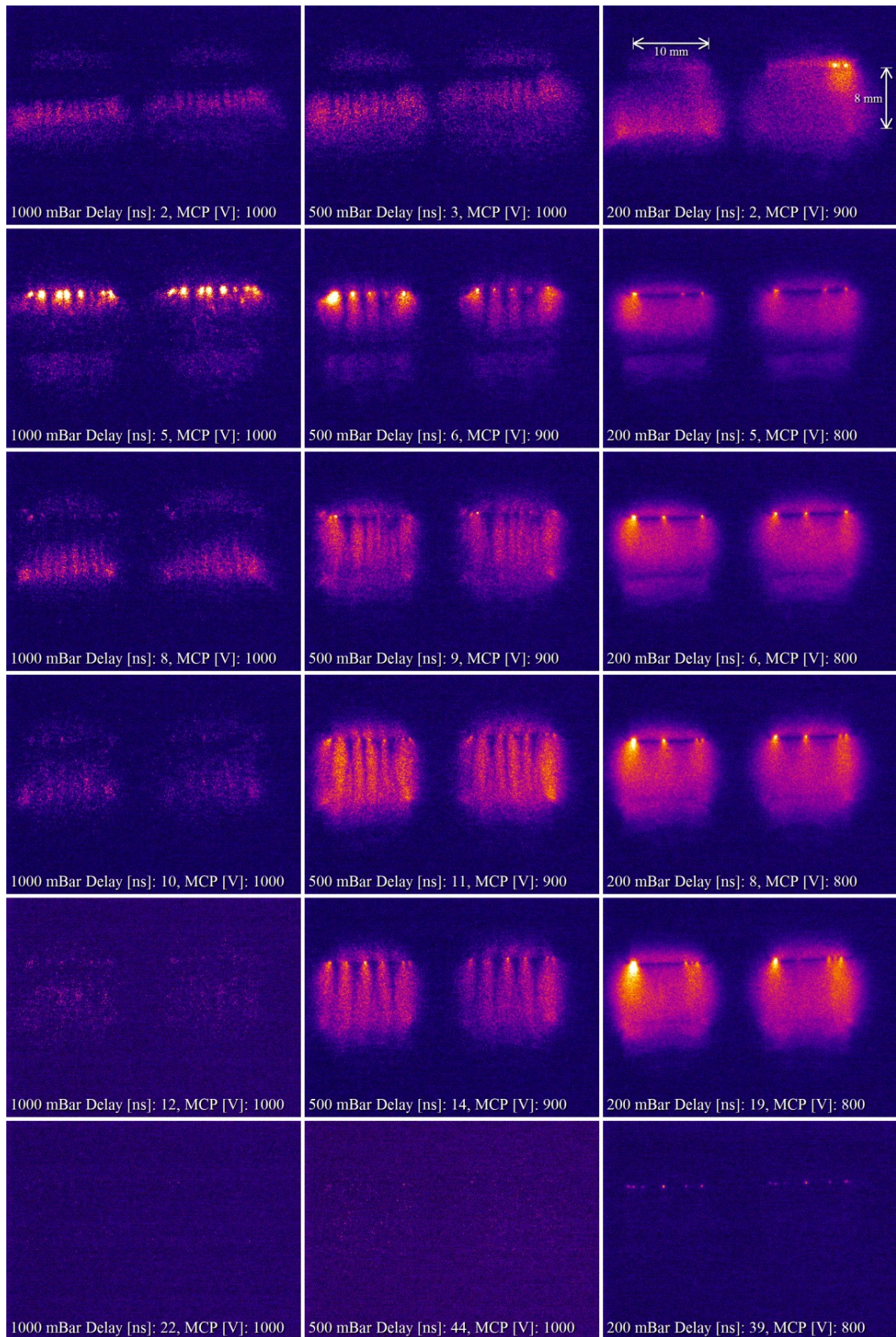


Figure 2-28. Development of the plasma using a peak charging voltage of 17 kV in air.

Two interesting plasma characteristics can be observed. Using 500 mBar, a dark horizontal line is observed just after the front of the plasma when it re-strikes to the source electrode. This band is observed consistently 5 ns after ignition of the plasma using both peak charge voltage settings. Using 200 mBar, a dark region is seen at the load electrode. This dark region is clearer for the 17 kV setting but is not observed for the other pressure settings.

Lowering the peak charging voltage to 17 kV has very little effect on the optical development of the discharge in the first 8 to 9 ns. The plasma behaves the same but with lower optical intensities. At 10 ns, where the plasma is forming conducting channels when using 38 kV, the effect of lowering the peak charging voltage becomes clear. There is too little energy to ionize the air to form the conducting channels. With 1000 mBar, the plasma is already more dim around 8 ns but around 10 ns it extinguishes. For 500 mBar, the plasma does continue to develop but does not form the bright conducting channels. Only in the 200 mBar case, conducting plasma is formed which shows similar conductive properties as in the 38 kV case.

Based on Table 2-1 and Table 2-2 the best results, from a switch perspective, are obtained with 200 mBar. The largest  $dV_{load}/dt$  is obtained with 1000 mBar at 38 kV but in this case the peak power and transferred energy are less than for 200 mBar. At 500 mBar more hotspots are formed on the load electrode than at 1000 mbar, resulting in a better spread of heat on the electrode. With 200 mBar the plasma surface coverage is largest and most homogeneous. Also the number of arcs is smallest, which could result in a longer electrode edge life time.

## 2.4.2 Discharge in Argon

For discharges in argon, reliable experiments were possible for pressures of 500 and 1000 mBar and at a charging voltage of 17 kV. For lower pressures, or higher charging voltage, discharges also occur at other positions than the discharge gap. A charge voltage of 38 kV results in discharges at the 5 kV voltage rise for 500 mbar, thus 75 ns too early with regard to the main voltage peak, see Figure 2-29 (a). It is possible to manually select discharges that do not ignite until the main peak, but this setting cannot be reproduced reliably and is therefore excluded from the analysis.

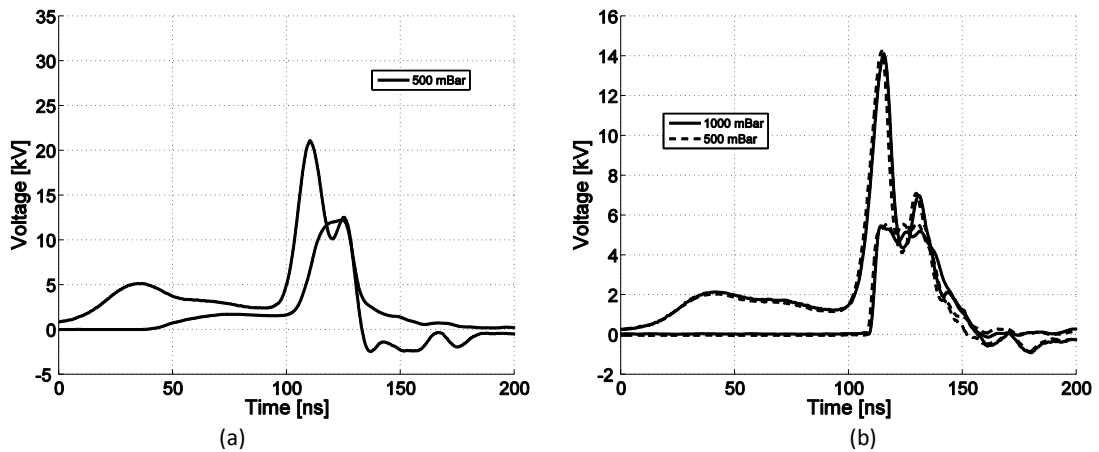


Figure 2-29. (a) Discharge in Argon at 500 mBar with 38 kV peak charging voltage. The plasma ignites before the main peak. (b) Source and load voltage in Argon with a peak charging voltage of 17 kV.

The source and load voltage of discharges in argon using a peak charging voltage of 17 kV are shown in Figure 2-29 (b).

Table 2-3. Peak power and energy delivered to the load electrode.

Pressure	[mBar]	1000	500
$V_{\text{charge}}$	[kV]	17	17
$P_{\text{peak}}$	[kW]	600	627
E	[mJ]	14.8	15.2
Max $dV_{\text{load}}/dt$	[kV/ns]	1.8	1.6

Once the load voltage reaches a steady level, the voltage difference between the source and load is very small. Argon behaves at 17 kV as air does at 38 kV. The difference between 1000 and 500 mBar is very small

### 2.4.2.1 Observations with the D-dot sensors

#### 2.4.2.1.1 Charging voltage 17 kV

The D-dot signals are shown in Figure 2-32. The left column shows the signals for 1000 mBar and the right column for 500 mBar. It can be observed that the difference between 500 and 1000 mBar is small. All D-dot sensors show two clearly distinguishable peaks, Figure 2-29 (e). The first peaks are all between 1000 to 1005 ns and the second peaks, spaced much closer to each other, are all around 1016 ns. The delay between the first peak on D-dot 4 and D-dot 3 is longer than the delay between the first peak on D-dot 3 and 2. And the delay between the first peak of D-dot 2 and D-dot 1 is even smaller. This decrease in delay could indicate an increase in propagation velocity. To verify this, the velocity of the avalanche is determined as a function of position based on the optical images. This is shown in Figure 2-30 (a) and (b). Each dot represents the average velocity based on one image. As can be seen, this measurement is only possible between 1 and 6 mm from the source electrode due to the fact that in both images the avalanche front must be detectable (see Figure 2-16). Figure 2-30 (b) compares the avalanche propagation velocity for 1000 mBar with that of 500 mBar. In this figure also a 0<sup>th</sup> and 1<sup>st</sup> order fit is applied to both data sets. As can be seen, the optical images show an increase in propagation velocity for 1000 mBar. This phenomenon was encountered clearly only in this case. As described in Figure 2-1, the direction of the electric field at the front of the plasma is expected to rotate forward. This might cause an increase in propagation velocity but, this effect is expected to occur in a distance equal to the dielectric thickness from the load electrode. The velocity increase observed in Figure 2-30 is not expected to be caused by this. The fact that this velocity change is observed both optically and with the D-dot sensors shows the potential of the combination of these measurement techniques.

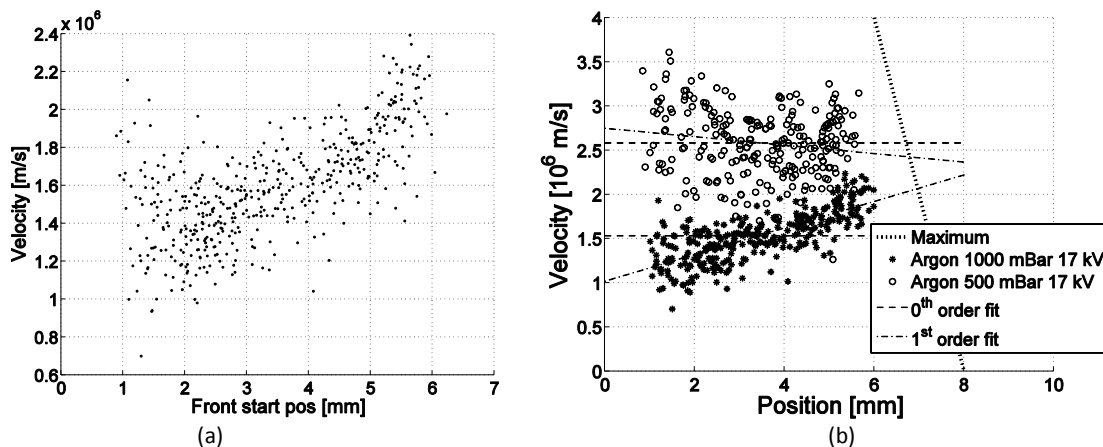


Figure 2-30. (a) Avalanche front propagation velocity as function of position for 1000 mBar based on optical images. (b) Comparison of avalanche propagation velocity for 500 and 1000 mBar. For 1000 mBar the velocity increases as the avalanche propagates.

For 500 mBar the velocity increase is not observed, Figure 2-29 (f). From 987 to 992 ns the spikes do not show the same timing consistency as with 1000 mBar. The time in between the first and the second peaks is roughly the same in 1000 and 500 mBar. Integrating the signals, Figure 2-29 (e) – (h) also shows the negative voltage at the load electrode before the discharge occurs, similar to air. The error due to integration of noise is very apparent in Figure 2-29 (d). Still the similarities between the four voltages are still clear and, as also seen with the North Star and Pearson probe, the voltage drop over the plasma is small.

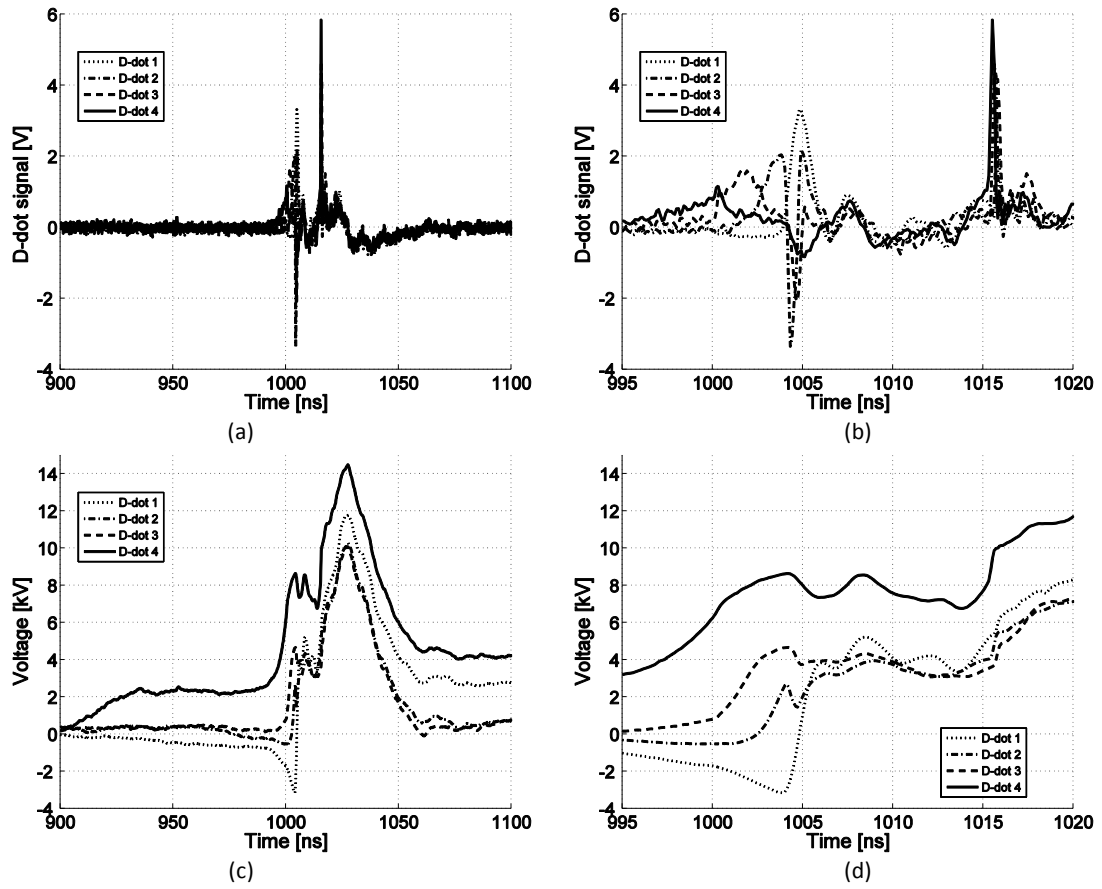


Figure 2-31. 1000 mBar, 17 kV. (a) D-dot voltage, (c) estimated electrode voltages. (b) and (d) respective zoomed views.

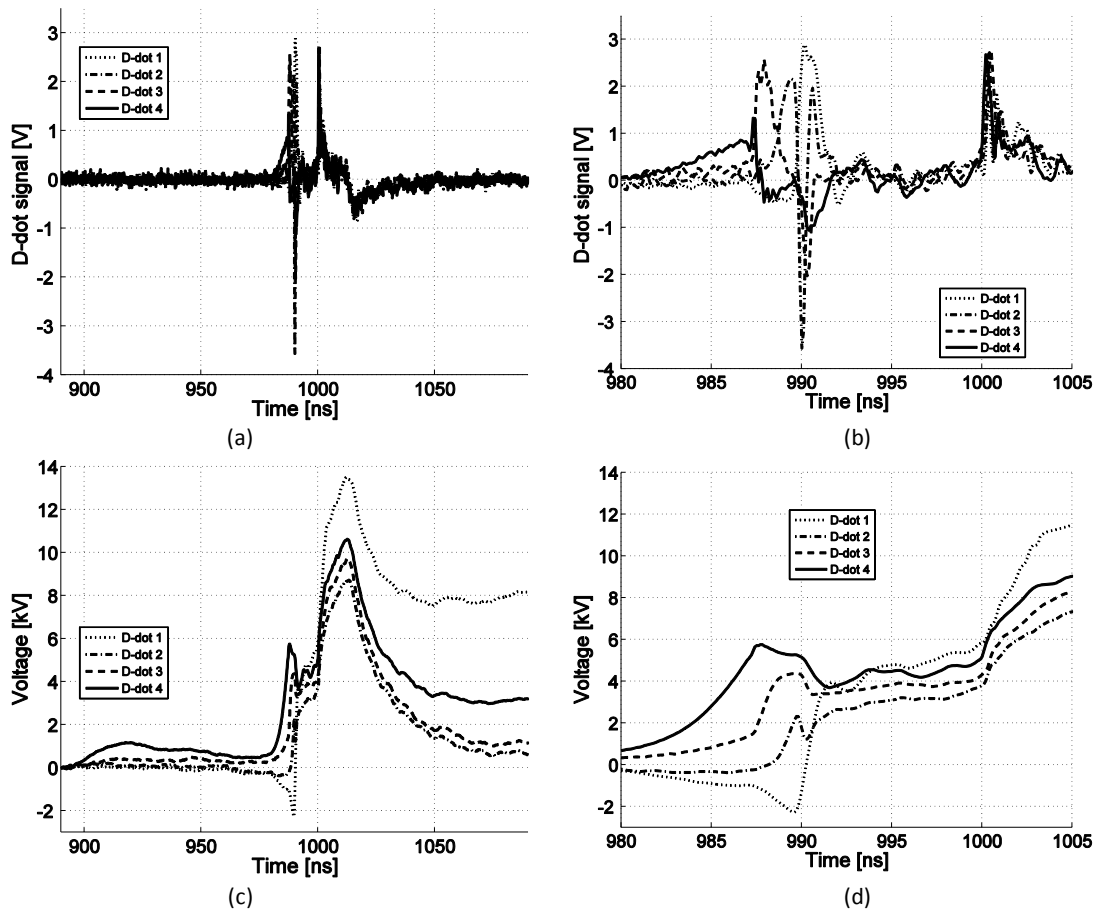


Figure 2-32. 500 mBar, 17 kV. (a) D-dot voltage, (c) estimated electrode voltages. (b) and (d) respective zoomed views.

### 2.4.2.2 Analysis of optical observations

The average velocities are shown in Table 2-4.

Table 2-4. Average propagation velocities during the avalanche phase.

Pressure	[mBar]	1000	500
$V_{\text{charge}}$	[kV]	17	17
$v$	$[10^6 \text{ m/s}]$	1.5	2.6
$\sigma_v$	$[10^6 \text{ m/s}]$	0.3	0.4

The optical images of the discharges in 1000 and 500 mBar are shown in Figure 2-34. The first row shows the avalanche phase, 4 ns after ignition. Between 6 and 8 ns, the conducting channels are formed directly after the avalanche reaches the load electrode. A second plasma wave travelling from the load to the source is not observed. This might cause the faster rise time of the load voltage. Also, in Argon no arcs are formed at the end of the pulse. This is a great advantage for the life time of the switch due to reduced local heating of the electrode edges and thereby reducing sputtering of the electrodes.



The discharges in 1000 mBar show the formation of sideways connection between the channels. These are not observed with 500 mBar which has a slightly more glow like discharge. This difference is pointed out in Figure 2-33.

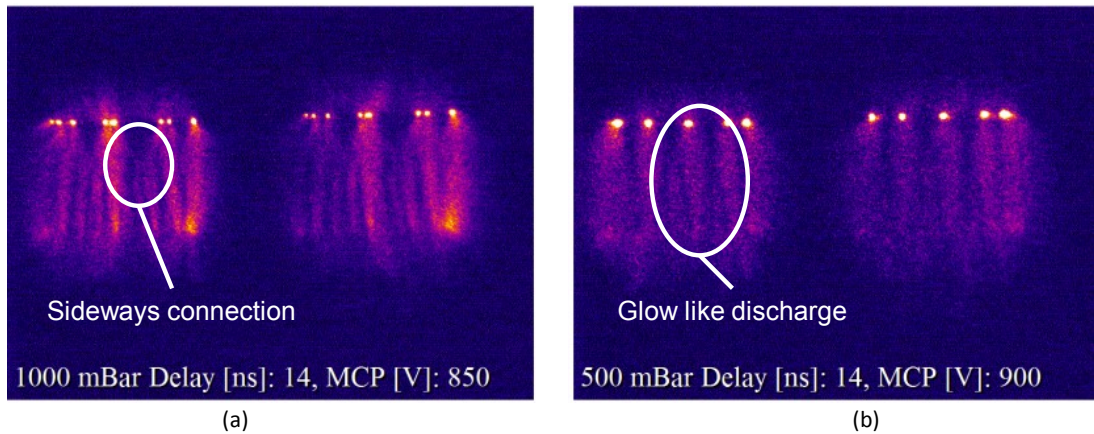


Figure 2-33. (a) at 1000 mBar Argon the surface discharge seems to form sideways connections. (b) At 500 mBar the sideways connections are no longer observed and the discharge shows a more glow like behavior.

The number of hotspots is the same for 1000 and 500 mBar but for 500 mBar the surface coverage is more homogeneous.

For 500 mBar the rise time on the load voltage, Table 2-3, is higher than in the case of air with 38 kV and the velocity of the avalanche is smaller. This indicates that the avalanche phase is not the only component of the discharge process that determines the time it takes to build a sufficiently conducting path to change the switch from opened to closed.



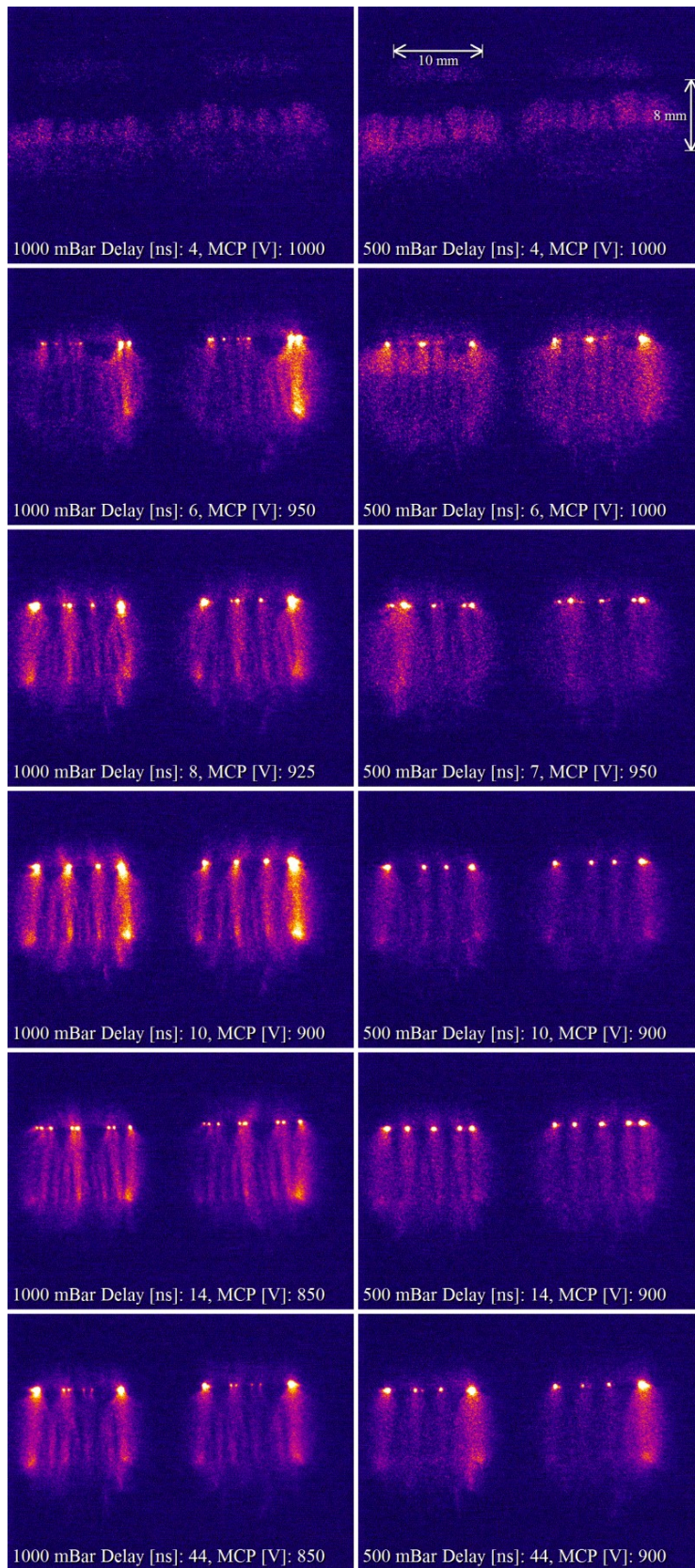


Figure 2-34. Optical imaging of discharges in Argon at 1000 (left) and 500 mBar (right) with a peak charging voltage of 17 kV.

### 2.4.3 Helium

For Helium successful results were obtained with a peak charging voltage of 17 kV. Figure 2-35 shows the measured source and load voltage as a function of pressure. The difference in load voltage for 1000 and 500 mBar is larger than for Argon. For 500 and 200 mBar the load voltage is very similar to each other. For 1000 mBar the load voltage is lowest suggesting the highest plasma impedance. For all three pressure settings, the source voltage drops below the load voltage. This is probably a damped resonance in the voltage measurement.

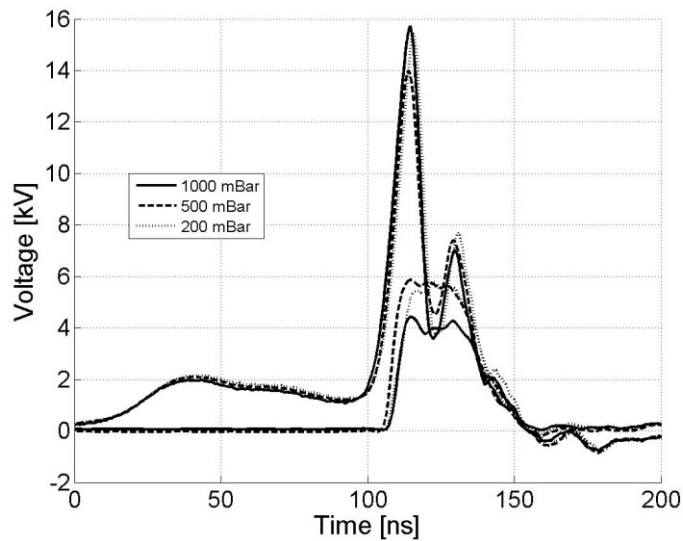


Figure 2-35. Source and load voltages in Helium as a function of pressure.

Using Helium at 500 or 200 mbar, a higher peak power is achieved compared to both Argon and Air. At 1000 mbar, the transferred energy is higher for Argon. At 500 mbar it is higher for Helium. For both pressures, Helium has a significantly lower  $dV_{load}/dt$ . Compared to air at 17 kV, both the peak power, transferred energy and  $dV_{load}/dt$  are larger.

Table 2-5. Peak power and energy delivered to the load electrode.

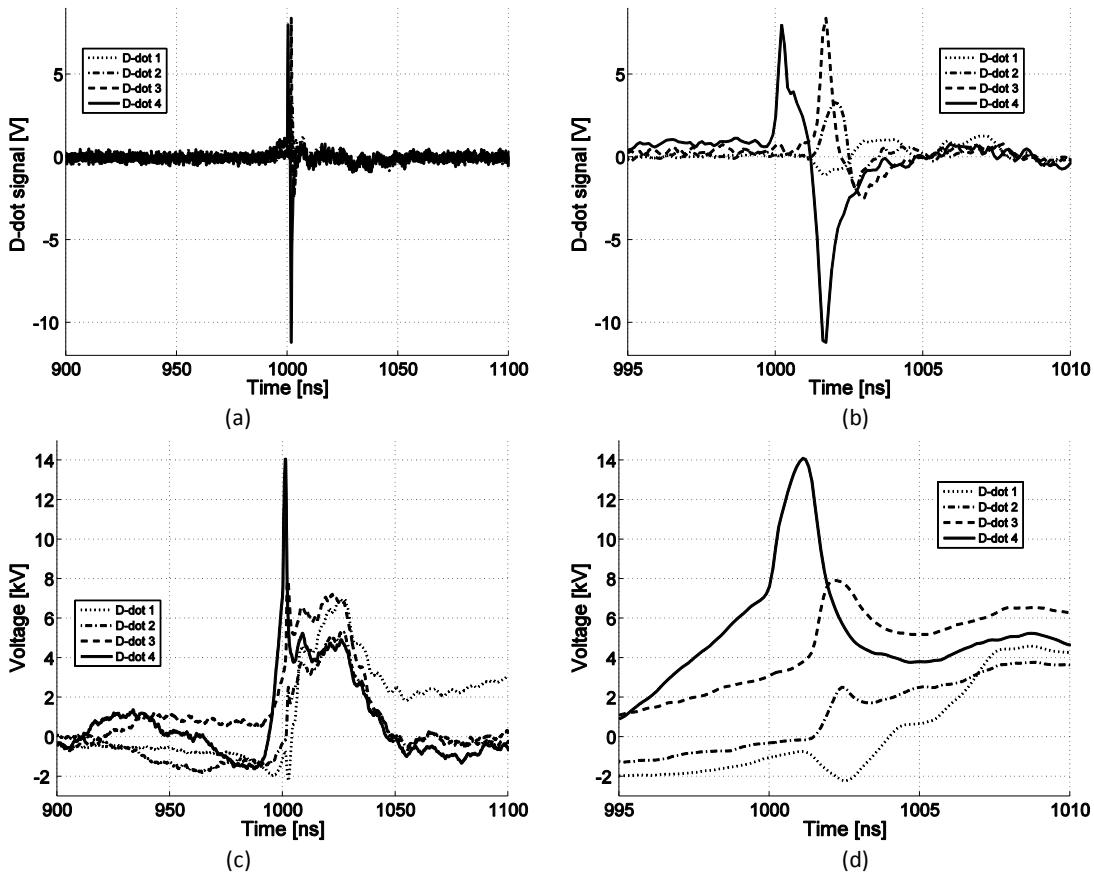
Pressure	[mBar]	1000	500	200
$V_{charge}$	[kV]	17	17	17
$P_{peak}$	[kW]	391	689	666
E	[mJ]	10.8	17.8	20.7
Max $dV_{load}/dt$	[kV/ns]	0.9	1.2	0.9

### 2.4.3.1 Observations with the D-dot sensors

#### 2.4.3.1.1 Charging voltage 17 kV

The D-dot signals are shown in Figure 2-36. Using Helium, only 1 peak in each of the D-dot signals is observed, whereas both air and Argon show 2 peaks. This could be explained by the fact that the discharges in Helium are much more glow like, as seen in the optical images no clearly distinguishable channels are formed. As a result, the plasma not only connects to the knife edge of the source electrode but to a larger area. This may prevent the sudden voltage change to occur.

Also here the calculated voltages are similar in shape, apart from the difference due to the error from integrating noise. This gives us reason to believe that the voltage drop over the plasma is small. This is in agreement with the North Star and Pearson measurement.



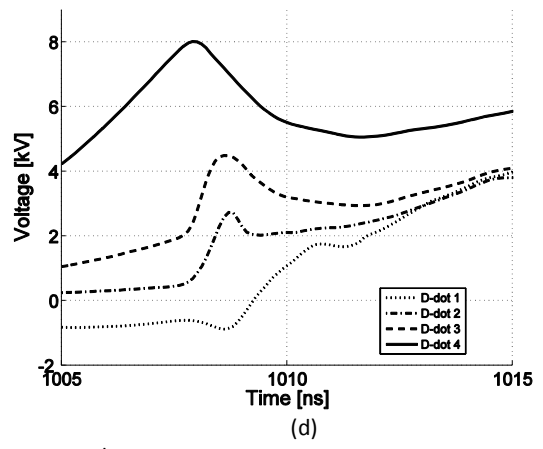
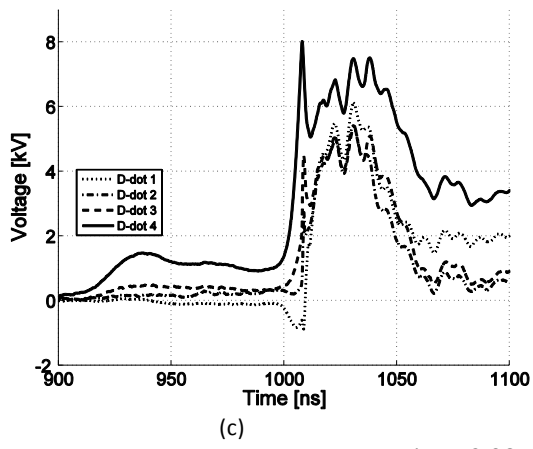
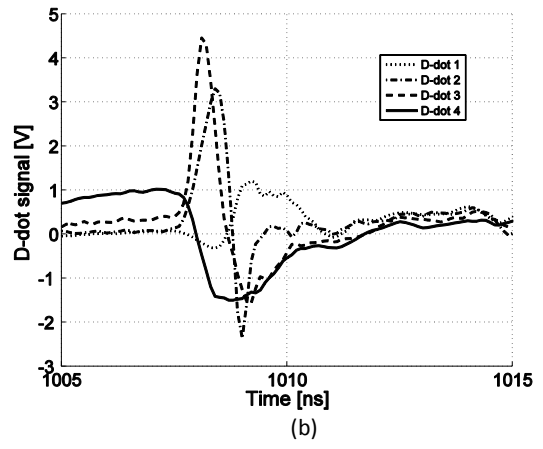
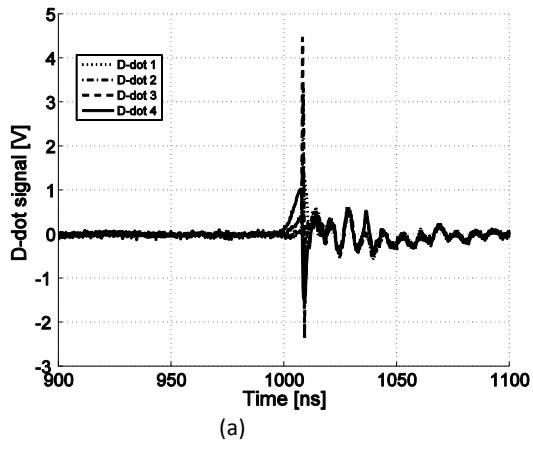


Figure 2-36. 500 mBar, 17 kV.

### 2.4.3.2 Analysis of optical observations

Table 2-6 shows the measured avalanche propagation velocity for Helium. The velocity is much higher for Helium than for either Argon or air. For 200 mBar the avalanche velocity is too high to measure.

Table 2-6. Average propagation velocities during the avalanche phase.

Pressure	[mBar]	1000	500	200
$V_{\text{charge}}$	[kV]	17	17	17
$v$	[ $10^6$ m/s]	4.6	4.7	*
$\sigma_v$	[ $10^6$ m/s]	1.1	0.8	-

\*  $> 16 \cdot 10^6$  m/s, out of range, gap crossed within 500 ps.

The optical images are shown in Figure 2-37. The discharges in Helium are much more glow like than both the discharges in air and in Argon. In the case of 1000 and 500 mBar only 1 or 2 hotspots are formed on the load electrode. From these hotspots a single intense and wide channel is formed. It is believed that most of the current is conducted through this channel. The disadvantage of a single channel is a severe reduction of life time of the switch due to electrode sputtering at the single hotspot whereas in the case of Argon there are 4 or more hotspots. With 200 mBar the behavior is different. Here, 4 or more hot spots are formed. During the development of the discharge these hotspots form a wide conducting channel which covers a significant portion of the gap surface and grows out to fully cover the gap. An interesting detail is the small difference in intensity of the hot spots and the rest of the plasma as well as the sizes of the hot spots which seem to be smaller than those in Argon and Air. This could indicate that the current through the plasma is more equally distributed over the entire surface.



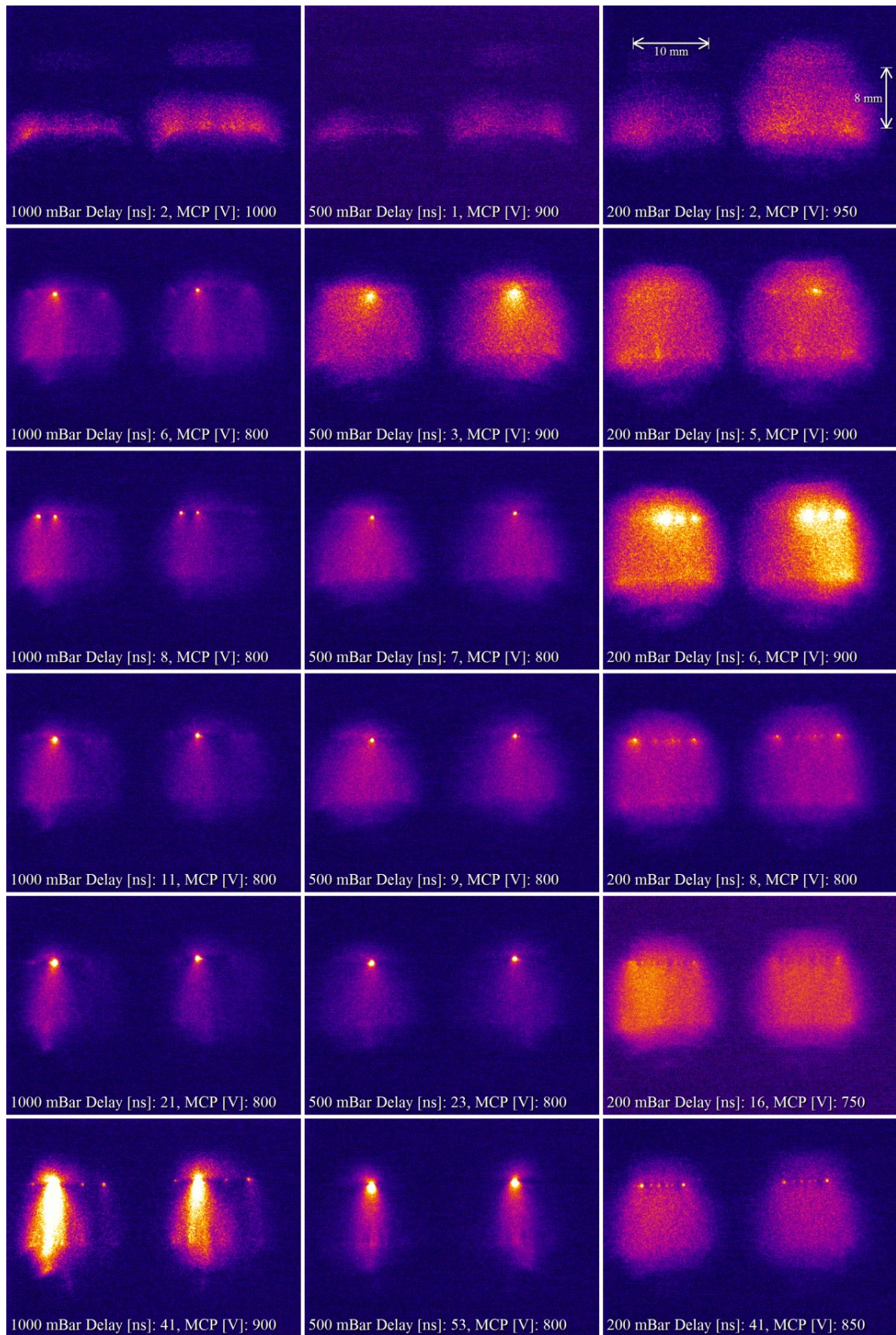


Figure 2-37. Discharges in Helium at 1000 (left), 500 (center) and 200 mBar (right) with a peak charging voltage of 17 kV.

#### 2.4.4 Discharges in Air using SrTiO<sub>3</sub>

In order to analyze the discharge development over a dielectric with high dielectric constant, a SrTiO<sub>3</sub> sample has been manufactured at the TU/e. SrTiO<sub>3</sub> powder is pressed into a circular disk using an oil press with 60 Bar and sintered at a temperature of 1200 degrees Celsius for 24 hours. The dielectric constant of the sample was measured from DC up to 5 MHz and was around 100. This is much lower than the 2000 as mentioned by [Robertson]. But still it is much larger than the dielectric constant of the glass sample we have used for the previous experiments. The discharges made over the SrTiO<sub>3</sub> sample show interesting differences with the glass sample and are discussed below.

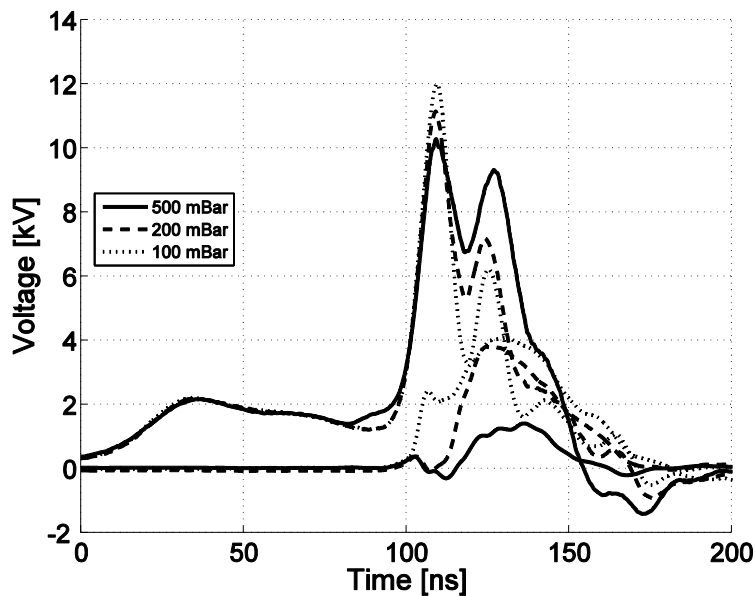


Figure 2-38. Source and load voltage using SrTiO<sub>3</sub> with 17 kV peak charging voltage as a function of pressure.

The measured source and load voltages are shown in Figure 2-38 for the 500, 200 and 100 mBar at a peak charging voltage of 17 kV. At 1000 mBar no reproducible discharge was obtained.

Table 2-7. Peak power and energy delivered to the load electrode.

P	[mBar]	500	200	100
V <sub>charge</sub>	[kV]	17	17	17
P <sub>peak</sub>	[kW]	40.6	291	405
E	[mJ]	0.8	7	15.7
Max dV <sub>load</sub> /dt	[kV/ns]	0.17	0.48	1.08

### 2.4.4.1 Observations with the D-dot sensors

#### 2.4.4.1.1 Charging voltage 17 kV

Due to the increased dielectric constant, the capacitive coupling between the high voltage electrodes and plasma to the D-dot sensors is much stronger. This results in larger voltages on the D-dot sensors. As can be seen in Figure 2-39 through Figure 2-41, the calculated voltages show very little resemblance with the voltages as measured with the North Star and Pearson probe. Only the D-dot 1, at the load electrode side shows some agreement for the pulse shape but indicates larger amplitudes. Due to this difference the D-dot signal could only be used reliably for timing purposes.

Here the discharges in 500 and 200 mBar show 2 spikes on each of the D-dot signals. For 100 mBar only 1 spike is observed. Due to the large uncertainty in the signals, the D-dot sensors do not yield very much valuable information. It can, however, be stated that the change in dielectric has a significant influence on the performance of the discharge from an electric point of view.

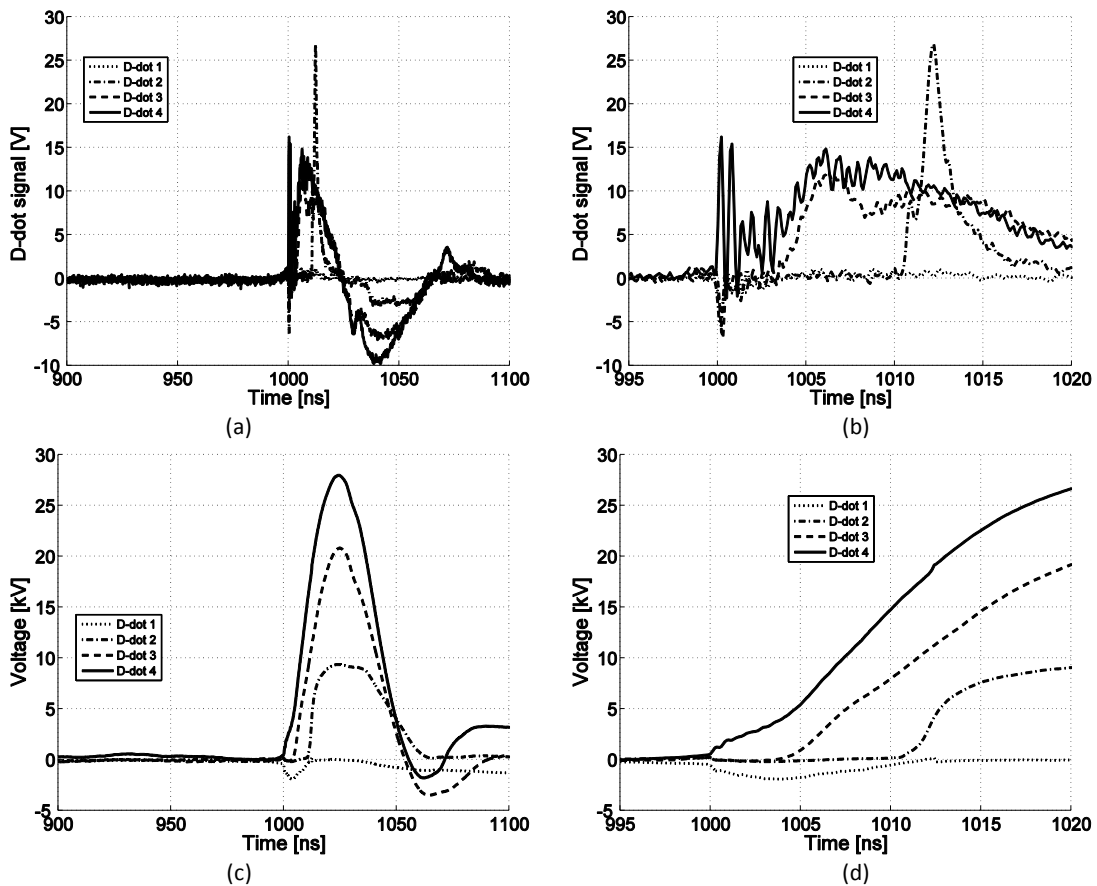
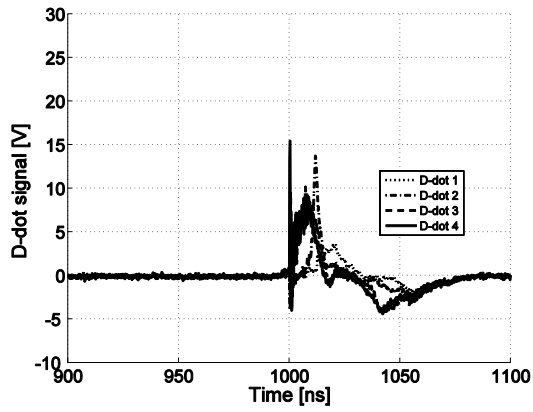
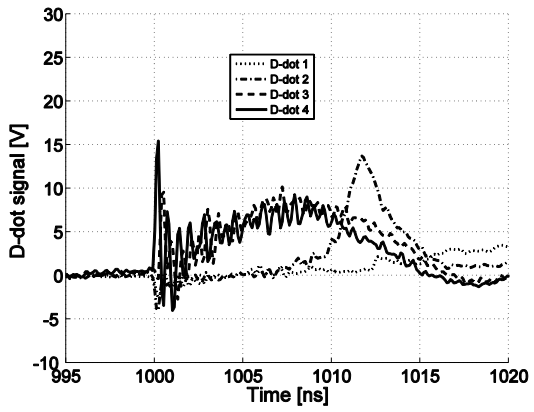


Figure 2-39. SrTiO3 500 mBar Air, 17 kV.

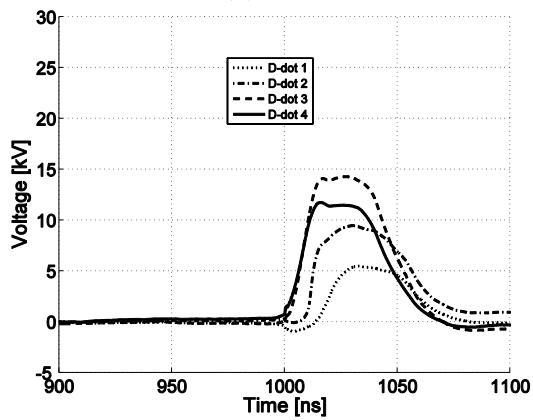




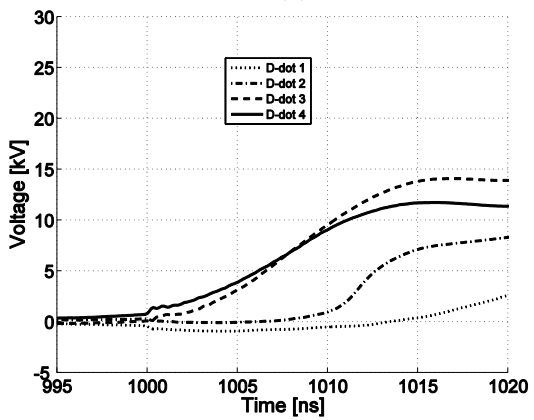
(a)



(b)



(c)



(d)

Figure 2-40. SrTiO<sub>3</sub> 200 mBar Air, 17 kV.

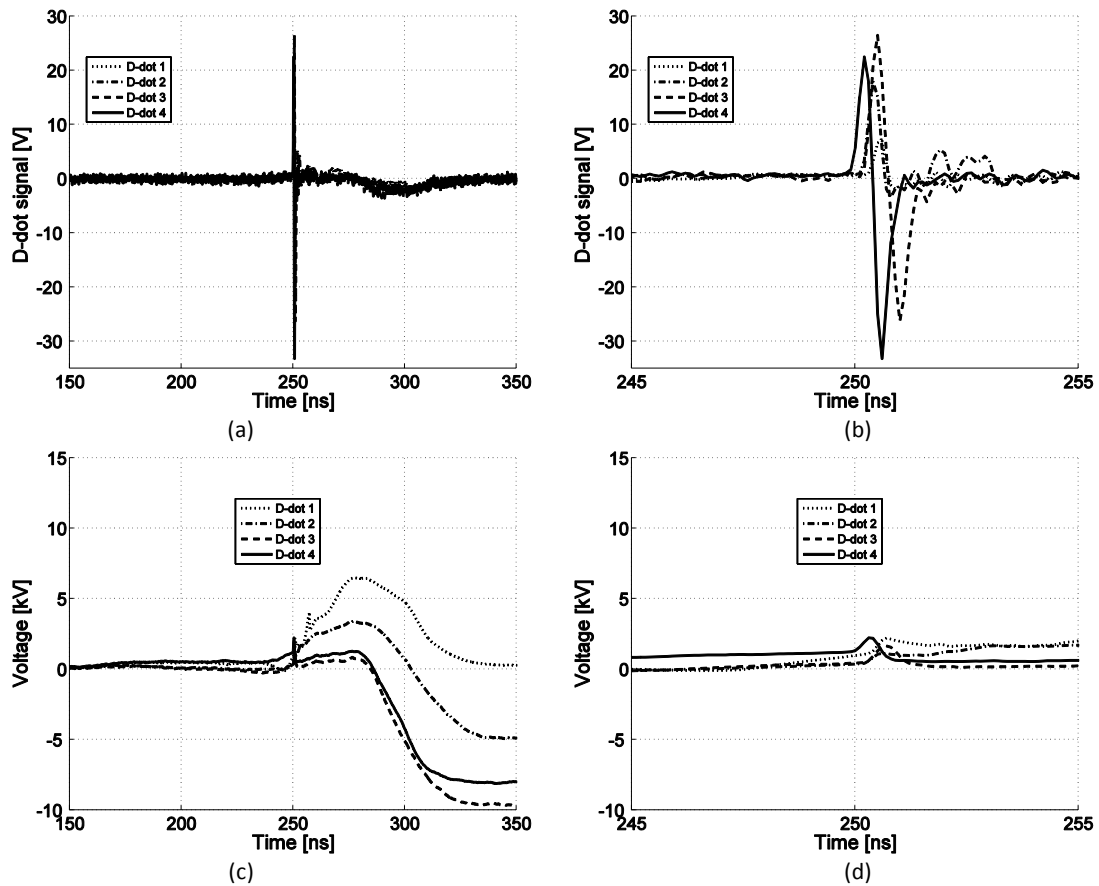


Figure 2-41. SrTiO<sub>3</sub> 100 mBar Air, 17 kV.

#### 2.4.4.2 Analysis of optical observations

Discharges were made using SrTiO<sub>3</sub> in air at a pressure of 500, 200 and 100 mBar. Optically the discharges, shown in Figure 2-42, are very different from the discharges with the glass dielectric. Using 500 mBar, it takes around 19 ns for the plasma to reach the load electrode. This is significantly longer than in any of the previously discussed experiments. Also, at 6 ns after inception of the plasma, bright spots are seen at the edge of the load electrode. This has not been observed using the glass sample. These spots indicate that plasma is also formed at the load electrode. This can be explained by the fact that the voltage on the source electrode does not collapse due to the formation of a conducting channel. This allows for the electric field at the load electrode to become large enough for a plasma to ignite. These spots are also observed at 200 and 100 mBar but do not grow as fast as the plasma from the source electrode.

Another striking difference in these discharges with respect to those made with glass is the shape of the plasma. The front half of the plasma is relatively dark and the bottom half, which is connected to the source electrode, is relatively bright.

The slower development of the plasma is most likely caused by the increase of capacitance of the dielectric since with an  $\epsilon_r$  of 100 the propagation velocity of electromagnetic waves is still in the order of  $3 \cdot 10^7$  m/s.

The average velocities are shown in Table 2-8.

Table 2-8. Average propagation velocities during the avalanche phase.

P	[mBar]	500	200	100
$V_{\text{charge}}$	[kV]	17	17	17
$v$	[ $10^6$ m/s]	0.7	1.1	2.5
$\sigma_v$	[ $10^6$ m/s]	0.2	0.5	0.7

For 500 and 200 mBar a nice, relatively homogeneous surface coverage is achieved. At 100 mBar the discharge develops into a single channel. But for 500 and 200 mBar the switch properties as shown in Table 2-7 are very poor, especially when compared to the discharges over glass. Still, these measurements definitely show very interesting plasma physics and the hypothesis of a reduction in the avalanche velocity due to increased  $\epsilon_r$  has been validated.

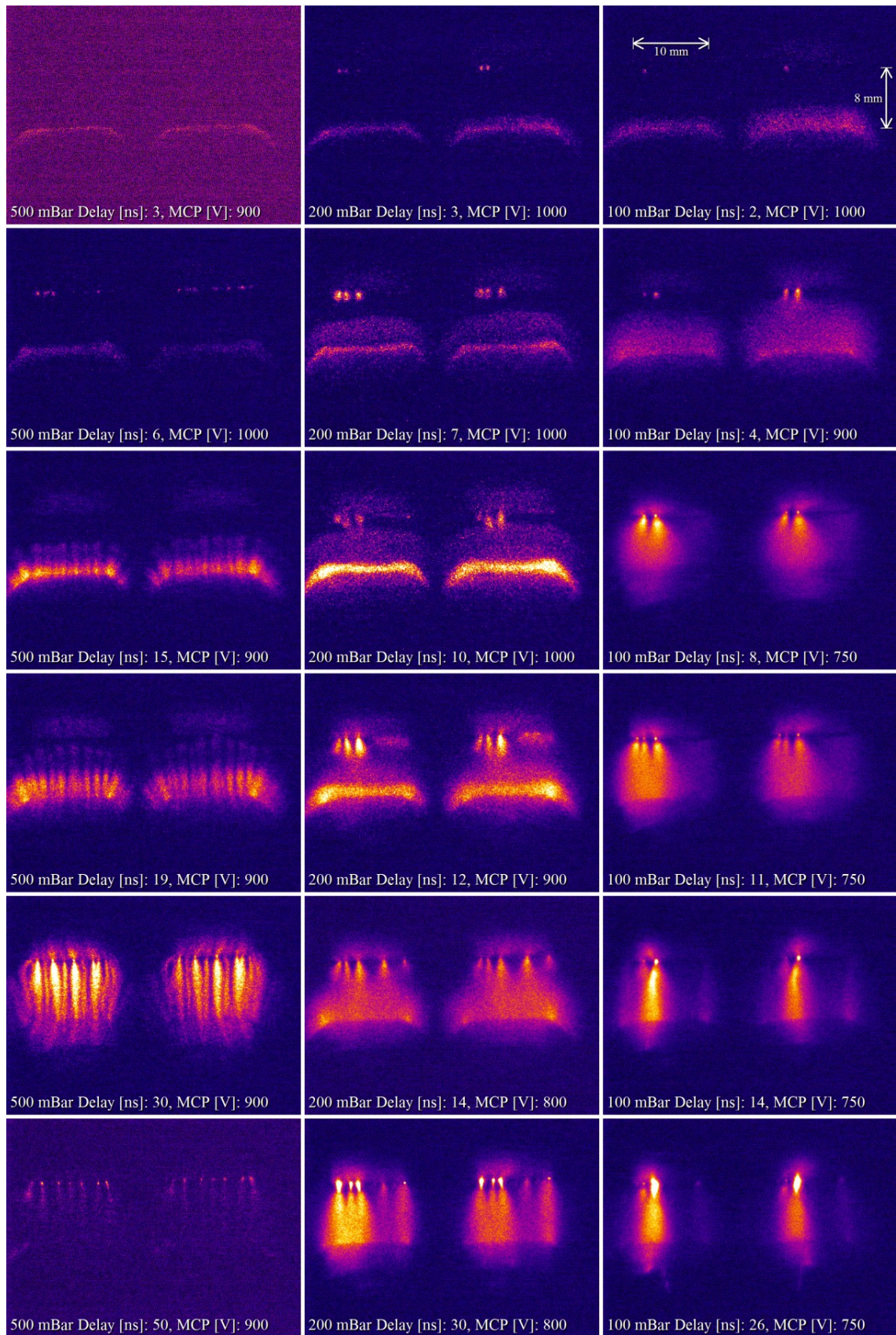


Figure 2-42. Discharges in air using SrTiO<sub>3</sub> at 500 (left), 200 (center) and 100 mBar (right) with 17 kV peak charging voltage.



### 2.4.5 Switch life time

The electrode tips are made of copper tungsten and are machined on a milling machine. To get a smooth and flat surface, new sharp tools are used. The images below show the knife edges of the load and source electrode and a glass dielectric plate after 10000 shots.

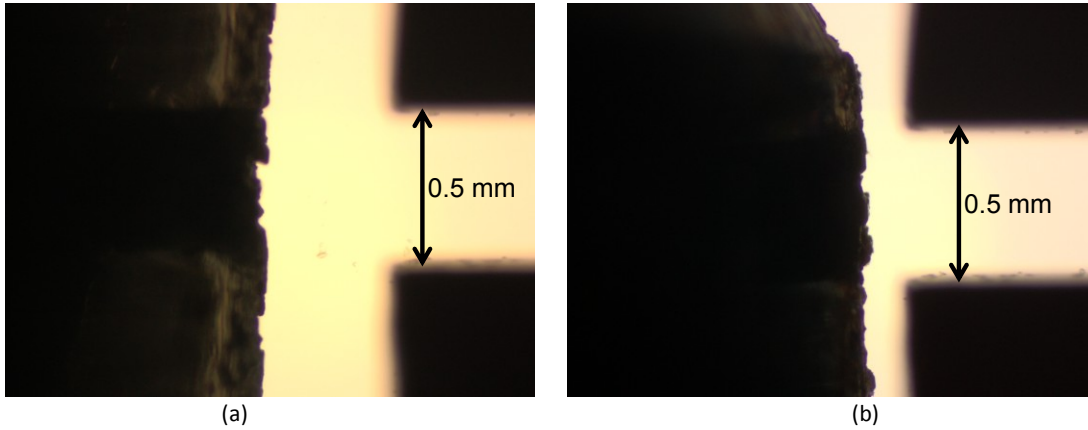


Figure 2-43. Edges of the load electrode (a) and source electrode (b) after 10000 shots.

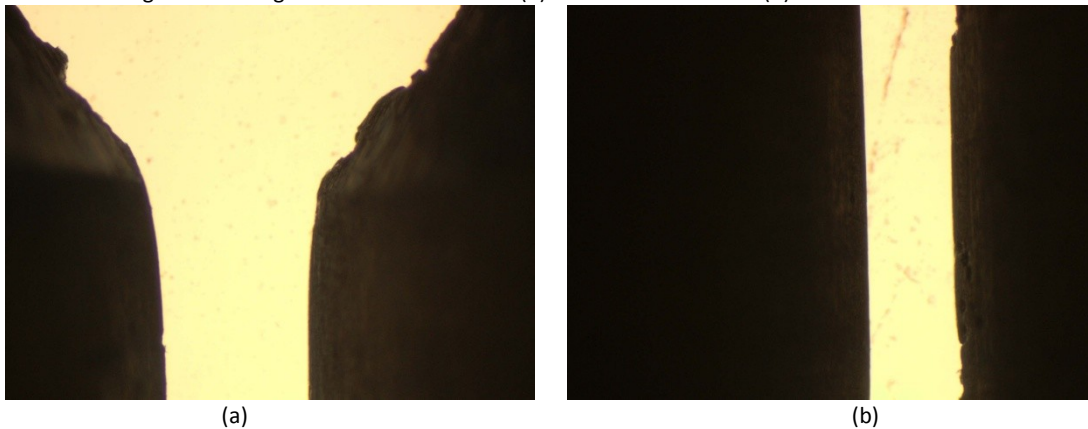


Figure 2-44. (a) Outer corner of both the source (left) and load (right) electrode after being refurbished as shown from above. (b) The refurbished electrode edge at the center. Scale is the same as in Figure 2-43.

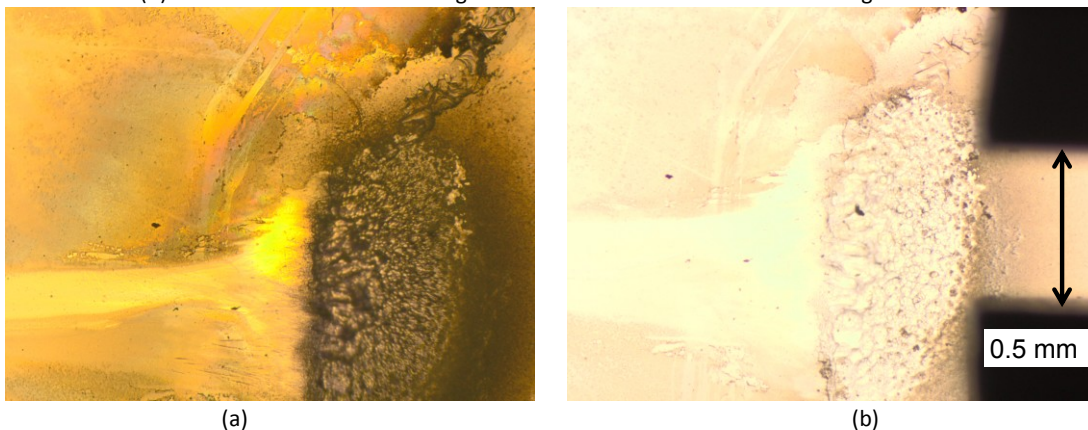


Figure 2-45. Glass dielectric after 10000 shots. Cracks underneath the electrode and deposition in the gap are clearly visible.

Both the source and load electrode edge show damage, the edges are covered with pits. Here the metal is sputtered away due to large localized currents. Figure 2-45 (a) and (b) show a small area of the

dielectric which was underneath the corner of the source electrode edge. The dielectric shows two types of damage that deteriorate the performance of the switch. First there is the deposition of metal and debris on the dielectric in the gap, Figure 2-45 (a). This deposition causes certain areas of the dielectric surface to be easier to cross for the plasma and to form conducting channels. As a consequence less parallel channels are formed and they are formed at the same position. Also high levels of deposition are found on the dielectric underneath the electrodes. This indicates the presence of plasma underneath the electrode. This supports the reasoning based on the observations made with the D-dot sensors in the previous sections; the first spike observed in the D-dot signals can be caused by a sudden change in capacitance due to the formation of plasma in between the source electrode and the dielectric.

The second type of damage, Figure 2-45 (b), are the small cracks in the glass directly underneath the electrodes. These cracks are believed to be caused by localized thermal stress.

During the experiments, the dielectric was replaced every 1000 shots. The electrodes are refurbished and were used during the experiments treated in the sections above.

## 2.5 Conclusions and discussion

We have tested the influence of gas type, pressure and dielectric constant on the behavior of a surface discharge in a 10 mm wide, 8 mm long gap.

All parameters have shown to significantly influence the behavior of the plasma as can be seen in the overview in Table 2-9 through Table 2-12 below.

By varying the pressure from 1000 to 100 mBar a surface discharge can be obtained with very different characteristics. Where in air at 1000 mBar arcs are formed in a later stage of the discharge, a glow like discharge is obtained at 200 mBar. Pressure has proven to be a good parameter to tune and optimize the discharge in a switch application.

Air showed similar behavior at 38 kV as Argon and Helium did at 17 kV. The behavior of Argon and Helium is very similar but Helium, at 200 mBar, gives the most homogeneous surface coverage. When taking all criteria into account, Argon shows the best overall performance for switch applications. Especially the high  $dV_{load}/dt$  makes Argon very interesting for fast high switching applications.

Using SrTiO<sub>3</sub> as dielectric shows significant changes in plasma behavior and proves that the dielectric plays an important role. Using SrTiO<sub>3</sub> not only the propagation velocity was lowered but also the plasma showed a separation in two phases. The measurements with SrTiO<sub>3</sub> show that the advantages of using high  $\epsilon_r$ , as mentioned in section 2.2.2 are accompanied with plasma behavior high at this moment is not fully understood. A more thorough study is needed to get a better understanding on the effect of high dielectric materials.

Three different measurement methods are combined to study the plasma. This combination has shown to be a powerful approach to study the plasma. The North Star and Pearson probes give reliable results but with a relatively low bandwidth. The D-dot sensors, whose output is more difficult to analyze, give more insight in the fast transients which are not observed with the North Star and Pearson probes. The optical images, and the synchronization of these with the electric measurements, are a very interesting tool to unravel and understand the plasma dynamics.

In this chapter an exploratory study in surface discharges has been described. The surface discharge is approached from an application point of view with the goal to find a plasma parameter setting which could be used in a high voltage surface discharge switch. Here, argon showed the best overall performance. Although it has a lower energy and power transfer than helium, argon does have the highest load voltage risetime which is considered, for our applications of interest, the most important parameter.

Table 2-9. Peak power and energy delivered to the load electrode.

Pressure [mBar]	Air						Argon		Helium		
	1000	500	200	1000	500	200	1000	500	1000	500	200
$V_{\text{charge}}$ [kV]	38	38	38	17	17	17	17	17	17	17	17
$P_{\text{peak}}$ [kW]	2110	1980	2770	5	50.5	346	600	627	391	689	666
$E$ [mJ]	44	52	70	0.05	0.7	6.9	14.8	15.2	10.8	17.8	20.7
Max $dV_{\text{load}}/dt$ [kV/ns]	2.2	1.2	1.3	0.1	0.3	0.7	1.8	1.6	0.9	1.2	0.9

Table 2-10. Average propagation velocities during the avalanche phase.

Pressure [mBar]	Air						Argon		Helium		
	1000	500	200	1000	500	200	1000	500	1000	500	200
$V_{\text{charge}}$ [kV]	38	38	38	17	17	17	17	17	17	17	17
$V$ [ $10^6$ m/s]	1.6	3.2	7.0	1.7	2.4	4.7	1.5	2.6	4.6	4.7	*
$\sigma_v$ [ $10^6$ m/s]	0.5	0.8	0.6	0.3	0.3	0.6	0.3	0.4	1.1	0.8	-

\*  $> 16 \cdot 10^6$  m/s, out of range, gap crossed within 500 ps.

Table 2-11. Peak power and energy delivered to the load electrode.

Pressure [mBar]	SrTiO <sub>3</sub> (Air)		
	500	200	100
$V_{\text{charge}}$ [kV]	17	17	17
$P_{\text{peak}}$ [kW]	40.6	291	405
$E$ [mJ]	0.8	7	15.7
Max $dV_{\text{load}}/dt$ [kV/ns]	0.17	0.48	1.08

Table 2-12. Average propagation velocities during the avalanche phase.

Pressure [mBar]	SrTiO <sub>3</sub> (Air)		
	500	200	100
$V_{\text{charge}}$ [kV]	17	17	17
$V$ [ $10^6$ m/s]	0.7	1.1	2.5
$\sigma_v$ [ $10^6$ m/s]	0.2	0.5	0.7





# 3 The Parallel Plate Transmission Line Transformer

---

## 3.1 Introduction

A Transmission Line Transformer, TLT, can be used to transform high-voltage nanosecond pulses. These transformers rely on the fact that the length of the pulse is shorter than the transmission lines used. This allows connecting the transmission lines in parallel at the input and in series at the output. The maximum theoretically achievable voltage gain is the square root of the ratio of input and output impedances. Without losses and with perfectly matched transmission lines, such structures achieve a voltage gain which equals the number of transmission lines used [37], [38], [39]. To achieve maximum efficiency, mismatch and secondary modes must be suppressed. Optimized transmission line transformers typically have up to 10 stages, limited by the practical limitations of the impedances at the input and output. The voltage gain achieved on a matched load ( $\sim 250 \Omega$ ) is around 7, or 70% of the theoretical limit [10].

Here we describe a TLT based on parallel plate transmission lines: a parallel plate transmission line transformer (PPTLT). The chosen geometry results in a high efficiency, due to good matching and minimized secondary modes. A second advantage of this design is that the electric field strength in the bulk between the conductors is the same throughout the entire TLT. This makes the design suitable for high voltage applications. Additionally this design has a high bandwidth causing minimal pulse broadening.

To investigate the concept of this TLT design, both numerical simulations and measurements have been done on a 4-stage and a 8-stage TLT design. Measurements with a 600 picosecond full width at half maximum (FWHM) Gaussian input pulse show that this structure achieves a voltage gain factor of 3.5 when using 4 transmission lines and 5.7 when using 8 lines on a matched load (88% and 71% of the theoretical limit). The investigation shows that the impedances of the transmission lines deviate from the values that were used in the design, due to edge effects. When these edge effects are taken into account in calculating the impedance ratio between the input and output of the TLT, this design achieves a voltage gain of 91% and 89%.

Here we give a proof of concept for the performance of the TLT based on parallel plate transmission lines. We compare a 4-line and an 8-line TLT to investigate the scalability of the gain of the PPTLT. The origin and effect of the secondary mode are studied using numerical simulations in comparison with network analyzer measurements. Finally, the possibilities to successfully adapt a PPTLT for pulsed high voltage application is discussed.

## 3.2 Transmission Line Transformer basics

Transmission line transformers rely on the fact that the length of the pulse is shorter than the transmission lines used. For these signals the in- and output of the transmission lines are isolated in

time. The time isolation allows for the input of  $N$  identical transmission lines to be connected in parallel and their outputs to be connected in series. This way an impedance ratio, equal to the number of transmission lines squared, can be obtained. In the ideal case such structures achieve a voltage gain which equals the number of transmission lines used. Coaxial transmission lines are the preferred choice for pulsed high voltage and high bandwidth applications. The basic structure of a TLT using coaxial transmission lines is schematically shown in Figure 3-1. The voltage amplification in a transmission line transformer is based on the impedance ratio between the in- and output ports and the conservation of power. Taking the impedance of one single transmission line as  $Z_0$ , the input impedance of the TLT,  $Z_{in}$ , equals  $Z_0/N$  and the output impedance  $NZ_0$ . With an input voltage,  $V_{in}$ , this results in an input power of

$$P_{in} = \frac{NV_{in}^2}{Z_0} \tag{3-1}$$

The ideal voltage gain  $G_i$ , the ratio between the in- and output voltage in the ideal lossless case where  $P_{out} = P_{in}$ , becomes

$$G_i = \sqrt{\frac{Z_{out}}{Z_{in}}} \tag{3-2}$$

Because the input impedance  $Z_{in}$  equals  $Z_0/N$  and the output impedance equals  $NZ_0$ ,  $Z_{out} = N^2Z_{in}$ , the voltage gain becomes  $G_i = N$ . This assumes ideal conductors, lossless dielectrics, perfectly matched interconnections and no secondary modes.

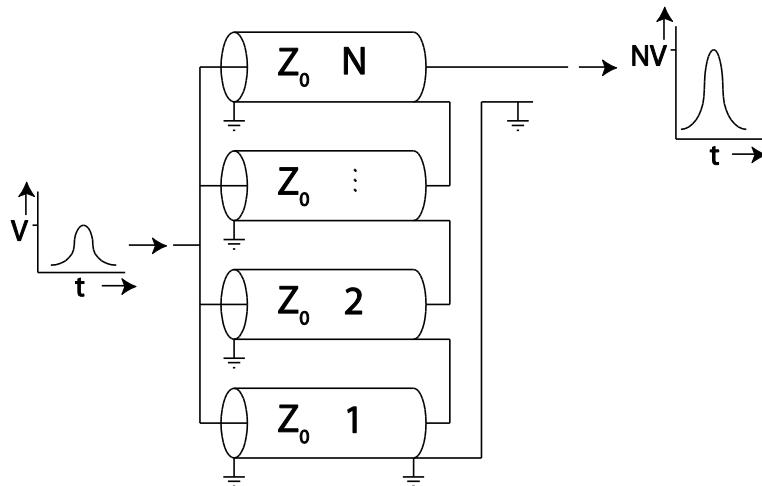


Figure 3-1. Schematic representation of a TLT.

Losses in a TLT occur in the dielectric and in the conductors. But these losses are very low and will be present independent of the TLT design. The bulk of the losses are caused at the series connection. When a pulse exits one of the transmission lines, it will propagate into any possible direction. This is shown in Figure 3-2. The voltage gain is limited by the mismatch at the interconnections between the different transmission lines, and by the so-called secondary mode [1]. This secondary mode is the part of the energy that propagates back in-between the transmission lines and is indicated with the solid red arrow in Figure 3-2. The dotted red arrows indicate reflection of the pulse at the output of the transmission line due to mismatch and propagation in the wrong direction in the series connection. As

a consequence, various reflections can be present in the output voltage pulses, as schematically shown in Figure 3-2.

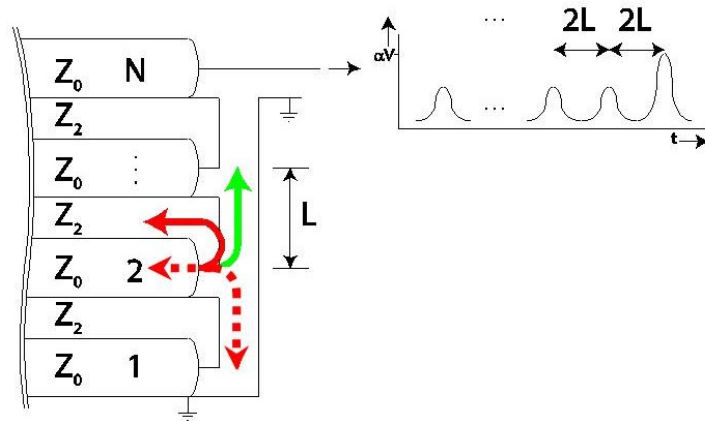


Figure 3-2. Secondary mode (solid red line), reflections and undesired propagation direction (dotted red line) and the desired propagation direction (green line) in a TLT.

Besides efficiency, pulse distortion is also an important performance characteristic of a TLT. Pulse distortion can be caused by differences in the length of the different transmission lines and by bandwidth limitations of the TLT.

To reduce the losses caused by reflections and the secondary mode, a novel TLT based on parallel plate transmission lines, PPTLT, has been designed. Besides an improvement in the efficiency also the pulse distortion has been reduced significantly.

### 3.3 Parallel Plate Transmission Line Transformer

Coaxial transmission lines are ideal for high bandwidth, pulsed applications. However, when making series or parallel connections, the geometry of the coaxial lines must be changed which results in reflections as briefly discussed above. The geometry of parallel plate transmission lines is better suited to make these connections resulting in considerably reduced reflections and a smaller influence of the secondary mode. The PPTLT has a very high bandwidth and therefore very little pulse distortion. In addition, a PPTLT can be designed in such a way that (very) high voltage pulses can be applied.

Here we will discuss this new, planar TLT topology and apply it for both a 4-stage and 8-stage PPTLT. Both designs are simulated and tested at low voltages.

The 4-stage PPTLT is shown in Figure 3-3. The model of both the 4- and 8-stage PPTLT is shown in Figure 3-4. The input of the PPTLT is at the top left of the figures. The output is at the bottom right. The PPTLT is made up of three sections

- i. The parallel connection directly after the input,
- ii. A center section with  $N$  separate transmission lines, and

- iii. The output section where all transmission lines are connected in series.

Losses due to mismatch at the interconnections of these sections is unavoidable, but by using parallel plate transmission lines, these losses can be kept relatively small.



Figure 3-3. The 4-stage PPTLT used in the experiments.

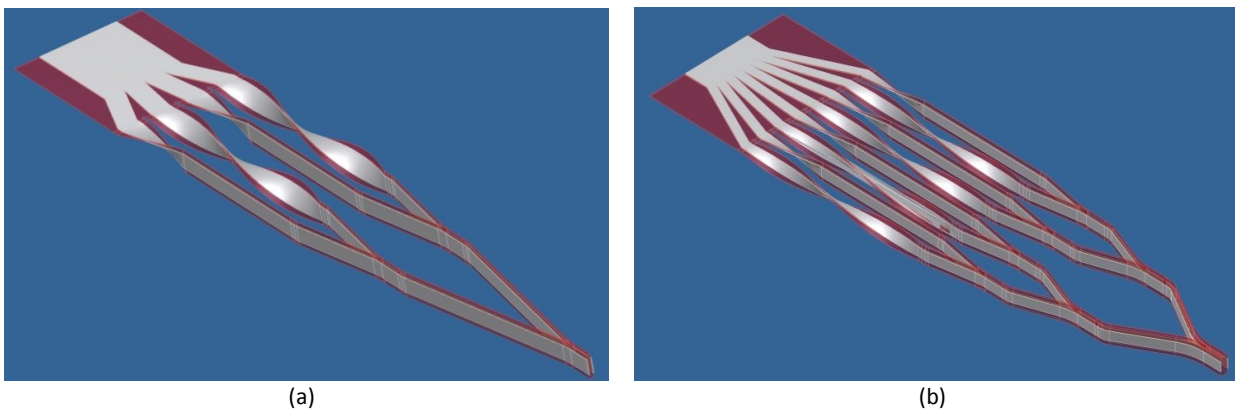


Figure 3-4. (a) The 4-stage PPTLT. (b) The 8-stage PPTLT.

Figure 3-5 shows the 3 different sections of the PPTLT. At the input side the PPTLT is constructed as a parallel plate configuration. The various outgoing parallel-plate transmission lines are created by splitting the input into the desired number of lines. The width of the incision in between the transmission lines is negligible with respect to the width of the transmission lines themselves.

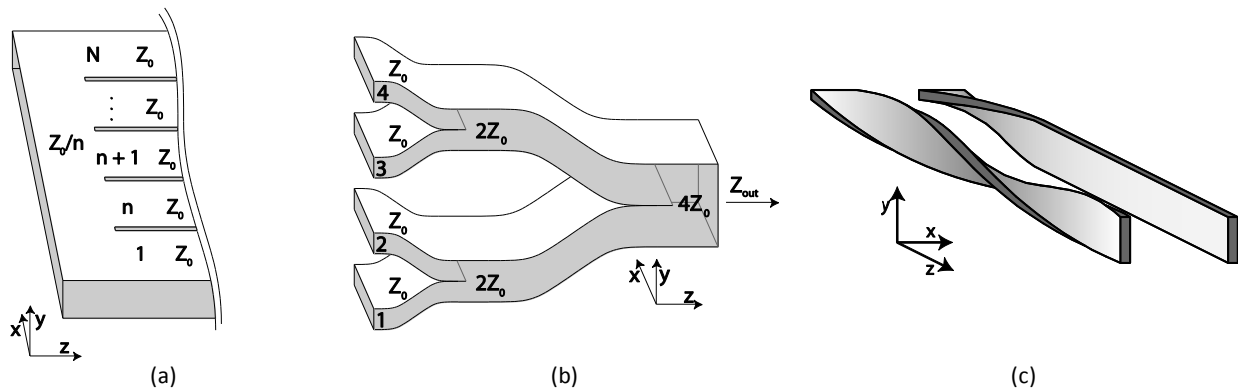


Figure 3-5. (a) Parallel input of the PPTLT. (b) Series connection of the transmission lines. (c) Rotation of the transmission lines needed to connect their outputs in series.

At the output section, all planar transmission lines are connected in series. This is done by stacking the transmission lines as shown in the center of Figure 3-5. This gives (in the case of Figure 3-5) a transmission line with four times the height and therefore four times the impedance. This structure has two distinct advantages. First, the electric field strength inside the incoming and outgoing transmission lines is the same. Secondly, because the field remains localized between the transmission lines, the secondary mode is small. By stacking the transmission lines pair wise, the length of the individual transmission lines is easily kept equal which is essential for timing purposes. Due to the skin effect, almost all of the current carrying the pulse is on the inside of the transmission line. This allows for a relatively loss-free series connection.

To connect all transmission lines in series, they must be positioned such that the positive plate of one line can be connected to the negative plate of its neighboring line. This is realized in the center section of the PPTLT, shown in the right of Figure 3-5, by rotating the transmission lines in opposite directions. If the transmission lines were all rotated in the same direction, the distance between the bottom electrode of one transmission line and the top electrode of the other would become so small that breakdown may occur. To prevent this, the rotation direction alternates between the transmission lines. The effect is shown schematically in Figure 3-6. Here two parallel transmission lines are shown with no rotation, similar rotation direction and opposite rotation direction.

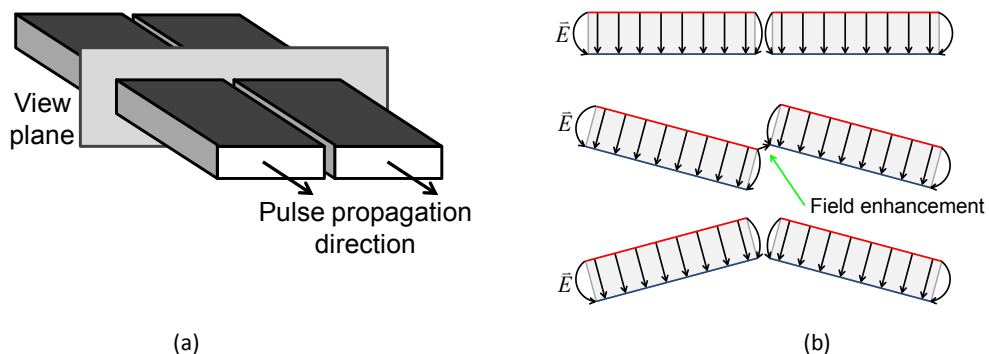


Figure 3-6. (a) view plane. Top right; two parallel transmission lines, only field enhancement due to edges and air gap in between the transmission lines. Red and blue lines indicate opposite conductors of the transmission lines. (b) Rotating the transmission lines in the same direction causes the opposite electrodes of the two transmission lines to get very close and cause field enhancement increasing the change of breakdown. By rotating the transmission lines in opposite directions no additional field enhancement occurs in between the transmission lines.

This structure is very suitable for fast high voltage applications. The breakdown strength of the dielectric in the transmission lines, the sharp edges of the electrodes at the sides of the transmission lines and the pulse length are limiting factors that dictate the maximum voltage that can be applied to the structure without breakdown. With good engineering, these issues can be solved and the applied voltage and electric fields strengths can be pushed to very high limits. In the design of the PPTLT as shown in Figure 3-3, two measures to make the PPTLT suitable for pulsed high voltage applications are implemented:

The first is the widening of the dielectric in the transmission lines. Increasing the width of the dielectric increases the path length for flash over. This has a minimal effect on the bandwidth or losses.

Secondly, the individual transmission lines are, directly after the input, placed further apart from each other to reduce the chance of breakdown.

The realized 4-stage and 8-stage PPTLT's are constructed of DiBond™ [4]. A cross section of these DiBond™ plates is shown in Figure 3-7. This material consists of a 2.2 mm thick, flat polyethylene inner core with a 0.3 mm thick aluminum sheet on both sides. In Figure 3-3, the polyethylene is black and the aluminum is blue. The width of the aluminum at the input of both the PPTLTs is 176 mm. With the dielectric constant of the polyethylene of 2.26, [5], we find an input impedance of 3.125 Ω, using

$$Z_0 = \sqrt{\frac{\mu}{\epsilon}} \frac{d}{w} \tag{3-3}$$

Here  $d$  is the thickness of the dielectric,  $w$  the width of the conductors,  $\mu$  the permeability,  $\epsilon$  the permittivity. For the 4-stage PPTLT the aluminum of the transmission lines, and thus also of the output, is 44 mm wide. At the output the polyethylene is 8.8 mm thick resulting in an output impedance of 50 Ω. The 8-stage PPTLT has 22 mm wide transmission lines and 17.6 mm thick dielectric at the output resulting in a 200 Ω output impedance.

The bandwidth of the PPTLT, defined as the lowest frequency below which no other modes than the TEM mode can propagate, can be found with [30]

$$f_c = \frac{1}{2d\sqrt{\mu\epsilon}} \tag{3-4}$$

Here  $f_c$  is the cut-off frequency in Hz,  $d$  the thickness of the dielectric,  $\mu$  is the permeability and  $\epsilon$  the permittivity. The bandwidth of the PPTLT is thus limited by the output since there the distance between the electrodes,  $d$ , is the largest. In the case of 4 transmission lines,  $d$  is 8.8 mm and  $f_c$  is 11.3 GHz. In the case of 8 transmission lines,  $d$  is 17.6 mm and  $f_c$  is 5.56 GHz.

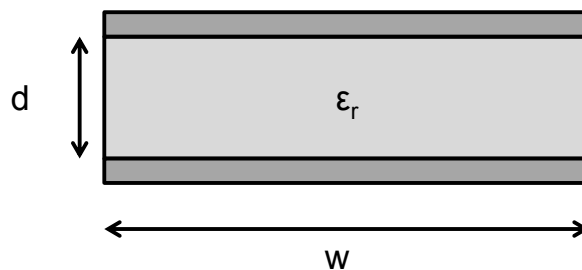


Figure 3-7. Dimensions used in the parallel plate transmission line.

### 3.4 Simulations of the PPTLT

To study the performance of the PPTLT, numerical time domain simulations on both a 4-stage and an 8-stage PPTLT are done in CST Microwave Studio. The models have the same dimensions as the real life structures. A time domain solver, with a bandwidth of 0 to 3 GHz, and a Gaussian input pulse with a full width at half maximum of 600 picoseconds, similar to the one used in the experiments, are used to simulate the performance of the PPTLTs. The input pulse is normalized to a peak power of 1 watt and is shown in Figure 3-8.

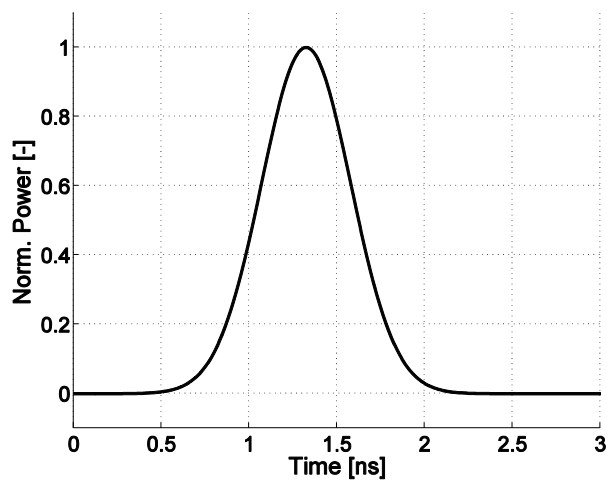


Figure 3-8. Normalized input power pulse with a FWHM of 600 ps.

For the aluminum conductors, a conductance of  $3.56 \cdot 10^7$  S/m is used and the polyethylene is simulated with an  $\epsilon_r$  of 2.26 and a  $\tan\delta$  of  $3.1 \cdot 10^{-4}$  at 3 GHz. These values are based on measurements, which are described in [6], and are in good agreement with values found in literature [5].

The impedances of the in- and output ports of the PPTLTs, as determined from the simulations, slightly differ from the ideal impedances as found by using eq. 3-3. Impedance values are shown in Table 3-1, the values between brackets are the expected values based on eq. 3-3.

Table 3-1. Simulated impedances of the PPTLT's

	4 stage PPTLT	8 stage PPTLT
<i>Input impedance</i> $Z_{in}$ [ $\Omega$ ]	3.07 (3.125)	3.07 (3.125)
<i>Line impedance</i> $Z_o$ [ $\Omega$ ]	11.70 (12.5)	21.64 (25)
<i>Output impedance</i> $Z_{out}$ [ $\Omega$ ]	40.45 (50)	114.5 (200)

Eq. 3-3 does not take edge effects into account. This leads to an overestimation of the impedance. This effect is larger for higher impedances where the ratio between the height and the width of the transmission line is larger. Also the extension of the dielectric in between the conductors lowers the impedance of the transmission lines. With the simulated impedances the ideal voltage gain,  $G_i$  (as



calculated with eq. 3-2) is 3.63 for the 4-stage and 6.11 for the 8-stage PPTLT respectively (see also Table 3-2).

### 3.4.1 Voltage gain

Figure 3-9 shows the simulated voltages at the in- and output of the 4-stage PPTLT when the pulse as shown in Figure 3-8 is fed to the input. Figure 3-10 shows these simulated in- and output voltages for the 8-stage PPTLT. As can be seen, the output pulses are not visibly distorted. The time lag between the in- and output pulses of both PPTLTs is 7.81 and 7.19 ns for the 4- and 8-stage PPTLT respectively. This corresponds with a distance of 1.55 and 1.43 m (at a wave velocity of  $2 \cdot 10^8$  m/s) which corresponds with the lengths of the PPTLTs which are 156.6 cm and 143.7 cm for the 4- and 8-stage PPTLT respectively.

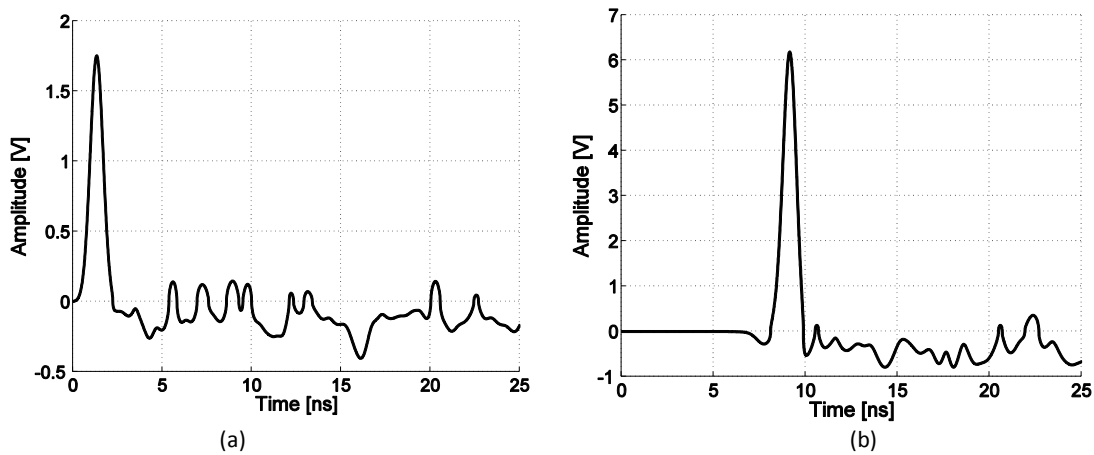


Figure 3-9. (a) Voltage at the input of the 4-stage PPTLT. (b) Voltage at the output of the 4-stage PPTLT.

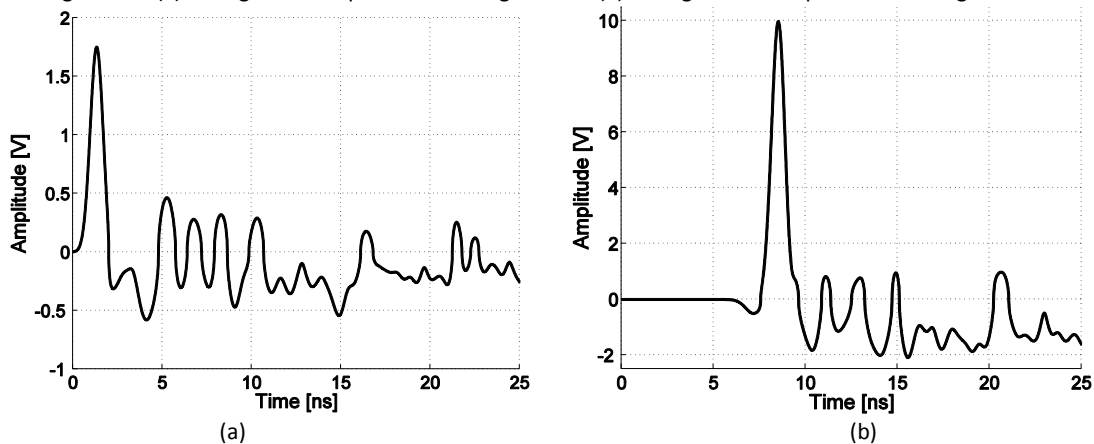


Figure 3-10. (a) Voltage at the input of the 8-stage PPTLT. (b) Voltage at the output of the 8-stage PPTLT.

The simulated output pulse of the 4-line PPTLT has a peak power of 0.945 and a FWHM of 600 ps. The peak value of the in- and output voltages are found using

$$V = \sqrt{PZ}$$

3-5

Here P is the power and Z the impedance of the port of interest. Table 3-2 shows these values for both the in- and output ports of the PPTLTs. Based on these results the 4-stage and the 8-stage PPTLT

have a voltage gain of 3.53 and 5.69 respectively. The voltage transformation efficiencies of both the PPTLTs are well above 90%. This is a significant improvement compared to TLTs based on coaxial transmission lines which typically reach less than 70% voltage transformation efficiencies [10], [37].

Table 3-2. In and output values of the 4-stage and 8-stage PPTLT.

		4-stage PPTLT		8-stage PPTLT	
		Input	Output	Input	Output
$P_{\max}$		1	0.945	1	0.868
$Z$		3.07	40.45	3.07	114.7
$V_{\max}$		1.75	6.18	1.75	9.98
Voltage gain	$G_i$ (eq. 3-2)	3.63		6.11	
	simulated	3.53		5.69	
	measured	3.32		5.43	
Voltage gain	simulated	97.2%		93.2%	
Efficiency	measured	91.5%		88.9%	

### 3.4.2 Reflections and mismatch

The difference between the ideal voltage gain  $G_i$  and the simulated voltage gain is mainly caused by reflections, due to mismatch, and by the secondary mode (as will be explained later). In the voltage signals at the inputs of the PPTLTs, as shown in Figure 3-9 and Figure 3-10, several distinct peaks can be observed. The time difference  $\Delta t_i$  between these peaks and the input pulse is used to find the location inside the PPTLT where these reflections occur. These times correspond with a reflection path length  $l_i$  of

$$l_i = \frac{\Delta t_i}{2} \cdot \frac{c}{\sqrt{\epsilon_r}}$$

3-6

Here  $\Delta t_i$  is the observed time difference,  $\epsilon_r$  the dielectric constant of the polyethylene and  $c$  the speed of light  $3 \cdot 10^8$  m/s. Table 3-3 shows the various reflection lengths for both PPTLTs.

Table 3-3. reflection lengths.

4-stage PPTLT		8-stage PPTLT	
Time $\Delta t_i$ [ns]	$l_i$ [m]	Time $\Delta t_i$ [ns]	$l_i$ [m]
2.95	0.29	2.78	0.28
9.90	0.98	8.73	0.87
14.78	1.47	13.56	1.35

The positions where these reflections occur, correspond with positions in the PPTLT where a “secondary mode” (see Figure 3-2) effect can be observed. This can be seen from the results of simulations as shown in Figure 3-11. In this figure, the current distribution in the conductors of a PPTLT is shown at three different times: (i) just before the input pulse reaches the series connection, (ii) when the input pulse arrived at the series connection, and (iii) shortly after the input pulse arrived at the series connection. These figures show the component of the surface currents in the pulse propagation direction on the transmission lines in the one of the series connections of the 8-stage PPTLT. The color scale has a very small range to clearly show the effect that causes the secondary mode. As can be seen in Figure 3-11, at the front of the pulse there is only current on the inside of the transmission line. Half

way the pulse, there is also a current at the outside of the transmission line. The current on the outside of the two inner most conductors, now travels in the area in between the two transmission lines which behaves as a waveguide. This current is called the secondary mode. The waveguide in between the transmission lines is short-circuited by the back of the series connection (Figure 3-11 top right) causing the secondary mode to be inverted and reflect back to the input of the PPTLT (Figure 3-11 bottom left). As a result, even though the secondary mode causes some energy loss, it does not distort the pulse. This is different from the situation in a TLT based on coaxial transmission lines. In those TLTs, secondary modes and reflections between the connections can propagate directly to the output of the TLT (see also Figure 3-2). In the PPTLT, the secondary modes are localized in between the transmission lines (on the outside of the transmission lines) and cannot propagate directly to the output.

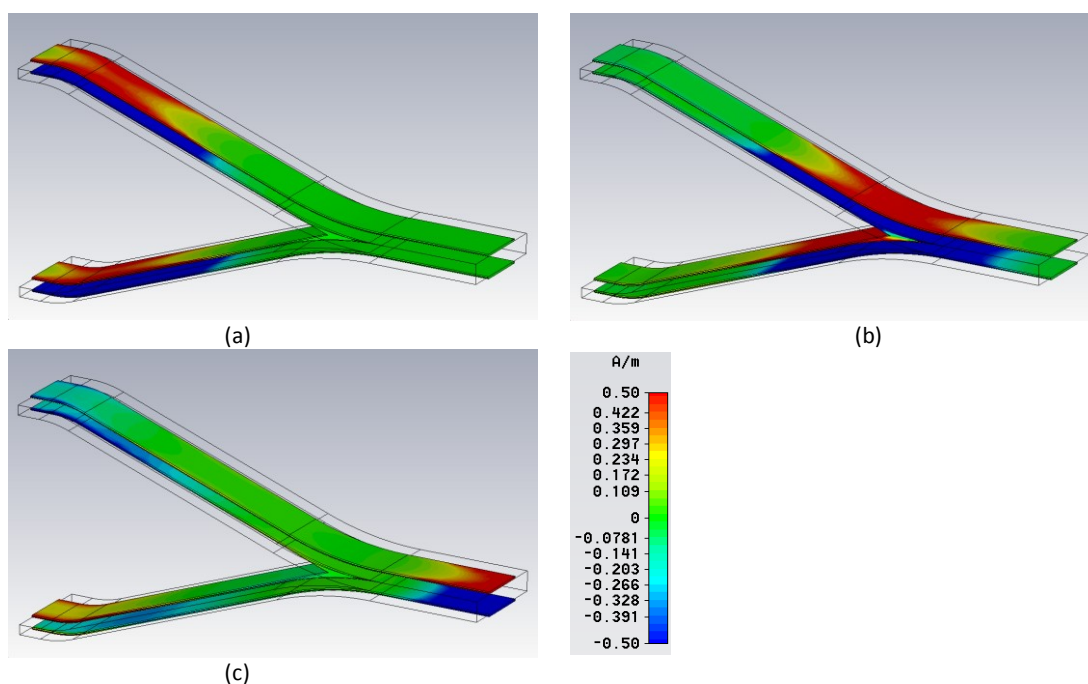


Figure 3-11. These figures show the simulated surface currents at the series connection as the pulse passes. (a) Pulse approaching the series connection. The small fraction of the current which travels on the outside of the inner transmission lines is the cause for the secondary mode. The color scale is saturated to show the secondary mode. (b) Pulse at the series connection. The current on the two outermost conductors simply continues. The current on the outside of the two innermost conductors is reflected back to the input. The space in between the two transmission lines forms a waveguide with a short-circuited end. (c) Reflected secondary mode returns to the input and the main pulse continues to the output.

### 3.4.3 Losses in the dielectric and conductors

With respect to the coaxial TLT, the simulations show a performance improvement due to a reduction in the losses caused by reflections and the secondary mode. These are not the only losses that occur in a TLT. Also losses in the dielectric and the conductors occur [30]. But these latter two will occur in both TLTs and are hard to reduce. Both are dependent on the quality of the used materials and manufacturing of the TLTs. These losses do not make the difference in the performance of the two designs. For completeness they will be treated in short.

### Losses in the dielectric

The losses in the dielectric in a parallel plate transmission line,  $\alpha_d$ , can be found with

$$\alpha_d = \frac{k \tan \delta}{2} \quad 3-7$$

Here  $\alpha_d$  is the loss in Np/m, which is 8.686 dB/m.  $\tan \delta$  is the loss factor of the dielectric and  $k$  is the wave number in the presence of loss,

$$k = \omega \sqrt{\mu_0 \mu_r \epsilon_0 \epsilon'} \quad 3-8$$

$k$  depends on the real part of the dielectric constant which is defined as.

$$\epsilon' = \frac{\epsilon_r^2}{\sqrt{1 + \tan^2 \delta}} \quad 3-9$$

For polyethylene, with an  $\epsilon_r$  of 2.26 and a  $\tan \delta$  of  $3.1 \cdot 10^{-4}$  [5], the losses in the dielectric increase linearly from zero to 0.057 dB/m, at 1.342 GHz, which is the highest frequency component in the test pulse.

### Losses in the conductors

The losses in the conductors,  $\alpha_c$ , for the TEM mode in a parallel plate transmission line are given by

$$\alpha_c = \frac{R_s}{\eta d} \quad 3-10$$

Here  $R_s$  is the surface resistance of the conductor. Surface resistance is the resistance of the conductor based on the skin depth.  $d$  is the height of the dielectric and  $\eta$  the wave impedance which is defined as

$$\eta = \sqrt{\frac{\mu_0 \mu_r}{\epsilon_0 \epsilon'}} \quad 3-11$$

The surface resistance is given by

$$R_s = \frac{1}{\sigma \delta_s} \quad 3-12$$

with  $\sigma$  the conductivity and  $\delta_s$  the skin depth.

$$\delta_s = \sqrt{\frac{2}{\omega \mu_0 \mu_r \sigma}} \quad 3-13$$

In these calculations perfectly smooth surfaces are assumed. In reality this will not be the case. The roughness of the surfaces will cause a measured attenuation to be bigger than the one given in eq. 3-10. To correct for the surface roughness the following empirical equation can be used [30]

$$\alpha_c' = \alpha_c \left[ 1 + \frac{2}{\pi} \tan^{-1} 1.4 \left( \frac{\Delta}{\delta_s} \right)^2 \right] \quad 3-14$$

Here  $\Delta$  is the RMS roughness of the conductor surface in meter. For a parallel plate transmission line with a dielectric thickness  $d$  of 2.2 mm, using aluminum conductors with a conductance of  $3.8 \cdot 10^7 \Omega^{-1}$ , the polyethylene described above and a  $\Delta = 10 \mu\text{m}$ , we find a total attenuation due to losses of  $\alpha_d + \alpha_c' = 0.3 \text{ dB/m}$  at 1.342 GHz.

The total losses in the dielectric material and the conductors amount to approximately 0.36 dB/m, or 4% loss per meter, for the entire PPTLT.

## 3.5 Measurements

### 3.5.1 Transient pulse

To test the PPTLT, a 4- and 8-stage PPTLT were built, see Figure 3-3 and Figure 3-4. The sizes are the same as in the models described in the previous section. Experiments, described in [6], show that the dielectric constant of the polyethylene is 2.26 +/- 0.07 which agrees with values mentioned in literature [5] and used in the simulations.

In the experiments, fast pulses are injected into the PPTLT's and the output signals are recorded. All signals are measured with a LeCroy WavePro 7300A oscilloscope using 50  $\Omega$  input impedance. The pulses are generated with an AVTECH AVMN-2-C pulse source, with the following parameters: FWHM of 602 ps +/- 6 ps, peak voltage of 320 mV +/- 3 mV. The output impedance of this source is 50  $\Omega$ .

To match the source to the PPTLT, a tapered transmission line is made as shown in Figure 3-12. The input is shown in the top left and the output at the bottom right. To connect the output of the tapered transmission line to the PPTLT, 16 SMA connectors, spaced 11 mm apart, are used. This spacing of 11 mm corresponds to an impedance of 50  $\Omega$  for the DiBond™. A schematic view of how the SMA connectors are connected to the DiBond™ is shown in Figure 3-13. Figure 3-13 shows the output pulse of one of the SMA connectors at the output of the tapered transmission line. These pulses will be the input pulses for the PPTLT and have a peak value of 56.4 +/- 0.8 mV and a FWHM of 611 +/- 10 ps over an average of 1000 pulses.

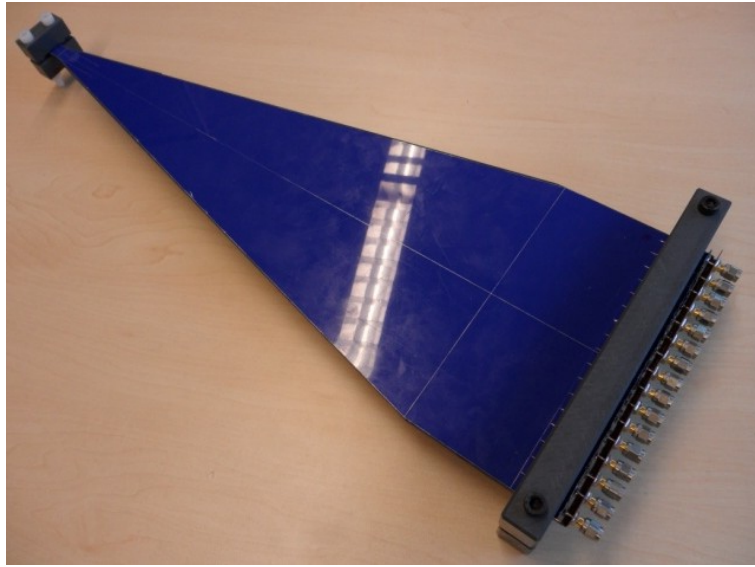


Figure 3-12. Tapered transmission line to match the pulse generator output impedance to the PPTLT input impedance.

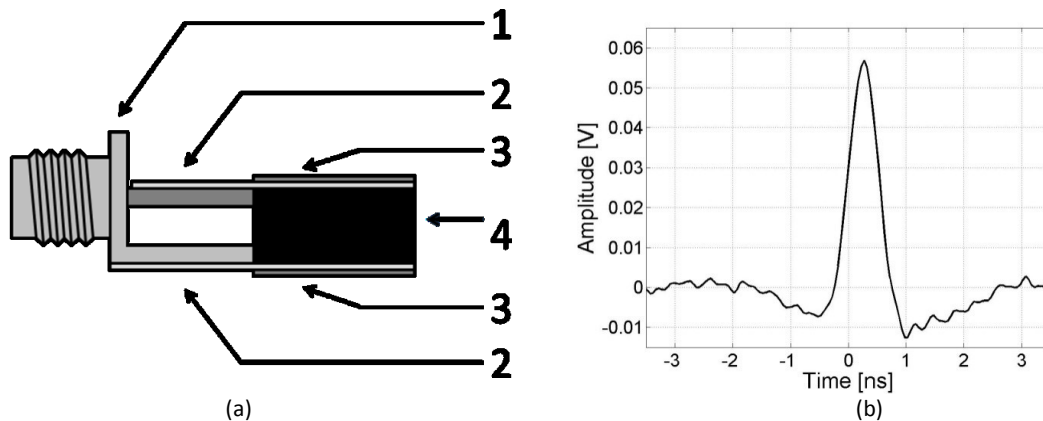


Figure 3-13. (a) Schematic representation of the connection of a SMA connector to the parallel plate structure. (1) SMA housing, (2) thin copper plate, (3) aluminum of the DiBond™, (4) PE of the DiBond™. (b) Input pulse for the PPTLTs.

### 3.5.1.1 4 STAGE PPTLT

The in- and output voltage of the 4-stage PPTLT is shown in Figure 3-14(a). The amplitude of the output voltage shown in Figure 3-14(a) is corrected for mismatch between the output of the TLT and the input of the oscilloscope

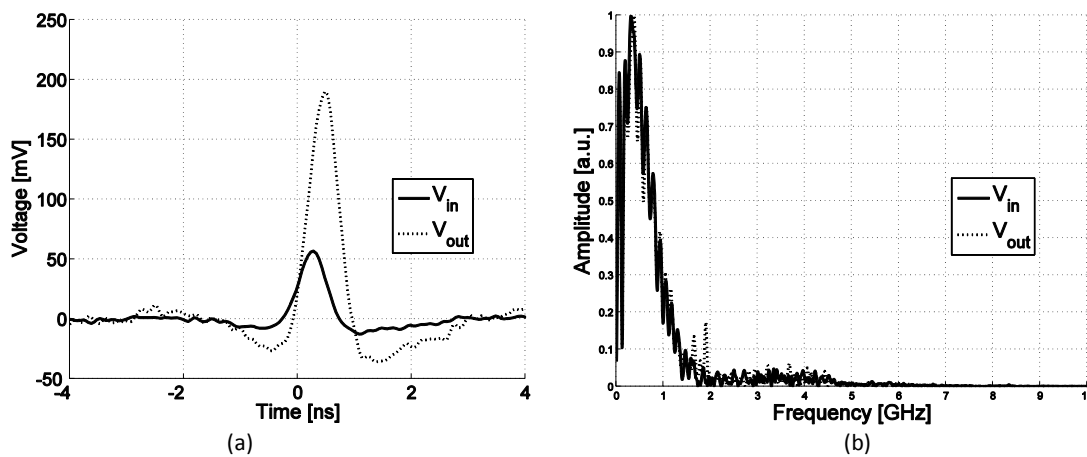


Figure 3-14. (a); in- and output voltage of the 4-line PPTLT. (b); in- and output signal power spectrum.

The correction for the mismatch between the 4-line PPTLT output impedance and the oscilloscope input impedance is based on

$$T = \frac{2Z_l}{Z_l + Z_0}$$

3-15

Here T is the transmission coefficient,  $Z_l$  the 50  $\Omega$  input impedance of the oscilloscope and  $Z_0$  the 40.53  $\Omega$  output impedance of the PPTLT. This gives a transmission coefficient of 1.1056 and a voltage at the output of the PPTLT of 187 mV. This results in a voltage gain of 187mV/56.4 mV = 3.32. The ideal voltage gain,  $G_i$ , based on the in- and output impedances (eq. 3-2), for this TLT is 3.63 (see also Table 3-2). The measured voltage transformation efficiency therefore is 91.3%, which means that reflections, mismatch and other losses amount to 8.7%.

A small increase in the FWHM of the output pulse is observed (Figure 3-14(a)). The bandwidth of the transmission lines is much higher than that of the pulse (see section 3.3, eq. 3-4). It is therefore unlikely that the pulse broadening is caused by bandwidth limitation. Figure 3-14 (b) shows the normalized power spectral density of both the in- and output pulse. Here we see that both signals have nearly the same power spectral density, which also indicates that the pulse shape is not influenced by bandwidth limitations. The broadening may be caused by small length differences in the 4 transmission lines. The PPTLT is handmade with a tolerance in the longitudinal direction of  $\pm 5$  mm. This corresponds to a variation in time of  $\pm 25$  ps, which is of the same order as the broadening observed in Figure 3-14 (a).

### 3.5.1.2 8-STAGE PPTLT

The pulse of Figure 3-13 is also applied as input for the 8-stage PPTLT. The output pulse, after applying correction factor for the mismatch at the output, is shown in Figure 3-15 together with the input pulse. The measured output pulse has a peak value of  $186 \pm 3$  mV and a FWHM of  $649 \pm 10$  ps over an average of 1000 pulses. As with the 4-stage PPTLT, the amplitude of the measured output pulse must be corrected for the mismatch between the output of the PPTLT and the oscilloscope. With the output impedance of the 8-line PPTLT of  $114.5 \Omega$  and the input impedance of the oscilloscope of  $50 \Omega$ ,  $T$  is 0.6079. This gives a peak voltage at the output of the PPTLT of 306 mV and a voltage gain of 5.43. The voltage gain efficiency is  $5.43/6.11 = 88.9\%$ .

Again we see a small increase of the FWHM. Also in this case the manufacturing accuracy is expected to be the main reason. As shown in Figure 3-15, the normalized power spectral density of both the in- and output pulse are the same.

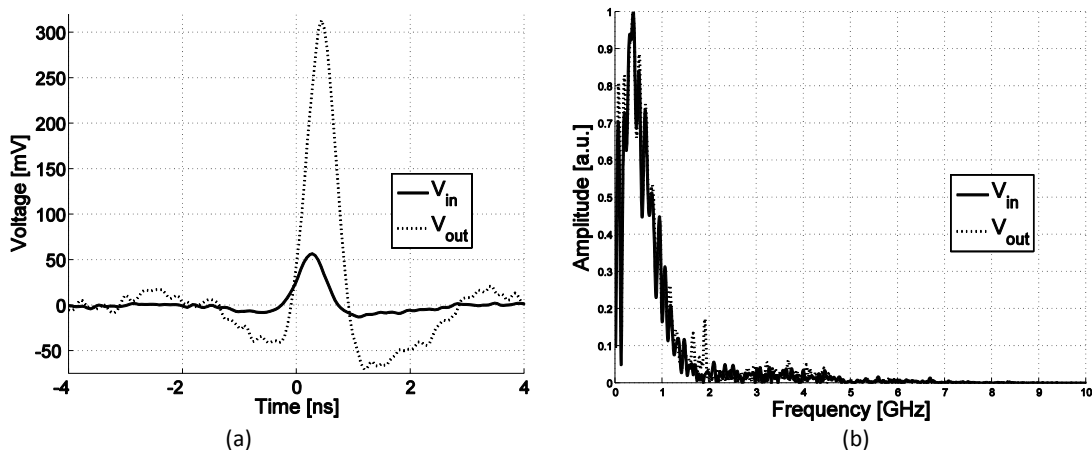


Figure 3-15. (a) Output voltage of the 8-line PPTLT. (b) Power spectrum of the in- and output pulse.



### 3.5.2 Scattering parameters

A commonly used technique to characterize high frequency electric components is the measurement of scattering parameters. A basic schematic example of scattering parameters on an N-port device is shown in Figure 3-16 (this figure is based on figure 4.10 of [7]). At each port, the voltage is the summation of an incident and reflected wave. These waves are related by the port impedances. Following the derivation as shown in [7], 2 new variables are introduced

$$a_n = V_n^+ / \sqrt{Z_{0n}} \quad 3-16$$

$$b_n = V_n^- / \sqrt{Z_{0n}} \quad 3-17$$

Now the voltage and current at each port can be described as

$$V_n = V_n^+ + V_n^- = \sqrt{Z_{0n}}(a_n + b_n) \quad 3-18$$

$$I_n = \frac{1}{Z_{0n}}(V_n^+ - V_n^-) = \frac{1}{\sqrt{Z_{0n}}}(a_n - b_n) \quad 3-19$$

The power at each port is given by

$$P_n = \frac{1}{2} \text{Re}\{V_n I_n^*\} = \frac{1}{2} |a_n|^2 - \frac{1}{2} |b_n|^2 \quad 3-20$$

Now the incident and reflected wave can be related through  $a_n$  and  $b_n$  using a generalized scattering matrix

$$[b] = [S][a] \quad 3-21$$

The components of the scattering matrix are given by

$$S_{ij} = \left. \frac{b_i}{a_j} \right|_{a_k=0 \text{ for } k \neq j} \quad 3-22$$

And by substituting eq. 3-16 and eq. 3-17 in eq. 3-22 results in

$$S_{ij} = \left. \frac{V_i^- \sqrt{Z_{0j}}}{V_j^+ \sqrt{Z_{0i}}} \right|_{V_k^+=0 \text{ for } k \neq j} \quad 3-23$$

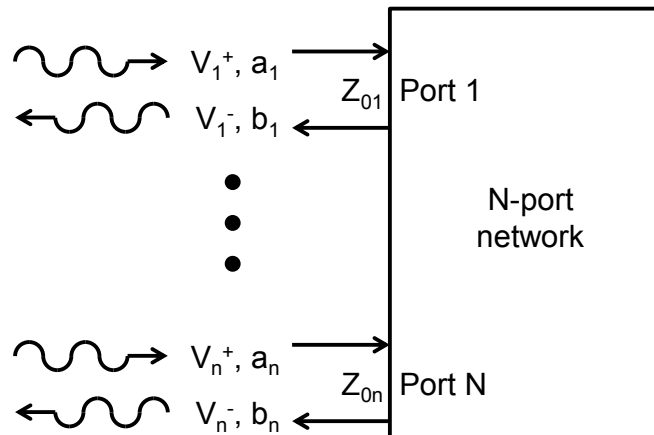


Figure 3-16. Scattering parameters on an N-port network. Based on figure 4.10 of [7].

Scattering parameters give a relation between the incident and reflected waves. Figure 3-17 shows the scattering parameters at a 2 port network.  $S_{11}$  gives the relation between the incident and reflected wave at the input port.  $S_{21}$  indicates the relation between the outgoing wave at port 2 and the incident wave at port 1. Scattering parameters are a very useful tool in determining the efficiency of a network.

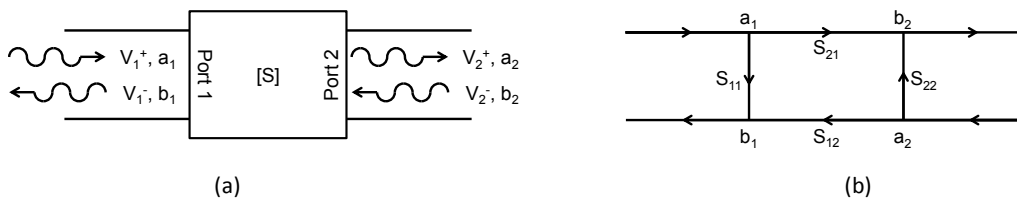


Figure 3-17. Scattering parameters of a 2-port network.

For both PPTLTs the scattering parameters are measured using a Hewlett Packard 8753C vector network analyzer. To measure the scattering parameters, 15 of the 16 SMA connectors at the input are terminated with  $50 \Omega$ . The remaining port is connected to one of the ports of the network analyzer. The output port of the PPTLT is connected to the other port of the network analyzer. The scattering parameters are indicated with  $S_{0X}$ ,  $S_{X0}$  and  $S_{XX}$ . The subscript 0 indicates the output port and X, which ranges from 1 to 16, one of the 16 input ports. The scattering parameters,  $S_{0X}$ ,  $S_{X0}$  and  $S_{XX}$ , are shown in Figure 3-18 through Figure 3-20 for the 4-stage PPTLT and in Figure 3-21 through Figure 3-23 for the 8-stage PPTLT. The left figures are the envelope of the 16 scattering parameters and the right images are a 3D plot of the scattering parameters. The right figures show that the behavior of the transmission line is different for the different input ports. Especially for the 4-stage PPTLT the 3D figures show a clear structure which correlates with the physical structure of the PPTLT.

A quick estimation can be made to estimate the transmission scattering parameter of the 4- and 8-stage PPTLT. At the input only one  $50 \Omega$  SMA connector is connected to the network analyzer. At this point the network analyzer sees a load of  $3.125 \Omega$  in parallel with 15 times  $50 \Omega$  of the 15 terminated SMA connectors. This is a total impedance of  $1.613 \Omega$ . This gives a transmission, in dB, of  $-24.08$  dB. The gain of the PPTLT, using the ideal gain of 3.63 from Table 3-2, is 11.2 dB and at the output the transmission coefficient is  $-0.97$  dB. The summation of these three,  $-13.85$  dB, is a rough estimate of what we might expect of the transmission scattering parameter. As we can see in the figures below, this is very close to the actually measured values for up to 1.5 GHz.

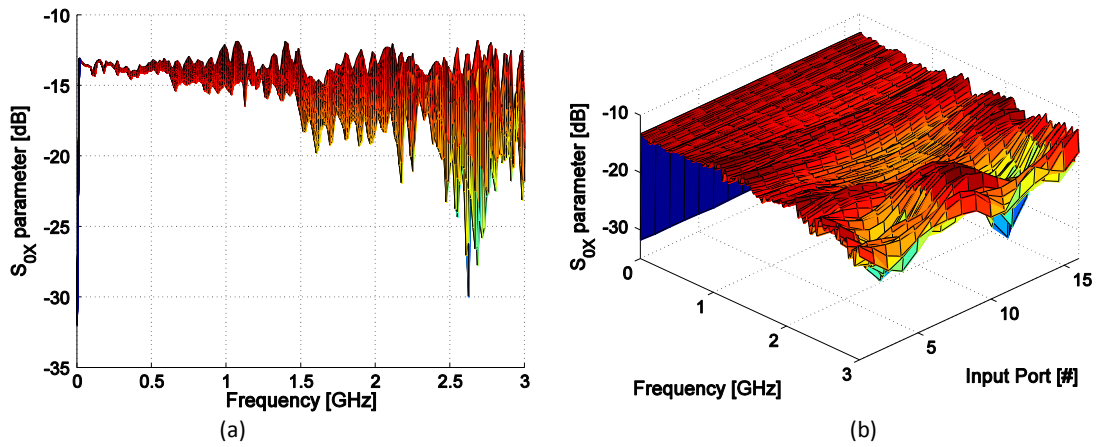


Figure 3-18.  $S_{0X}$  scattering parameters.

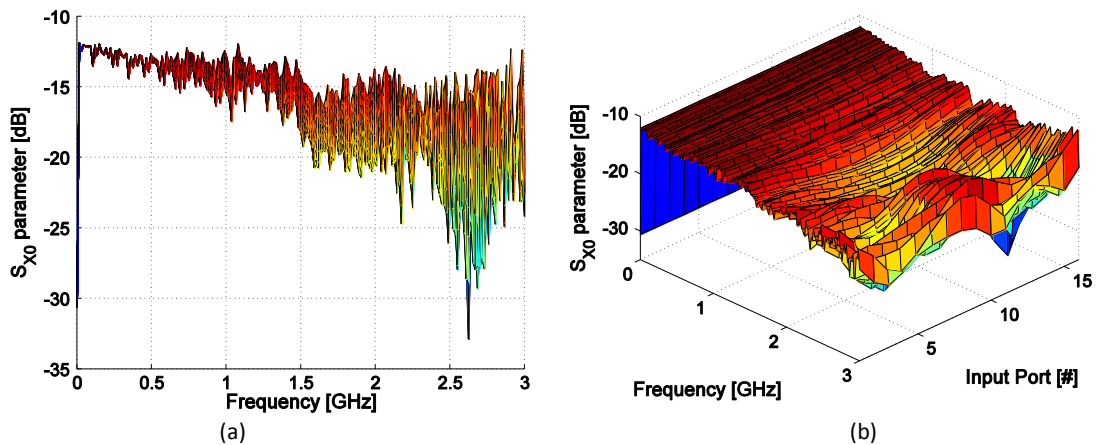


Figure 3-19.  $S_{X0}$  scattering parameters.

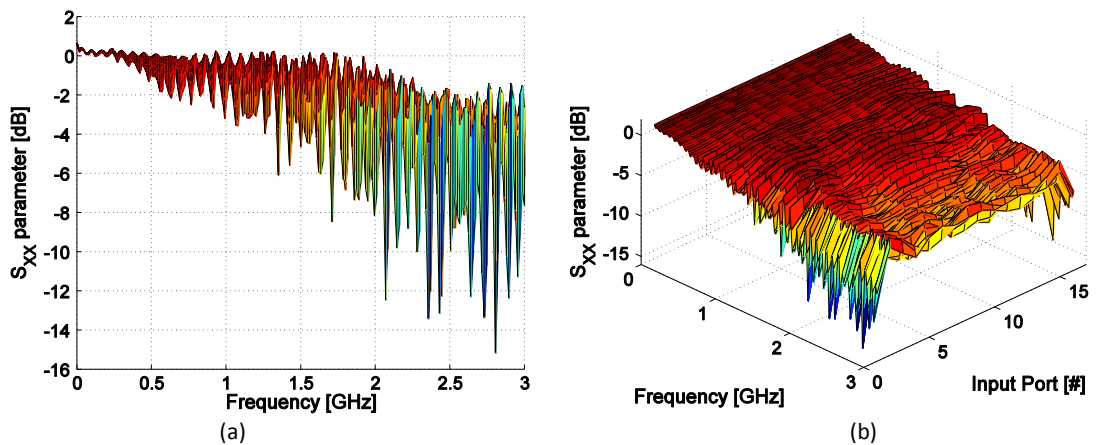


Figure 3-20.  $S_{XX}$  scattering parameters.

At 1.5 and 2.25 GHz a clear change in the scattering parameters is observed. Here the attenuation increases. This attenuation increase is expected to be linked to the secondary mode. The space in between the transmission lines functions as a transmission line on itself which absorbs energy and reflects it back to the input of the PPTLT. An electromagnetic wave with a frequency of 1.5 GHz has a wavelength of  $\lambda = c/f = 3 \cdot 10^8 / 1.5 \cdot 10^9 = 20$  cm, and for a frequency of 2.25 GHz we get a wavelength of

13.3 cm. So the corresponding half wavelengths fit in the spaces between the transmission lines. The 1.5 GHz wave fits in the largest space just in front of the last series connection. The 2.25 GHz wave fits in the smaller spaces at the first series connections. Because these spaces become smaller, closer to the series connections they will also influence higher frequencies as seen in the frequency plots.

The measurement of  $S_{0x}$  and  $S_{x0}$  gives a fingerprint of the structure; the locations of stronger attenuation in the figures correlate with the physical structure of the PPTLT.

At very low frequencies the transmission becomes very poor as expected; for signals longer than the PPTLT, it is simply a short circuit.

For the 8-stage PPTLT we obtained similar results and these are shown in Figure 3-21 through Figure 3-23. Here the rough estimate of the transmission scattering parameter gives us -24.08 dB at the input, 15.72 dB for the gain factor of 6.11 and -4.33 dB for the mismatch at the output which totals to -12.7 dB for the transmission scattering parameter. As we can see, the measured results are quite close and again we see additional attenuation which can be ascribed to the spaces in between the transmission lines. Here the structure is harder to see. We still use 16 input ports to measure the scattering parameters but the number of transmission lines has doubled. This can be seen as a decrease in 'resolution'.

Following the reasoning above for the 4-stage TL, there are three different sizes of spaces in between the transmission lines. We therefore expect to see three steps in the attenuation in Figure 3-21, at 0.6 GHz, 1.5 GHz and 2.2 GHz, corresponding to distances from the input to the interconnects of 13.7 cm, 20 cm and 50 cm, respectively. The steps are not very obvious in Figure 3-21, but some variation in the attenuation can nevertheless be observed around these frequencies.

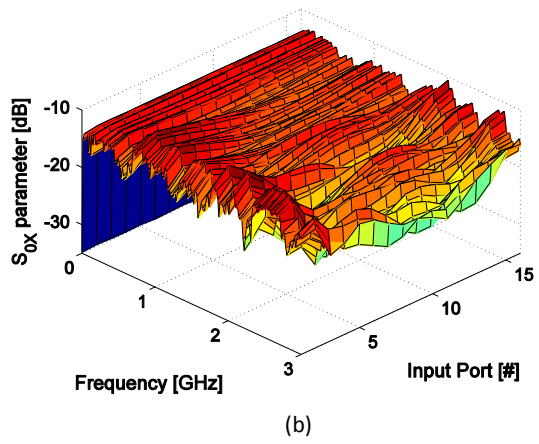
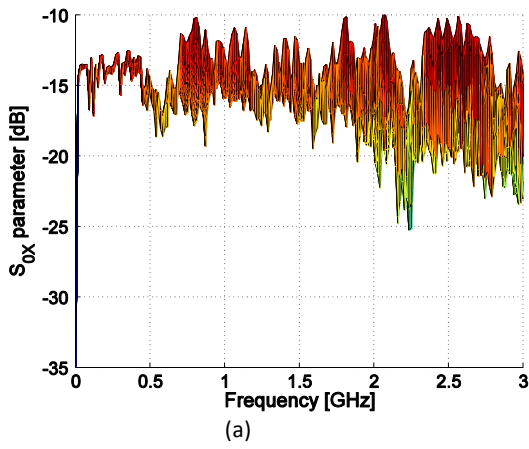


Figure 3-21.  $S_{0X}$  scattering parameters

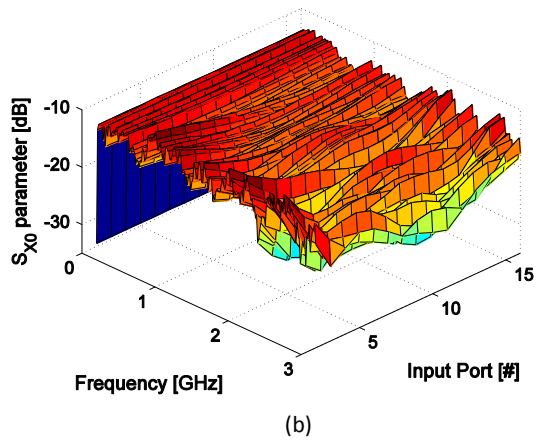
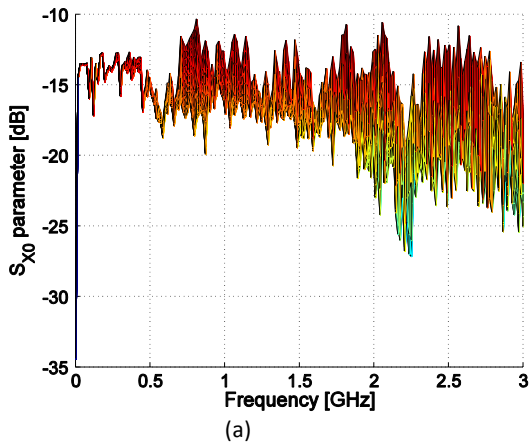


Figure 3-22.  $S_{X0}$  scattering parameters

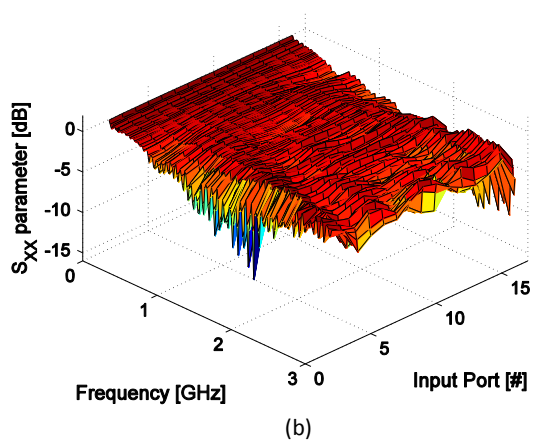
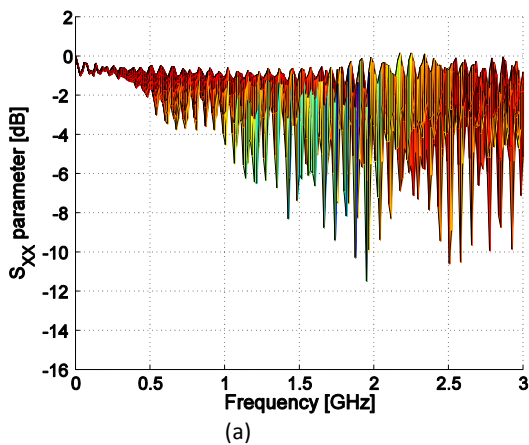


Figure 3-23.  $S_{XX}$  scattering parameters

## 3.6 High voltage application considerations

The PPTLT is in principle very well suited for high voltage application. Even though the voltage at the output is much higher than at the input, the electric field strength inside the transmission lines is the same, everywhere. The impedance of the lines scales linearly with the thickness and with the width of the lines. Whenever two transmission lines are added, both the voltage and the thickness of the transmission line doubles, so that the electric field strength remains the same. In principle, this means that there is no critical part at which breakdown will occur.

However, three areas in the PPTLT must be treated with caution when using the PPTLT for high voltage applications: rotation of the transmission lines, transmission line edges and stacking of the transmission lines. At all three areas high electric fields and thus breakdown can occur. Here all three areas are discussed in short together with options to improve their use in a high voltage environment.

### 3.6.1 Rotation of the transmission lines

To stack the transmission lines they need to be rotated 90 degrees. Rotating all transmission lines in the same direction allows for significant field enhancement. This is shown in Figure 3-6. Here an electric field plot is given of two adjacent transmission lines that are rotated in the same direction. The plot is perpendicular to the transmission lines. To show the effect most clearly, the transmission lines are placed directly next to each other. As Figure 3-6 shows, when rotating the transmission lines in the same direction, a significant field enhancement occurs at the position where the lower conductor of the left transmission line comes close to the upper conductor of the right transmission line. The highest electric field in Figure 3-6, is focused in this gap.

Rotating the transmission lines in alternating direction, as shown in the bottom right of Figure 3-6, reduces the field enhancement. Here the electric field in between the two transmission lines is in the same order as the electric field inside the transmission lines.

### 3.6.2 Transmission line edges

The edges of the transmission lines are sharp by nature. It is not possible to give these edges a curvature which forces the electric fields to be below the breakdown field. To improve the high voltage performance of the transmission lines, the dielectric in between the conductors is widened to the sides, see Figure 3-3. If a discharge occurs at the edges, it will have to travel around the dielectric material to make a short circuit. Just as long as the elongated path length is longer than the time needed for the discharge to cross it, it is very unlikely for an actual short circuit to appear here. Based on the propagation velocities as measured with the surface discharge switch investigated in chapter 2, where velocities as high as  $8 \cdot 10^6$  m/s are measured, and based on the fact that the PPTLTs are designed for pulses of 1 ns, a path length of 8 mm should suffice. We have made a 1 cm extension of the dielectric giving a total path length elongation of 22.2 mm.

### 3.6.3 Series stacking of transmission lines

The series stacking of the transmission lines shows one area, on the inner side of the stacking, where the distance between the conductors becomes increasingly smaller. At a given potential

difference between the lines, one would expect the electric field strength to increase in this region, see Figure 3-24. This could lead to a situation of high electric field strengths and thus breakdown. However, this turns out not to be the case.

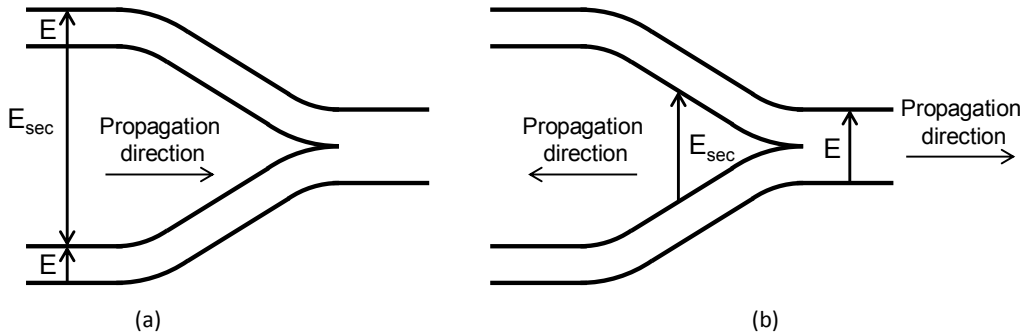


Figure 3-24. The electric field in between 2 transmission lines approaches a short circuit. Due to the decreasing spacing between the transmission lines the electric field might increase beyond the breakdown field strength.

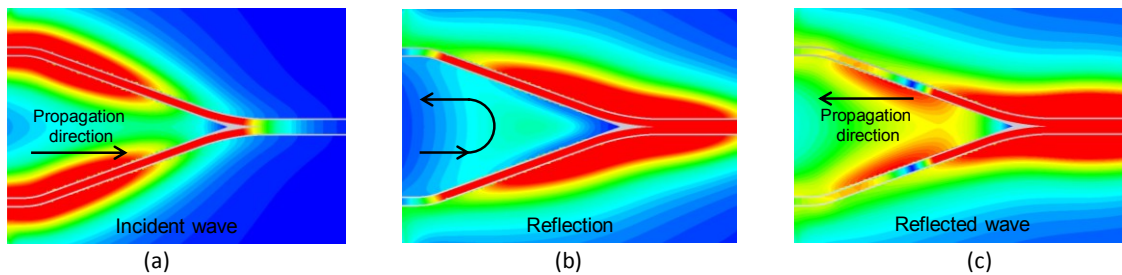


Figure 3-25. Electric field simulations of the series connection. Absolute field values are shown.

The inside of the series stacking can be interpreted as a transmission line on its own which has been short circuited at the end. Because the ‘transmission line’ is tapered this causes a gradual reduction of the impedance. For a given intensity, or power density of the secondary mode, this means that the electric field is reduced. The short circuit termination will also result in a reflection and sign inversion of the travelling pulse in this transmission line. Because of the sign inversion, the forward and backward travelling pulses will cancel each other. The inside of the series connection has an optimum for the angle of the two transmission lines and the rise time of the pulse. This optimization was not performed for the present design.

The advantage of equal electric field strengths inside the transmission lines throughout the entire PPTLTs does not hold for the space in between the series connections. Every doubling of the transmission lines also doubles the voltage in the space in between the transmission lines but because every series stack is the same, the electric field increases. This does not have to be a problem. In our simulations a factor of at least 10 in electric field strength is seen between the electric field inside the center of the transmission lines and the electric field in between two transmission lines in the taper just before each series connection. Because a TL has a gain factor in the order of 10 or less, even in later stages of series stacking, the field in the taper will be manageable.

## 3.7 Conclusions

A transmission line transformer, based on parallel plate transmission lines (PPTLT), is presented. This transmission line transformer allows efficient high voltage pulse transformation with minimal pulse distortion. A major advantage of the planar design as introduced here, is that the secondary mode is much smaller (and can be ignored in practice) as compared to currently used TLT concepts.

Simulations show voltage gain efficiencies of 97.2% and 93.2% for a 4 and 8-stage PPTLT respectively. Measurements show efficiencies of 91.3% and 88.9% respectively. The simulations and the measurements are in good agreement. The difference between the simulations and the measurement can be ascribed to small path length differences in the transmission lines. The PPTLTs were made with accuracy in the longitudinal direction of  $\pm 5\text{mm}$  or  $\pm 25\text{ps}$ . This path length difference can explain both the pulse broadening and the decrease of the gain. The deviation from the ideal gain factor, eq. 3-2, can be ascribed to losses in the dielectric, losses in the metal conductors due to skin effect and to the secondary mode.

The achieved efficiencies are higher than those of a coaxial transmission line. The efficiency decreased with increasing the number of transmission lines but within acceptable limits. A TLT is not very well suited for amplification factors above 10 due to the quadratic increase of impedance difference between in- and output.

The design did not take edge effects of the transmission lines into account. Therefore the impedances of the transmission lines are not perfectly matched. As a result the voltage gain for the 4-stage PPTLT is 3.63, based only on the (square root of the) ratio of the input and output impedances (6.11 for the 8-stage PPTLT). The design can be adapted to improve the matching by changing the width of the transmission lines. This will improve the voltage gain and bring it closer to 4 and 8, respectively.

The measurement of the scattering parameters confirms the presence of a small secondary mode. The effect of this secondary mode is not the same everywhere in the PPTLT. The secondary mode has little influence on the shape of the output pulse.

Several methods have been shown to adapt the PPTLT for high voltage applications. Based on the requirements of the application, several standard techniques can be used to make the PPTLT suitable for pulsed high voltage applications. Examples are an SF<sub>6</sub> environment or submerging the PPTLT in oil.





# 4 Comparison of a D-dot sensor and a Capacitive Voltage Divider to measure nanosecond high-voltage pulses

## 4.1 Introduction

To assess the performance of any high voltage pulse source, the output pulse must be measured. Measuring such pulses is a non trivial task since a sensor must be able to handle both high frequencies and high voltages.

To measure fast high voltage signals a D-dot sensor has been developed. A D-dot sensor basically consists of a very small capacitive tip that measures the time derivative of the electric field [40][41–44]. Hence the name ‘ $\dot{D}$ ’. To be able to measure absolute voltages, the sensor has to be calibrated. Here the sensor parameters are estimated using numerical simulations and validated by comparing numerical simulations with measurements. The steps taken to characterize and calibrate the sensor are shown in Figure 4-1.

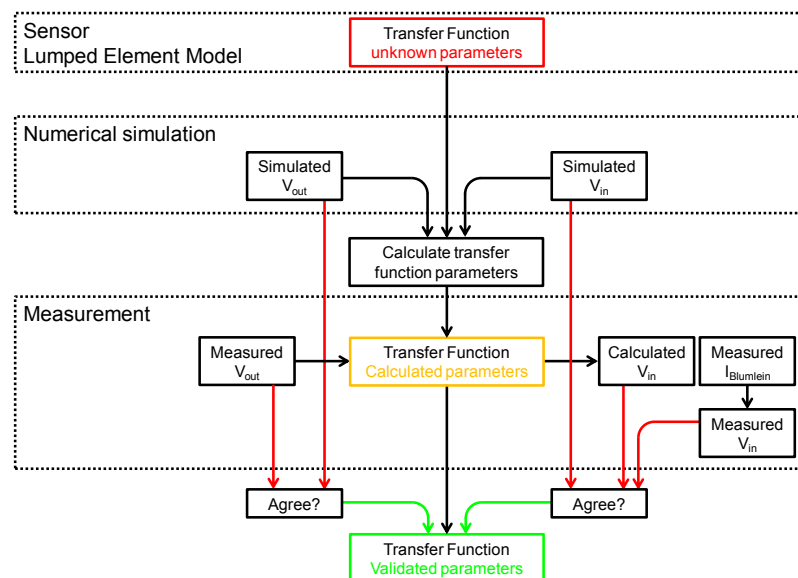


Figure 4-1. Sensor calibration process.

First a simplified RC model of the sensor is proposed based on the geometry of the sensor and the high voltage pulse generator whose output it measures. Based on this model a transfer function for the sensors in- and output voltage is defined.

The parameters of the transfer function, the  $R$  and  $C$  values, are not known. To estimate these parameters, a numerical simulation of the D-dot sensor together with the pulse source is used. In this numerical simulation both the voltage at the input and at the output of the sensor can be monitored. Using these voltages together with the transfer function of the simplified RC model, the  $R$  and  $C$  values can be estimated.

To validate the performance of the sensor, it is used in an actual measurement. Thanks to the Kumamoto University of Technology the D-dot sensor has been tested on a triaxial Blumlein nanosecond pulse source. Besides testing the D-dot sensor it has also been compared to a capacitive voltage divider, CVD, and a current sensor, both used to measure the output voltage of the Blumlein pulse generator [45].

In the first section of this chapter the Blumlein topology and its triaxial implementation are discussed. In the second section the simplified models and the transfer functions of both the CVD and the D-dot sensor are derived. In the third section the numerical model is presented and estimations for the  $R$  and  $C$  values are given followed by the last section in which the measurement results are shown.

Both the D-dot sensors and the capacitive voltage divider measure the shape of the Blumlein output pulse. The amplitude based on the capacitive voltage divider is lower than expected and the sensor shows more oscillations in the experiment than in the numerical simulations.

The developed sensors give a clear image of the behavior and propagation of the electric fields in the Blumlein. The numerical simulation is successfully used to parameterize the sensors. Experiments agree with the numerical simulations and the absolute value of the Blumlein output pulse has been successfully measured.

## 4.2 The Blumlein topology and its implementation

Figure 4-2 shows a schematic representation of a Blumlein pulse generator [10], [46]. This concept has three main advantages: (i) a square pulse form will be generated over the load (for matched conditions), (ii) the magnitude of the voltage that is generated over the load is equal to the charging voltage, and (iii) the duration of the pulse is defined by the transit time of the Blumlein's transmission lines. An important disadvantage is that the current in the switch is twice the current into the matched load. The rise and fall times of the generated voltage pulses depend on the bandwidth of the used transmission lines and the performance of the switch. In addition, pulse distortions will occur for non-matched loads.

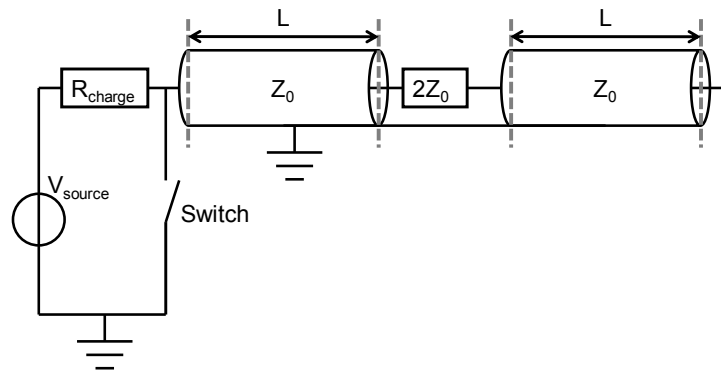


Figure 4-2. Schematic representation of a Blumlein based pulse source.

A Blumlein generator as shown in Figure 4-2, basically consists of two transmission lines with the same characteristic impedance  $Z_0$  and equal transit time  $\tau$  which depends on the length,  $L$ , of the transmission lines and the dielectric material in the transmission lines

$$\tau = \frac{L}{c/\sqrt{\epsilon_r}}$$

4-1

By means of a charging circuit, both lines are charged to an initial DC voltage  $V_0$ . Here, the charging circuit consists of a DC voltage source and charging resistor  $R_{charge}$ . The load is connected to the two inner conductors of the two lines. For proper matching, this load must have an impedance of  $2Z_0$ , twice the characteristic impedance of the transmission lines.

Figure 4-3 shows the voltage levels along the length of the two transmission lines at various times during the pulse forming process. At  $t < 0$ , the transmission lines will be charged to a voltage  $V_0$ . During this phase, no voltage will be present over the load impedance, as can be seen in Figure 4-3. At  $t = 0$ , the switch will be closed and the pulse forming process will start.

Upon closing of the switch, the input of the left transmission line is short circuited. As a consequence, a voltage front with a magnitude of  $-V_0$  will propagate along the left transmission line making the electric field inside this line to go to zero (see Figure 4-3b). This phase has a duration  $\tau$ , and during this phase the voltage over the load remains zero.

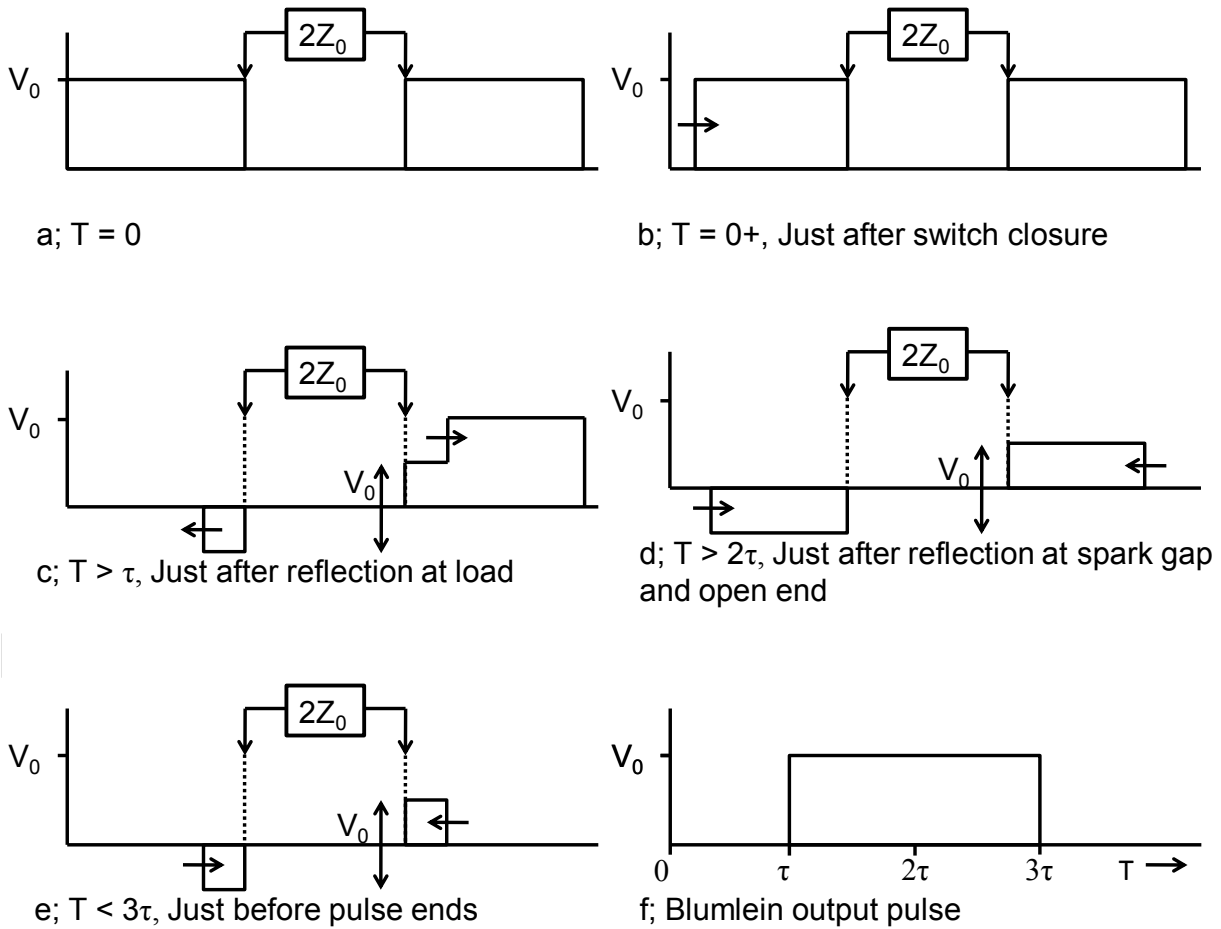


Figure 4-3. The pulse formation process in the Blumlein pulse source.

After the transit time  $\tau$ , the voltage front  $-V_0$  arrives at the load. Here the voltage front encounters the impedance of the load,  $2Z_0$ , plus the input impedance  $Z_0$  of the right transmission line. Consequently, a part of this front will be reflected back along the left line, and a part will continue via the load along the right transmission line (see Figure 4-3c). The reflection coefficient for the reflected voltage front is given in eq. 4-2, and the transmission coefficient for the voltage front that continues is given by eq. 4-3. So a voltage front with a magnitude of  $\Gamma \cdot -V_0 = -0.5V_0$  travels back into the left transmission line; the electric field in this line becomes half its original amplitude with inversed polarity. The voltage over the load and the right transmission line gets a magnitude of  $T \cdot -V_0 = -1.5V_0$ . Since the right line is initially charged to  $V_0$ , and since the load has an impedance of  $2Z_0$  while the right transmission line has an impedance of  $Z_0$ , the voltage wave that finally continues along the right transmission line has a magnitude of  $-0.5V_0$ . Consequently during this entire phase with a duration  $\tau$ , a voltage with a magnitude  $V_0$  will be present over the load.

$$\Gamma = \frac{Z_l - Z_0}{Z_l + Z_0} = \frac{(2Z_0 + Z_0) - Z_0}{(2Z_0 + Z_0) + Z_0} = \frac{1}{2} \quad 4-2$$

$$T = 1 + \Gamma = 1 + \frac{1}{2} \quad 4-3$$

For both transmission lines, the voltage fronts will propagate towards their outer ends. The short-circuited end (for the left line) and the open end (for the right line) will both be reached after transit time  $\tau$ . The open end of the right transmission line gives a reflection coefficient of +1 and a voltage front with a magnitude  $-0.5V_0$  will be reflected back along the transmission line towards the load end. Behind this voltage front the electric field in the transmission line becomes zero. For the left line, the short-circuit end gives a reflection coefficient of -1 resulting in a  $0.5V_0$  voltage front to travel back towards the load. Behind this voltage front the electric field in the transmission line also becomes zero. This is shown in Figure 4-3d. During this entire phase, which again has a duration of  $\tau$ , the voltage over the load will be  $V_0$  until the electric field along both transmission lines has become zero (see Figure 4-3e). The voltage pulse that will be generated along the load is shown in Figure 4-3f. The voltage over the load appears a time  $\tau$  after switch closure, and has a duration of  $2\tau$ . The square wave voltage waveform has an amplitude which is equal to the charging voltage  $V_0$ .

Namihira, Wang et. al. [45], [47–51] have developed a triaxial Blumlein pulse source for the purpose of plasma generation in a wire-cylinder corona reactor. This Blumlein can generate high-voltage pulses with a duration of 5 to 10 ns. The amplitude can be varied between 10 and 60 kV, depending on the gas type and pressure in the spark gap switch. Here the two transmission lines are placed concentric around each other. This allows a very compact construction and a highly efficient pulse source with very good pulse characteristics. Because in this chapter, the focus is on testing the sensors, the Blumlein will be connected to a matched 50  $\Omega$  resistive load instead of to a wire cylinder corona reactor.

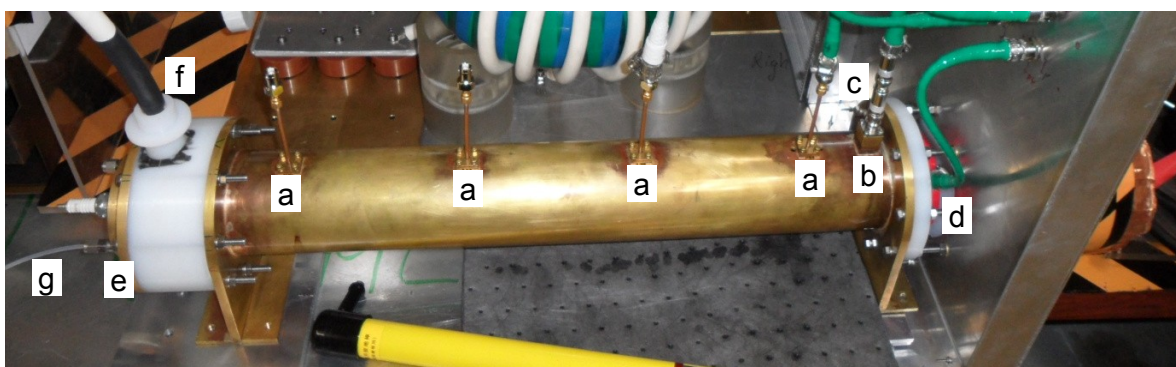


Figure 4-4. The Kumamoto Blumlein generator. a; D-dot sensors, b; CVD, c; matching resistors, d; Bergoz current sensor, e; spark gap chamber, f; Charging port, g; Gas feed for spark gap chamber.

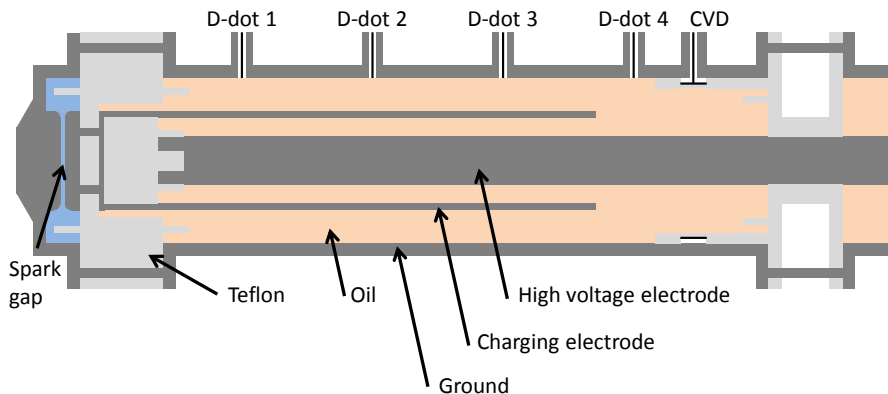


Figure 4-5. Schematic view of the Kumamoto Blumlein generator. Here the coaxial transmission line at the right functions as the load of  $2Z_0$ . During experiments a coaxially connected resistor is used to mimic this load, see Figure 4-4.

The Blumlein generator is shown in Figure 4-4 and a cut-view is shown in Figure 4-5. A spark gap switch is positioned at the left side of the generator. The gap distance between the two electrodes in the spark gap is 1 mm. The breakdown voltage (and thus the switching voltage) is set by the gas type and pressure. The spark gap is filled with  $\text{SF}_6$  at a pressure of 7 Bar. Based on the Paschen curve [52] the breakdown voltage of this gap is expected to be just below 60 kV.

The grounded outer conductor of the generator has an inner diameter of 84 mm and the Blumlein has a total length of 575 mm (between the two Teflon support insulators). A first transmission line is formed by the charging electrode and the grounded outer conductor. The charging electrode has an inner and outer diameter of 40 and 42 mm respectively. At the left side, this line can be short circuited to ground by the spark gap switch. The second transmission line is formed by the high-voltage electrode, with a diameter of 20 mm, and the charging electrode. This line is connected to the resistive load via the transmission line that is formed between the high voltage electrode and the ground electrode. In between the 2 Teflon disks the triaxial Blumlein is filled with transformer oil, Shin-Etsu KF-96-100CS. This oil has a dielectric constant of 2.7 at 1 GHz and a loss tangent of 0.005 at 1 GHz. At the Teflon disks the outer parts are held together with 8 stainless steel bolts.

One capacitive voltage divider (indicated with b in Figure 4-4) is positioned at the output of the Blumlein generator. Four D-dot sensors (indicated with a in Figure 4-4) are placed, 150 mm apart of each other, along the length of the Blumlein generator.

To operate the Blumlein generator, first the charging electrode is charged to the desired charging voltage. As soon as the breakdown voltage of the spark gap is reached, it closes and the process as described with Figure 4-3 is initiated. This is illustrated with numerical simulations with CST Microwave Studio [53]. Figure 4-6 through Figure 4-10 show the simulated electric fields along the Blumlein just before switching the spark gap and at 2, 6 and 10 ns after switching the spark gap. In the figures the radial electric field is shown.

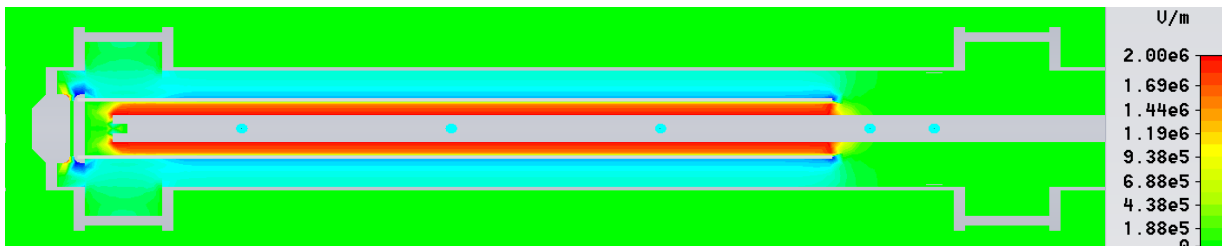


Figure 4-6. Radial electric field just before the spark gap switches.

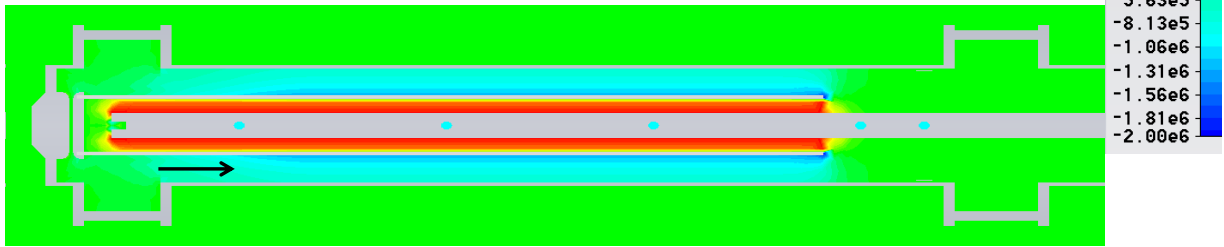


Figure 4-7. Just after switch closure a negative voltage step starts to travel to the right in the outermost transmission line.

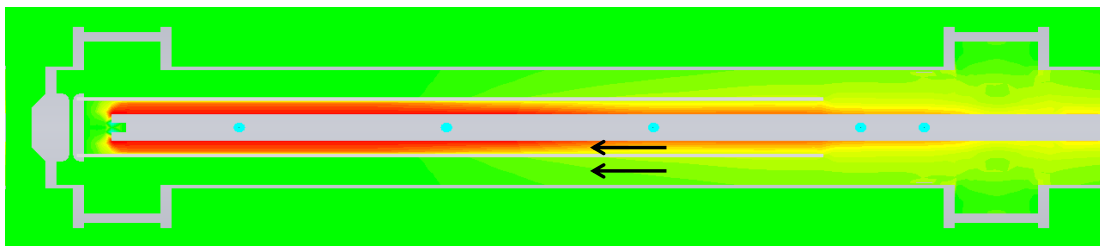


Figure 4-8. Just after the step hits the end of the triaxial structure.

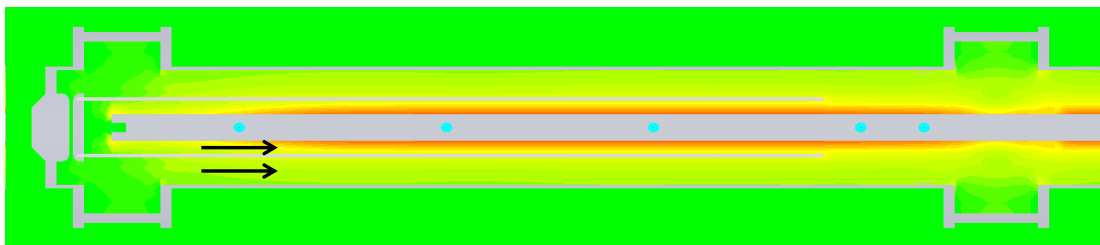


Figure 4-9. Pulse reflects back on the ends of both transmission lines and propagates again towards the load.

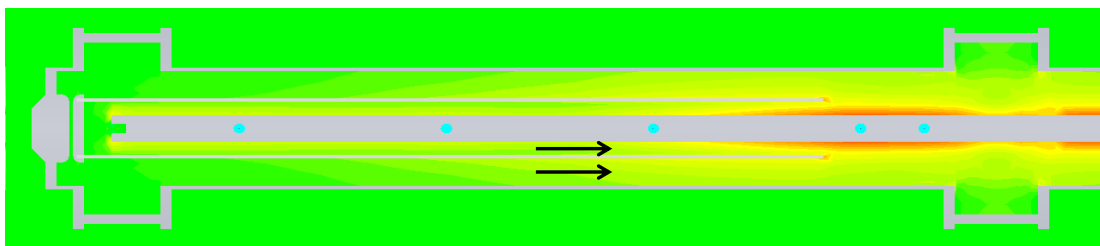


Figure 4-10. Just before the Blumlein is depleted.

All metal parts are simulated as perfect electric conductors and the Teflon insulators are simulated as being lossless. The oil in the simulations has a dielectric constant and loss tangent as defined by the manufacturer. To simulate the spark gap itself, we use the same technique as described in appendix A. The spark gap chamber volume is simulated as vacuum. After the spark gap is closed, the electric field at the spark gap drops to zero. This step propagates to the right as can be seen in Figure 4-7, similar to Figure 4-3b. Once it reaches the end of the triaxial structure it reflects and the electric field in the outer



transmission line reverses (marked by an inversion of the colors), Figure 4-8. This is in agreement with the theory as described in Figure 4-3c. When the wave reaches the left end of the triaxial line it reflects again, Figure 4-9, similar to Figure 4-3d. In these simulations the Blumlein is not perfectly matched at its output due to the Teflon coupling at its output. This causes reflections that prevent the electric field to go to zero completely.

With the dielectric constant of the oil of 2.7, the velocity of an electromagnetic wave is found using

$$v = \frac{c}{\sqrt{\epsilon_r}} \quad 4-4$$

With this velocity and the length of the transmission lines of 535 mm, the time it takes to traverse through the Blumlein is determined to be 2.93 ns using

$$\tau = \frac{L}{c/\sqrt{\epsilon_r}} \quad 4-5$$

This results in the generation of a high-voltage pulse with a duration of 5.86 ns.

The characteristic impedances for both the inner and outer transmission line in the Blumlein can be calculated using eq. 4-6.

$$Z_0 = \sqrt{\frac{\mu \ln(b/a)}{\epsilon}} \quad 4-6$$

Here  $a$  and  $b$  are respectively the inner and outer radius of a transmission line,  $\mu$  the magnetic susceptibility and  $\epsilon$  the dielectric permittivity. For both the inner and outer coaxial line in the triaxial Blumlein we find an impedance of 25.2  $\Omega$ . The coaxial load structure which connects the triaxial structure to the load has an impedance of 52.1  $\Omega$ .

The bandwidth of the three transmission lines is found using eq. 4-7 [30] and are given in table 1.

$$f_c = \frac{ck_c}{2\pi\sqrt{\epsilon_r}} \quad 4-7$$

Here  $c$  is the speed of light,  $3 \cdot 10^8$  m/s and  $\epsilon_r$  the relative permittivity of the dielectric in the transmission line.  $k_c$  is the cut off wave number and is estimated by, [30],

$$k_c = \frac{2}{a+b} \quad 4-8$$

Table 4-1. Blumlein impedances and bandwidths.

	Impedance [ $\Omega$ ]	Bandwidth [GHz]
Blumlein outer line	25.2	1.02
Blumlein inner line	25.2	2.15
Transmission line to the load	52.1	1.24

### 4.3 Blumlein charging circuit

To charge the Blumlein, the circuit as shown in Figure 4-11 is used. A DC voltage source charges  $C_1$ , together with the diode  $D$ , functions as a protective buffer circuit for the source.  $C_1$  is connected through a high-voltage resistor,  $R_{charge}$ , to  $C_2$ , a fast high-voltage capacitor. These capacitors are connected to the primary side of a 2:12 high-voltage pulse transformer. The primary winding can be switched to ground through a thyatron. The secondary side of the transformer is connected to ground on one side and to the charging electrode of the Blumlein.

The primary circuit is charged until the thyatron switch is closed. At this moment the voltage on the secondary side of the transformer starts to increase rapidly, and charges the Blumlein pulser until the breakdown voltage of its spark gap switch is reached. With this charging circuit, charging voltages up to 60 kV can be reached using 10 kV DC at the input.

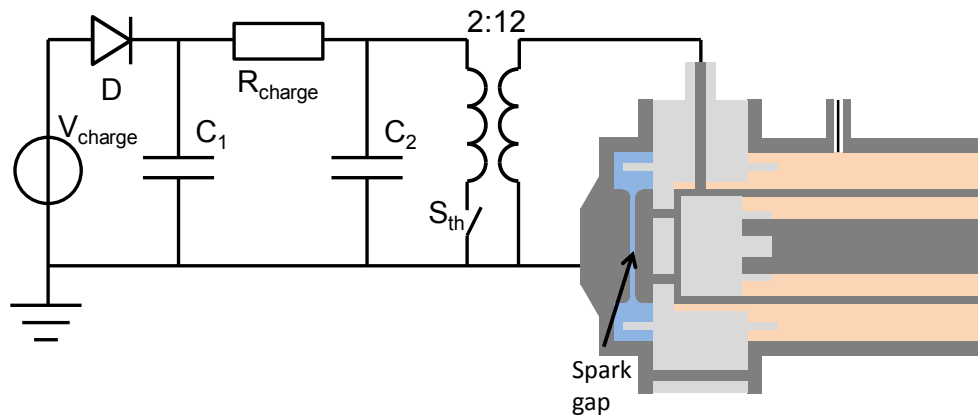


Figure 4-11. Schematic of the Kumamoto Blumlein charging circuit.

## 4.4 Blumlein voltage sensors

To measure the voltage at the output of the Blumlein generator, two different sensors are used; a capacitive voltage divider, develop by Namihira et. al. and the D-dot sensor. Here we discuss the implementation of these sensors on the Blumlein pulse generator. This paragraph describes the first step shown in Figure 4-1, the sensor model. After the description of the construction of the sensors, a lumped element model of both the CVD and D-dot sensor is given. These lumped element models are used to define the transfer function of the sensors. The lumped element models will be parameterized using numerical simulations in the paragraph 4.5. Finally, the parameterized transfer functions are used to determine the actual Blumlein voltage in the experimental setup in paragraph 4.6.

### 4.4.1 Capacitive voltage divider

The capacitive voltage divider, CVD, consists of a thin copper ring placed coaxially around the high-voltage conductor at the output of the Blumlein as shown in Figure 4-12. It has a diameter of 82 mm, and is 12 mm wide. The output of the CVD is connected to a tuning resistor  $R_1$  of 2600  $\Omega$  (indicated with 'c' in Figure 4-5). The tuning resistor is connected, through a 50  $\Omega$  coaxial cable, to the 50  $\Omega$  input of a Tektronix DPO 7254 oscilloscope via a 20 dB attenuator.

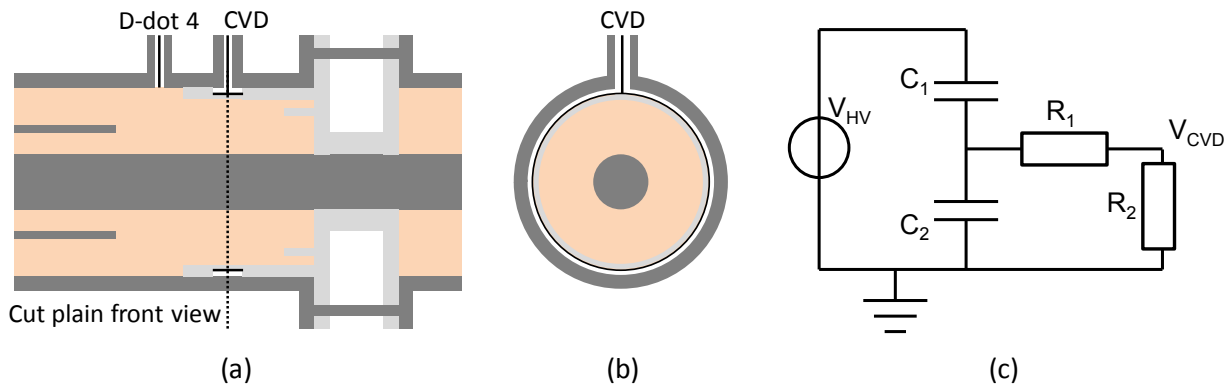


Figure 4-12. (a) Side view of the CVD, constructed as a thin copper ring. (b) Frontal view. (c) Lumped element model of the CVD.

A lumped element model of the CVD is shown in Figure 4-12 (c). Here  $C_1$  is the capacitance between the high-voltage electrode and the ring and  $C_2$  is the capacitance between the ring and ground.  $R_1$  is the matching resistor and  $R_2$  is the characteristic impedance of the measurement cable of 50  $\Omega$ . The transfer function (in the Laplace domain) of the lumped element model of Figure 4-12 is

$$\frac{V_{CVD}}{V_{HV}} = \frac{sR_2C_1}{s(R_1 + R_2)(C_1 + C_2) + 1} \quad 4-9$$

Here  $V_{CVD}$  is the output voltage of the CVD and  $V_{HV}$  is the voltage on the high voltage electrode. This transfer function has a zero for DC voltages and a pole at  $\omega_p = -1/(R_1 + R_2)(C_1 + C_2)$ .  $V_{CVD}$  will behave as the time derivative of  $V_{HV}$  for the frequency components between 0 and  $1/(R_1 + R_2)(C_1 + C_2)$  rad/sec. For frequencies far above  $\omega_p$ ,  $V_{CVD}$  will be a scaled representation of  $V_{HV}$  with a scaling factor of

$$\frac{V_{CVD}}{V_{HV}} \approx \frac{R_2 C_1}{(R_1 + R_2)(C_1 + C_2)} \quad 4-10$$

To obtain the voltage of the Blumlein generator, based on  $V_{CVD}$ , we invert eq. 4-9,

$$V_{HV} = \frac{s(R_1 + R_2)(C_1 + C_2) + 1}{sR_2 C_1} V_{CVD} \quad 4-11$$

Due to limitations of size and complexity of the numerical model, the 2600  $\Omega$  matching resistor  $R_1$  is omitted in the numerical simulations. Without the tuning resistor  $R_1$ , the lumped element model of the CVD simplifies to that shown in Figure 4-13. Here  $C_1$ ,  $C_2$  and  $R_2$  are the same as in Figure 4-12.

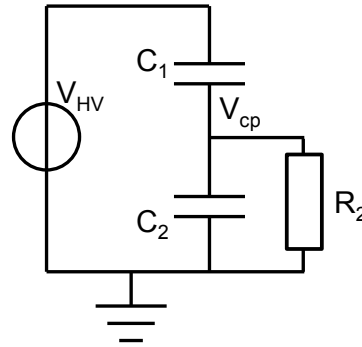


Figure 4-13. Lumped element model of the simulated CVD.

For the numerical simulation the transfer function of the CVD is found to be

$$\frac{V_{CVD}}{V_{HV}} = \frac{sR_2 C_1}{sR_2(C_1 + C_2) + 1} \quad 4-12$$

In eq. 4-12 the pole is positioned at the frequency  $\omega_p$  which is  $1/R_2(C_1 + C_2)$ . For frequencies well below  $\omega_p$  the CVD behaves as a differentiator and for frequencies above  $\omega_p$  it behaves as a voltage follower with a fixed gain of  $C_1/(C_1 + C_2)$ . The relation between the output voltage of the CVD and the Blumlein voltage at the input of the CVD for the numerical simulations is given in eq. 4-13.

$$V_{HV} = \frac{sR_2(C_1 + C_2) + 1}{sR_2 C_1} V_{CVD} \quad 4-13$$

The output of the numerically simulated CVD cannot be compared directly to its measured counterpart due to the absence of tuning resistor  $R_1$  in the numerical simulation. But using the transfer function of eq. 4-12 together with the numerically simulated voltages at the input and the output of the CVD, values can be found for  $C_1$  and  $C_2$  and the transfer function of eq. 4-9 can be fully parameterized. This transfer function can then be used in measurements to determine the voltage in the Blumlein based on  $V_{CVD}$ .

#### 4.4.2 D-dot sensor

Figure 4-14 shows the concept of a D-dot sensor on a coaxial transmission line. The D-dot sensor consists of a small coaxial cable, placed perpendicular on the transmission line. The sensor tip forms a very small capacitor with the high-voltage conductor,  $C_1$ , and with the grounded outer conductor,  $C_2$ , as shown in Figure 4-15.

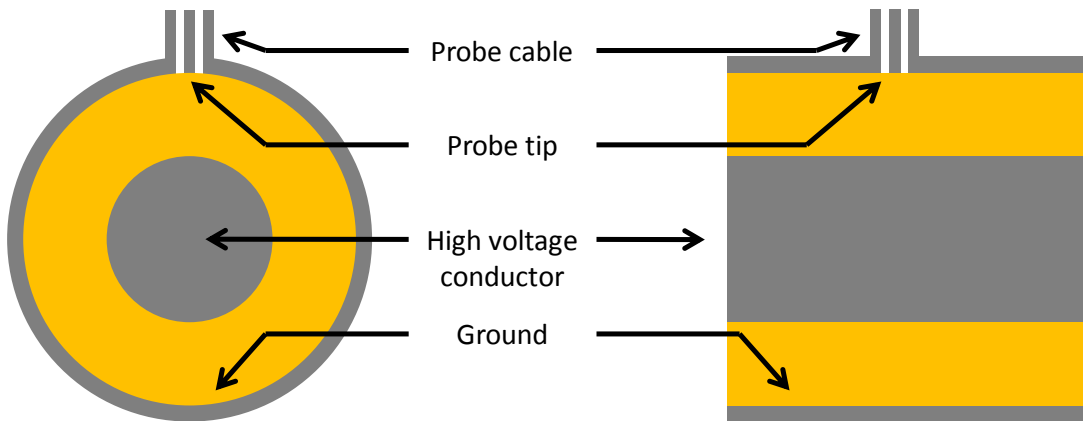


Figure 4-14. Front and side view of the D-dot sensor placed perpendicular on top of the coaxial high voltage pulse line.

Because the D-dot sensor is constructed from a coaxial cable directly connected to the grounded conductor of the transmission line, the impedance of the sensor is equal to the characteristic impedance of the coax cable ( $R_1$  in Figure 4-15). This allows us to describe the D-dot sensor using a simple RC circuit as shown in Figure 4-15.

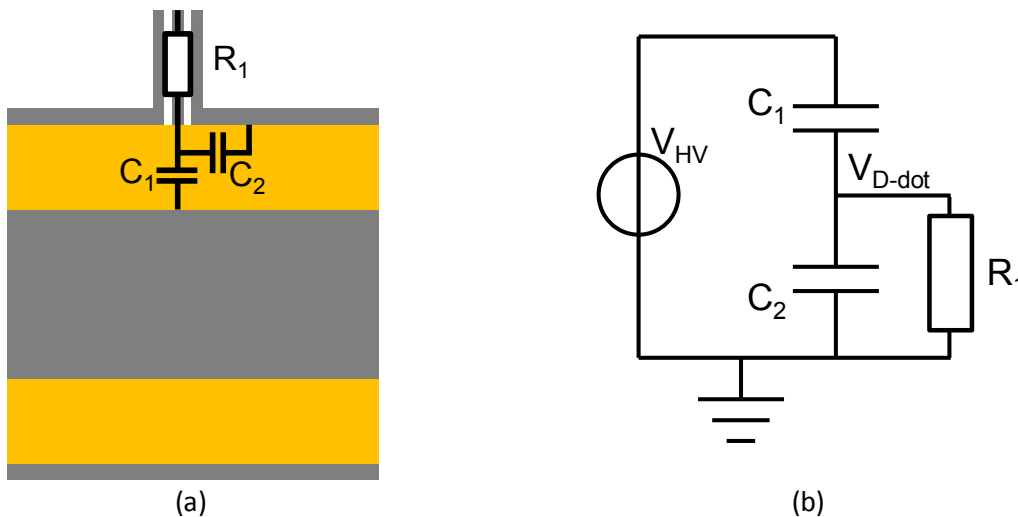


Figure 4-15. (a) Schematic representation of the D-dot sensor. (b) Lumped element model.

Now the transfer function becomes:

$$\frac{V_{D-dot}}{V_{HV}} = \frac{sR_1C_1}{sR_1(C_1 + C_2) + 1}$$

4-14

Where  $V_{D-dot}$  is the output voltage of the D-dot sensor. This transfer function is similar to the transfer function of the CVD. However, the dimensions of the D-dot sensors, and therefore also the capacitive

values, are much smaller than those of the CVD. Thus the bandwidth of the D-dot sensors is expected to be much larger. This large bandwidth causes the D-dot sensors to behave solely as a differentiating sensor for the frequencies that occur in the Blumlein. As a consequence, the model can be simplified to that shown in Figure 4-16. Here  $C_1$  is the capacitance between the high-voltage electrode and the D-dot sensor tip and  $R_1$  the characteristic impedance of the coaxial cable that is used to construct the D-dot sensor.

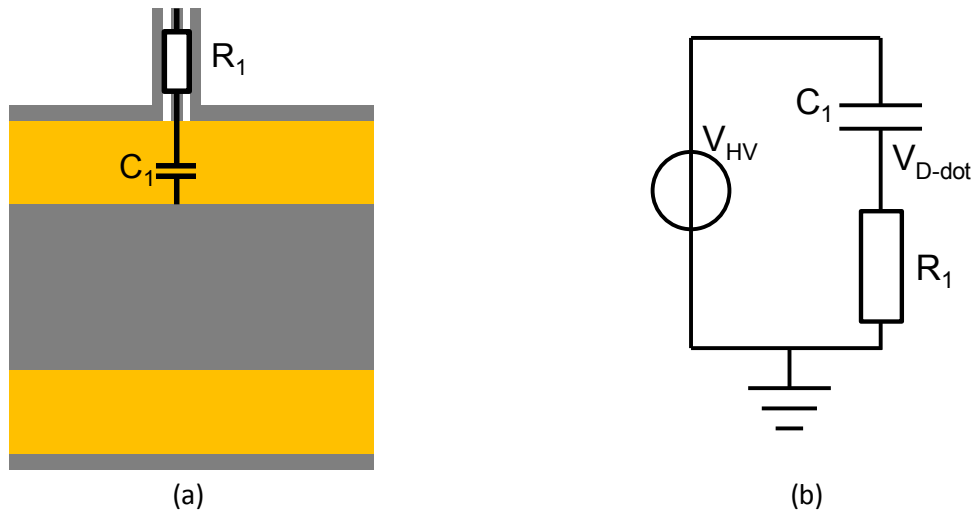


Figure 4-16. (a) Simplified model of the D-dot. (b) Simplified lumped element model.

Now the transfer function of the D-dot sensor is

$$\frac{V_{D-dot}}{V_{HV}} = \frac{sR_1C_1}{sR_1C_1 + 1} \quad 4-15$$

When inverting eq. 4-15 we obtain

$$V_{HV} = \frac{sR_1C_1 + 1}{sR_1C_1} V_{D-dot} \quad 4-16$$

Now eq. 4-15 can be used to find the value for  $C_1$  using the Blumlein voltage at the input of the sensor and the sensor output voltage both obtained from the numerical simulations. Once the transfer function of eq. 4-15 has been parameterized, eq. 4-16 can be used to determine the actual voltage in the Blumlein generator, at the position of the sensor, based on the measured output voltage of the D-dot sensor  $V_{D-dot}$ .

## 4.5 Numerical simulation results

To obtain a good insight in the temporal and spatial behavior of the electric fields in the Blumlein pulse generator, numerical simulations have been performed as discussed in section 4.2. These numerical simulations are also used to calculate both the voltages in the Blumlein at the sensor positions, as well as the sensors output voltages. We use these simulated voltages together with the transfer functions, as defined in the previous section, to find the capacitances of the sensor models. The numerical simulation also allows us to verify that the voltages in the Blumlein can indeed be determined from the measured output voltages of the sensors and their simplified lumped element models.

We will also look at the time delay between the signals of the 4 D-dot sensors. This time delay will be compared to the delays measured in the experiment to verify that the dielectric constant for the oil in the numerical simulation is the same as that of the oil in the real Blumlein.

The numerical simulations are done in Microwave Studio [53]. In the first 200 ns of the simulation, the Blumlein is charged to 60 kV. Then the spark gap in the Blumlein is closed and the discharge process begins.

To obtain the values of the capacitances in the lumped element models, the simulated output signals of the sensors are divided by their simulated input signals in the frequency domain. This results in a frequency domain response of the sensors. The transfer functions of eq. 4-12 and 4-15, based on the lumped element models of the CVD and the D-dot sensors, are fitted to these frequency domain responses to obtain an estimate for the capacitances in the sensors.

To check the accuracy of the lumped element models of the sensors, the recorded sensor output voltages are multiplied with the inverse of the lumped element transfer functions, eq. 4-13 and 4-16. These calculated Blumlein voltages are then compared to the simulated Blumlein voltages. The comparison shows that the simplified lumped element models can be used to accurately determine the Blumlein voltages from the measured sensor outputs.

### 4.5.1 Capacitive voltage divider

The simulated voltage in the Blumlein at the capacitive voltage divider is shown in Figure 4-17. The simulated output signal of the capacitive voltage divider is shown in Figure 4-18. The amplitude spectra of the voltages in Figure 4-17 and Figure 4-18 are shown in Figure 4-19. The phase of the voltages is not discussed here because it is not measured in the actual setup and the transfer function can be reconstructed without the phase information.

The amplitude spectra are divided to obtain the transfer function of the capacitive voltage divider. This is shown in Figure 4-20, in blue. The differentiating behavior for lower frequency components, a rising slope of 20 dB per decade, and the attenuating behavior for higher frequency components, the horizontal part of the graph, can be clearly recognized. The transfer function, eq. 4-12, of the CVD is manually fitted to the data of the numerical simulation. This is shown in red in Figure 4-20. The capacitances we found are shown in Table 4-2.

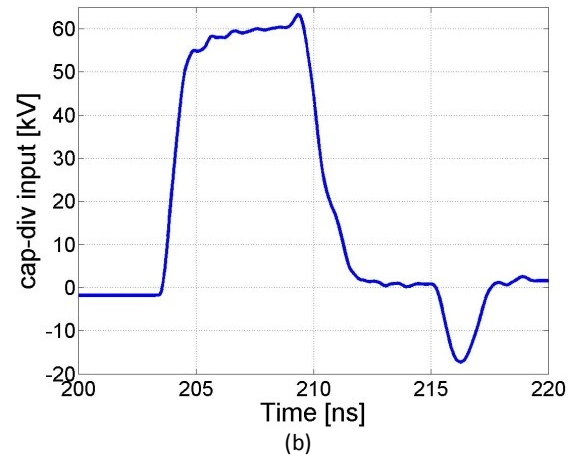
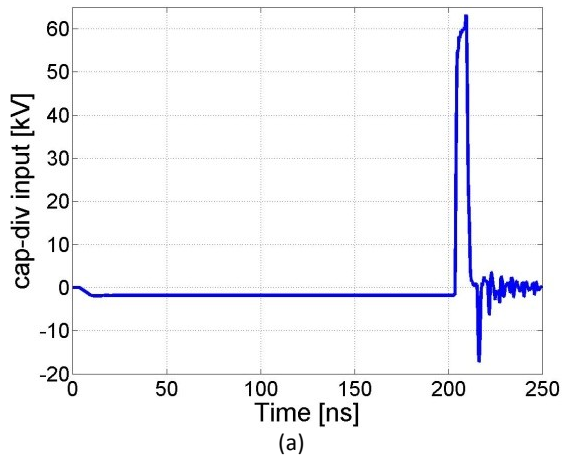


Figure 4-17. (a) Simulated Blumlein voltage.at the CVD during pulse formation. (b) Zoomed view of the Blumlein pulse.

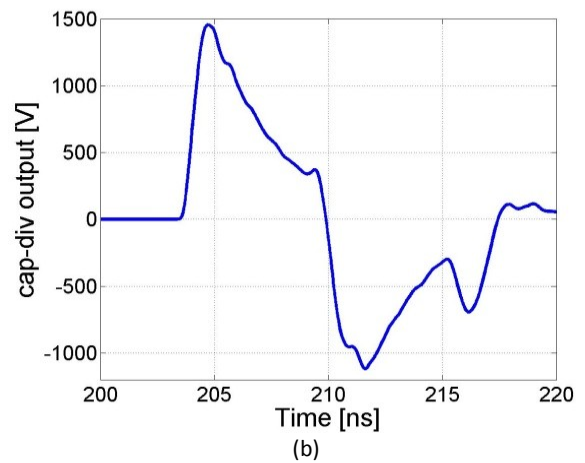
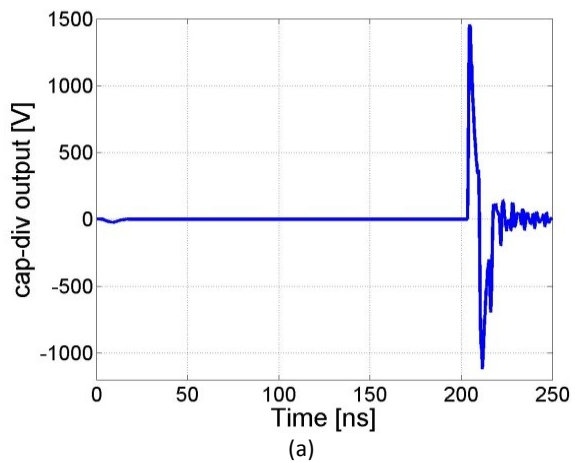


Figure 4-18. (a) Simulated CVD output voltage. (b) Zoomed view of the CVD output voltage.

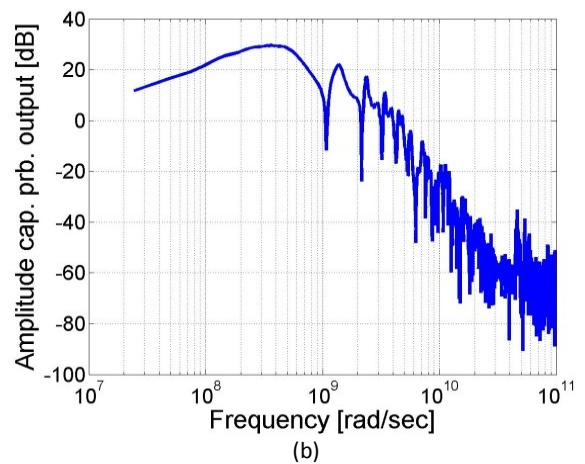
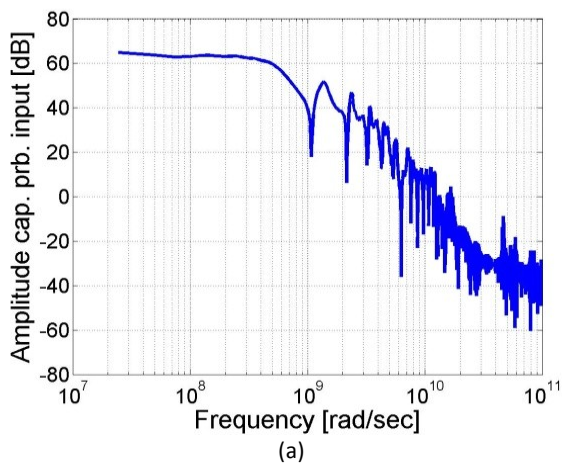


Figure 4-19. (a) Amplitude spectrum of the simulated Blumlein voltage at the input of the CVD. (b) Amplitude spectrum of the CVD output voltage.



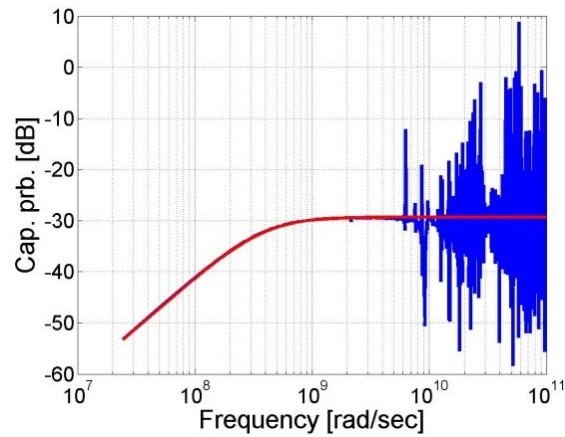


Figure 4-20. (Blue) amplitude frequency characteristics of the CVD sensor based on the numerical simulations. (Red) manually fitted transfer function using eq. 4-12

Table 4-2. Capacitances of the CVD based on the manual fitting of the data from the numerical model.

	Capacitance [F]
$C_1$	$1.775 \cdot 10^{-12}$
$C_2$	$5 \cdot 10^{-11}$

Using the simulated output signal of the CVD, shown in Figure 4-18, and the transfer function of eq. 4-12 with the values of Table 4-2, we find an estimate for the voltage in the Blumlein at the CVD. This voltage is shown in red in Figure 4-21 together with the numerically simulated voltage in the Blumlein shown in blue. As can be seen, the voltages are in good agreement with each other.

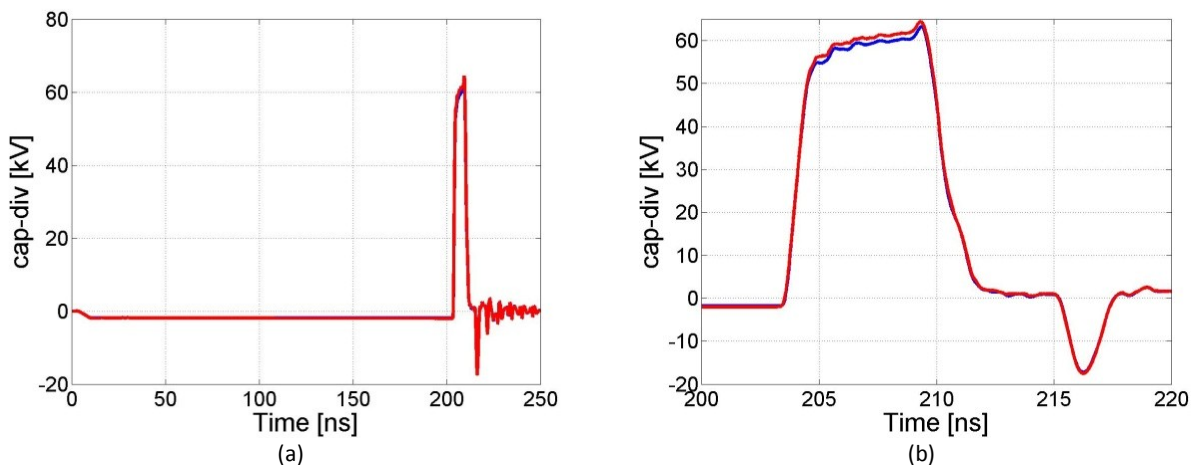


Figure 4-21. (a) Blue; Blumlein voltage at the CVD according to the numerical simulations. Red; Blumlein voltage at the CVD based on CVD output voltage, transfer function eq. 4-12 and capacitances as in Table 4-2. (b) Zoomed view.

Please note that in these simulations the 2600 ohm matching resistor was omitted. Nevertheless the values we have found for both  $C_1$  and  $C_2$  can be used in the lumped element model of the CVD, given by eq. 4-9, for the measurements.

#### 4.5.2 D-dot sensor

Figure 4-22 and Table 4-3 show estimated times at which characteristic events in the Blumlein occur that can be observed by the D-dot sensors. These times are based on the size of the Blumlein and an  $\epsilon_r$  of 2.7 for the oil.

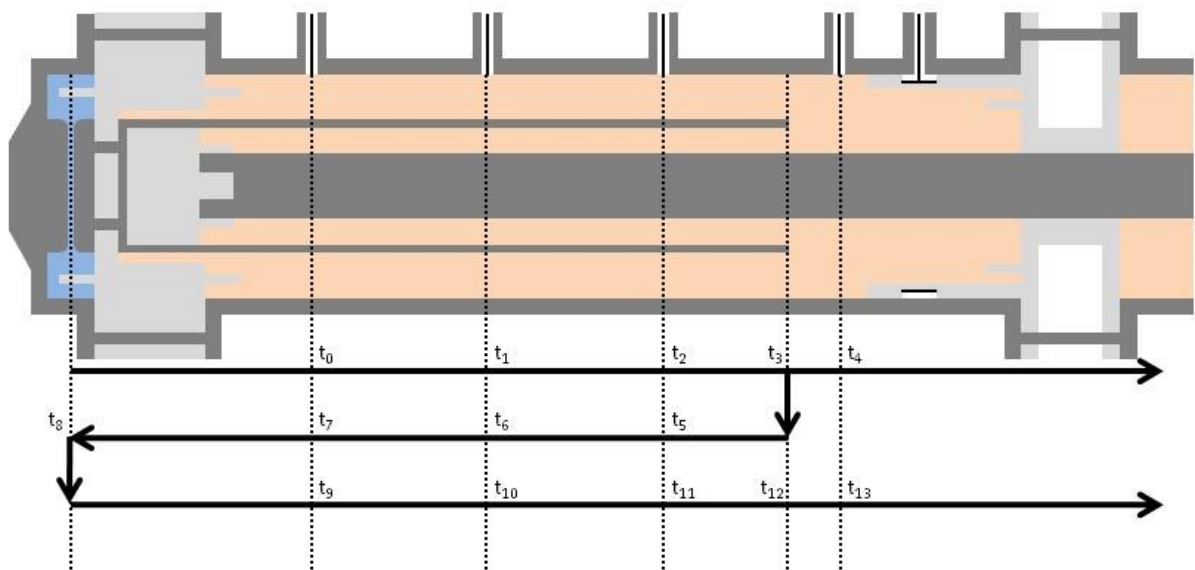


Figure 4-22. Characteristic moments in time during pulse formation in the Blumlein.

Table 4-3. Characteristic events during discharge of the Blumlein.

	Time [ns]	Position		Time [ns]	Position
$t_0$	0	Passing D-dot 1	$t_7$	4.71	Passing D-dot 1
$t_1$	0.83	Passing D-dot 2	$t_8$	5.36	Reflecting on Spark gap
$t_2$	1.65	Passing D-dot 3	$t_9$	6.00	Passing D-dot 1
$t_3$	2.36	Reflecting on edge	$t_{10}$	6.83	Passing D-dot 2
$t_4$	2.48	Passing D-dot 4	$t_{11}$	7.65	Passing D-dot 3
$t_5$	3.06	Passing D-dot 3	$t_{12}$	8.36	Reflecting on Edge
$t_6$	3.89	Passing D-dot 2	$t_{13}$	8.48	Passing D-dot 4

The simulated voltages in the Blumlein at the position of the D-dot sensors are shown in Figure 4-23. Blue is the Blumlein voltage at D-dot sensor 1 and red, green and yellow are the Blumlein voltages at D-dot sensors 2, 3 and 4.

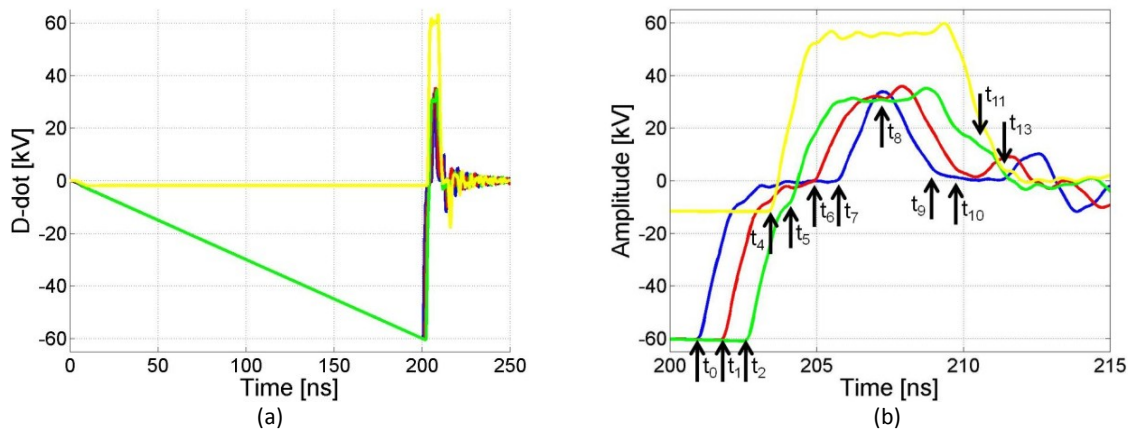


Figure 4-23. (a) Simulated Blumlein voltage at the D-dot sensors during pulse formation (blue; D-dot 1, red; D-dot 2, green; D-dot 3, yellow; D-dot 4). (b) Zoomed view of the blumlein pulse.

In Figure 4-23, the voltage in the Blumlein at D-dot sensor 1 through 3 goes to  $-60$  kV in the first 200 ns. During this time interval, the Blumlein is charged. When the charging voltage reaches  $-60$  kV the spark gap closes and the pulse forming process starts. This pulse forming process is described in the previous section, and illustrated in Figure 4-6 through Figure 4-10. After the closing of the spark gap, it can be seen from Figure 4-23 that the voltage in the Blumlein at D-dot sensors 1 through 3 becomes zero (blue, red and green line). This happens respectively at  $t_0$ ,  $t_1$  and  $t_2$  (as in agreement with Figure 4-7). As expected, the voltage front in the Blumlein reflects at the end of the charging electrode, at  $t_3$ , and the voltage of the charging electrode goes to  $+30$  kV. The corresponding voltage front with an amplitude of  $+30$  kV passes the D-dot sensors 3 through 1 at respectively  $t_5$ ,  $t_6$  and  $t_7$  (in agreement with Figure 4-8). Finally the voltage front reflects at the spark gap side of the Blumlein at  $t_8$ . A voltage front with an amplitude of  $+30$  kV returns again to the end of the charging electrode and passes D-dot sensors 1 through 4 at  $t_9$  through  $t_{13}$  (where, at  $t_{12}$ , the voltage front passes the end of the charging electrode again).

After time  $t_{12}$  the Blumlein is discharged and the pulse forming process is finished. The small oscillations as seen in Figure 4-23 are caused by Teflon separation disks that result in a not perfectly matched construction. As expected, the output voltage of the Blumlein becomes about  $60$  kV at  $t_3$  and goes back to zero at  $t_{12}$  and has an expected duration of about 6 ns. This output voltage arrives slightly delayed, at  $t_4$ , at D-dot sensor 4.

Figure 4-24 show the simulated output voltages of the D-dot sensors. Here the same color scheme is used as in Figure 4-23. The signals of D-dot 1 through 3 are very similar, as expected. The output signal of D-dot 4 deviates from the other 3 D-dot sensors as expected.

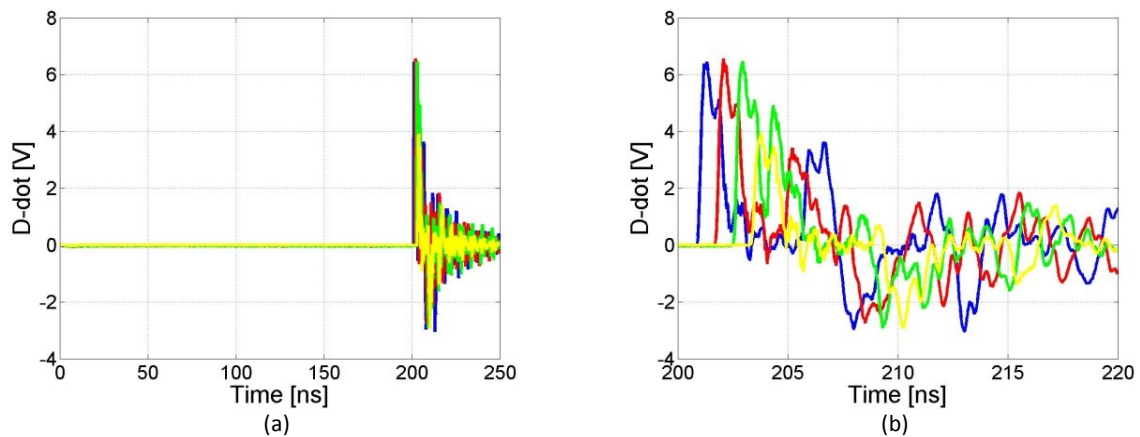


Figure 4-24. (a) Simulated D-dot sensor output voltage during pulse formation (blue; D-dot 1, red; D-dot 2, green; D-dot 3, yellow; D-dot 4). (b) Zoomed view of the simulated D-dot sensor output voltage.

Figure 4-25 through Figure 4-28 show the amplitude spectra of both the in- and output voltages of all D-dot sensors, where the input voltages are the Blumlein voltages at the positions of the sensors. Now the transfer characteristics of the D-dot sensors can be determined by dividing the spectrum of a D-dot sensor output voltage by the spectrum of the input voltage of the same sensor. These transfer characteristics are shown in Figure 4-29 for D-dot 1 and 2 and Figure 4-30 for D-dot 3 and 4 in blue. The red curves in these figures shows the transfer functions eq. 4-13, after fitting the capacitances. The fitted values for the lumped element model are given in Table 4-4. As can be seen in Figure 4-29 and Figure 4-30, the D-dot sensors behave like nearly perfect differentiators for the frequency range in which the Blumlein operates; they have a rising slope of 20 dB/decade.

Table 4-4. Capacitances used for the D-dot sensors in the RC models.

	High-voltage electrode	Charged electrode
D-dot 1 – 3	0	$2.25 \cdot 10^{-15}$ F
D-dot 4	$1.225 \cdot 10^{-15}$ F	0

Now we can use the transfer function, eq. 4-15, of the lumped element model for the D-dot sensor to calculate the voltages in the Blumlein generator from the numerically simulated D-dot output voltages (shown in Figure 4-24). The calculated voltages are shown in Figure 4-31 through Figure 4-34 in red. The numerically simulated Blumlein voltages are shown in blue in the same figure.

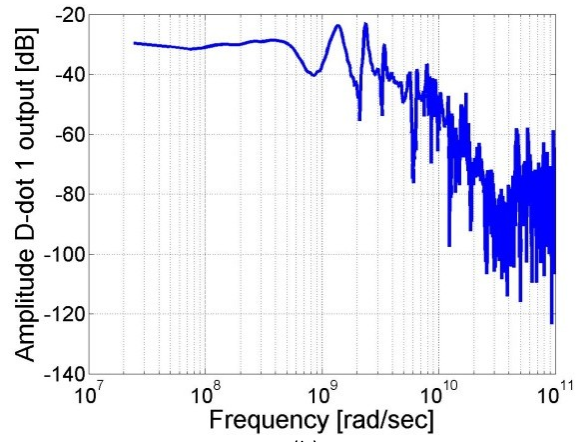
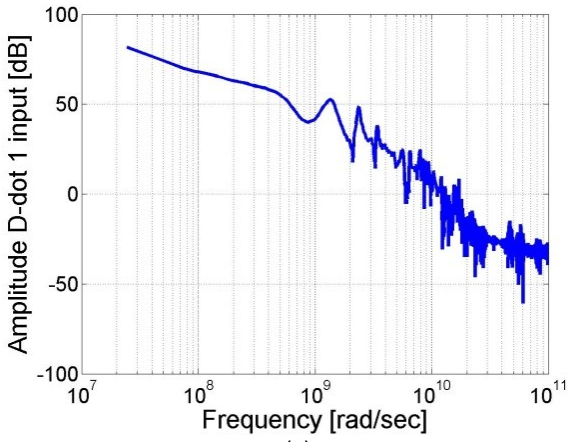


Figure 4-25. (a) D-dot 1 input spectrum. (b) D-dot 1 output spectrum.

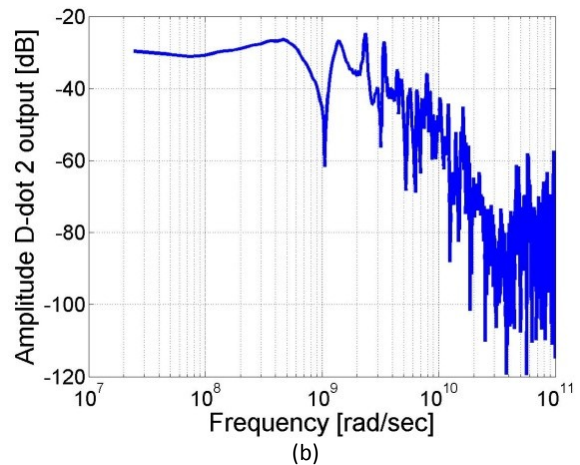
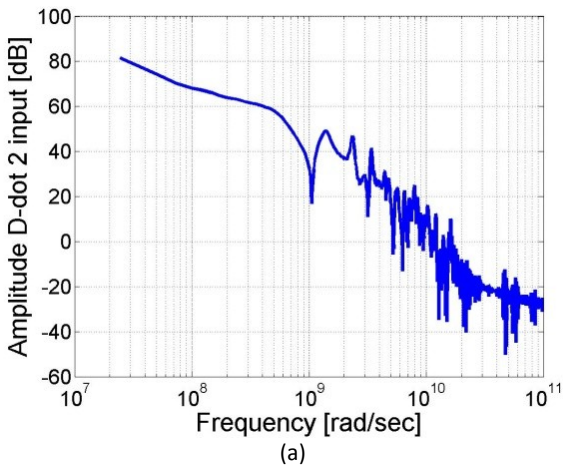


Figure 4-26. (a) D-dot 2 input spectrum. (b) D-dot 2 output spectrum.

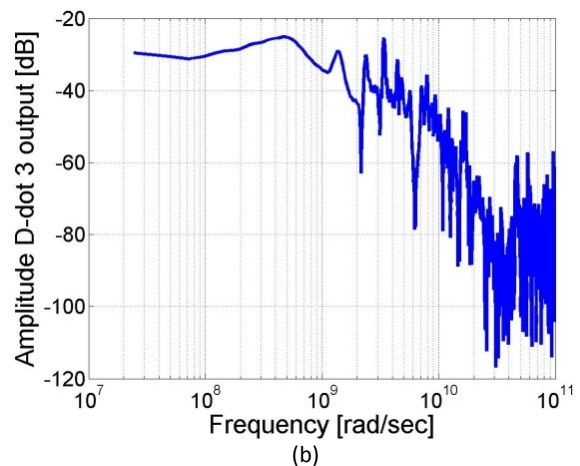
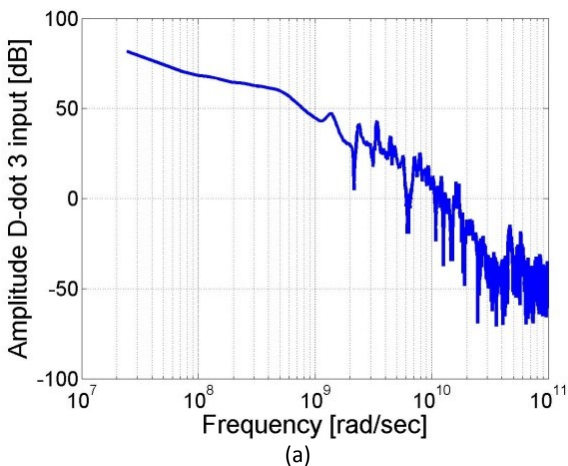


Figure 4-27. (a) D-dot 3 input spectrum. (b) D-dot 3 output spectrum.



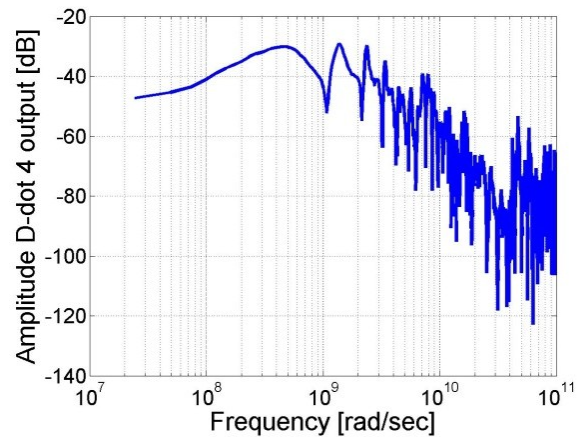
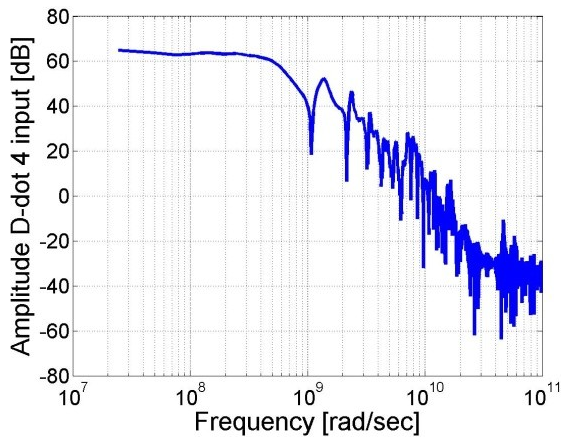


Figure 4-28. (a) D-dot 4 input spectrum. (b) D-dot 4 output spectrum.

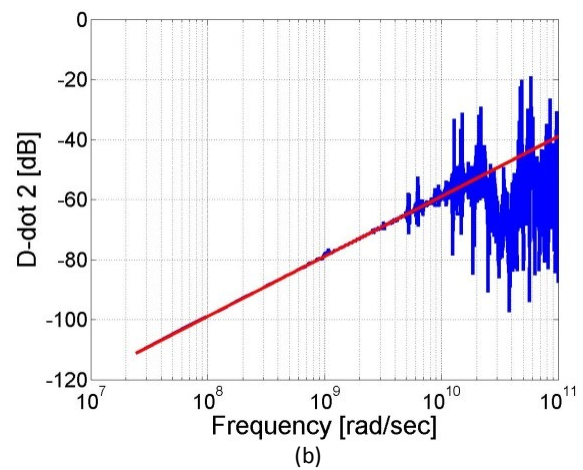
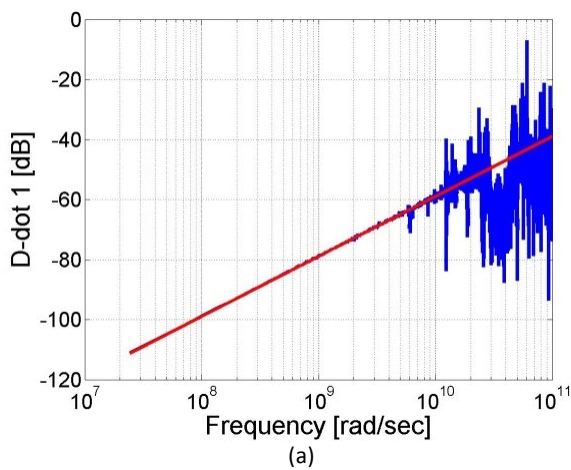


Figure 4-29. (a) Blue; Amplitude Bode plot of D-dot 1. Red; transfer function of D-dot 1. (b) Blue; Amplitude Bode plot of D-dot 2. Red; transfer function of D-dot 2.

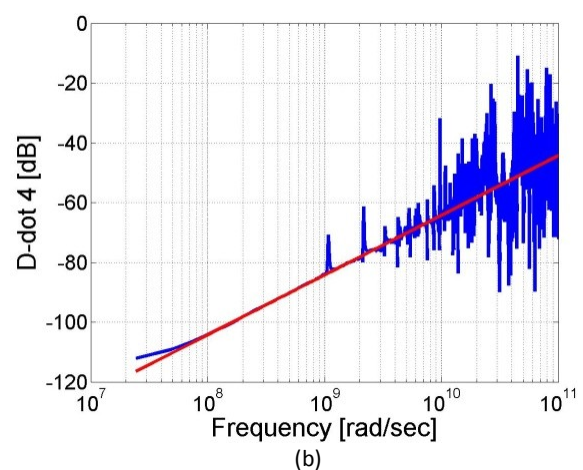
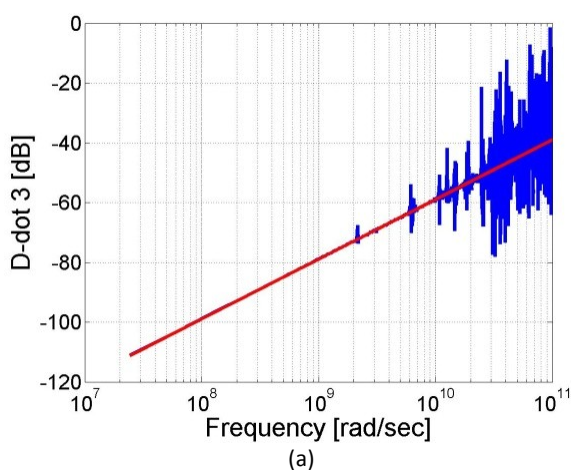


Figure 4-30. (a) Blue; Amplitude Bode plot of D-dot 3. Red; transfer function of D-dot 3. (b) Blue; Amplitude Bode plot of D-dot 4. Red; transfer function of D-dot 4.

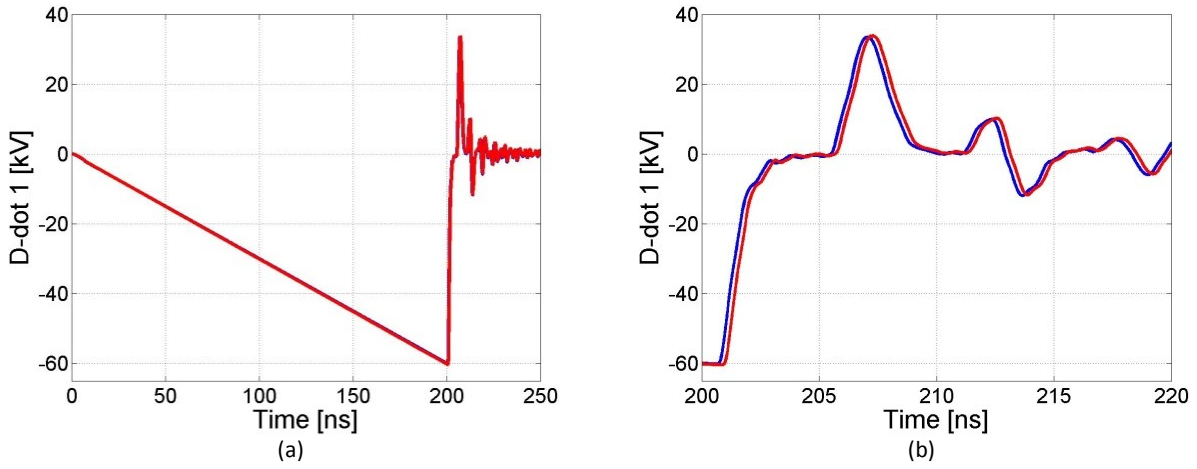


Figure 4-31. (a) Blue; numerically simulated Blumlein voltage at the input of D-dot 1. Red; Blumlein voltage at D-dot 1 using the parameterized transfer function and the numerically simulated D-dot output voltage. (b) Zoomed view of pulse formation.

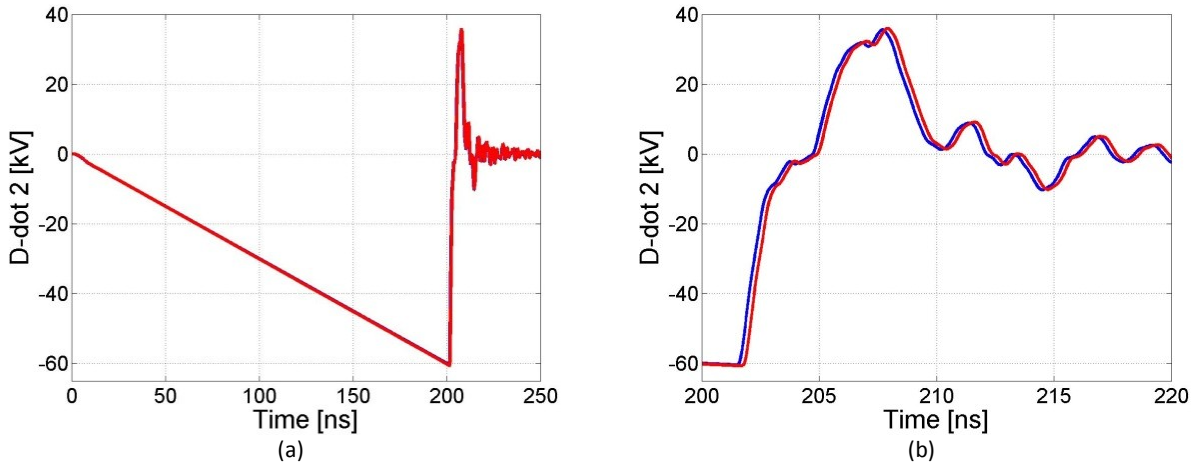


Figure 4-32 (a) Blue; numerically simulated Blumlein voltage at the input of D-dot 2. Red; Blumlein voltage at D-dot 2 using the parameterized transfer function and the numerically simulated D-dot output voltage. (b) Zoomed view of pulse formation.

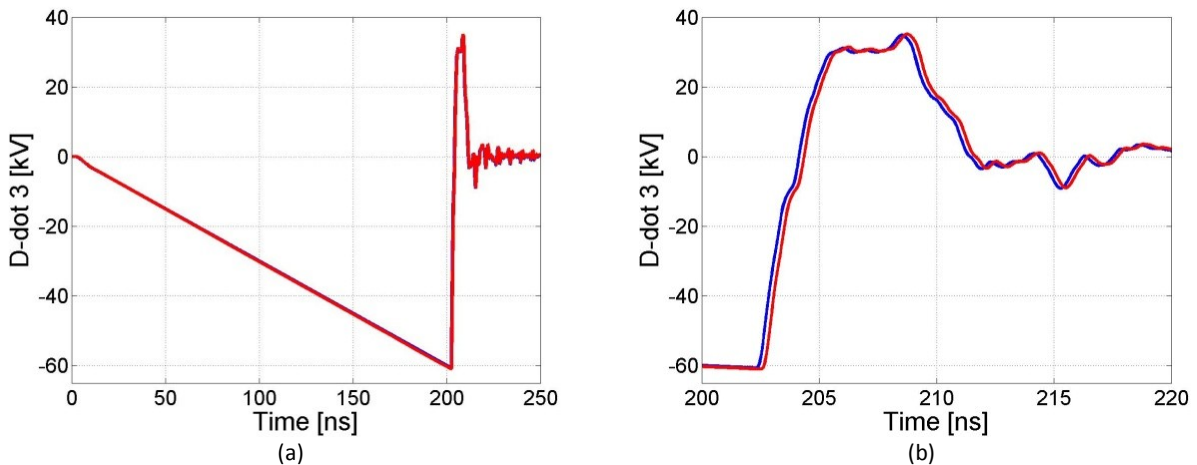


Figure 4-33 (a) Blue; numerically simulated Blumlein voltage at the input of D-dot 3. Red; Blumlein voltage at D-dot 3 using the parameterized transfer function and the numerically simulated D-dot output voltage. (b) Zoomed view of pulse formation.

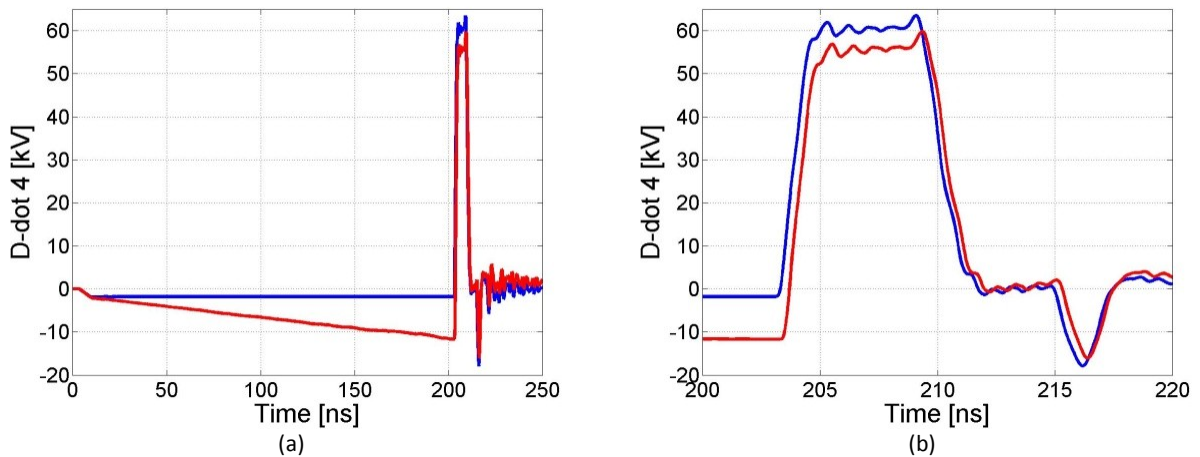


Figure 4-34 (a) Blue; numerically simulated Blumlein voltage at the input of D-dot 4. Red; Blumlein voltage at D-dot 4 using the parameterized transfer function and the numerically simulated D-dot output voltage. (b) Zoomed view of pulse formation.

As can be seen in Figure 4-31 through Figure 4-33, the calculated voltages in the Blumlein at the sensor positions 1 through 3, based on the output voltage of the D-dot sensors and their transfer function, are in good agreement with the numerically simulated Blumlein voltages. A small time delay is observed, which is caused by the distance between the positions where the in- and output voltages of the sensors are recorded in the simulation.

The calculated Blumlein voltage at D-dot sensor 4 differs from the numerically simulated Blumlein voltage at the same position. This is due to the fact that this D-dot sensor has both a capacitive coupling with the charging electrode and with the high voltage electrode which both are in the same order of magnitude. The voltage, calculated using the output voltage of D-dot sensor 4, is the summation of the voltage on the charging electrode, attenuated, and the voltage on the high voltage electrode. This can clearly be seen in Figure 4-34 (Left). The calculated amplitude of the pulse is lower than the actual amplitude. The difference is half the charging voltage,  $\beta/2$ , as measured by D-dot 4, as shown in Figure 4-35.

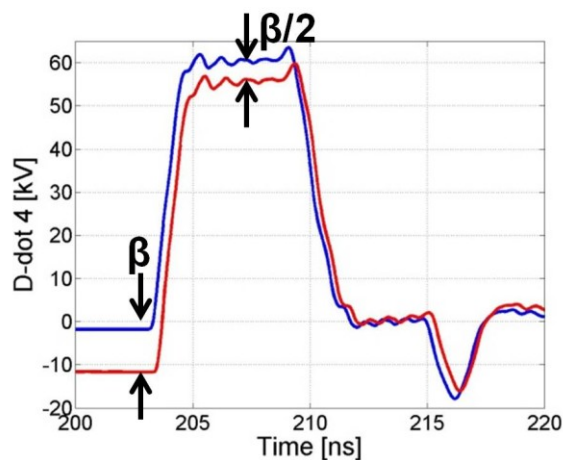


Figure 4-35. The Blumlein voltage based on D-dot 4. The calculated amplitude (red) has an offset equal to half the charging voltage,  $\beta/2$ , as measured by D-dot sensor 4, with respect to the actual Blumlein output voltage (blue).



### 4.5.3 Time delay determination

In the previous section we have shown that the D-dot sensors can be used to measure the voltages inside the Blumlein, and that their behaviour can be described by a simple RC network. To be able to use this RC network, and its capacitance values of Table 4-2 and Table 4-4, in actual measurements, we must verify that the dielectric constant of the oil, as used in the numerical simulation, is the same as the one used in the experiment. Only if the dielectric constants of the numerical simulation and the measurement are the same, we can use the capacitances found in the previous section. This can be verified by measuring the time delay between the different D-dot sensor signals. Knowing the distance between the sensors and the measured time delay between them, the dielectric constant of the oil can be determined using

$$v_c = \frac{c}{\sqrt{\epsilon_r}} \quad 4-17$$

This can be rewritten to

$$\epsilon_r = \left( \frac{c\Delta t}{\Delta l} \right)^2 \quad 4-18$$

Here  $\Delta t$  is the time difference and  $\Delta l$  the distance between the sensors. Table 4-5 shows the time delay of the numerical simulations and the calculated  $\epsilon_r$  using eq. (4-18).

Table 4-5.  $\epsilon_r$  based on simulated time delays between the D-dot sensors.

	Time delay [ns]	$\epsilon_r$ [-]
D-dot 1 – D-dot 2	0.827±0.025	2.729 ±0.053
D-dot 1 – D-dot 3	1.653±0.025	2.727 ± 0.026
D-dot 1 – D-dot 4	2.459±0.025	2.683 ± 0.017

Both the time delay between sensor 1 and 2 and the time delay between sensor 1 and 3 give the correct  $\epsilon_r$ . The time delay between sensor 1 and 4 deviates too much. This error in the measurement is due to the fact that the transmission line geometry changes between D-dot sensors 3 and 4. This disturbs the forward propagation of the electromagnetic wave.

The error tolerance in the dielectric constant is calculated using eq. 4-19. Here  $\Delta t_{err}$  is 0.25 ps and  $\Delta l_{err}$  is 1 mm.

$$\epsilon_{r,err} = \left| \left( 2\Delta t \frac{c}{\Delta l} \right)^2 \right| \cdot \Delta t_{err} + \left| -2 \frac{(c\Delta t)^2}{\Delta l^3} \right| \cdot \Delta l_{err} \quad 4-19$$

## 4.6 Measurement results

Now we have found the transfer functions of the D-dot and the capacitive sensors and the respective capacitances, we can use them to calculate the voltage in the real Blumlein generator. We first have to determine the time delay between the 4 D-dot sensor signals to verify the dielectric constant of the oil.

### 4.6.1 Time delay verification

Table 4-6 shows the measured time delays between sensors 1, 2, 3 and 4 and the  $\epsilon_r$  based on these time delays.

Table 4-6.  $\epsilon_r$  based on measured time delays between the D-dot sensors.

	Time delay [ns]	$\epsilon_r$ [-]
D-dot 1 – D-dot 2	$0.83 \pm 0.05$	$2.74 \pm 0.33$
D-dot 1 – D-dot 3	$1.69 \pm 0.05$	$2.85 \pm 0.17$
D-dot 1 – D-dot 4	$2.59 \pm 0.05$	$2.98 \pm 0.12$

Here the errors are based on a 50 ps uncertainty in the time measurement, based on the oscilloscope sampling rate, and 0.1 mm accuracy of the sensor placement.

The time delays between sensors 1 and 2 and sensors 1 and 3 give a measure for  $\epsilon_r$  that agrees with both the specifications supplied by the manufacturer of the used oil, Shin-Etsu KF-96-100CS, and the  $\epsilon_r$  used in the simulations. The parameters as found in the simulations of the previous section can thus be used to analyze the measured results.

### 4.6.2 Current sensor measurement

The output voltage of the Blumlein generator is measured with both the capacitive voltage divider and with the D-dot sensors. As a third method to measure this output voltage, the output current is measured with a Bergoz CT-F-2.5 current sensor and multiplied by the load impedance (50 ohm). This sensor is positioned at the output of the generator as shown in Figure 4-4. The output voltage, based on the current sensor is shown in Figure 4-36.

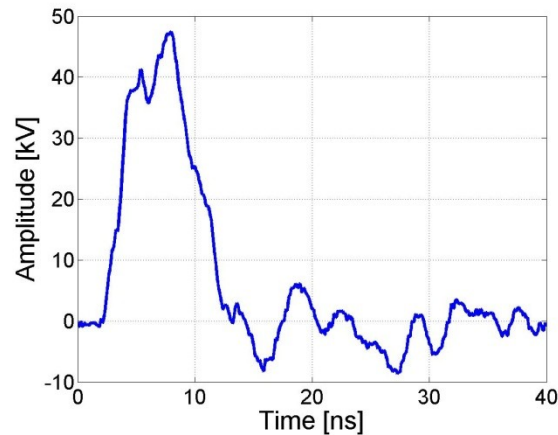


Figure 4-36. Blumlein output voltage as measured with a Bergoz CT-F-2.5 current sensor.

It shows that the Blumlein output voltage has a peak value of 47 kV and the pulse width is longer than expected. The voltage pulse derived from the Bergoz current sensor is not a flat top pulse as expected from the numerical simulation. The bandwidth of the current sensor is 400 MHz, which is too low to correctly measure the output voltage pulse. Also, during the measurement, sparking between the outside of the current sensor to ground was observed which might have disturbed the measurement. The sparking could be caused by the fact that the current sensor is too close to the high voltage electrode and the insulation of the Teflon disk is not good enough, shown in Figure 4-37. Another possible cause could be the capacitive coupling between the hull of the current sensor and the HV electrode. If this coupling is strong enough, the voltage on the hull of the current sensor rises such that discharges can occur. Since the current sensor is connected with a coaxial cable to a grounding plane roughly 40 cm further away, there is a large induction between the sensor and ground.

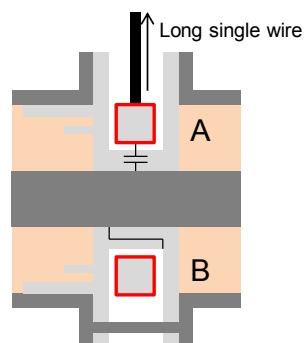


Figure 4-37. Two possible causes for the observed discharges at the current sensor. A; the capacitive coupling between the current sensor and the HV electrode. B; a discharge forms from the HV electrode through the small gap in between the two Teflon disks to the shield of the current sensor.

### 4.6.3 Capacitive Voltage Divider (CVD)

Due to the fact that the 2600  $\Omega$  matching resistor is not included in the simulations (as described in section 4.5.1), the measurement and simulation results cannot be compared directly. Figure 4-38

shows the output signal of the CVD. Figure 4-39 shows the output voltage of the Blumlein as reconstructed from  $V_{CVD}$  and the transfer function of eq. 4-9, with the values for the capacitors of table 2.

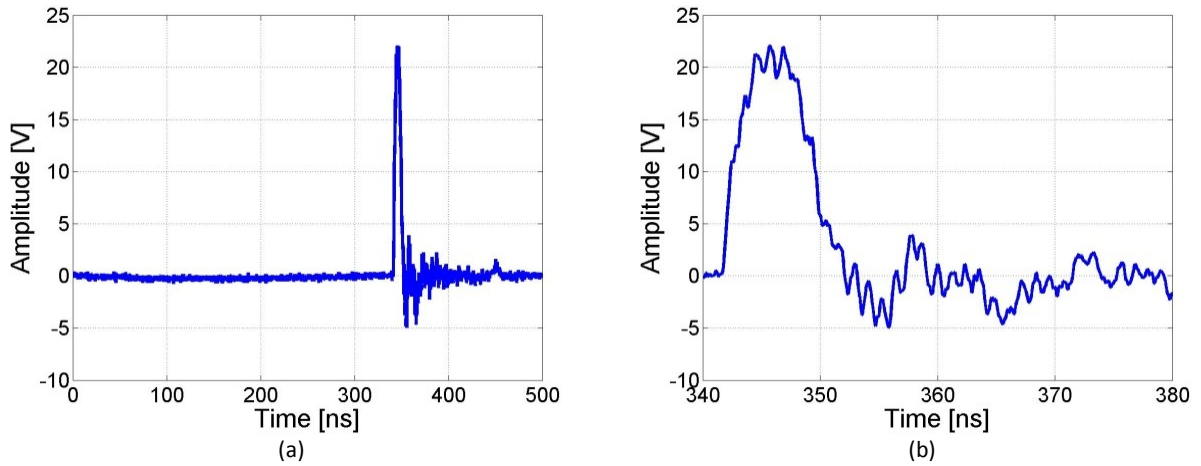


Figure 4-38. (a) Measured CVD output voltage. (b) Zoomed view.

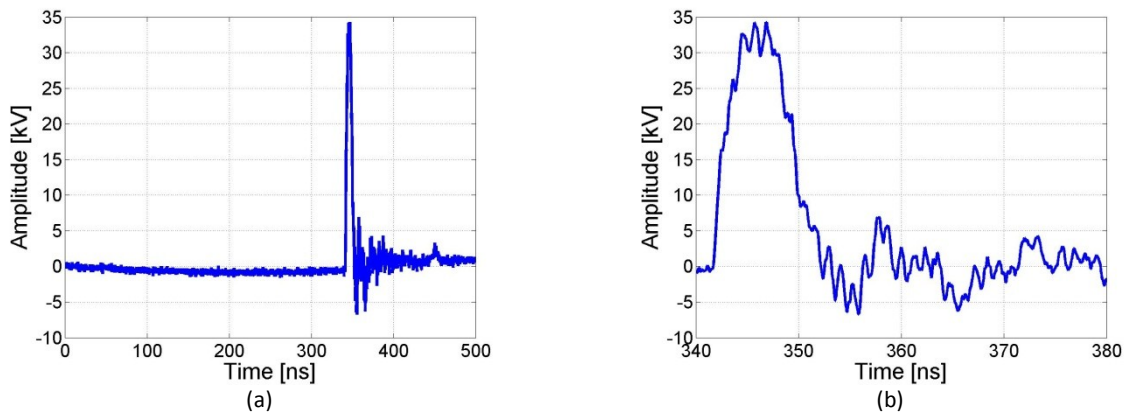


Figure 4-39. (Left) Blumlein voltage at the CVD based on the measured CVD output voltage (Figure 4-38). (Right) zoomed view.

The amplitude of the output voltage is about 32 kV. This amplitude is lower than expected. Also the measured signal shows more oscillations than expected from the numerical simulations. The shape of the output voltage of the CVD, Figure 4-38, is similar to the shape of the reconstructed Blumlein voltage, Figure 4-39. This was not the case for the numerical simulation results and this difference is caused by the addition of the 2600  $\Omega$  matching resistor. Looking at the characteristic RC time of the CVD with the matching resistor, eq. 4-9, we get

$$\omega_{CVD} = \frac{1}{(R_1 + R_2)(C_1 + C_2)} = 7.67 \cdot 10^6 \text{ rad/sec} = 1.22 \text{ MHz} \quad 4-20$$

This frequency is so low that it can be assumed the CVD functions as an attenuating sensor for the pulses of the Blumlein pulse generator with an attenuation factor of 1500 according to eq. 4-8. With a peak voltage of 60 kV in the Blumlein, the peak value of  $V_{CVD}$  will be around 40 V.

#### 4.6.4 D-dot sensor

Figure 4-40 through Figure 4-43 show the measured (blue lines) and the simulated (red lines) output signals of the four D-dot sensors.

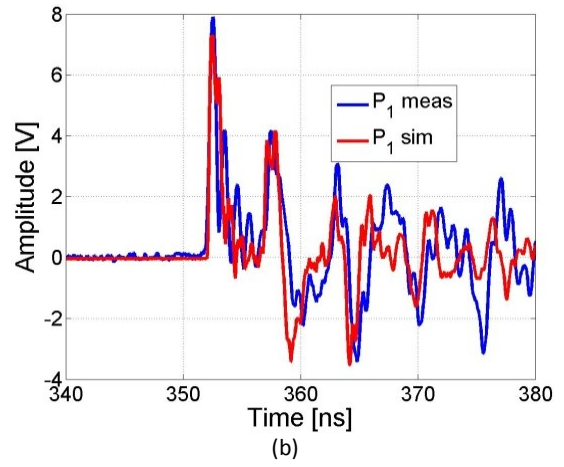
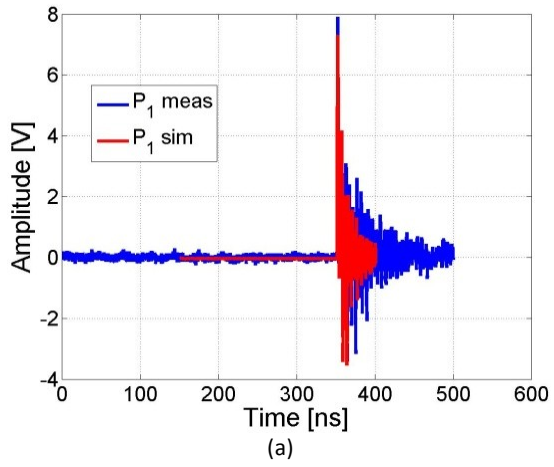


Figure 4-40. (a) Blue; measured D-dot 1 output voltage. Red; Simulated output voltage. (b) Zoomed view.

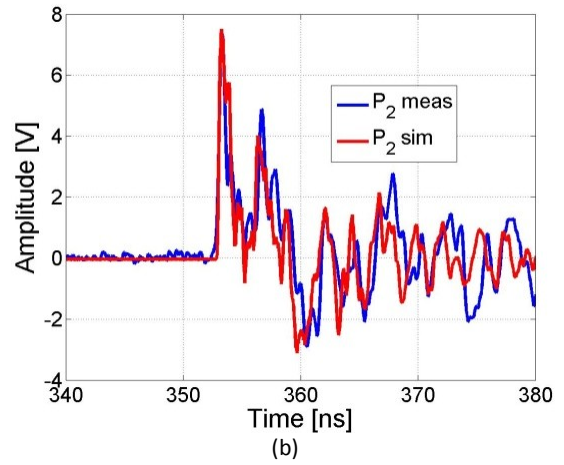
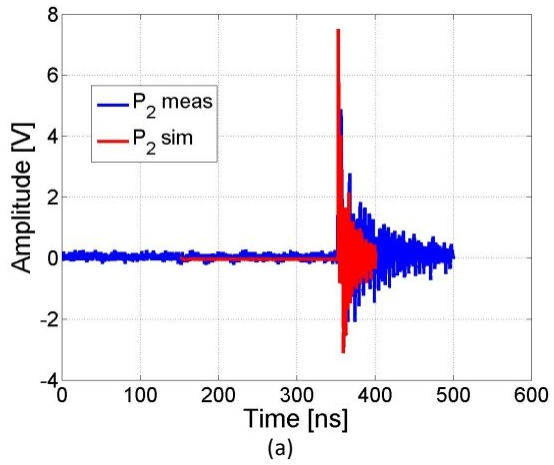


Figure 4-41. (a) Blue; measured D-dot 2 output voltage. Red; Simulated output voltage. (b) Zoomed view.

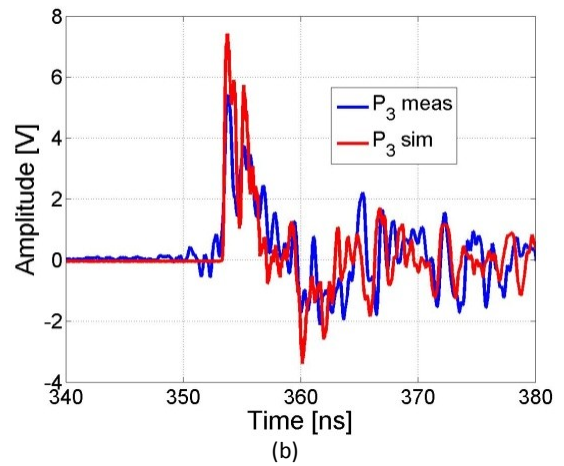
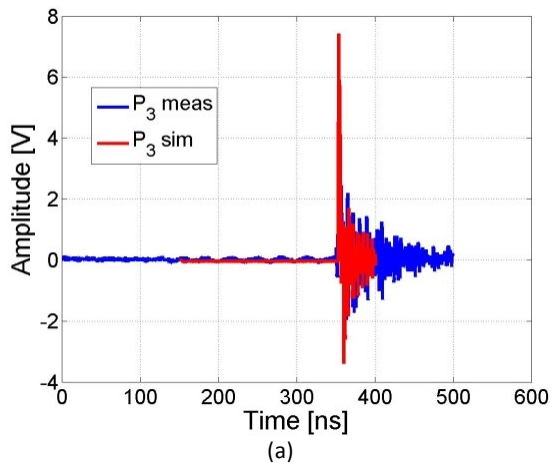


Figure 4-42. (a) Blue; measured D-dot 3 output voltage. Red; Simulated output voltage. (b) Zoomed view.

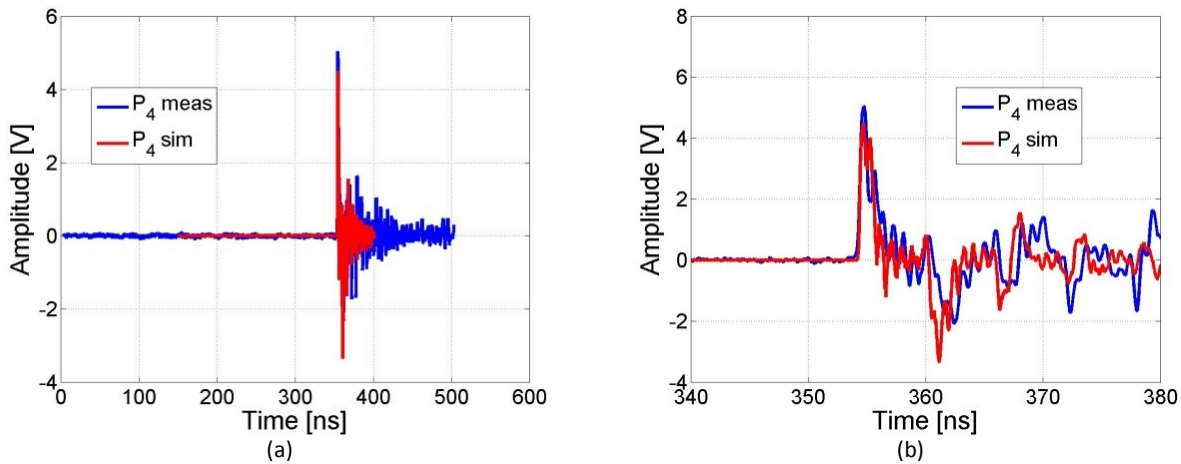


Figure 4-43. (a) Blue; measured D-dot 4 output voltage. Red; Simulated output voltage. (b) Zoomed view.

As can be seen, the measured D-dot sensor signals are predicted quite accurately by the model. Both the simulated and measured amplitude spectra of the D-dot sensors are shown in Figure 4-43 for D-dot 1 and 2 and in Figure 4-44 for D-dot 3 and 4.

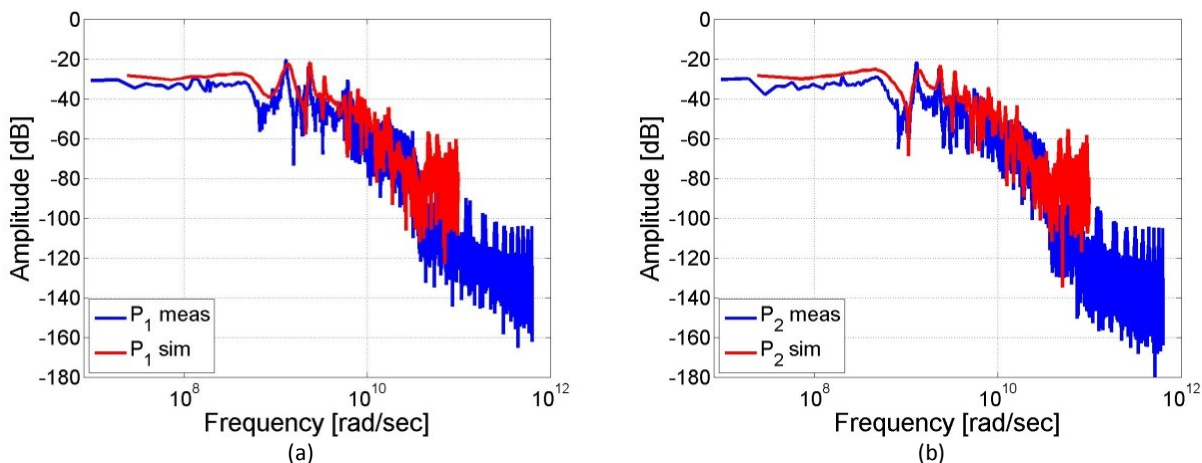


Figure 4-44. (a) Blue; measured voltage amplitude spectrum of the output voltage of D-dot 1. Red; simulated spectrum. (b) Blue; measured voltage amplitude spectrum of the output voltage of D-dot 2. Red; simulated spectrum.

The amplitude spectra of the measurements have the same features as those of the simulations. Using the transfer function of eq. 4-15, the capacitance values of Table 4-4 and the measured D-dot sensor output voltages, we determine the voltages inside the Blumlein at the D-dot sensor positions. These voltages are shown in Figure 4-45.

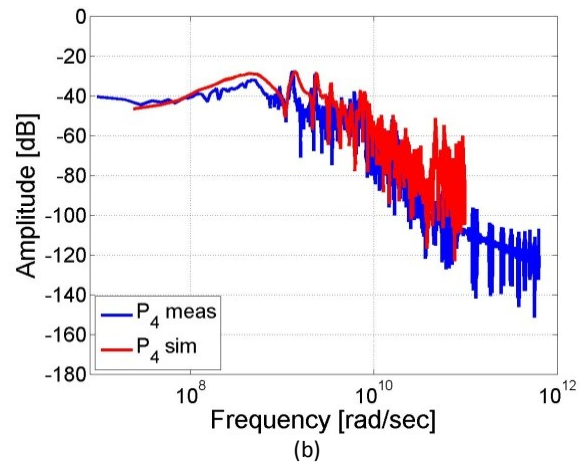
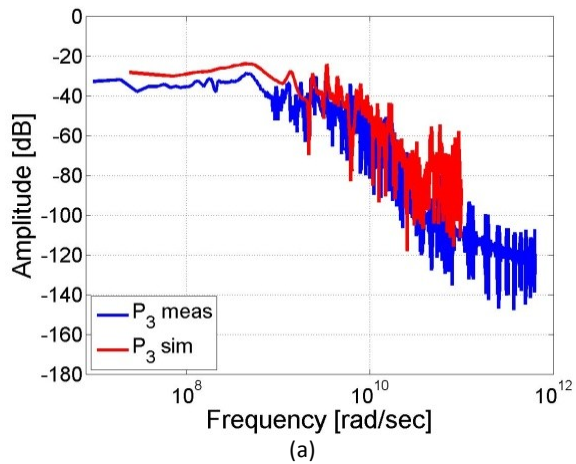


Figure 4-45. (A) Blue; measured voltage amplitude spectrum of the output voltage of D-dot 3. Red; simulated spectrum. (b) Blue; measured voltage amplitude spectrum of the output voltage of D-dot 4. Red; simulated spectrum.

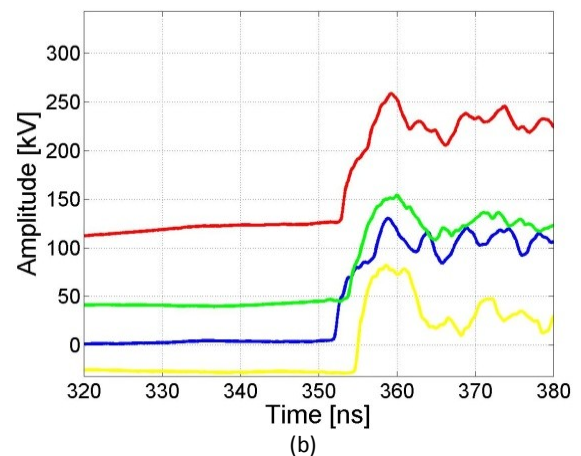
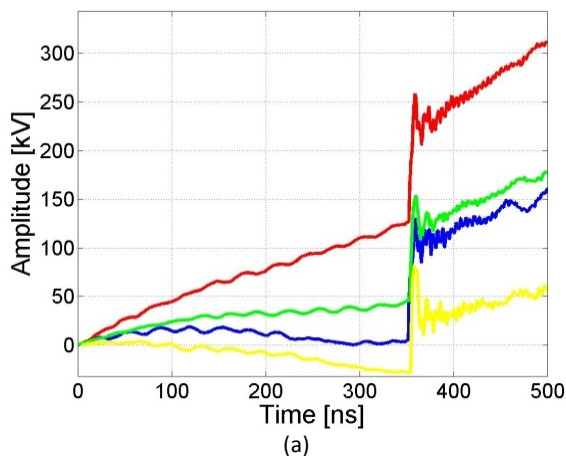


Figure 4-46. (a) Voltages in the Blumlein based on the measured D-dot sensor signals. Blue; D-dot 1, red; D-dot 2, green; D-dot 3, yellow; D-dot 4. A linear offset due to noise is seen with each D-dot sensor. (b) Zoomed view.

Figure 4-46 clearly shows a linear offset in all four signals, each with a different slope. This offset is caused by the integration of the noise in the D-dot output voltage. Applying a linear correction for this noise gives the voltages shown in Figure 4-47.



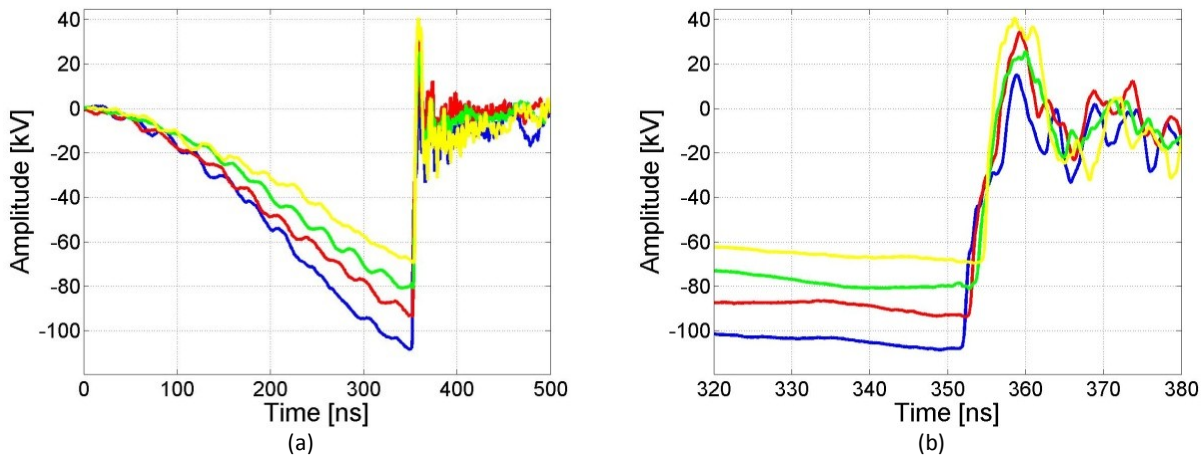


Figure 4-47. (a) Measured Blumlein voltages at the D-dot sensors after noise correction. (b) Zoomed view.

Figure 4-47, reveals two other measurement distortions. All D-dot sensors show a different charging voltage, all lower than the expected -60 kV, and after the spark gap closes the calculated voltages do not go to zero. We know that during charging of the Blumlein, the D-dot sensors 1 through 3 should all measure nearly the same voltage and after closing of the spark gap their voltage should rise to half the inverted charging voltage. We use this information to apply a second correction. Looking, for each D-dot sensor, at the difference between the minimum and maximum voltage we know that 2/3 of this should be below zero and 1/3 should be above zero. When correcting for this for each sensor, we get Figure 4-48. Here we see that the voltage in the Blumlein at the different sensors goes to zero after the pulse has been formed as expected. This makes the correction and the assumptions it is based on likely to be valid.

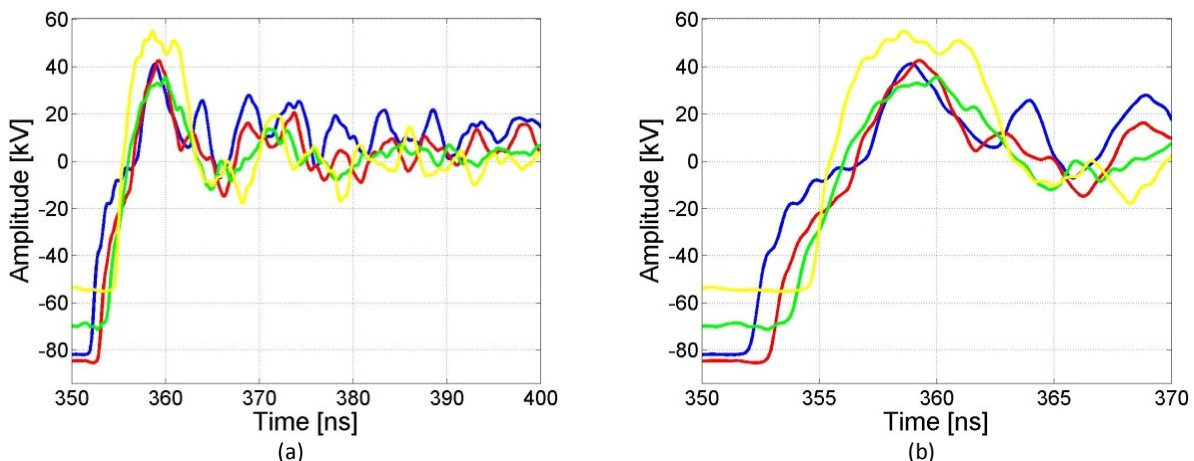


Figure 4-48. (Left) measured Blumlein voltages at the D-dot sensors after second correction. (Right) zoomed view.

In Figure 4-49 we compare the measured Blumlein voltages at the D-dot sensors with those of the numerical simulations. It can be seen that the reconstructed Blumlein voltage, based on the measured D-dot sensor output voltages, is in agreement with the simulations. Characteristic points in time from

Table 4-3 have been indicated with arrows in Figure 4-49. In Figure 4-49 a, again the numerical simulation results are shown.

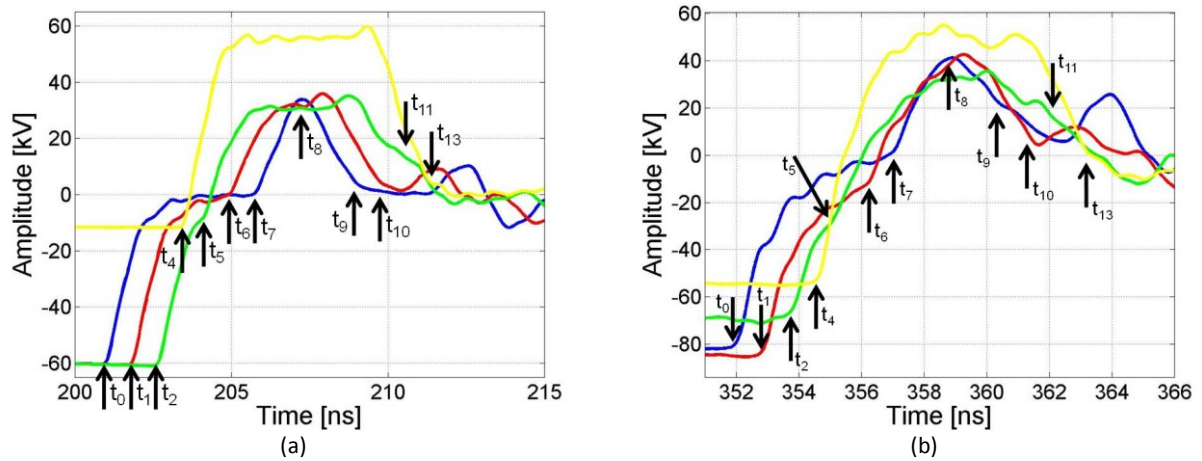


Figure 4-49. (Left) simulated Blumlein voltage at the D-dot sensors (same as Figure 4-23). (Right) measured Blumlein voltage at the D-dot sensors and the characteristic times as mentioned in Table 4-3.

As can be seen,  $t_0$  through  $t_8$  are easily identified but  $t_9$  and later are not distinctly observed in the signal and are found based on the time delays in Table 4-3. Table 4-3 shows the times at which something happens which we should be able to observe with the D-dot sensors. D-dot 1 (blue) shows a good return to 0 volts in Figure 4-49 before its amplitude rises to half the charging voltage again. The charging voltage of D-dot 1 and 2 are 83 kV +/- 2 kV. D-dot sensor 2 does not go to zero volts before it rises to half its charging voltage. D-dot sensor 3 clearly shows a smaller amplitude. This is not expected based on simulations and could be caused by manufacturing and assembly inaccuracies. Either the capacitance of D-dot sensor 3 is larger or it has a higher resistance due to the mechanical connection of the sensor to the Blumlein. D-dot sensor 4 shows an even smaller amplitude. A remarkable feature of D-dot sensor 4 is the fact that the amplitude, before closure of the spark gap, is almost as big as the amplitude of the pulse. This is not expected when looking at the simulation results. The amplitude of the pulse as measured with D-dot sensor 4 does, however, agree with the amplitude as measured with the current sensor. The capacitive coupling between D-dot 4 and the charging electrode might be stronger than in the simulations.

The signals of the D-dot sensors show all the expected characteristics of the pulse forming process in the Blumlein generator. The observed characteristics are in agreement with theory and are predicted by numerical simulations. After correcting for noise, the amplitudes differ between the D-dot sensors. This could be caused by (small) deviations of the capacitance of a D-dot sensor, and/or by resistance due to the connection between the D-dot sensors and the Blumlein.

The amplitude of the pulse as measured with D-dot sensor 4 differs from the one measured with the CVD but agrees with the current sensor measurement. The deviation in the CVD result might be caused by size limitations in the simulations. In reality the CVD is a very thin copper ring. But in the simulations, this ring is thicker due to minimal size limitations of the mesh grid; a very thin ring would require an extremely fine mesh. The increased ring thickness in the simulation changes the capacitance  $C_2$ .

Although a lot of effort has been done to have good shielding and grounding, improving the grounding and EMC shielding even further, could reduce noise levels and improve the quality of the measurement.

The D-dot sensors are more sensitive to noise than the capacitive voltage divider due to two reasons; first, they measure the derivate and the measured signal needs to be integrated. The noise in the signal is thus integrated, resulting in a drift or offset of the signal. Secondly their output voltage is about a factor of 10 lower than that of the capacitive voltage divider, reducing the signal-to-noise ratio.

## 4.7 Conclusions

Here we have successfully measured the voltage in a high voltage nanosecond pulse source. To do this we have developed a D-dot sensor. Using a simplified RC model of the sensor based on its physical implementation on a pulse source, we obtained a transfer function, between the sensors in and output voltage. With numerical simulations the capacitances of each sensor are estimated. The performance of the D-dot sensor is validated in measurements on the Kumamoto Blumlein pulse source. Besides testing the D-dot sensors we have also compared them with a capacitive voltage divider and a current sensor.

Both the D-dot sensors and the capacitive voltage divider measure the shape of the Blumlein output pulse. The amplitude based on the capacitive voltage divider is lower than expected and the sensor shows more oscillations in the experiment than in the numerical simulations.

The four D-dot sensors give a clear image of the behavior of electric fields in the Blumlein. The numerical simulation has been successfully used to parameterize the sensors. Because the capacitive coupling between the charging electrode and D-dot 4 is in the same order of magnitude as the coupling between the high voltage electrode and D-dot sensor 4, the calculated Blumlein voltage based on D-dot sensor 4 is a summation of both. Still, the Blumlein output pulse can be extracted from this. Experiments agree with the numerical simulations and the absolute value of the Blumlein output pulse was successfully measured. Combining the results of the D-dot sensors and the capacitive voltage divider a very complete image of the electric fields in the Blumlein is obtained.

As stated in the introduction, the D-dot sensors and the capacitive voltage divider are essentially the same but due to the differences in their sizes they are used in different modes. The D-dot sensor is a differentiating sensor, thus the output signal corresponds to the derivative of the signal to be measured. The output voltage of the CVD is equivalent to the signal it measures. Due to the large attenuation factor of the D-dot sensor it is more sensitive to noise when compared to the capacitive voltage divider.



# 5 Measuring the rise time of (high) voltage pulses using autocorrelation

---

## 5.1 Introduction

When working with short electric pulses, the rise time is a parameter of great interest. For example the laser switched spark gap as described in [1] has an expected rise time in the order of 35 ps. Such fast changes can be measured nowadays with sampling oscilloscopes, which go up to a bandwidth of 100 GHz. However, equipment of this calibre is anything but cheap and therefore, alternative solutions are worthwhile to be explored.

Here we propose a new method to measure pulse rise-times, based on autocorrelation. This method is commonly used with femtosecond laser systems to determine the width of very short pulses. When working with femtosecond laser pulses and or electron bunches, there are several methods to measure bunch lengths with resolutions ranging from sub-picoseconds to several picoseconds. Sub picosecond relativistic electron-bunch lengths can be measured using coherent Smith-Purcell radiation [2-5]. Another method would be to use electro-optical detection techniques [6-8]. Coherent transition or diffraction radiation can also be used. If the spectrum of the bunch is known, or if a reliable assumption of the bunch shape can be made, the autocorrelation of this radiation can be obtained by use of an interferometer. Usually a Michelson interferometer is used [9-13].

Using autocorrelation, the length of a pulse can be determined. But when the pulses have a length of 10 to 100 ps, optical measurement methods become impractical or even impossible due to the long wavelengths. To be able to measure these pulse lengths, a fully electric technique, based on autocorrelation, is presented. The autocorrelator described here can measure pulse lengths in the order of 10 to 100 ps with a resolution of 4 ps.

To be able to use this autocorrelator to measure the rise time of the high voltage pulse, it is combined with the D-dot sensor as shown in Figure 5-1. The output of the D-dot sensor is the time derivative of the high voltage pulse it measures. This derivative is a representation of the rise time of the pulse and can be used directly as an input for the autocorrelator to determine the risetime.

The advantage of the autocorrelator, with respect to a real time or sampling scope, is its low frequency output. This gives the opportunity to obtain very high amplification factors, and thereby increasing the sensitivity of the device.

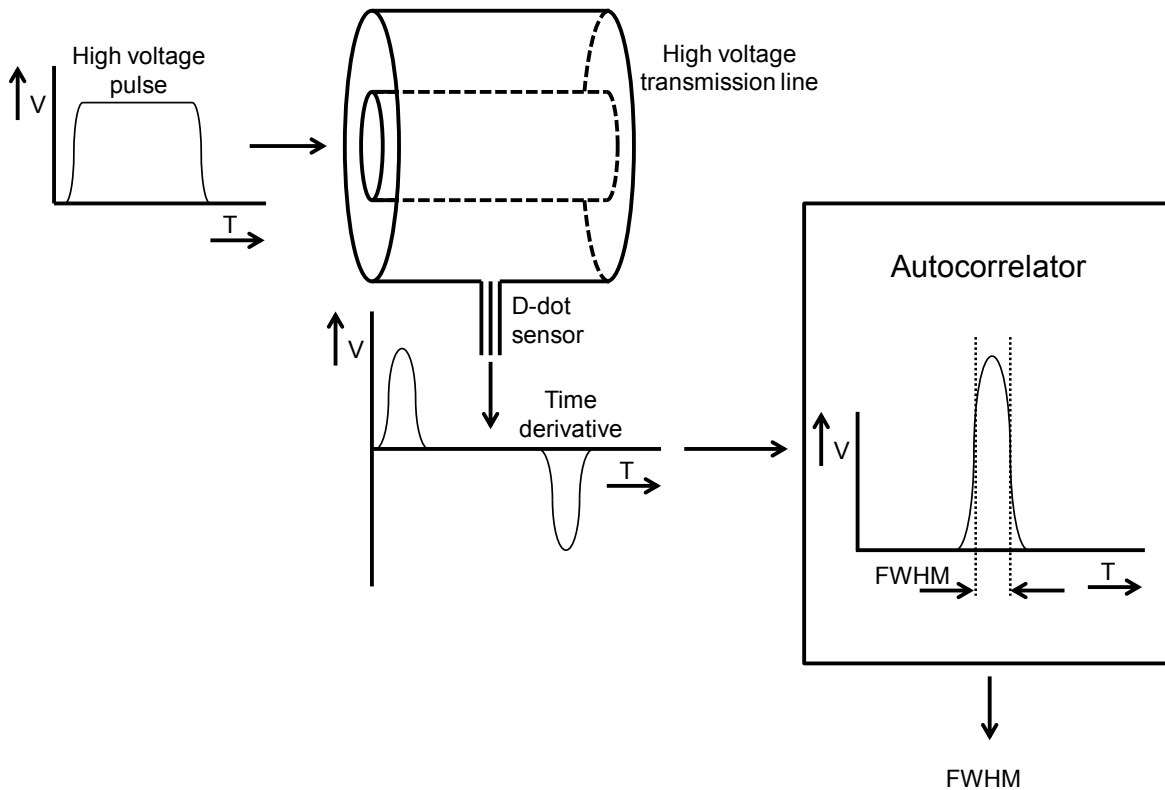


Figure 5-1. The D-dot sensor measures the time derivative of the high voltage pulse. This time derivative is a measure for the rise time of the high voltage pulse. By connecting the autocorrelator to the output of the D-dot sensor the FWHM of the time derivative signals, and thus of the rise time of the high voltage pulse, can be measured

Here we describe the basic idea behind the autocorrelator and discuss simulations followed by measurements. The measurements show that the output of the autocorrelator gives a good measure for the full width at half the maximum, FWHM, of the pulse under test.

To test the autocorrelator, well defined pulses with a FWHM of 40 ps are used. These pulses are generated with a SHF BPG 40A 40 BG/s bit pattern generator. This generator can make these pulses at a repetition rate of 2.5 GHz. Even though this repetition rate is much higher than in the actual application, the results prove the concept. Using well known charge amplification techniques, the autocorrelator can be modified to low rep rate applications relatively easily. These adaptations are discussed briefly later in this chapter.

## 5.2 Auto-correlation

### 5.2.1 Theoretical description

The autocorrelate of a signal is defined as the correlation of that signal with itself

$$R_{ff}(\tau) = \int_{-\infty}^{+\infty} f(t)\bar{f}(t-\tau)dt \quad 5-1$$

Here  $\bar{f}$  is the complex conjugate of the signal  $f$ . In our case, we calculate the autocorrelate of measured signals which contain no imaginary components, so the complex conjugate  $\bar{f} = f$ . Autocorrelation is used in signal processing to find repeating patterns that are hard to find due to poor signal to noise ratio's. We will use autocorrelation to determine the *FWHM* of a pulse. We will demonstrate the use of autocorrelation for a Gaussian pulse. We use a Gaussian pulse for two reasons. The first reason is that actual measured data can often be fit with good accuracy with a Gaussian pulse. The second reason is that the Gaussian pulse has the advantage that its autocorrelate is again a Gaussian pulse. This latter pulse has a *FWHM* that is a factor  $\sqrt{2}$  larger than the *FWHM* of the pulse under test which will be shown here. A Gaussian pulse can be defined by its *FWHM* and amplitude  $A$  by

$$f(t) = Ae^{-4\ln(2)\left(\frac{t}{FWHM}\right)^2} \quad 5-2$$

The autocorrelate of this signal is given by

$$R_{ff}(\tau) = \int_{-\infty}^{+\infty} \left( Ae^{-4\ln(2)\left(\frac{t}{FWHM}\right)^2} Ae^{-4\ln(2)\left(\frac{t-\tau}{FWHM}\right)^2} \right) dt \quad 5-3$$

Rewriting eq. 5-3 and taking the components not dependent on time out of the integral results in:

$$R_{ff}(\tau) = A^2 e^{\frac{-4\ln(2)}{FWHM^2}\tau^2} \int_{-\infty}^{+\infty} e^{-\frac{8\ln(2)}{FWHM^2}t^2 - 2\frac{-4\ln(2)}{FWHM^2}tt} dt \quad 5-4$$

In order to write eq. 5-4 in a more convenient form, we apply the transformation

$$\int_{-\infty}^{+\infty} e^{-at^2} e^{-2bt} dt = \sqrt{\frac{\pi}{a}} e^{\frac{b^2}{a}} \quad 5-5$$

which brings us to the expression for the autocorrelate:



$$R_{ff}(\tau) = A^2 \sqrt{\frac{\pi FWHM^2}{8 \ln(2)}} e^{\frac{-4 \ln(2)}{(\sqrt{2} FWHM)^2} \tau^2}$$

5-6

As we can see, the correlation of a Gaussian pulse with itself is again a Gaussian pulse but now in  $\tau$  instead of in  $t$  and with a  $FWHM$  which is a factor  $\sqrt{2}$  larger than the  $FWHM$  of the pulse under test. Thus if the autocorrelation of a Gaussian pulse can be obtained, the  $FWHM$  of the pulse under test can be found.

### 5.2.2 Electric autocorrelator

In this section we describe the hardware implementation of the electric autocorrelator as schematically shown in Figure 5-2 and in Figure 5-3.

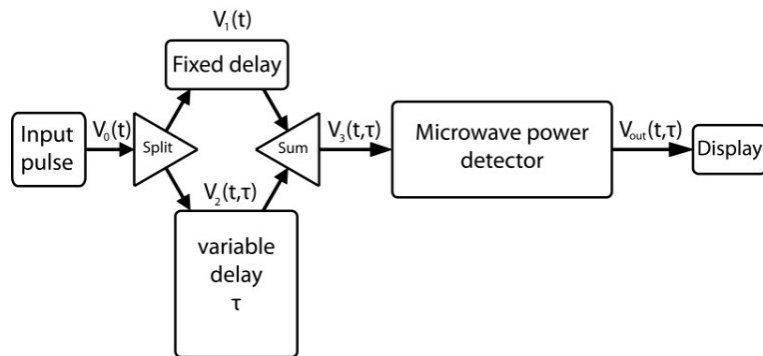


Figure 5-2. Schematic layout of the autocorrelator.

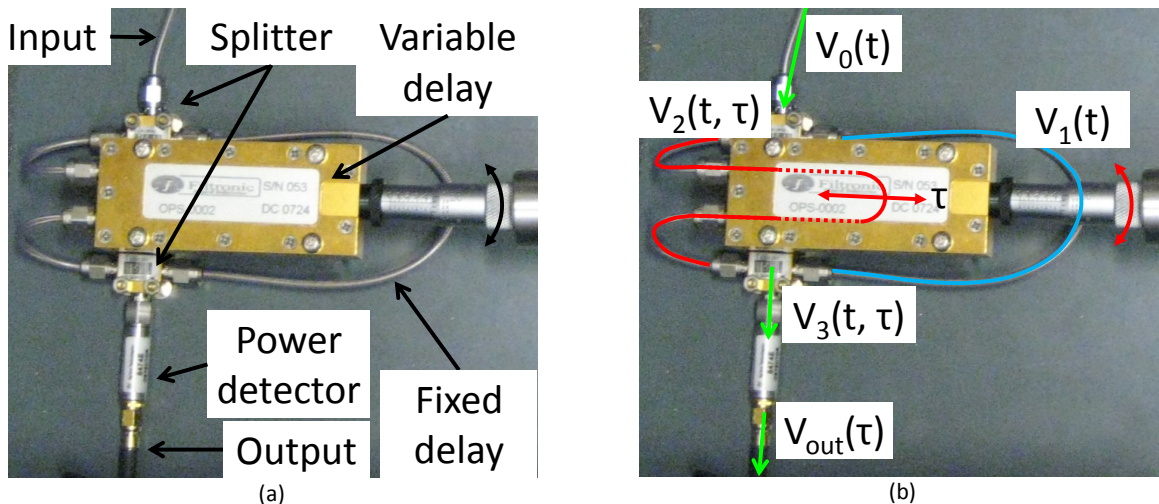


Figure 5-3. (a) In- and output of the autocorrelator and the components. (b) locations of the different signals.

The input pulse,  $V_0(t)$  is split with a resistive power divider in two equal pulses,  $V_1(t)$  and  $V_2(t, \tau)$ . The split causes 6 dB attenuation. The pulse  $V_2(t)$  is shifted in time by means of a variable time delay,  $\tau$ , and is recombined with pulse  $V_1(t)$  using a second power divider. This results in a signal  $V_3(t, \tau)$  which is equal to

$$V_3(t, \tau) = \frac{1}{4}(V_0(t) + V_0(t + \tau))$$

5-7

$V_3(t, \tau)$  goes into an Agilent 8474E microwave power detector of which a simplified schematic is shown in Figure 5-4.

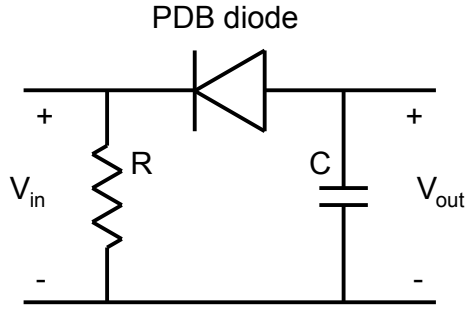


Figure 5-4. Simplified model of the microwave power detector.

The microwave power detector consists of a GaAs Planar Doped Barrier (PDB) diode in reverse. The output of this diode is connected to a 27 pF capacitor,  $C$ . The resistor  $R$  at the input is a 50  $\Omega$  matching resistor. The voltage over the diode,  $V_D$ , is the difference between the in- and output voltage,  $V_3(t, \tau) - V_C$ . The current through the diode,  $I_D$ , equals:

$$I_D = I_0 \left( e^{\frac{-qV_D}{nkT}} - 1 \right)$$

5-8

Here  $I_0$  is the reverse saturation current,  $q$  the electron charge,  $k$  the Boltzmann constant,  $T$  the temperature and  $n$  the dimensionless ideality factor. As we will see later, this equation for the diode current works well for this application.

The diode current,  $I_D$ , charges the capacitor  $C$ . The microwave power detector output voltage,  $V_{out}(\tau)$ , is the voltage over the capacitor,  $V_C$ . In our case, the output of the power detector is connected to such a large impedance that the current through the load can be neglected.  $V_{out}(\tau)$  is given by:

$$V_{out}(\tau) = V_C = \frac{1}{C} \int I_0 \left( e^{\frac{-qV_D}{nkT}} - 1 \right) dt$$

5-9

With  $C$  the value of the capacitor.  $V_C$  is generally small compared to the peak value of  $V_3(t, \tau)$  so that  $V_D \approx V_3$ . In the simulations we will omit this simplification and we will take  $V_C$  into account in determining  $V_D$ . Approximating the exponent in eq. 5-9 with its Taylor expansion to the 2<sup>nd</sup> order and replacing  $V_D$  with the expression in eq. 5-7 gives

$$V_{out}(\tau) = \frac{1}{C} \int I_0 \left( \frac{-q(V_0(t) + V_0(t + \tau))}{4nkT} + \frac{1}{2} \left( \frac{-q(V_0(t) + V_0(t + \tau))}{4nkT} \right)^2 \right) dt$$

5-10

Rewriting eq. 5-10 gives

$$V_{out}(\tau) = \frac{-qI_0}{4CnkT} \int (V_0(t) + V_0(t + \tau))dt + \frac{q^2I_0}{32C(nkT)^2} \int (V_0^2(t) + V_0^2(t + \tau)) dt + \frac{q^2I_0}{16C(nkT)^2} \int (V_0(t)V_0(t + \tau))dt \quad 5-11$$

Because  $\tau$  only changes the position of  $V_2$  with respect to  $V_1$  and not the signals themselves, the first two terms in eq. 5-11 give a constant offset. These two terms will together be referred to as  $K_0$ . The final term in eq. 5-11 represents the autocorrelate as given in eq. 5-1. The constant factor in front of the autocorrelate will be referred to as  $K_1$ . The final expression for  $V_{out}$  becomes

$$V_{out}(\tau) = K_0 + K_1 \int V_0(t)V_0(t + \tau)dt \quad 5-12$$

For the Gaussian pulse as defined in eq. 5-2 the output of the autocorrelator becomes;

$$V_{out}(\tau) = K_0 + K_1 \int A e^{-4\ln(2)\left(\frac{t}{FWHM}\right)^2} A e^{-4\ln(2)\left(\frac{t+\tau}{FWHM}\right)^2} dt \quad 5-13$$

Rewriting again, similarly as done in 5-3 through eq. 5-6 we find that the output of the autocorrelator is a Gaussian pulse with a dc offset given by  $K_0$  and the amplitude of the integral is scaled with  $K_1$ .

$$V_{out}(\tau) = K_0 + K_1 A^2 \sqrt{\frac{\pi FWHM^2}{8\ln(2)}} e^{\frac{-4\ln(2)}{(\sqrt{2}FWHM)^2} \tau^2} \quad 5-14$$

Here we see that the  $FWHM$  of the autocorrelate is a factor  $\sqrt{2}$  larger than the  $FWHM$  of the pulse under test. Important to notice is that the parameters of the diode in the power detector, do not influence the width of the Gaussian output pulse. This is of course under the assumption that the exponential diode equation is used where the second order Taylor expansion is accurate enough and that the input pulse is a Gaussian pulse.

### 5.2.3 Microwave power detector; GaAs Planar Doped Barrier Diode

Because the diode in the detector plays a crucial role in the autocorrelator we discuss its basics in short. The diode in the detector is a so called GaAs Planar Doped Barrier Diode. These diodes are very suitable for mixer and detector applications for very fast signals because they utilize majority carriers [54], the barrier height can be controlled very well by the production process and the  $p-n$  junction makes it very stable [55]. The structure of such a diode is shown in Figure 5-5 which is based on the work of R.J. Malik [56].

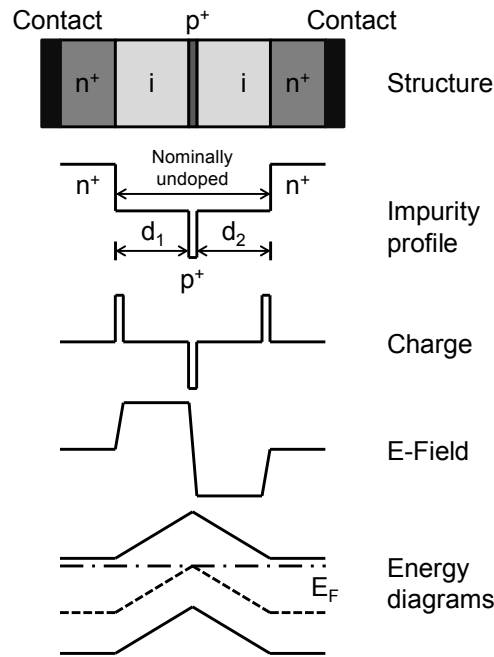


Figure 5-5. Structure, impurity profiles, charge, E-field and energy diagrams of a GaAs PDB diode. This figure is based on the work of R.J. Malik [56].

In [56], [57] the specific details of the GaAs PDB diode are discussed and explained in great detail. The treatment of the GaAs PDB diode is beyond the scope of this thesis. Important to notice is the fact that, even though the structure of a PDB diode is different from a standard diode, still the standard diode equation as given in [9] can be used. This is explained as follows. According to [56] the total diode current for a PDB diode can be expressed as

$$I = aA^*T^2 e^{-q\phi_{B0}/kT} (e^{q\alpha_2 V/kT} - e^{-q\alpha_1 V/kT}) \quad 5-15$$

Here  $T$  is the temperature in Kelvin,  $k$  the Boltzmann constant,  $q$  the elementary charge,  $A^*$  the effective Richardson constant for electrons,  $a$  the area of the GaAs PDB diode.  $\phi_{B0}$ ,  $\alpha_1$  and  $\alpha_2$  are defined as

$$\phi_{B0} = \frac{(d_1 d_2) Q_p}{(d_1 + d_2) \epsilon_s} \quad 5-16$$

$$\alpha_1 = \frac{d_1}{d_1 + d_2}, \alpha_2 = \frac{d_2}{d_1 + d_2} \quad 5-17$$

The length of the intrinsic areas,  $d_1$  and  $d_2$ , can be chosen arbitrarily. For a PDB diode  $d_1$  can be made very small, such that  $-q\alpha_1 V/kT$  goes to zero, causing the last exponential term in eq. 5-15 to go to 1 and we again obtain the standard diode equation as defined in eq. 5-8 with  $I_0$  given by  $aA^*T^2 e^{-q\phi_{B0}/kT}$ .

### 5.2.4 Characterization of the microwave power detector

To find the characteristics of the diode, the DC V-I characteristic has been measured by applying a DC voltage at the input and measuring the output current. This measurement allows for determining the characteristics of the diode with minimal influence of the capacitor C at the output of the detector. The scattering parameters of the detector have also been measured. But because the detector is a nonlinear device, due to the presence of the diode, the scattering parameters only provide information on the input impedance which is 50 Ω over the entire frequency range from 0 to 40 GHz.

To assess the influence of the frequency and power of the input signal on the output of the power detector, the detector has also been subjected to RF input signals with different frequencies and power levels.

The DC measurement is shown in Figure 5-6 (a). In Figure 5-6 (b) it is shown together with a fit using eq. 5-8 and a fit using the second order Taylor expansion. The parameters used for both the diode model fit and the second order Taylor expansion fit are shown in Table 5-1.

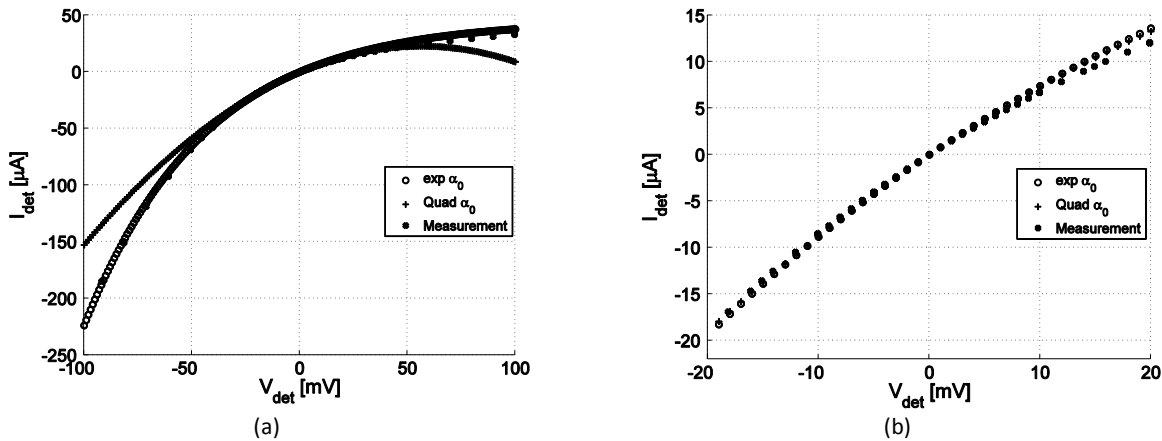


Figure 5-6. DC V-I characteristic of the Agilent 8474E Microwave Power Detector.

Table 5-1. Microwave power detector PDB diode DC V-I parameters.

$I_0$	$-45.4 \mu\text{A} \pm 2 \mu\text{A}$
$\frac{q}{nkT}$	$17.8 \text{ V}^{-1} \pm 0.2 \text{ V}^{-1}$

The behavior of the microwave power detector and the quadratic model agree very well for input pulses with a maximum absolute amplitude of 20 mV. Looking at Figure 5-2 and eq.5-7 this means that the maximum amplitude of the autocorrelator input voltage,  $V_0(t)$ , must be below 40 mV. This can be explained as follows; according to eq. 5-7 the amplitude of  $V_3(t, \tau)$  is  $\frac{1}{4}$  of the autocorrelator input voltage amplitude  $V_0(t)$ . But when the variable time delay  $\tau$  is zero,  $V_1(t)$  and  $V_2(t, \tau)$  overlap exactly and the amplitude of  $V_3(t, \tau)$  will be half the amplitude of the autocorrelator input amplitude. So the maximum amplitude of  $V_0(t)$  must be below 40 mV for the microwave power detector to behave quadratically. Figure 5-7 shows the relative pulse amplitudes for  $V_0(t)$ ,  $V_1(t)$ ,  $V_2(t, \tau)$  and  $V_3(t, \tau)$ . Also the output of the autocorrelator is shown for a complete scan of  $\tau$  over the full width of the input pulse  $V_0(t)$ . The amplitude of the output of the autocorrelator is not to scale in Figure 5-7.

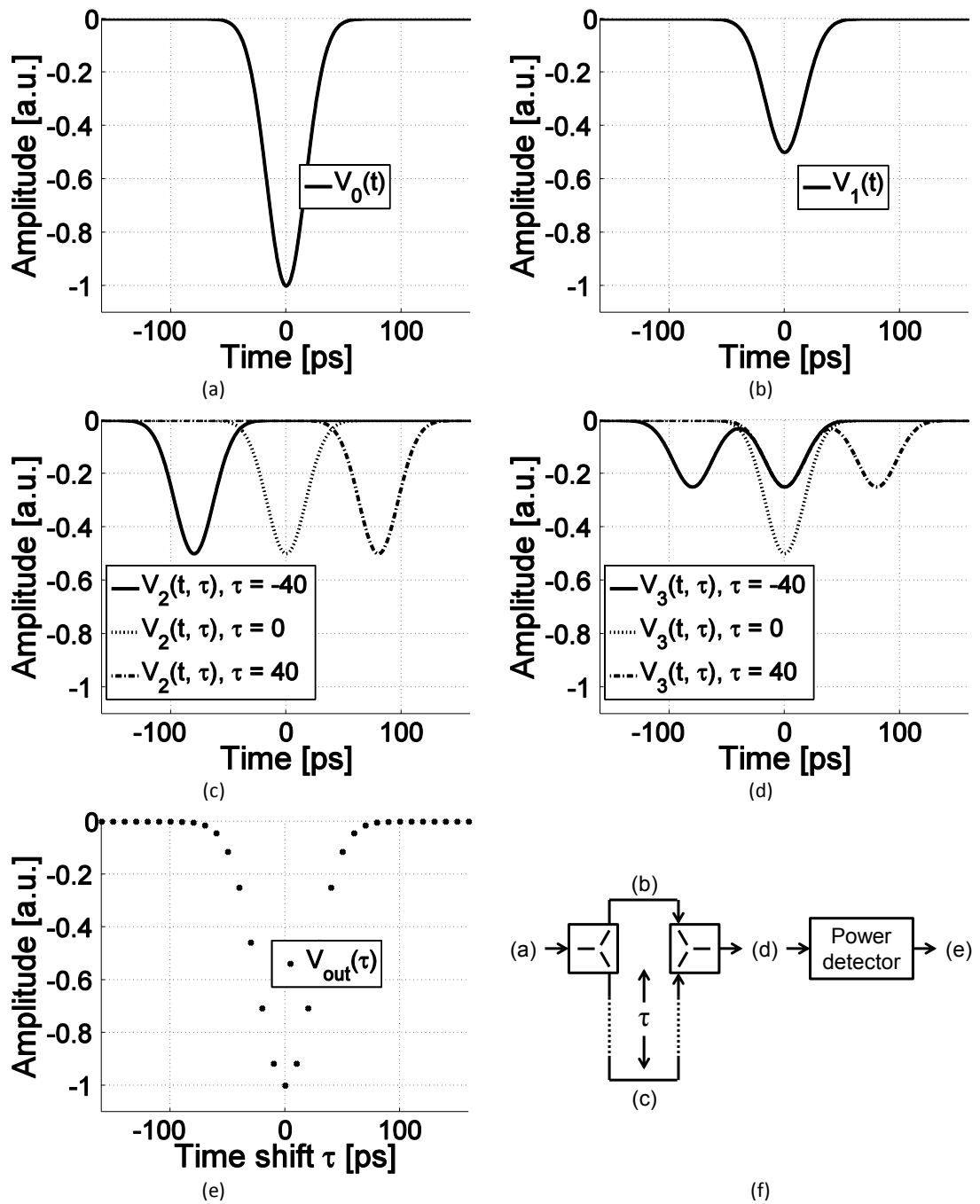


Figure 5-7. Signals and their relative amplitudes throughout the autocorrelator.

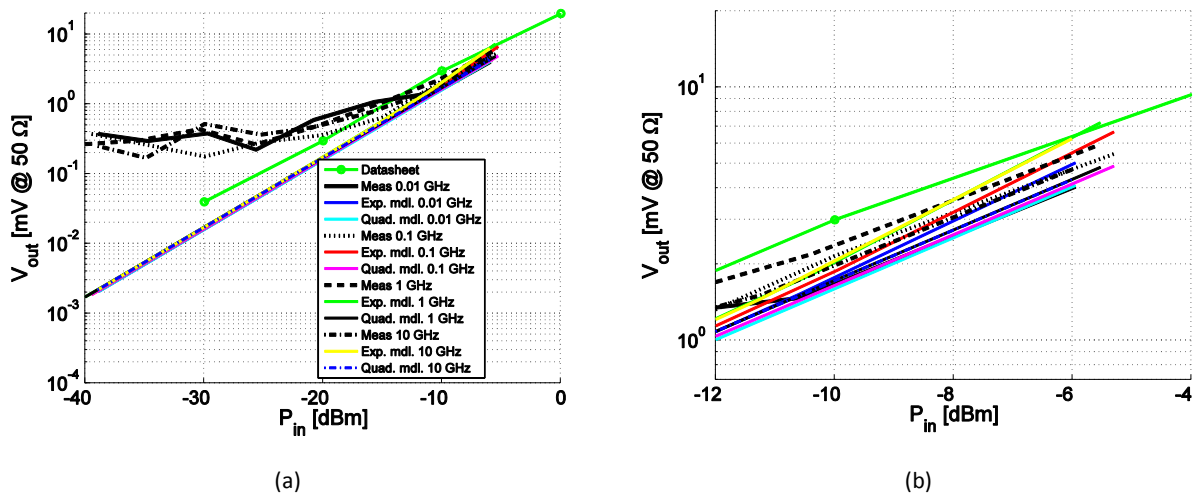


Figure 5-8. (a) Power detector mean output voltage on a 50  $\Omega$  load as a function of RF input power at different frequencies. (b) zoomed view of largest input power range.

The influence of power and frequency of the input signal is assessed by using different RF signals with frequencies ranging from 10 MHz to 10 GHz and power levels ranging from -40 dBm to -5 dBm. The results are shown in Figure 5-8.

The green line in Figure 5-8a is copied from the Agilent datasheet [58]. This line is based on a 30  $\Omega$  load impedance. The measurements, the black lines, are in good agreement with the data from the datasheet. For input powers below -20 dBm the output voltage disappears in the noise hence the detector output voltage levels 300  $\mu$ V. This is not entirely unexpected since the output voltage of the power detector was recorded with an oscilloscope. For input powers between -5 and -20 dBm the measured detector output voltage and data from the datasheet have the same slope indicating that the detector indeed behaves quadratically.

Against expectations based on the datasheet, the measured detector output voltage, with a 50  $\Omega$  load, is lower than the output voltage on a 30  $\Omega$  load as shown in Figure 5-8b. Because only one detector is measured, the cause of this discrepancy cannot be explained.

The response of both the exponential detector DC model, eq. 5-9, and the quadratic model, eq. 5-11, are also shown in Figure 5-8a. Both models fit with the measured output at the higher input powers from -10 to -5 dBm and show good quadratic behavior over the full range of input power.

At the lower power levels, below -10 dBm, the model and the measurement start to deviate from each other. -10 dBm, which is equivalent to a sine wave with a 100 mV amplitude on a 50  $\Omega$  load, is much larger than the amplitude range for which the detector behaves quadratically. This means that the measured and simulated power detector will show the same behavior, same slope in Figure 5-8, but at different amplitudes. The model is expected to be sufficient to give a good indication of trends but not at the correct amplitudes. As stated earlier, the determination of the FWHM of a Gaussian pulse does not depend on the amplitude. Hence the model is expected to give a prediction of the FWHM of a measured pulse similar as the real detector.

### 5.3 Pulse measurement

In this section we discuss the results of pulse measurements and compare them with simulation results to verify the concept of the autocorrelator. To test the autocorrelator a SHF BPG 40 A, 40 GB/s pattern generator is used to generate pulses with a *FWHM* of approximately 40 ps at a repetition rate of 2.5 GHz. The pulse  $V_0(t)$  is measured with a 100 GHz sampling scope and is shown in Figure 5-9 (black). The signal is fitted with a Gaussian pulse. This is the red line shown in Figure 5-9.

Two experiments were done. In the first experiment, the pulse, as shown in Figure 5-9, is used directly as input signal for the autocorrelator. We will refer to this pulse as ‘pulse 1’. In the second experiment ‘pulse 1’ is attenuated with 6 dB resulting in half the amplitude. This attenuated pulse will be referred to as ‘pulse 2’. The parameters of the pulses, based on the Gaussian fit, are shown in Table 5-2.

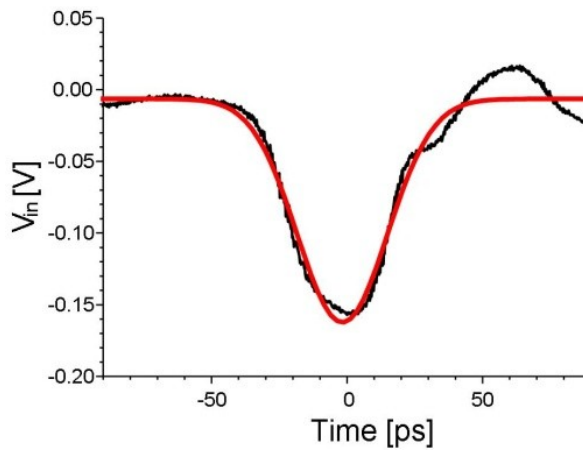


Figure 5-9. Test pulse 1 (black) and its Gaussian fit (red).

Table 5-2. Fitting parameters of the autocorrelator input pulses.

	Pulse 1	Pulse 2
Amplitude [mV]	$-155 \pm 5$	$-78 \pm 5$
FWHM [ps]	$39 \pm 2$	$39 \pm 2$
Offset [mV]	$-6 \pm 4$	$-3 \pm 4$

The summation of the time-shifted pulses,  $V_3(t, \tau)$ , directly in front of the power detector, is also measured with a 100 GHz sampling scope. These signals are shown in Figure 5-10 for different time delays. As can be seen, a full scan over the width of the input signal can be made. Here the time delay  $\tau$  is set to -80 ps, 0 and 80 ps respectively.



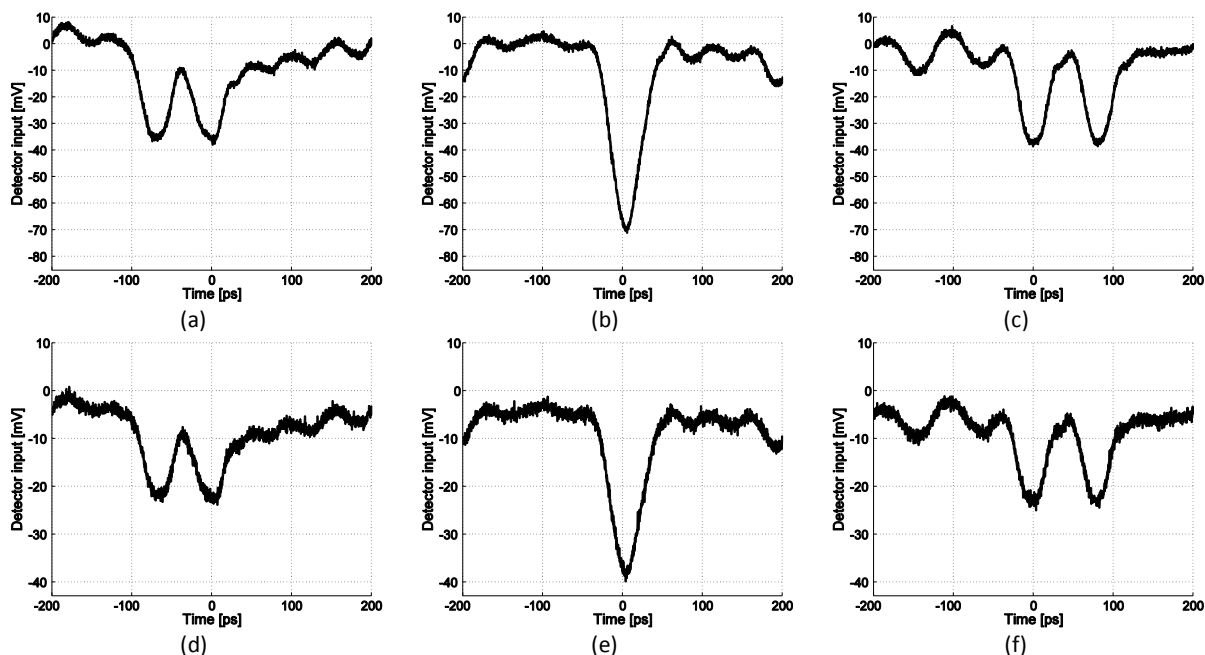


Figure 5-10. Detector input signal. ‘pulse 1’ is shown in the top row and ‘pulse 2’ is shown in the bottom row.  $\tau = -80$  ps (left column),  $\tau = 0$  ps (center),  $\tau = 80$  ps (right column).

The relatively high amplitude of ‘pulse1’ will cause the detector to operate outside its quadratic range. The error will be largest when  $\tau$  is zero because this causes the largest input amplitude at the input of the detector, Figure 5-10b and e. At an input voltage of -80 mV, the error between the measured V-I diode characteristic and its quadratic model is around 20 %, Figure 5-6. The exponential model on the other hand still follows the measured diode characteristic with a very small, nearly neglectable, error.

The amplitude of ‘pulse2’ is on the edge of where both the quadratic and the exponential model yield good agreement with the measurement.

Figure 5-11a and d shows the measured autocorrelator output in black for ‘pulse 1’ in the left column and for ‘pulse 2’ in the right column. The output of the exponential and the quadratic model, using the ideal Gaussian input, are shown in blue and red. Due to the difference in amplitude and offset between the models and the measurement, a comparison is not easily made from these figures. As can be seen in eq. 5-14, the relation between the FWHM of the pulse under test and the output pulse is independent of the amplitude of the output signal. Hence the offset of both the measured and the simulated output signals can be removed, Figure 5-11c and d, and the amplitudes can be normalized, Figure 5-11e and f. Now the agreement between the measurement and the simulation is apparent. The results of both the models and the measurement are shown in Table 5-3. Based on Table 5-2, the FWHM of the output pulse is expected to be  $(39 \pm 2) \cdot \sqrt{2} = (55.2 \pm 3)$  ps. For ‘pulse 1’ the measurement gives, as expected, a too low FWHM. For ‘pulse 2’ it gives a FWHM that is very close to the expected FWHM. The exponential model shows the same deviation from the expected FWHM for ‘pulse 1’, albeit less severe. For ‘pulse 2’ the exponential model gives a FWHM value well within the uncertainty boundaries. The quadratic model gives a FWHM of 54 ps for both input pulses as expected

since it is the ideal model. The percentages shown in Table 5-3 behind the FWHM values represent the deviation from the expected FWHM. The FWHM of 'pulse 1' has a measured error of 22.1% but 'pulse 2' only has an error of 5.8%. This difference in the errors supports the idea that the amplitude of the input signals must be kept small, below 20 mV, to obtain a reliable measurement of the FWHM.

Table 5-3. Fitting parameters of the autocorrelator output pulses.

			Output signal using 'pulse 1'	Output signal using 'pulse 2'
Amplitude	[mV]	Measured	$-3.9 \pm 0.2$	$-0.75 \pm 0.03$
		Exp. Model	-2.71	-0.57
		Quad. Model	-1.76	-0.45
Offset	[mV]	Measured	$-2.5 \pm 0.5$	$-0.5 \pm 0.5$
		Exp. Model	-11.6	-5.5
		Quad. Model	-11.4	-5.4
FWHM	[ps]	Measured	$43 \pm 1$ (22.1%)*	$52 \pm 1$ (5.8%)*
		Exp. Model	50 (9.4%)*	54 (2.2%)*
		Quad. Model	54 (2.2%)*	54 (2.2%)*

\* % deviation from expected value of  $55.2 \pm 3$  ps.

To get a better insight in the quality of the model, the measured detector input signal, Figure 5-10, is used as input signal for both power detector models. The results are shown in Figure 5-12 in a similar fashion as Figure 5-11. As can be seen, the model reproduces the behaviour as observed in the measurement with good accuracy. Still the amplitudes of the output signals from the models do not agree with the measured amplitudes.

The discrepancy between the absolute value of the offset and the amplitude between the models and the measurement can be explained with the calibration measurement shown in Figure 5-8. For high frequencies, the absolute output voltage of the modelled power detector is larger than that of the measured power detector at high frequencies. Currently there is no possibility to correct for this because the model is based on the measured detector DC V-I characteristic. This model does not include the diode's frequency dependence.

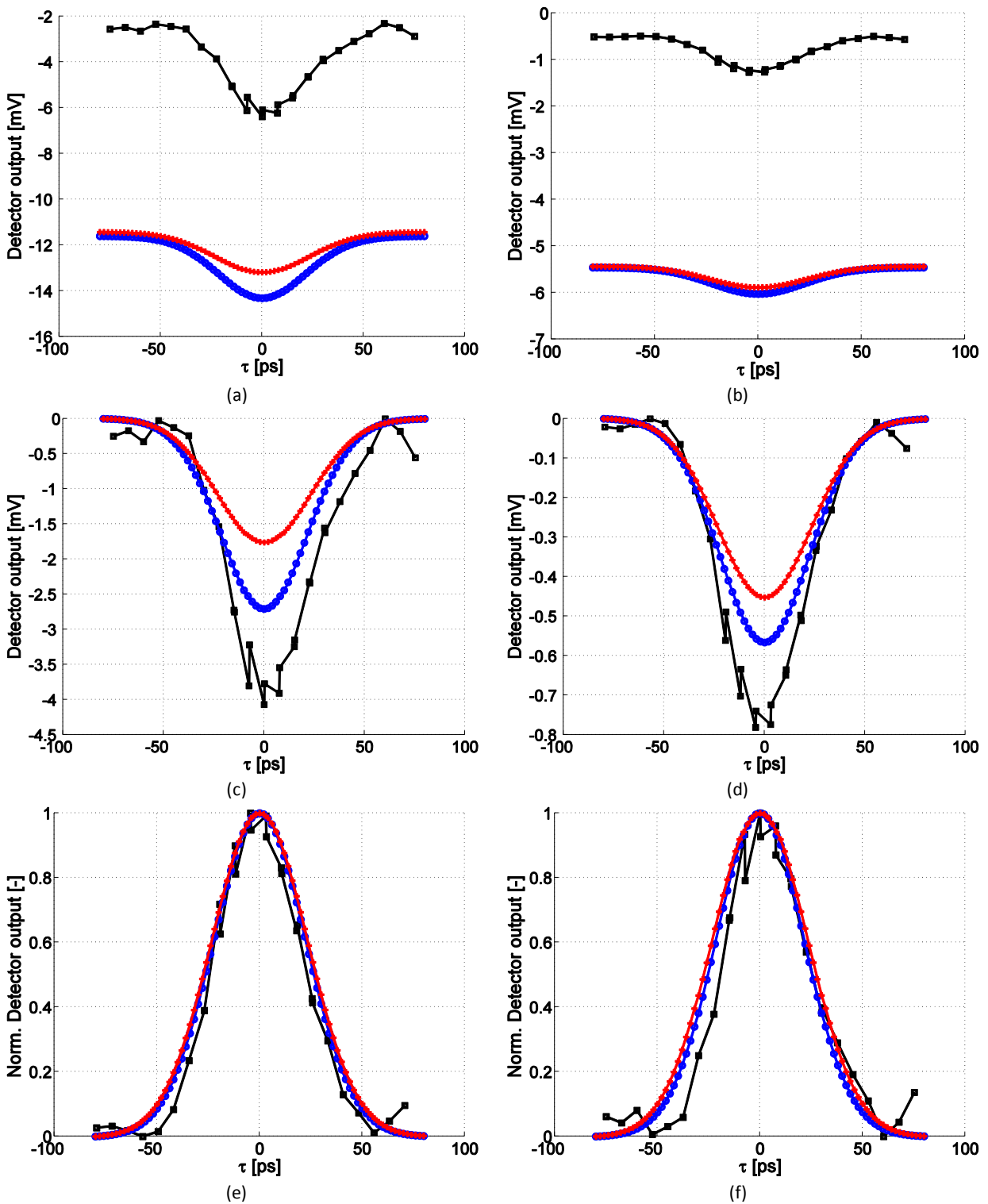


Figure 5-11. Measured (black), exponential model (blue) and quadratic model (red) output of the autocorrelator. For the models the ideal Gaussian input pulse is used based on the parameters in Table 5-2. The results for 'pulse 1' are shown in the left column and the results for 'pulse 2' are in the right column.

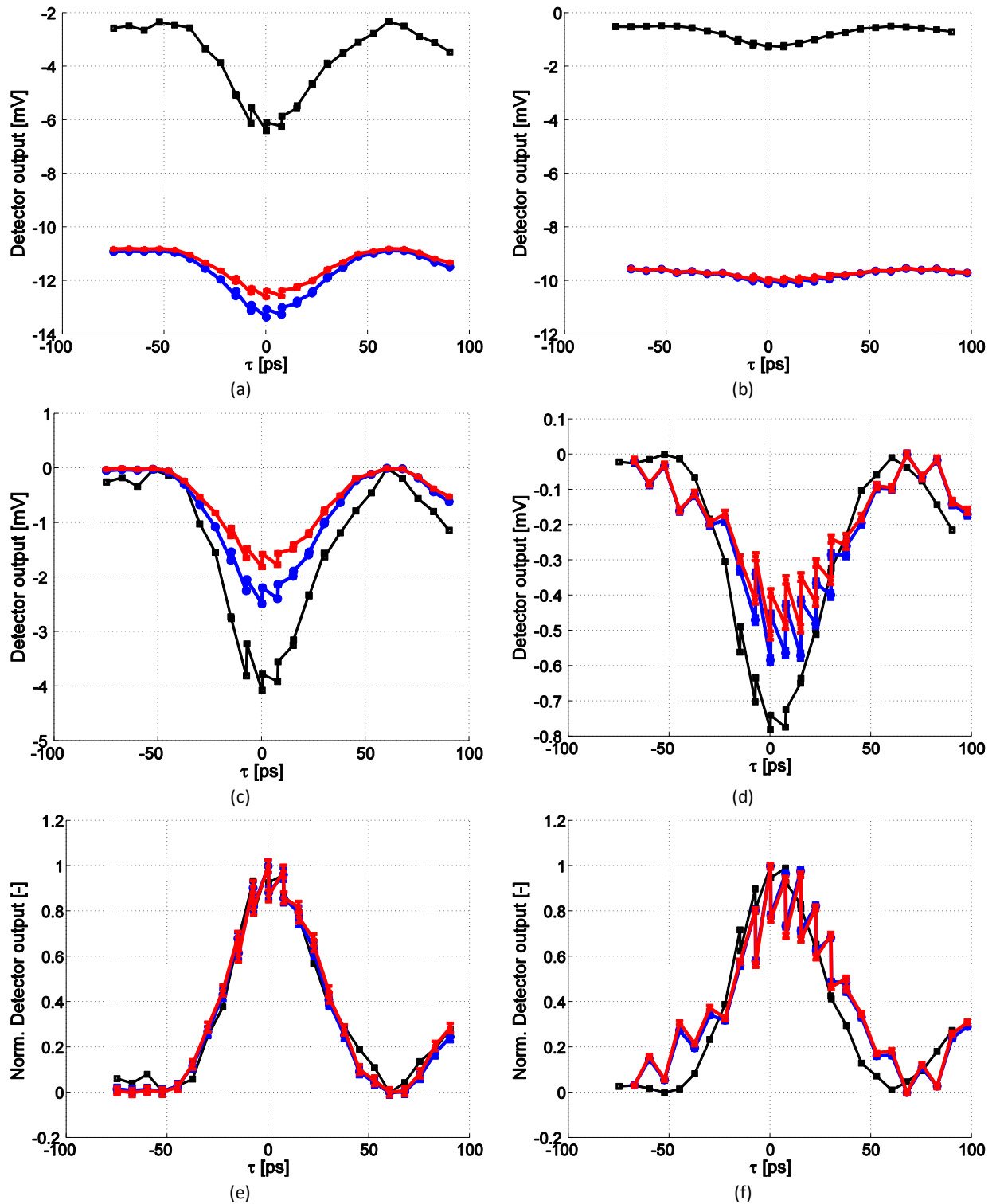


Figure 5-12. Measured (black), exponential model (blue) and quadratic model (red) output of the autocorrelator. As input for the models the measured detector input is used. The results for 'pulse 1' are shown in the left column and the results for 'pulse 2' are in the right column.

## 5.4 Practical implementation in a high voltage pulse source

The measurements described above are done at a repetition rate of 2.5 GHz. As both the simulations and the measurements have shown, the charge in the capacitor  $C$  in the power detector reaches an equilibrium point. The charge that enters the capacitor through the diode while it is conducting equals the charge that leaks out of the capacitor through the same diode while it is not conducting since the diode is not perfect.

Pulsed high voltage systems rarely, if at all, achieve such high repetition rates. Many of these sources work at single shot repetition rates up to several kHz. To still be able to use the autocorrelator in such an environment, an additional piece of hardware is needed after the autocorrelator.

Because the repetition rates of high voltage pulse sources is much lower than we used here, the capacitor  $C$  in the power detector most likely fully discharges through the leaking current of the PDB diode between two shots. The same simulations used above are used to simulate the autocorrelator output signal when it receives only one single Gaussian pulse at its input with an amplitude of -40 mV. Using a single Gaussian pulse with a *FWHM* of 40 ps and an amplitude of -40 mV at the input of the autocorrelator we obtain the pulses, as shown in Figure 5-13, at the input of the power detector for a time delay  $\tau$  of 0 ps, 40ps, 80 ps and 120 ps respectively. Using these 4 pulses on the exponential power detector model, we obtain at the output of the power detector the signals shown in Figure 5-14.

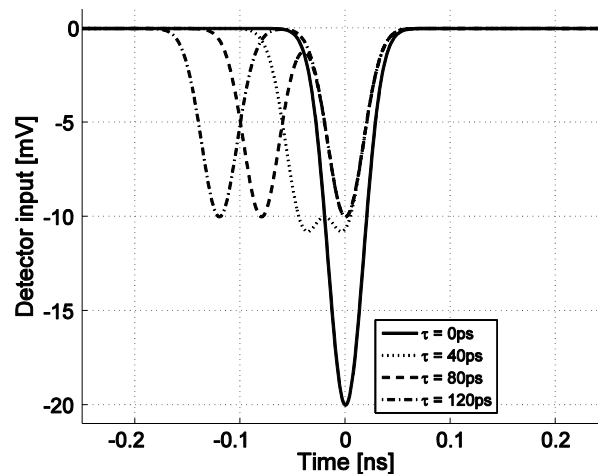


Figure 5-13. The power detector input signal when using a single shot pulse at the input of the autocorrelator.

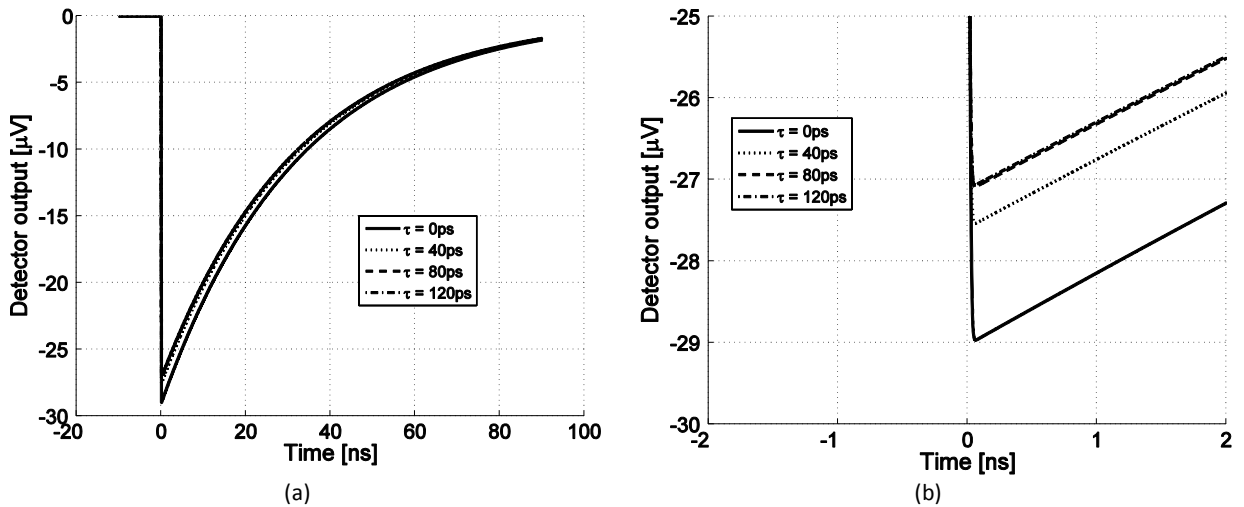


Figure 5-14. (a) Microwave power detector output for a single input pulse as shown in Figure 5-13. (b) Zoomed view of the different peak values of the microwave power detector output.

The difference in the peak amplitudes of the autocorrelator output ranges in the single  $\mu\text{V}$ . Such small signals can still be detected but this is not a trivial design task.

A typical circuit that could be used to measure these signals is a charge amplifier, [14]. Figure 5-15 shows the integration of a basic charge amplifier with the power detector.

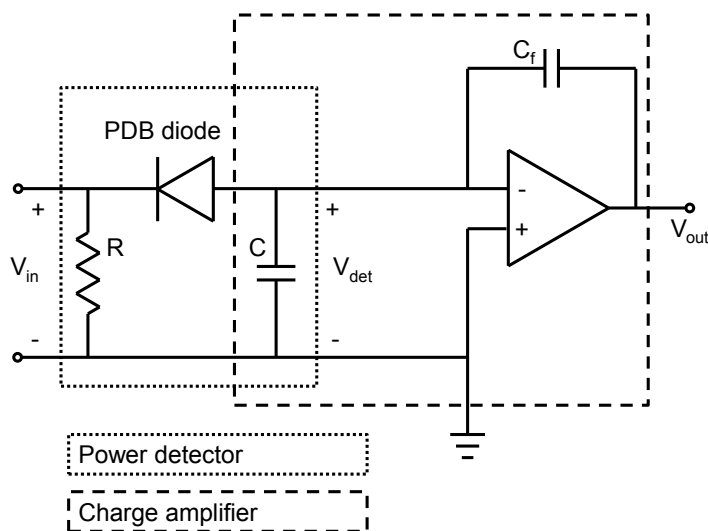


Figure 5-15. Power detector combined with a charge amplifier.

The negative input of an operational amplifier is connected to the output of the microwave power detector. And the output of the operational amplifier is fed back to its negative input with a capacitor  $C_f$ . As soon as the voltage on  $C$  changes, a voltage difference occurs between the two input pins of the operational amplifier, opamp. This causes the output of the opamp to generate a voltage with opposite sign. This voltage charges  $C_f$  which then removes the charge on  $C$  and pulls the negative input of the opamp back to ground potential.

$V_{out}$  is given by

$$V_{out} \approx -\frac{Q}{C_f} \quad 5-18$$

With  $C_f$  the capacitor in the charge amplifier feedback loop and  $Q$  the charge collected on the power detector output capacitance  $C$ . Simulations give a charge in the microwave power detector output in the order of  $0.85 \pm 0.03$  pC, depending on the time delay  $\tau$ . Using a  $C_f$  of 1 pF should result in an output voltage around 800 mV and will allow for enough accuracy to detect the changes in the output pulse due to changes in  $\tau$ . The gain  $A$  of the opamp must adhere to

$$A \gg \frac{C + C_f}{C_f} \quad 5-19$$

To be able to measure, the capacitor  $C_f$  must be discharged in between shots. This can be done in different ways but it has been omitted here since it does not influence the basic functioning of the charge amplifier.

Using the autocorrelator in conjunction with a charge amplifier, data-points of the autocorrelate can be determined with only a single measurement using standard available techniques. This enables the application of the autocorrelator in experiments with low repetition rates which are very common when working with high voltage.

## 5.5 Conclusions

A method based on autocorrelation has been proposed to measure the FWHM of electric pulses in the order of 10 to 100 ps. Based on the assumptions that the shape of the pulse is known, theoretical calculations show that autocorrelation is a promising and accurate technique to determine the FWHM of the pulses. A device, the autocorrelator, was simulated and built to measure the FWHM pulse length in the range of 10 to 100 ps of electric pulses.

Measurements have proven that the determination of a 40 ps FWHM Gaussian pulse, with a 2.5 GHz repetition rate, can be determined with an error as small as 6%. Both measurements and models also give reason to believe that smaller errors can be obtained if the amplitude of the input signal is smaller. This is due to the fact that the detector has to be operated in its quadratic range.

The behavior of the autocorrelator is described accurately using only the simple detector model based on the DC V-I characteristic of its internal PDB diode. Also an even further simplified quadratic model describes the behavior of the autocorrelator with adequate accuracy for autocorrelator input voltages ranging between -40 and 40 mV. The autocorrelator shows to be a promising pulse width measurement technique.

Although the autocorrelator can be used to determine the FWHM length of the input pulse and both the exponential and quadratic model show good agreement, the measured amplitudes and offset could not be reproduced with either of the models. As found in Figure 5-8, there is a frequency dependence in the power detector which is not accurately represented by the models. This is expected to be the cause of the difference in the amplitudes. The model does not take the frequency dependence of the PDB diode into account. To improve the model, the PDB diode frequency dependence should also be taken into account.

For single shot or low repetition rate measurements the autocorrelator can be modified with a charge amplifier. We have described the basics of such a modification and expect that the FWHM of a 40 picosecond pulse can be measured.





## 6 Application of developed technologies

---

The studies discussed in this thesis have given insight in the different aspects of a high voltage nanosecond pulser. As the title of the thesis suggests, the goal is to match the different basic components, shown in Figure 1-4 in the introduction, to come to an efficient pulse source. Here we discuss two different conceptual models to illustrate possible applications for the findings of this thesis.

In section 6.1 a switch, using the surface discharge as discussed in chapter 2, is presented.

In section 6.2 an existing DC accelerator, as used at the Eindhoven University of Technology, is used as a starting point for a pulsed accelerator. The pulsed accelerator model is designed such that it can replace the existing DC accelerator.

### 6.1 Surface discharge and plasma research

The surface discharge has been studied from an application point of view. The goal was to optimize its behavior for high voltage switching applications. Therefore the focus was on the voltage over and current through the plasma and the development of the plasma. Due to time limitations, a more thorough study of the plasma itself, its kinetics and dynamic behavior were left out of the scope of this thesis since this is a whole area of research on itself.

The surface discharge studied in chapter 2 is ignited by a pulsed source. Therefore the used setup is not yet a complete switch. Here we propose, based on the results of chapter 2, a triggered, coaxial surface discharge switch. A schematic, radially symmetric, representation is shown in Figure 6-1. Table 6-1 gives a description of the different components of the coaxial surface discharge switch.

Table 6-1. Description of the components in the coaxial surface discharge switch.

Nr	Description
1	Outer conductor of the output coaxial transmission line
2	Inner conductor of the output coaxial transmission line
3	Trigger electrode
4	Dielectric medium (gas) of the output coaxial transmission line
5	Dielectric surface for the surface discharge switch
6	Gas chamber for trigger spark
7	Inductive coupling between the ground electrode and trigger electrode
8	Schematic representation of the charging source.

The surface discharge switch is the dielectric interface between 4 and 5. The sharp point in the outer coaxial conductor, 1, at the left side of the dielectric interface is the source electrode of the switch and the rounded electrode edge, 2, is the load electrode of the surface discharge switch. The surface discharge switch is thus a cylindrical surface. This shape has the advantage that there are no edge effects.

With the voltage source, 8, the coaxial transmission line, consisting of items 1, 2 and 4, is charged until the desired field strength is achieved. During this process, the trigger electrode, 3, remains at ground potential due to the inductive connection, 7, with the grounded outer conductor, 1, of the coaxial transmission line.

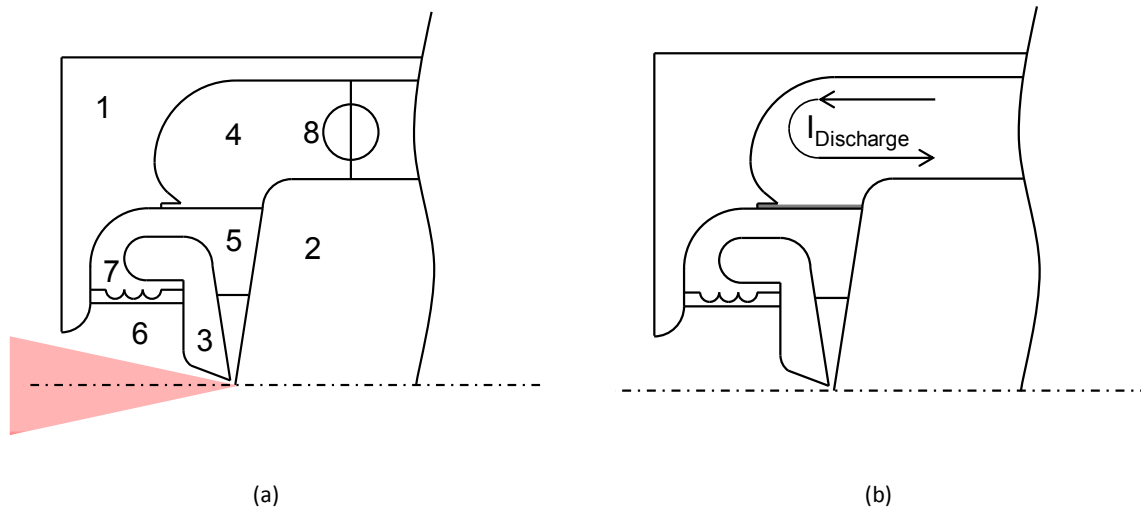


Figure 6-1 Cut through view of the triggered coaxial surface discharge switch concept. (a) Radial symmetric schematic representation. 1; ground, 2; HV electrode, 3; trigger, 4; dielectric gap of the transmission line, 5; Dielectric surface for the surface discharge, 6; entrance port for trigger signal, 7; inductor, 8; charging source. The red cone represents a triggering laser pulse. (b) After switch closure, the surface discharge forms a nearly ideal short circuited end of the transmission line. The current to build the discharge comes from this transmission line.

The center conductor, 2, is charged by voltage source 8. During the charging process, which happens at much lower frequencies than discharging, the electric field builds up. The trigger electrode, suspended in the dielectric material, 5, has a capacitive coupling with the center conductor causing its voltage to increase as well. To prevent this, it is inductively coupled to ground, 1. In the source electrode of the switch, both a sharp edge and a small gap are applied to enhance the electric field. Because the trigger electrode remains at ground potential, the sharp electrode of the surface discharge switch is shielded from the electric field. This is shown in Figure 6-2 (a). Once the spark gap closes, the potential of the trigger electrode rises resulting in a strong electric field in between the sharp electrode and the trigger, Figure 6-2 (b). This causes a strong electric field at the edge of the sharp electrode allowing for the ignition of the surface discharge. Simulations show, Figure 6-3, that the electric field strength increases roughly 10 times and becomes almost twice as large as the electric field strength in the transmission line section. This indicates that a field strength can be obtained strong enough to ignite the discharge. Once the surface discharge has reached the load electrode, it forms a nearly perfect closed end at this end of the coaxial transmission line as shown in Figure 6-1 (b). Also here, skin effect works in favor of the switch; due to the high frequencies, the current will have a very small penetration depth into the plasma.

Here we assumed the possibility of laser triggering but as can be seen, the structure allows for other triggering techniques as well. Because the spark gap chamber is separated from the gas compartment of the surface discharge, different gas compositions can be used allowing for optimization of gas conditions for both the surface discharge and spark discharge.

These simulations are valid up to the point where a surface discharge would be ignited. At that point, the structure changes due to the plasma. The rise time of the electric field at the sharp edge is in the order of 0.5 nanoseconds.

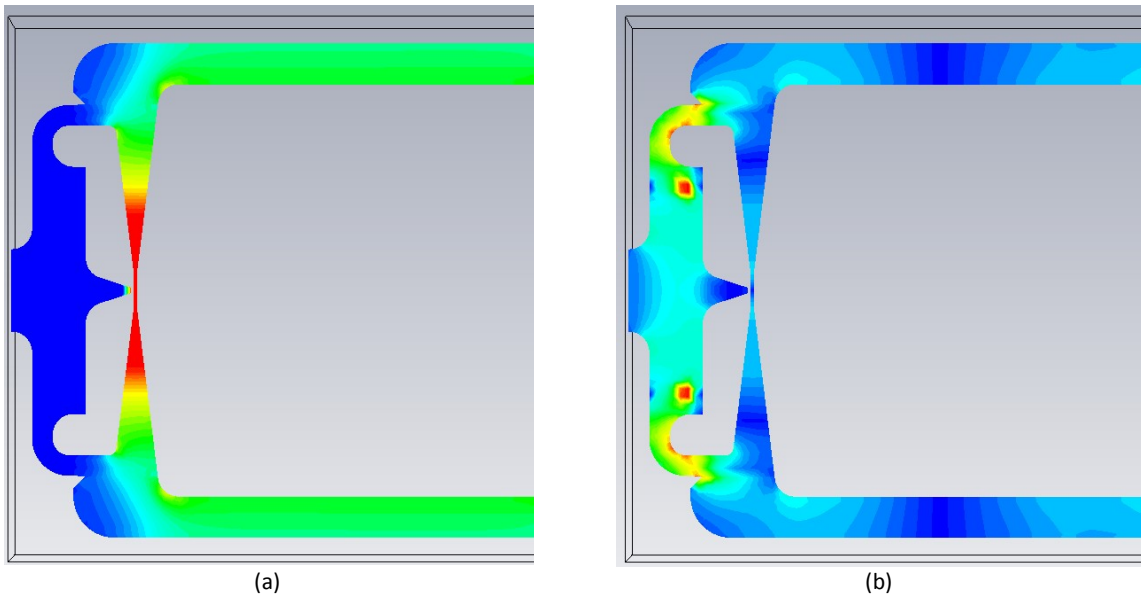


Figure 6-2. Electric field before and after ignition of the spark gap. Left; before ignition, the sharp edge of the trigger electrode is shielded and has relatively low local electric field strength. Right; after ignition the electric field strength at the sharp edge has increased 10 times enabling the ignition of a surface discharge. The red spots to the left of the trigger electrode are simulation anomalies due to the placement of a lumped LR component.

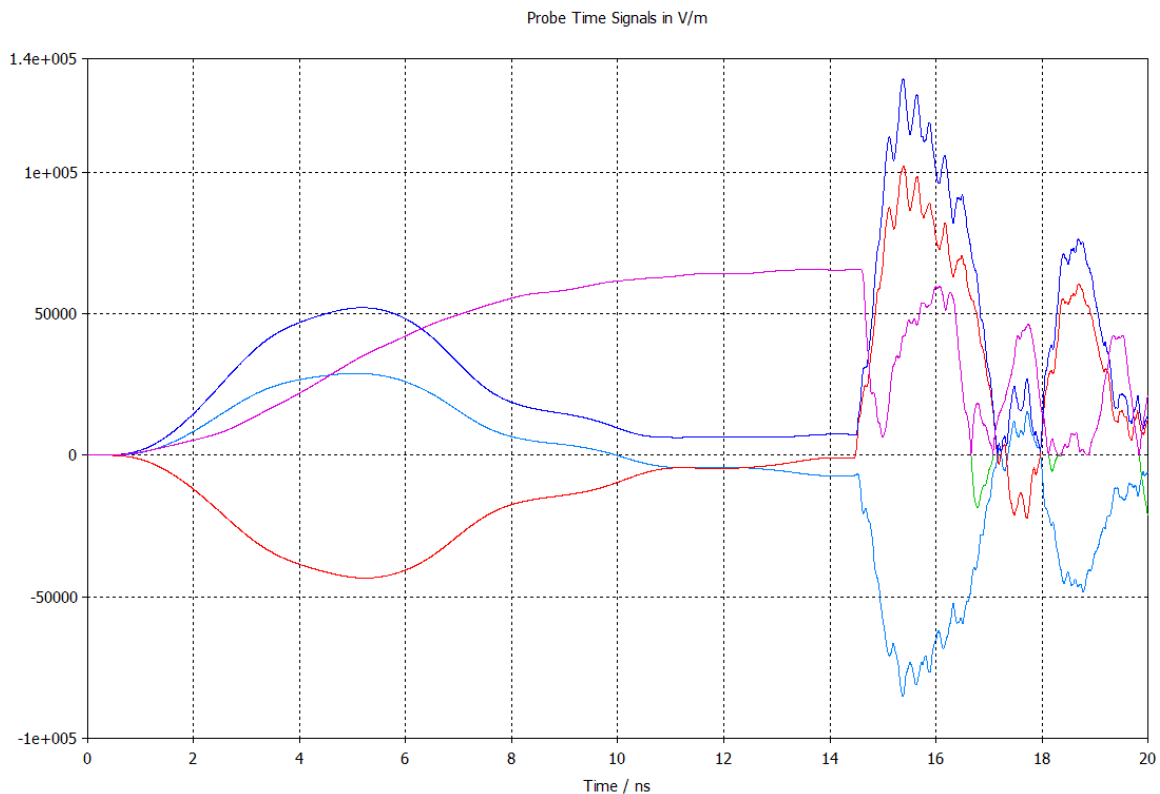


Figure 6-3. Electric field strengths in the triggered surface discharge switch. Blue; absolute field strength at sharp electrode tip, magenta; e-field in transmission line section, light blue; forward E-field at sharp tip, red; radial E-field at sharp tip.

## 6.2 Accelerator structure

At Eindhoven University of Technology a Magneto Optical Trap, MOT, is used to make an ultra cold ion source [7]. The same source can also be used to make electron bunches [6]. The source uses a DC 30 kV accelerator to generate the acceleration field. This source is shown in Figure 6-4. We will not go into the details of a MOT, for this device is described in detail in both references.

The MOT collects neutral particles at the acceleration point indicated in Figure 6-4. Once enough particles are collected, they are ionized in two steps with lasers, and the electrons and ions are both accelerated by the DC electric field. Depending on the potential of the DC accelerator either the electrons or the ions can be selected to exit the accelerator. The advantage of using a Dc accelerator in this case is its voltage stability. But the drawback is the relatively low limit of the maximum acceleration field that can be applied.

Figure 6-5 gives a more detailed view of the present accelerator structure of the MOT. This figure is taken from [6]. The entire structure is placed in vacuum. The 30 kV DC voltage enters the accelerator through a coaxial cable on the left side. On the right side, indicated with 'acceleration point', the acceleration field is formed.

The techniques studied in this thesis enable the development of a pulsed source as an alternative for the DC source to achieve higher acceleration field strengths. The pulsed source is based on the triaxial Blumlein accelerator [59] discussed in chapter 4.

The difference between the Kumamoto pulse source and this accelerator is the fact that here the load is an open end transmission line designed to make an acceleration field where as the Kumamoto Blumlein pulse source is designed to power a plasma reactor which has an inherent dynamic response due to the plasma. The accelerator application seems simpler from this point of view, but the demands for the electric field in terms of stability, jitter and repeatability are much more stringent.

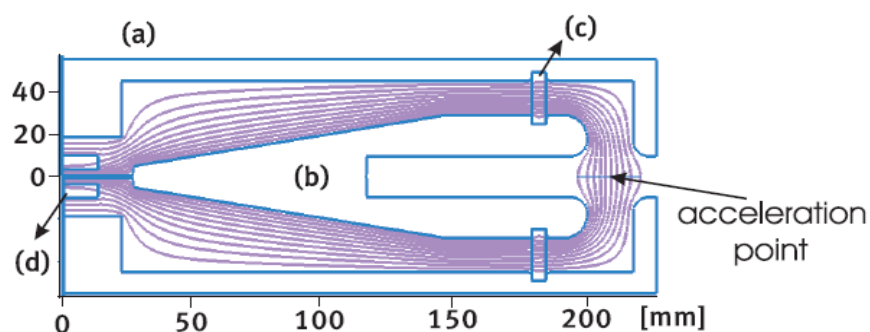


**Figure 3.2:** Equipotential field lines inside the accelerating structure calculated with SUPERFISH. (a) outer conductor; (b) inner conductor; (c) glass ring; (d) ceramic of the high voltage feedthrough.

Figure 6-4. Equipotential line plot of the 30 kV DC accelerator design currently used in the MOT of the Eindhoven University of Technology. Image from [6].

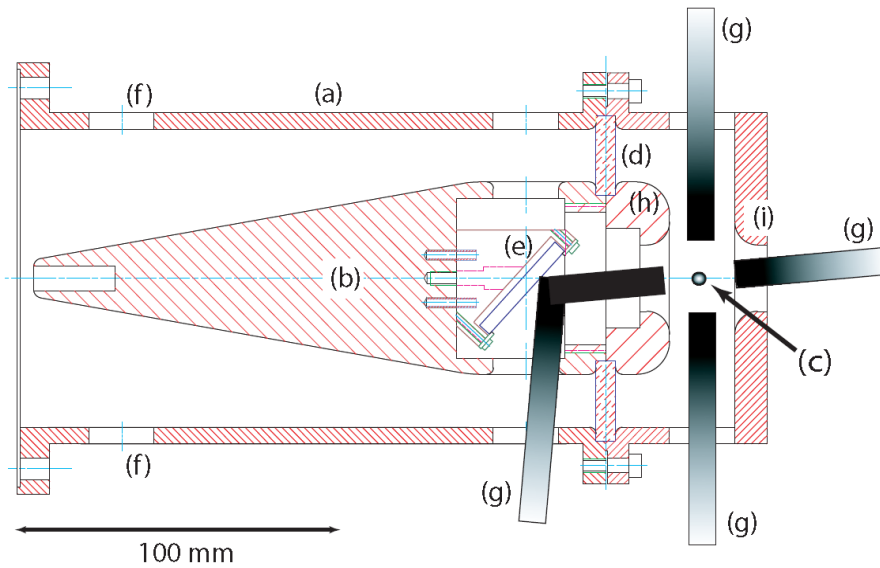


**Figure 3.1:** Technical drawing of the accelerator (cross-section): (a) outer conductor; (b) inner conductor; (c) acceleration point; (d) glass ring; (e) mirror; (f) pumping holes; (g) laser beams; (h) radius of curvature on the inner conductor  $R_i$ ; (i) radius of curvature at the acceleration point  $R_o$ .

Figure 6-5. Detailed schematic of the 30 kV DC accelerator design currently used in the MOT of the Eindhoven University of Technology. Image from [6].

Figure 6-6 shows the pulsed accelerator structure that we propose. The dimensions of the accelerator structure and the outer diameter are kept the same as in the original accelerator.

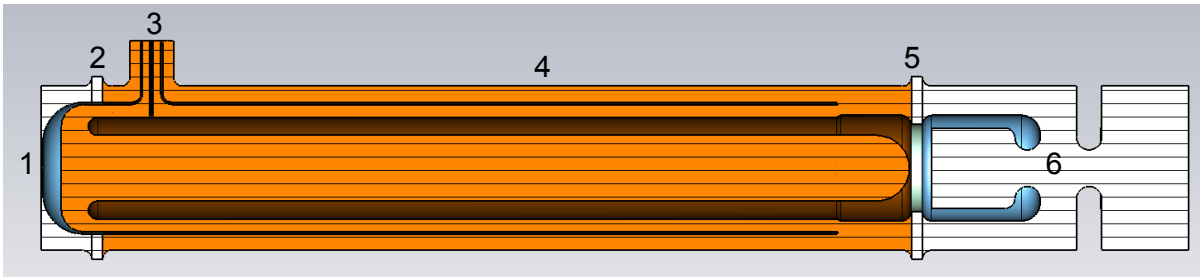


Figure 6-6. Simulated pulsed accelerator structure. 1; Spark gap, 2; quartz support ring, 3; High voltage charging feed and inductive grounding feed for the inner conductor, 4; triaxial Blumlein, 5; quartz support ring, 6; MOT accelerator area.

Because the inner most conductor now has a floating potential, it is connected inductively with ground through the feedthrough indicated in Figure 6-6 with 3. By choosing the inductance correctly, it will have low impedance during charging; allowing the innermost conductor to remain at ground potential. During discharge it will have a high impedance. Charging can be done using a DC source. The breakdown voltage of the spark gap can be regulated with the gas and pressure in the spark gap chamber. To achieve higher voltages, the charging can also be done with a ramping voltage as done with the Kumamoto pulser.

The simulated voltages at the output of the pulser and the accelerating field strength in the accelerator are shown in Figure 6-7 (c) and (d). The absolute values do not play a significant role here since the actual amplitude is determined by the breakdown voltage of the spark gap. What is important to notice is that the electric field in the accelerator has a rise time of well below 0.5

nanosecond. The duration of the pulse, in this case 5 ns, can be adjusted by changing the length of the triaxial Blumlein but also by changing the dielectric. In the simulation we used oil with an  $\epsilon_r$  of 2.33. By using vacuum, a pulse duration of 3 ns could be achieved.

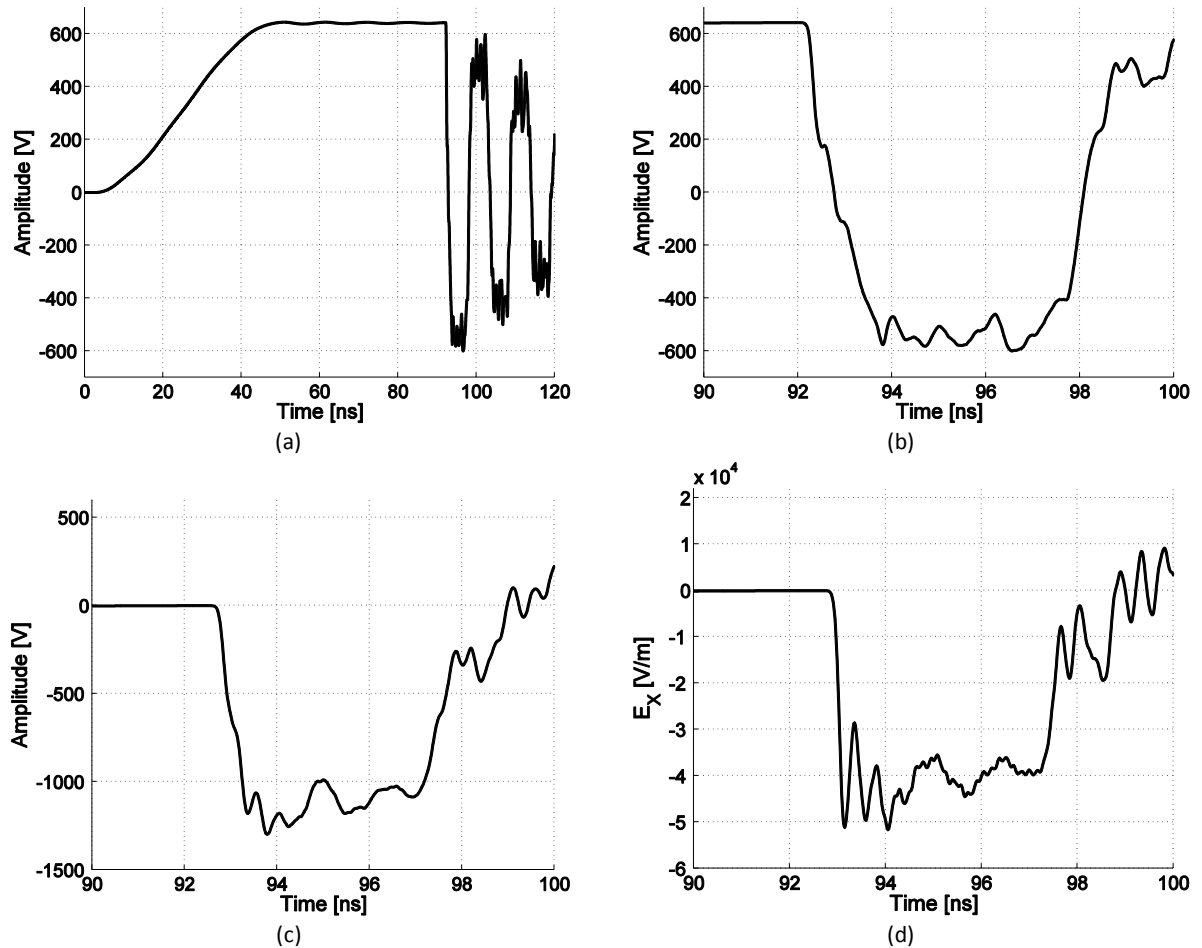


Figure 6-7. (a) Charging and discharging of the Blumlein. At 90 ns the spark gap is closed. (b) Zoomed view of the pulse in the outer transmission line. (c) Voltage at the input of the accelerator chamber. (d) Electric field strength at the accelerator gap.

Due to the fact that the accelerator is an open end of the transmission line, voltage doubling occurs. This can be seen by comparing Figure 6-7 (b), the voltage in the outer transmission line, with Figure 6-7 (c).





## 7 Conclusions

---

A surface discharge over glass and SrTiO<sub>3</sub> is studied using air, helium and argon at pressures ranging from 10 to 1000 mBar. The best overall performance, with respect to load voltage rise time, energy transfer and plasma homogeneity, is achieved with argon.

Although the results with SrTiO<sub>3</sub>,  $\epsilon_r \approx 100$ , are not as promising as the results with glass,  $\epsilon_r = 6.7$ , from a switch performance point of view, the optical images show significant differences in the plasma behavior with respect to plasma sliding over glass.

The behavior of the plasma and the performance of the switch is successfully measured optically and electrically. With D-dot sensors, implemented in the grounding plane of the switch, fast transient signals of the plasma are measured. This measurement allows for the determination of the moment of plasma ignition and the moment the plasma makes contact with the load electrode. With the D-dot sensors, both the electric and the optical measurements can be coupled which gives a good insight in the development of the plasma in time.

The conceptual study in chapter 6 explores a possible implementation of the surface discharge switch with the option to trigger it. Simulations show that the triggering system can create an electric field at the edge of the switch less than 20% of the bulk electric field strength before triggering and achieves an electric field strength in the order of 150% of the bulk electric field after triggering. This change in electric field strength at the sharp electrode, due to the trigger, shows great potential for the controlled ignition of a plasma.

The 4-line PPTLT and a 8-line PPTLT have an ideal gain, based on the square root of the ratio between the input and output impedance, of 3.63 and 6.11 respectively. The developed PPTLTs show a measured gain efficiency of 91.3% and 88.9% for the 4-line and 8-line PPTLT. These measurements, together with the numerical models, show that the secondary mode has a minimal effect on the performance of the PPTLT and losses are smaller than those of a TLT based on coaxial transmission lines. Measurements also show that pulse distortion is minimal for a Gaussian pulse with a FWHM of 600 ps.

Several modifications for the PPTLT are demonstrated to make it suitable for high voltage applications.

The developed D-dot sensors successfully measured 60 kV nanosecond pulses in the Kumamoto Blumlein. The small size of the sensors inherently results in a high bandwidth, making them nearly ideal differentiators. The small size also makes that the sensors cause very little infringement in the pulse source.

D-dot sensors can also be used in a dynamic environment such as the surface discharge switch. Due to the changes in capacitive coupling, which are not known exactly, it is not trivial to exactly

retrieve the actual high voltage signals. The D-dot sensors show the fast transients and thereby allow for a better understanding of the switching characteristics of the plasma.

Calibration of the D-dot sensors has been done using accurate numerical models together with a simplified RC lumped element model.

The autocorrelator has been tested using a Bit Pattern Generator with 40 picosecond pulses at a 2.5 GHz rep rate and showed that the FWHM of the pulses can be measured with an accuracy of 6%. The measurements show that the autocorrelator works better for smaller input amplitudes since for small input signals the diode in the power detector behaves quadratically.

Although the autocorrelator was tested with a very high repetition rate, it allowed for the verification of the model which predicts the output of the autocorrelator using the static V-I characteristic of the power detector.

Combining the autocorrelator with a charge amplifier allows the application of the autocorrelator on applications with a low, less than 100 Hz, repetition rate.

## 8 Summary

---

A surface discharge over glass and SrTiO<sub>3</sub> is studied using air, Helium and Argon at pressures ranging from 10 to 1000 mBar. To obtain a discharge over the surface with a uniform surface coverage, the pressure range has to be between 100 and 1000 mBar. At 100 mBar and lower pressures the discharge becomes more diffuse and loses its surface discharge characteristics. At 1000 mBar the discharge quenches faster resulting in less surface coverage.

The propagation velocity of the initial discharge phase range from  $0.5 \cdot 10^6$  m/s, using SrTiO<sub>3</sub> in air, to over  $5 \cdot 10^6$  m/s, using glass in Helium. The dielectric constant of the surface material has a significant influence on discharge behavior.

The unique feature of the TLT as proposed in this thesis is that secondary mode effects can almost be ignored. This results in a highly efficient transmission line transformer and nearly ideal voltage gains. Also the input pulse of the TLT suffers minimal distortion and reflections while propagating through the TLT. Detailed 3D and time-domain modeling of the electromagnetic waves in the TLT provide good insight in the way such a TLT operates and must be optimized. Experiments confirm these modeling results.

Two transmission line transformers, a 4- and an 8-line TLT, based on parallel transmission lines have been built and experimentally tested with respect to their theoretical performance. The 4 and 8-line TLT produce voltage gains of 3.6 and 5.8 respectively. This is within 90 % of the ideal voltage gain which is expected based on the input and output impedances of the TLTs.

Different modifications to the TLT design have been proposed to make it suitable for pulsed high voltage applications.

To validate the performance of a nanosecond high voltage pulse source, differentiating electric field probes are proposed to measure the pulses. The small size of these probes has a twofold advantage; they cause very little infringement in the pulse source and have an inherently very wide bandwidth. The small size allows for these sensors to be modeled as a simple RC circuit. Using numerical models the capacitive coupling of the sensors with the high voltage electrode of interest could be estimated with a relative high accuracy. By also measuring with other high voltage sensors, the capacitive values obtained from simulations could be validated.

The D-dot sensors are successfully used both in a coaxial transmission line and underneath a surface plasma. For the measurements on the coaxial transmission line, performed at Kumamoto University in Japan, the sensors perform in full agreement with the theoretically expected behavior. For the surface plasma setup, even though the surface plasma setup was neither ideal nor optimized for this application, satisfactory results are obtained. The D-dot sensors showed more dynamic details of the discharge process allowing for a better understanding of the switching characteristics of the plasma.

The rise time of the desired nanosecond pulses is in the order of tens of picoseconds. To measuring such fast rise times of high voltage signals an autocorrelator method is proposed. Using autocorrelation of the derivative of the voltage pulse a measure for the full width at half maximum of

the rise time can be found. The autocorrelator has been tested using a Bit Pattern Generator with 40 picosecond pulses. The measurements show that the autocorrelator works best for very small input amplitudes since here the diode in the power detector behaves quadratically. Although the autocorrelator was tested with a very high repetition rate, it allowed for the verification of the model which predicts the output of the autocorrelator with satisfactory accuracy using the static V-I characteristic of the power detector.

The autocorrelator can be combined with the D-dot sensors. This results in a sensor which can directly measure the rise time of a high voltage pulse.

## 9 Samenvatting

---

Een oppervlakte ontlading over glas en  $\text{SrTiO}_3$  is bestudeerd gebruikmakende van lucht, argon en helium bij drukken variërend van 10 tot 1000 mBar. Om een uniform dekkende ontlading over het oppervlakte te verkrijgen moet de druk tussen de 100 en 1000 mBar zijn. Bij 100 mBar en lagere drukken wordt de ontlading meer diffuus en verliest het zijn oppervlakte ontlading eigenschappen. Bij 1000 mBar knijpt de ontlading sneller samen wat resulteert in lagere oppervlakte dekking.

De propagatiesnelheid van de initiële fase van de ontlading varieert van  $0.5 \cdot 10^6$  m/s, bij  $\text{SrTiO}_3$  in lucht, tot meer dan  $5 \cdot 10^6$  m/s bij glas in helium. De dielectrische constante van het oppervlakte materiaal heeft een significante invloed op het gedrag van het plasma.

De unieke eigenschappen van de Transmissie Lijn Transformator gebaseerd op parallelle plaat transmissie lijnen, PPTLT, zoals voorgesteld in dit proefschrift is dat effecten van de secundaire mode bijna genegeerd kunnen worden. Dit resulteert in een zeer efficiënte transmissie lijn transformator met een nagenoeg ideale spanningsversterking. De puls die door de PPTLT propageert wordt minimaal verstoord en of gereflecteerd. Gedetailleerde 3D tijdsdomein modellen van de elektromagnetische golven in de PPTLT geven een goed inzicht hoe een dergelijke TL functioneert en geoptimaliseerd moet worden. Experimenten bevestigen deze gemodelleerde resultaten.

Twee transmissie lijn transformatoren, een 4-lijns en een 8-lijns PPTLT, zijn gebouwd, getest en vergeleken met hun theoretische prestaties. De 4-lijns en de 8-lijns PPTLT produceren een spanning versterkingsfactor van respectievelijk 3.6 en 5.8. Dit is binnen 90% van de ideale spanning versterkingsfactor welke verwacht wordt gebaseerd op de in- en uitgang impedantie van de PPTLTs.

Verschillende modificaties voor het PPTLT ontwerp zijn voorgesteld om deze geschikt te maken voor gepulste hoogspanning applicaties.

Om de prestaties van een nanoseconde hoogspanning pulsbron te valideren, zijn differentiërende elektrisch veld sensoren voorgesteld om de pulsen te meten. Het kleine formaat van deze sensoren heeft een tweeledig voordeel; de sensoren veroorzaken zeer weinig inbreuk in de pulsbron en hebben een inherent hoge bandbreedte. Het kleine formaat van deze sensoren maakt het mogelijk dat ze gemodelleerd kunnen worden als een eenvoudig RC netwerk. Door middel van numerieke modellen kan de capacitieve koppeling tussen de sensoren en de hoogspanningselektrode berekend worden met een relatief hoge nauwkeurigheid. Door ook met andere hoogspanning sensoren te meten konden de gevonden capacitieve waarden gevalideerd worden.

De D-dot sensoren zijn succesvol gebruikt in zowel een coaxiale transmissie lijn en onder een oppervlakteontlading plasma. Bij de metingen in de coaxiale transmissie lijn, welke gedaan zijn bij Universiteit van Kumamoto in Japan, functioneren de sensoren in volledige overeenstemming met het theoretisch verwachte gedrag. Bij de oppervlakte ontlading opstelling, ondanks het feit dat de

opstelling noch ideaal noch geoptimaliseerd was voor deze applicatie, zijn er toch bevredigende resultaten behaald. De D-dot sensoren tonen meer dynamisch gedrag van de ontlading waardoor een beter begrip van het schakelend karakter van het plasma verkregen kan worden.

De stijgtijd van de gewenste nanoseconde pulsen is in de orde van tientallen picoseconden. Om zulke snelle stijgtijden van hoogspanningspulsen te meten is een elektrische autocorrelator voorgesteld. Door autocorrelatie toe te passen op de afgeleide van de hoogspanningspuls kan er een maat gevonden worden voor de ' volledige breedte op halve hoogte' van de stijgtijd. De autocorrelator is getest met een Bit Patroon Generator welke pulsen met een ' volledige breedte op halve hoogte' van 40 picoseconden genereert. De metingen laten zien dat de autocorrelator het best werkt met zeer kleine ingangssignalen gezien de diode in de vermogensdetector voor kleine signalen een kwadratisch gedrag vertoont. Ondanks dat de autocorrelator getest is met een zeer hoge puls repetitie frequentie, is het mogelijk geweest om het model te valideren dat het uitgangssignaal van de autocorrelator voorspeld met een bevredigende nauwkeurigheid (6%) door gebruik te maken van de statische spanning-stroom karakteristiek van de vermogensdetector.

De autocorrelator kan gecombineerd worden met de D-dot sensoren. Dit resulteert in een sensor die direct de stijgtijd van een hoogspanning puls kan meten.

# 10 Appendix

---

## 10.1 Modeling of a laser triggered spark gap

Numerical models to simulate transmission lines and wave guides are a great tool to verify once design. But changes in geometry takes place, for instance the development of a plasma or spark, cannot be handled by most of the numerical models. In such a case either a further simplification of the design can be made by modeling it with lumped elements or a more detailed model can be made which takes the plasma dynamics into account. Both approaches have their advantages and disadvantages. Here we propose a simple method to simulate spark gaps in numerical models without losing model detail nor significantly increasing required computational time or capacity.

As an example the coaxial spark gap [20] is used. The spark gap is shown in Figure 10-1 (a), as taken from [20], and the measured output pulse is shown in Figure 10-1 (b) as a function of used laser energy and in (c) as a function of charging voltage.

The numerical model is schematically shown in Figure 10-2 (a) together with the critical dimension. The model is a simplification of Figure 10-1 (a), the laser entrance port and the diagnostic port are omitted. In the model all background material is set to perfect electric conductor, PEC. The outer conductor of the coaxial transmission line is not shown. Because the background material is set to PEC it is modeled automatically. The space in between the conductors is set to vacuum except for the plasma.

The center conductor is a floating conductor and the right conductor, the output, touches a so called open boundary. This means that it is simulated as if it continues indefinitely and can be considered a virtual ground.

Figure 10-2 (b) shows a close up of the spark gap. The spark itself is modeled as a conductive cylindrical rod and allows the user to set its conductance, permeability and permittivity. These properties can be set, but cannot change during the simulation. Therefore this method is best applicable to spark gaps where the plasma develops to a steady conducting channel much faster than the development of the electromagnetic fields, which is the case for this laser triggered spark gap where the conductive channel is formed in roughly 100 femtoseconds. In this model both  $\epsilon_r$  and  $\mu_r$  are set to 1. The resistance of the plasma is set to  $82.5 \Omega$  and its diameter is set to 0.1 mm. The diameter is larger than the real spark diameter. This is done for meshing purposes. The difference in diameter will have limited effects on both the capacitive and inductive properties of the arc but, this does not affect the general applicability of this simulation method.

The simulation has two phases;

1. Setting up the electric fields as they are just before switch closure
2. Closing the switch and actually model the electromagnetic field propagation



The first phase of the model is needed because in CST Microwave studio simulations begin with zero energy in the simulation domain. In the center of the plasma rod a current source is placed. This current source is used to build the electric fields in the first phase. The current source is in parallel with the plasma resistance, Figure 10-2 (c). The current from the current source will go through the plasma resistance thereby charging the source electrode and as such, creates the desired electric field. The desired potential on the source electrode just before switch closure can thus be set by the amplitude of the current source. Once the desired electric field strength is achieved and all transients have sufficiently damped, the current source is switched off and the second phase of the model begins. By switching off the current source, it effectively 'disappears' from the simulation, it no longer has any effect on the simulation. The time taken to turn off the current source can be used to simulate, to some extent, the time needed to form a good conducting channel.

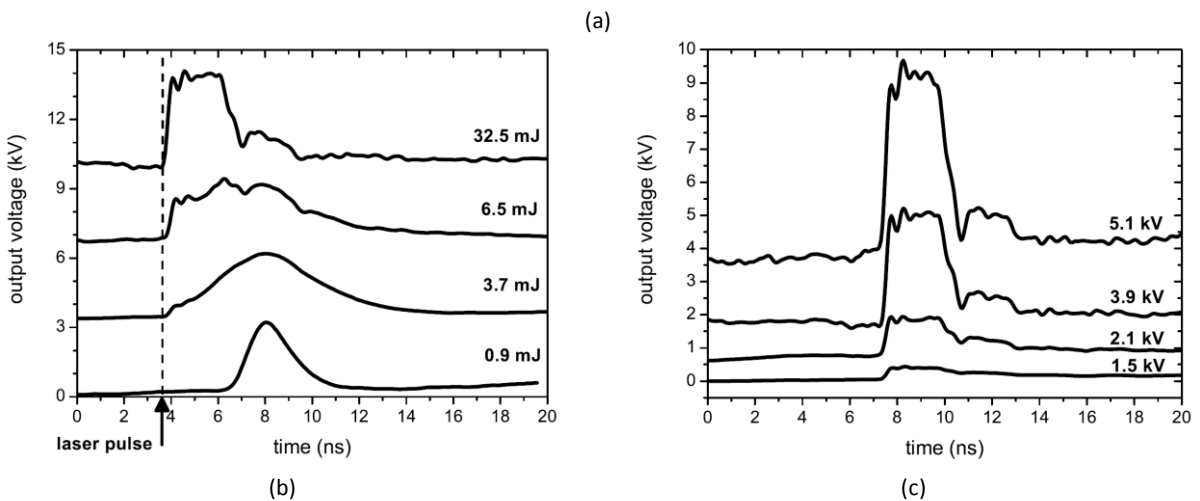
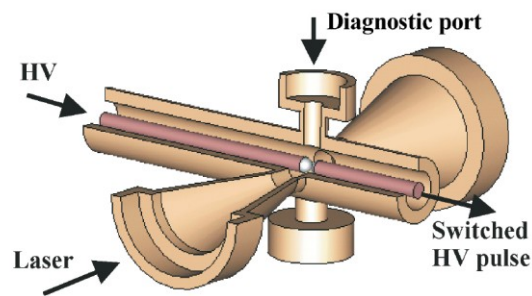


Figure 10-1. (a) Laser triggered spark gap. (b) Output pulse as function of used laser energy. (c) Output pulse as function of charging voltage.

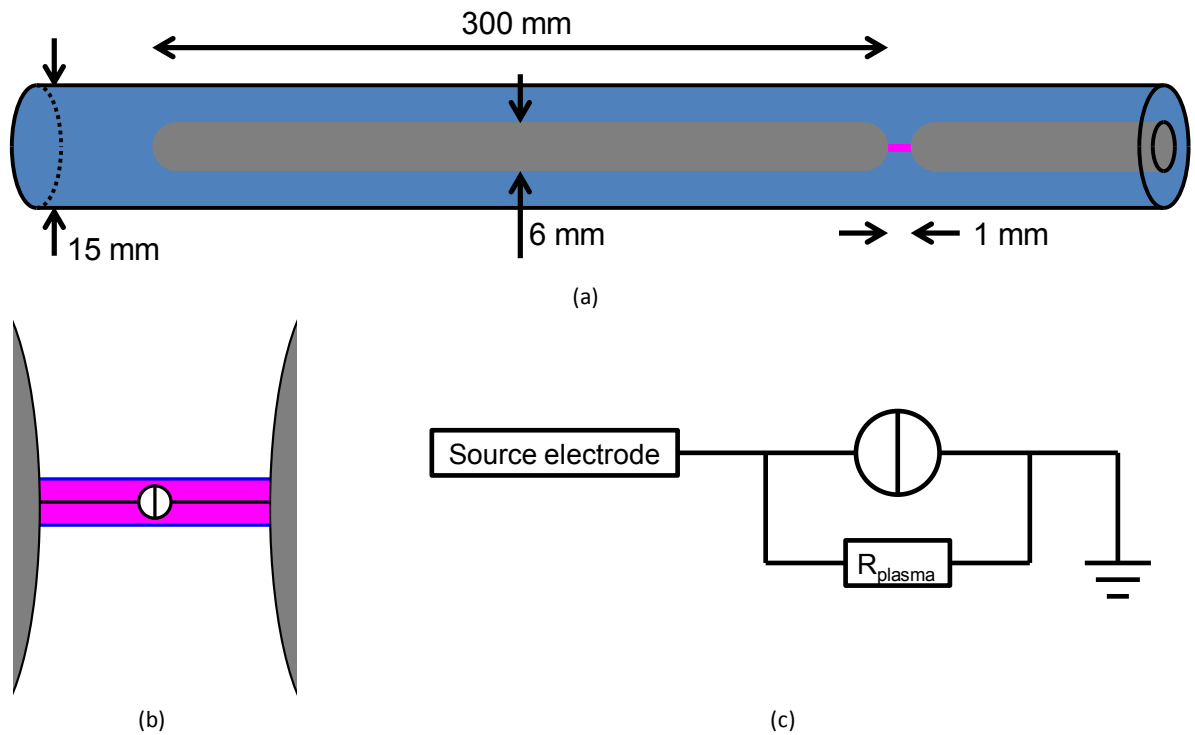


Figure 10-2. (a) Schematic representation of the numerical model and the critical dimensions. (b) The spark gap and the current source. (c) Simplified lumped model of the spark gap.

Figure 10-4 shows the normalized charging current. In the first 10 ns of the simulation it slowly rises to its maximum value. Between 10 and 15 ns it is constant. This period is used to let all transients, caused by the charging, to damp. At 15 ns all electric fields are stabilized and the simulation represents the real spark gap just before it closes. Figure 10-4 shows the simulated voltages normalized to the maximum charging voltage. Until 15 ns the current source charges the source electrode. During this period, the load voltage becomes negative. Once the charging current becomes constant, at 10 ns, the load voltage drops back to 0 V. Also here it can be seen that just before 15 ns, all transients are gone and the voltage on the load electrode has dropped to 0 V indicating a steady state is reached.

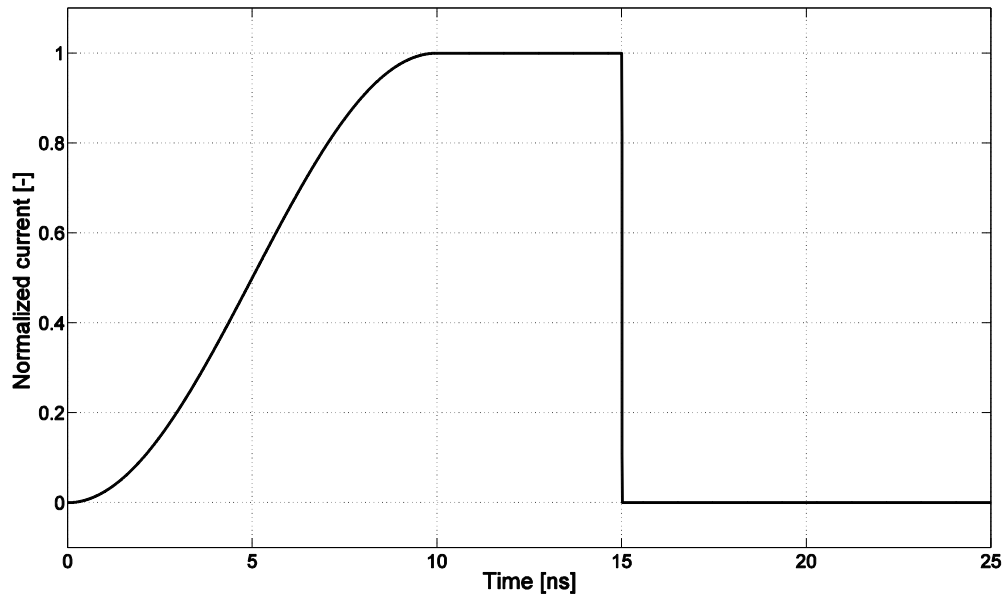


Figure 10-3. Normalized charging current in the simulated spark gap. Phase 1, charging, lasts until 15 ns, at 15 ns the current source is turned off and phase 2, modeling of the propagating electromagnetic waves, starts. By turning off the current source it no longer influences the simulation.

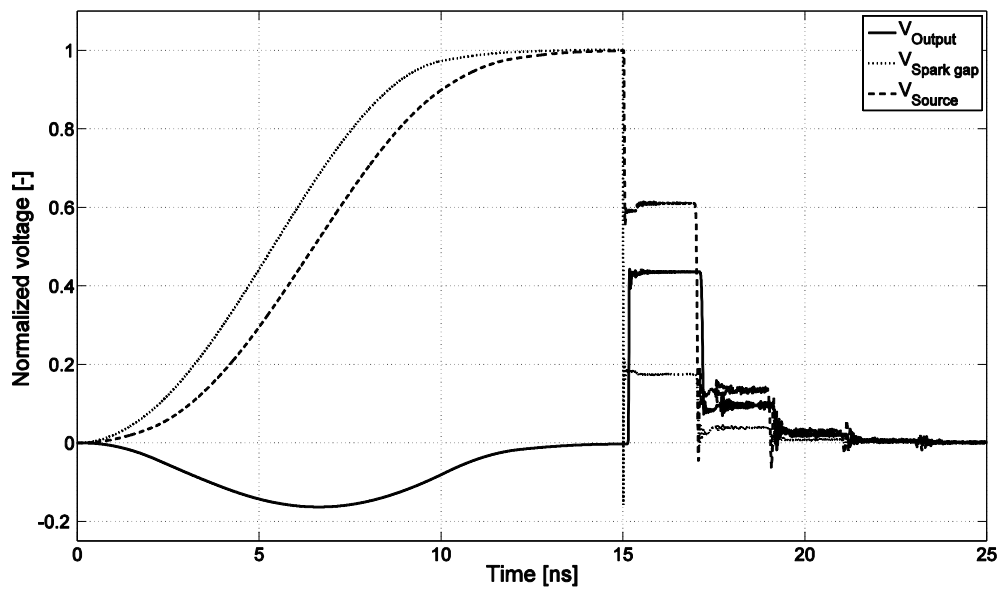


Figure 10-4. Normalized voltages in the simulated spark gap. Phase 1, charging, lasts until 15 ns, at 15 ns the current source is turned off and phase 2, modeling of the propagating electromagnetic waves, starts.

The simulated voltages show the same characteristics as those of the measurement.

In Figure 10-1 (c) it can be seen that, independent of the charging voltage, the first output pulse is followed directly by a second pulse. This second pulse is also seen in the simulation. The amplitude of

the second pulse is matched to the measurement by changing the plasma impedance. This leads to the 82.5  $\Omega$  plasma resistance mentioned earlier.

## 10.2 D-dot sensor calibration

### 10.2.1 Model

The D-dot sensor is made of RG-405 rigid coax cable. This cable has an inner conductor with a diameter of 0.51 mm and a Teflon dielectric with an outer diameter of 1.67 mm. these rigid cables have a bandwidth of 18 GHz. The small size of these cables makes that the D-dot sensor can be assumed to behave as an ideal differentiator for the frequencies we can measure. Under this assumption a simplified model of the D-dot sensor directly underneath the source electrode is shown in Figure 10-7. In this model we treat the coaxial cable as a real impedance of 50  $\Omega$ . The capacitance in this model is the capacitance between the tip of the inner conductor of the coaxial cable and the high voltage electrode. Figure 10-5 shows a 3D model of the SDS and Figure 10-6 shows a cut-plane view of the SDS with the D-dot sensors in the grounding plane.

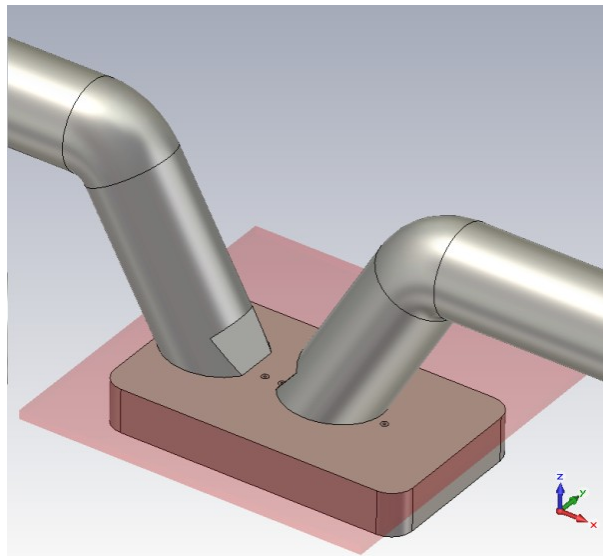


Figure 10-5. The surface discharge switch with the D-dot sensors in the grounding plane.

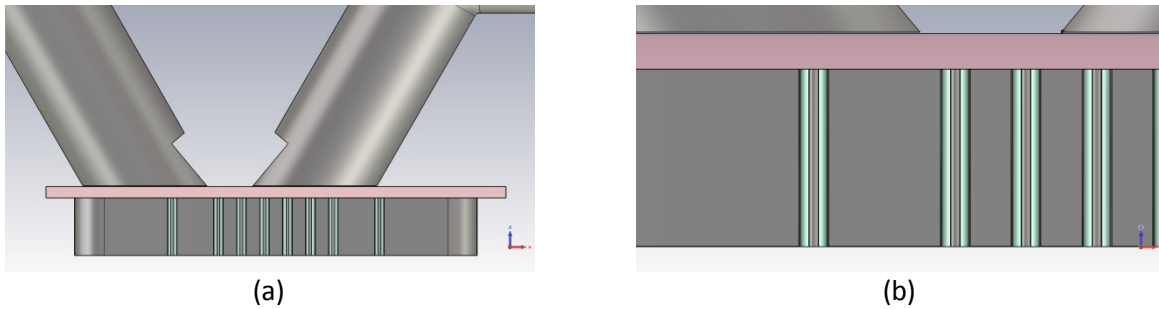


Figure 10-6. (a) A cut view from the side of the SDS. 8 D-dot sensors are placed in the grounding plane. The source electrode is on the right. (b) Zoomed view of the used D-dot sensors.

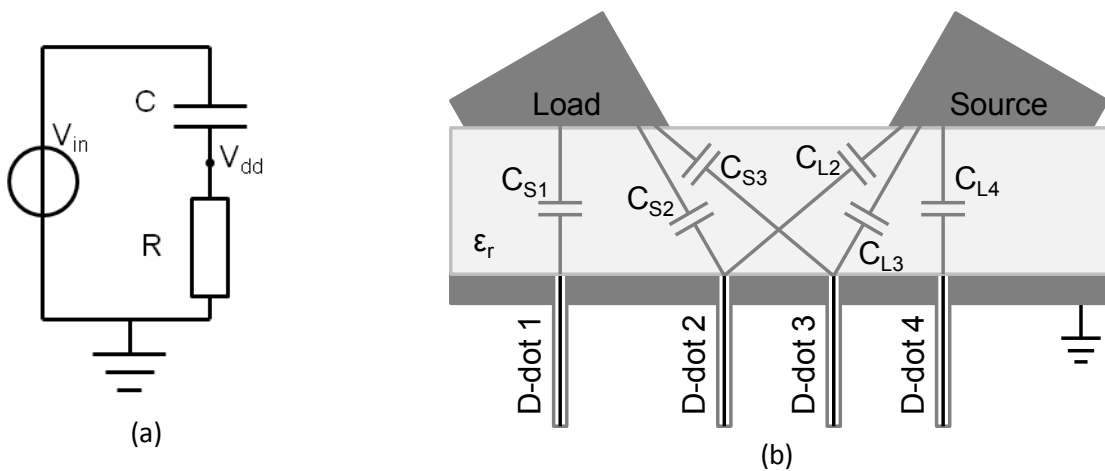


Figure 10-7. (a) Simplified RC network of the D-dot sensor directly underneath a high voltage electrode (D-dot 1 and 4). (b) All capacitive couplings between the high voltage electrodes and the D-dot sensors.

For D-dot 1 and 4 we can use

$$\frac{V_{dd}(t)}{R} = C \frac{d(V_{in}(t) - V_{dd}(t))}{dt} \quad 10-1$$

Here  $V_{in}$  is the voltage on either the load or the source electrode. This can be simplified because  $V_{dd}$  is in the order of several volts whereas  $V_{in}$  is in the order of kilovolts.

$$\frac{V_{dd}(t)}{R} = C \frac{dV_{in}(t)}{dt} \quad 10-2$$

Rewriting this gives for  $V_{in}$

$$V_{in}(t) = \frac{1}{RC} \int V_{dd}(t) dt \quad 10-3$$

In the frequency domain the transfer function between  $V_{dd}$  and  $V_{in}$  is

$$\frac{V_{dd}}{V_{in}} = \frac{sRC}{sRC + 1} \quad 10-4$$

Here  $R$  is  $50 \Omega$ , the RG-405 cable impedance and  $C$  is the capacitance between the tip of the sensor and the high voltage electrode. This transfer function has a zero in the origin, a pole at  $\omega = 1/RC$  and a gain of  $RC$ . For frequencies well below  $1/RC$ , the transfer function has a slope of +20dB/dec and it behaves as a perfect differentiator with the constant gain of  $RC$ . Due to the pole the transfer function approaches 1 for frequencies above  $1/RC$  rad/sec. With  $R$  known, only  $C$  has to be found.

To find the value of  $C$  we measure  $V_{dd}$  underneath the source electrode with conditions such that no discharge occurs. This is described in section 10.2.2. With the measurements a capacitance of 11 fF is found. With numerical electrostatic field simulations we find 13.6 fF for  $C$ . The simulated capacitance agrees very well with the measured value. This gives reason to believe that the quality of the simulation method is such that it can be used to give a rough estimation of the capacitive coupling with an error in the order of 25 % or less. Even though this is a large error margin the numerical simulations give a good starting point to estimate the change in capacitive coupling during a discharge. This change can then be incorporated in the processing of the measured D-dot signals.

### 10.2.2 Measurement without discharge

A calibration measurement is done to find the capacitive coupling between the high voltage source electrode and the D-dot sensor directly underneath it. For this calibration the vacuum vessel was filled with air and the pressure was reduced until no discharge takes place. The absence of the discharges is verified optically and with the Pearson probe. The voltage at the source electrode is monitored with the North Star probe and the D-dot sensor. Using these signals for  $V_{in}$  and  $V_{dd}$  in eq. 10-4 enables us to find a value for  $RC$  and thus  $C$ .

Figure 10-8 (a) and (b) show the voltages as recorded with the North Star probe in blue and the D-dot sensor in red (time domain) and green (frequency domain). Figure 10-9 shows the Bode plot of the magnitude of  $V_{dd}/V_{in}$  as a function of frequency in rad/sec. For frequencies below  $4 \cdot 10^6$  rad/sec the data in the bode plot is unreliable due to the limited length of the recorded signals. At  $300 \cdot 10^6$  rad/sec a peak in the bode plot is observed. This is caused by bandwidth limitations of the overall measurement setup. In between the 4 and  $300 \cdot 10^6$  rad/sec we see a +20 dB/dec slope. In this frequency domain the calibration measurement allows for the determination of the  $RC$  value. This is done by taking a single magnitude point on the bode plot (green line) at one frequency. Using eq. 10-4 we find for  $RC$  a value of  $500 \cdot 10^{-15} \text{ rad}^{-1}/\text{sec}^{-1}$  and a capacitance of 11 fF.

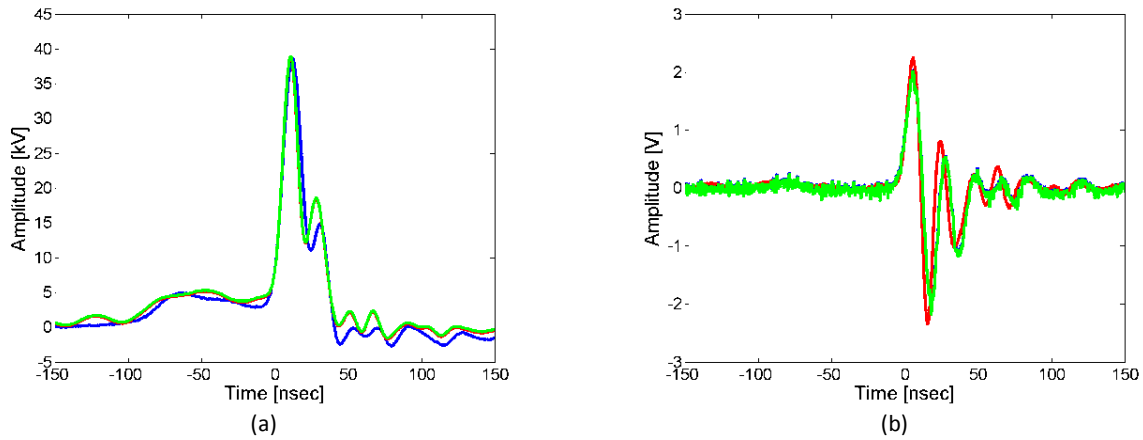


Figure 10-8. (a) Input voltage. Blue is the North Star signal, green the time integrated D-dot signal and red (directly under the green line) is the voltage based on the D-dot signal and the transfer function in eq. 10-4. (b) Time derivative of the input voltage. Blue (directly underneath the green line) is the time derivative of the North Star signal, green is the derivative of the North Star signal obtained through eq. 10-4 and red is the D-dot signal.

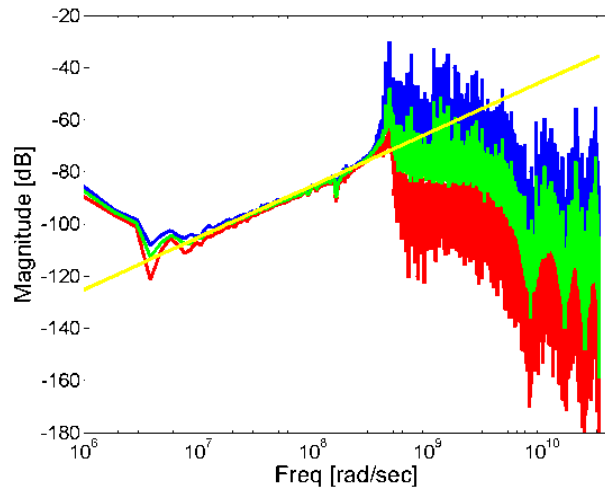


Figure 10-9. Bode plot of the magnitude of  $V_{dd}/V_{in}$ . Blue is the upper limit, red the lower limit and green the average amplitude measured.

So when there is no discharge, the capacitive coupling between the D-dot sensor and the high voltage electrode is 11 fF. This calibration method is only possible with the D-dot sensor directly underneath the source electrode to obtain a sufficient signal noise ratio.

### 10.2.3 Numerical simulation

The electrostatic field simulation package of CST is used to find an estimate for the value for  $C$ . The static field simulations give a value of 13.6 fF. In these simulations there is a 0.1 mm gap between the bottom side of the source electrode and the dielectric plate. This small air gap is incorporated because the electrodes in the setup cannot be positioned 100 % perfectly on top of the dielectric. Based on observations and the construction used to place the electrodes on the dielectric surface, an air gap of this size is to be expected.

#### 10.2.4 Measurement with discharge

When a discharge does occur, the voltage measurement becomes a lot more tricky. Due to the plasma, the capacitive coupling between the high voltage electrodes and the D-dot sensors changes. In this case, eq. 10-4 is no longer correct, now also the change in capacitance must be accounted for. To take the change in capacitance into account we use , [34],

$$I = C(t) \frac{dV(t)}{dt} + V(t) \frac{dC(t)}{dt} \quad 10-5$$

Replacing  $I$  with  $V_{ad}/R$  and integrating both sides gives

$$\frac{1}{R} \int V_{ad}(t) dt = C(t)V(t) \quad 10-6$$

Which can be rewritten to

$$\frac{1}{RC(t)} \int V_{ad}(t) dt = V(t) \quad 10-7$$

Here  $C(t)$  is the capacitance between the tip of the D-dot sensor and the high voltage electrode,  $V(t)$  the voltage over this capacitance, which in our case is assumed to be equal to the applied high voltage and  $R$  is the characteristic impedance of  $50 \Omega$  of the d-dot sensor cable. Eq. 10-7 shows only  $C(t)$  is needed to find  $V(t)$ .

To get an impression of the effect of the increasing capacitance we use the discharge images to determine the propagation velocity of the plasma front. Figure 10-10 (a) and (b) show a discharge in 250 mBar Argon. In Figure 10-10 (a) the discharge is shown in an early stage, just after the avalanche reaches the load electrode (here at the bottom of the image). In Figure 10-10 (b) the discharge is shown at a later stage where channels have formed. As can be seen, the plasma not only propagates in between the two electrodes but it develops circular around the source electrode up to a distance from the source electrode which is equal to the gap length.



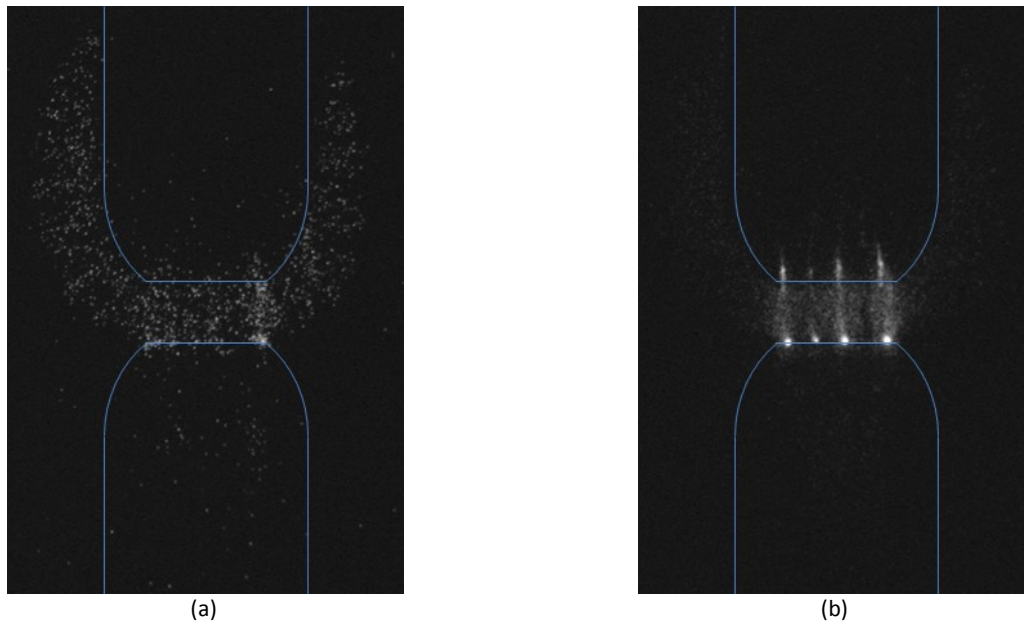


Figure 10-10. Discharge in 250 mBar Argon. Before the plasma reaches the load electrode, a plasma disks with a uniform intensity forms around the source electrode. When the disk touches the load electrode, its intensity increases significantly in the gap.

Two simulation runs were done, Figure 10-11. One with the plasma expanding circularly, Figure 10-11 (a) and one with the plasma expanding linearly only in the gap between the electrodes, Figure 10-11 (b). In these simulations the plasma is modeled as a perfect electric conductor.

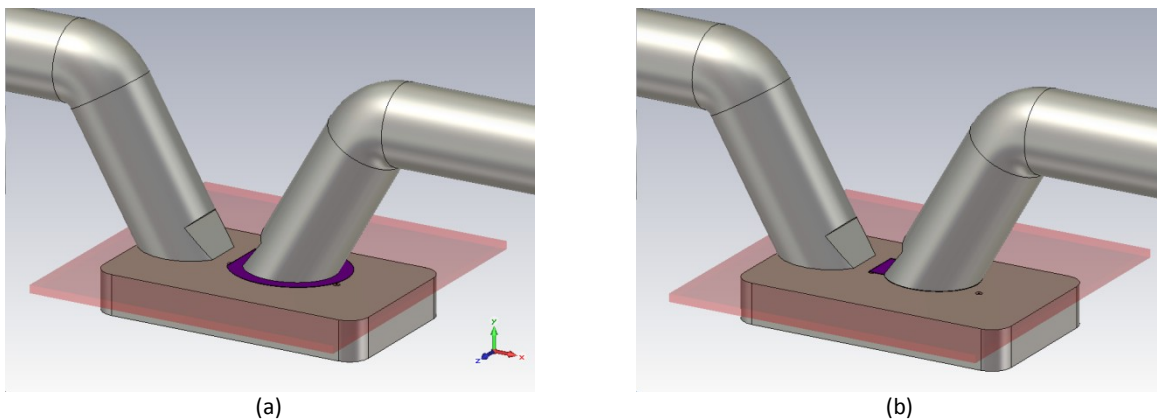


Figure 10-11. Numerical static field simulations done to find the capacitive coupling between the D-dot sensors and the high voltage electrodes. Left, the plasma is modelled as a perfectly conducting circular growing disk. Right, the plasma is modelled as a linear growing strip in between the electrodes.

The simulations consist of four steps;

1. At first there is no plasma present and there is a small gap between the dielectric and both the high voltage electrodes.
2. To model the ignition of the plasma, only the gap between the source electrode and the dielectric is filled with plasma.

3. The avalanche phase is modeled by increasing the size of the plasma as shown in Figure 10-11 until the load electrode is reached.
4. Finally, once the plasma reached the load electrode, also the gap between the load electrode and the dielectric is filled with plasma.

Figure 10-12 and Figure 10-13 show the capacitance between the different D-dot sensors and the electrodes as a function of the plasma length.

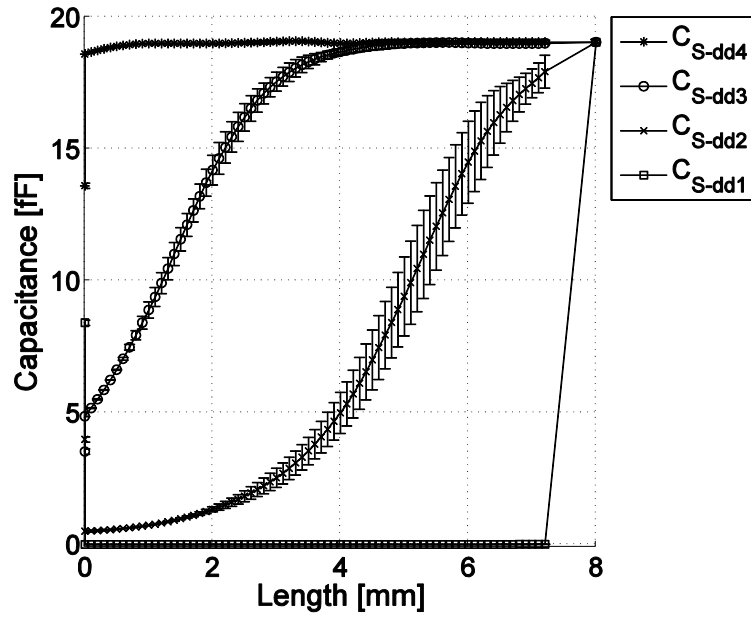


Figure 10-12. Simulated capacitances between the source electrode and the D-dot sensors.

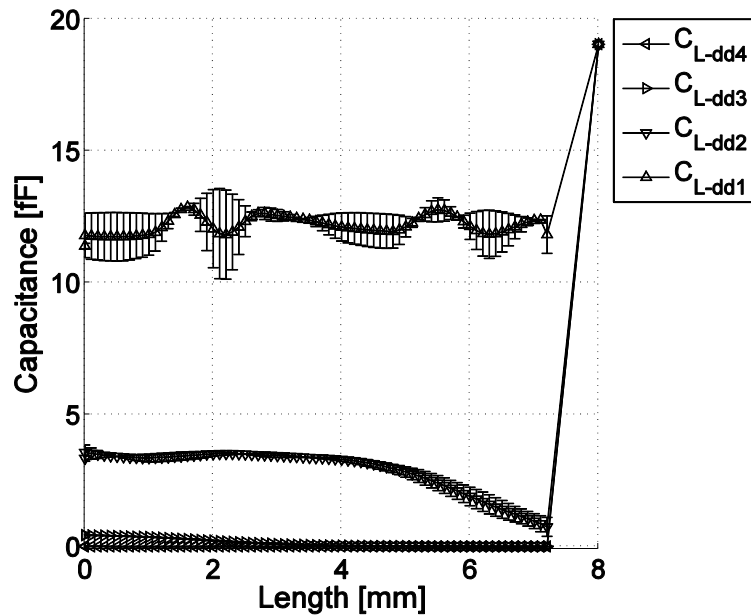


Figure 10-13. Simulated capacitances between the load electrode and the D-dot sensors.

The capacitances vary more than 3 orders of magnitude. The ignition of the plasma underneath the source electrode causes a step in the capacitances directly after 0 mm in Figure 10-12 and Figure 10-13. At 8 mm all capacitances are set to the final value of 19 fF. This is due to the fact that when the plasma connects both high voltage electrodes, they are seen as one electrode in the simulation. In this case, D-dot sensor 1 becomes just as sensitive to the source electrode as D-dot sensor 4.

D-dot 4 and D-dot 1 both have a relatively constant capacitive coupling with the source and load electrode respectively. Only D-dot 4 changes significantly when the plasma 'ignites' underneath the source electrode. D-dot 2 and 3 have a capacitive coupling with both the source and the load electrode. Their coupling increases with the source electrode when the plasma expands and their coupling with the load electrode decreases respectively. The decrease of the coupling is caused by the plasma that shields the load electrode from the D-dot sensors. The initial capacitive value of D-dot 3 and the source electrode is similar to the initial capacitive coupling between D-dot 2 and the load electrode. The same holds for D-dot 2 and the source electrode and D-dot 3 and the load electrode. This is to be expected since the setup is symmetric.

Having found an estimate for the capacitances and their change as a function of the plasma size, we need to transform these capacitances from position dependent to time dependent. To do this we need 2 things from the measurements;

1. The first spike in the output signal of D-dot 4, caused by the sudden change in capacitance between the source electrode and D-dot sensor 4, is used to indicate that the capacitances start to change.
2. The time needed for the plasma to fully close the gap. This is based on the avalanche propagation velocity as measured with the optical images. The analysis of these images is discussed in appendix 10.3.

Here we make 3 assumptions;

1. The increase in capacitance is achieved during the avalanche phase.
2. The capacitance changes only during the avalanche phase after which it remains constant for the remainder of the discharge.
3. Any effects due to residual surface charge are not taken into account.

In the following section we discuss the analysis of the optical images from which the propagation velocity is determined as a function of the plasma front position. After converting this to a velocity as function of time, the capacitance as a function of time is given.

## 10.3 Analysis of optical images

### 10.3.1 Definition of the discharge front

We define the plasma front as

*'The lowest possible detectable light intensity increase above the noise level over the full width of the discharge gap'*

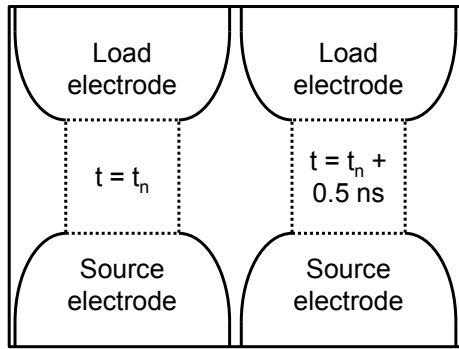
There are 2 main motivations to use this as a definition. First, when analyzing the discharge images, the plasma does not only move forward but it also intensifies the shape of the discharge changes. Therefore the reference and delayed image cannot be compared directly. The part of the plasma which is least influenced by the intensification of the plasma and most by the forward movement of the plasma is front with the lowest detectable intensity. The second reason for choosing this definition is its generality. The plasma front shows a lot of variation for different parameter settings.

The advantage of this definition is its straightforwardness. The image intensity in front of the discharge is that of the noise level. This level has proven to be very consistent throughout the various measurements. Relatively simple code already does a great job in finding a front of the discharge using the above given definition. Another advantage is that this definition comes very close to what looks like the discharge front as seen by just looking at the images.

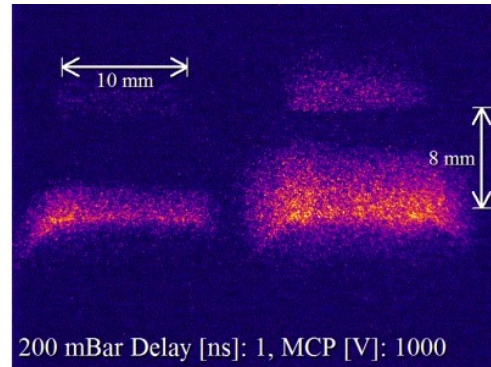
### 10.3.2 Image calibration

To determine the avalanche velocity, we determine the travelled distance in the images as show in Figure 2-16. To be able to determine the travelled distance a reference point, which is the same in both images, must be found. Two methods to find the reference point are possible;

1. Make images of the gap with normal lighting and find a reference point in this image.
2. Use a discharge image in which the electrodes are clearly visible.



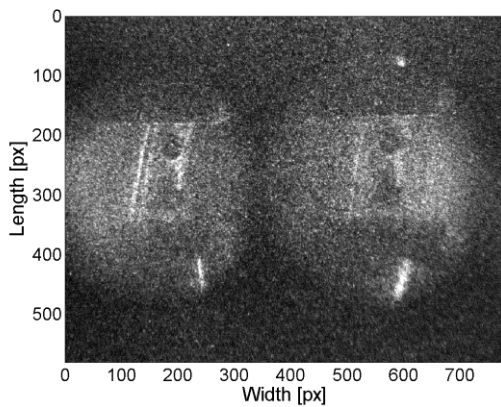
(a)



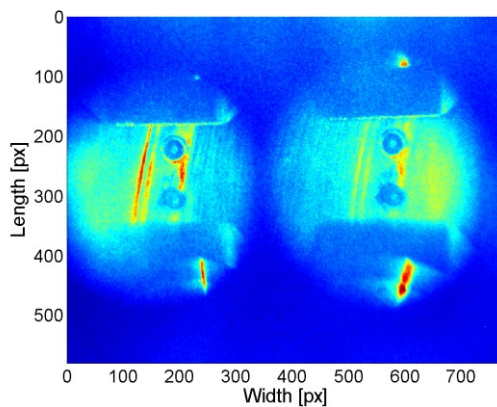
(b)

Figure 10-14. (Left) schematic image of a discharge, The left and right image are similar but have a time delay of 500 ps  $\pm$ 17 ps. (Right) example of a discharge image in air at 200 mBar.

For the first method, several images are taken and summed to find a reliable reference point. A single image is shown in Figure 10-15 (a) and the summation over 50 images is shown in Figure 10-15 (b). It is difficult to obtain equal light intensity over the entire gap. This causes areas that are overexposed. In the case of Figure 10-15, the bottom left corner of the discharge gap is hard to distinguish in the reference (left) side and a reference point is not found with enough accuracy.



(a)



(b)

Figure 10-15. (a) Image of the gap taken with normal lighting. (b) Integration of 50 images.

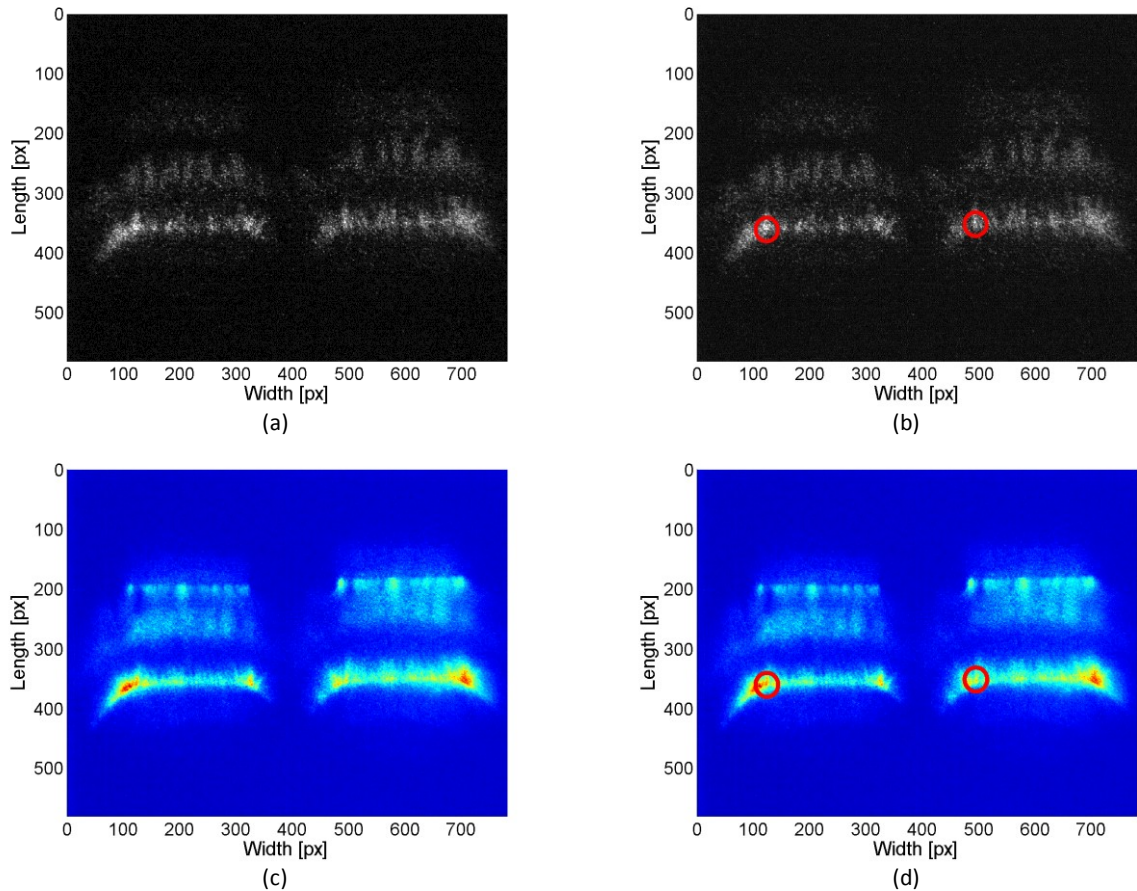


Figure 10-16. (a) Single shot discharge used to find a reference point. (b) Similar as (a) but with the reference point. (c) 50 integrated images. (d) Similar as (c) but with the reference point.

For the second method several discharge images are used. This is shown in Figure 10-16. Because in these images the discharge is used as the light source, the electrode edges are much more distinct. Here the left corner of the source electrode can be clearly distinguished in both the discharge images allowing for a reliable calibration. Another advantage is the fact that by taking the reference from the actual discharge images there is no change that something changed in the optical setup between calibration and the actual measurement.

### 10.3.3 Absolute size

The length that is represented by 1 pixel is based on the width of the electrodes. The electrodes are 10 mm wide which in the images corresponds with 200 pixels. This gives 50  $\mu\text{m}$  per pixel.

### 10.3.4 Single Image

The propagation velocity of the discharge is defined as

$$\bar{v} = \frac{1}{N} \sum_{n=1}^{200} \frac{x_{t+\Delta t}(n) - x_t(n)}{\Delta t}$$

10-8

Here  $N$  is the number of pixel columns over the full width of the electrode, 200.  $n$  is the column index,  $x_{t+\Delta t}(n)$  is the position of the discharge front in the right image,  $x_t(n)$  the position in the left image and  $\Delta t$  is the 500 ps time delay between the two images.

As an example we will use the discharge image shown in Figure 10-17 (a). This image is taken at the beginning of the discharge and is made using air at 1000 mBar over 2 mm thick glass with an  $\epsilon_r$  of 6.7. The source and load voltages are shown in Figure 10-17 (b). In the following sections the processing of the image to obtain  $\bar{v}$  is treated step by step.

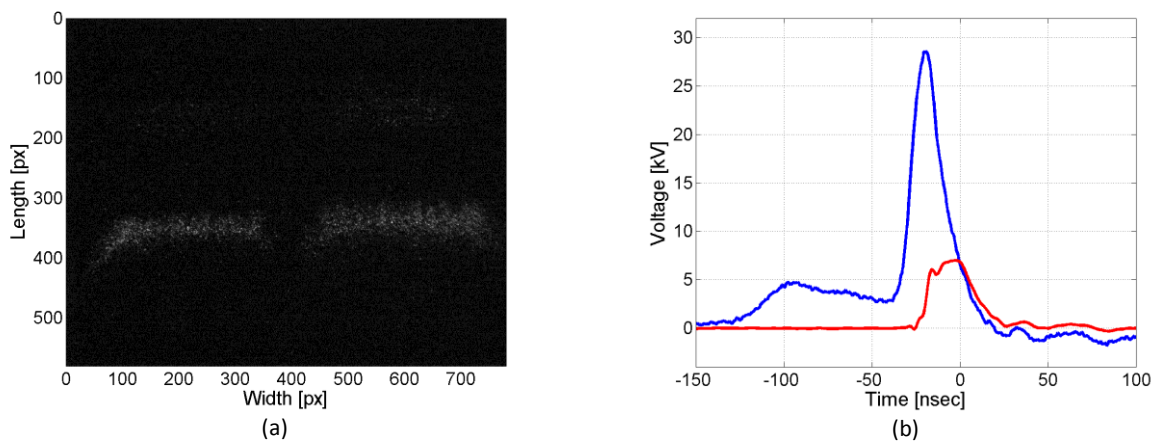


Figure 10-17. (a), avalanche image of the discharge (b). Source (blue) and load (red) voltage during the discharge.

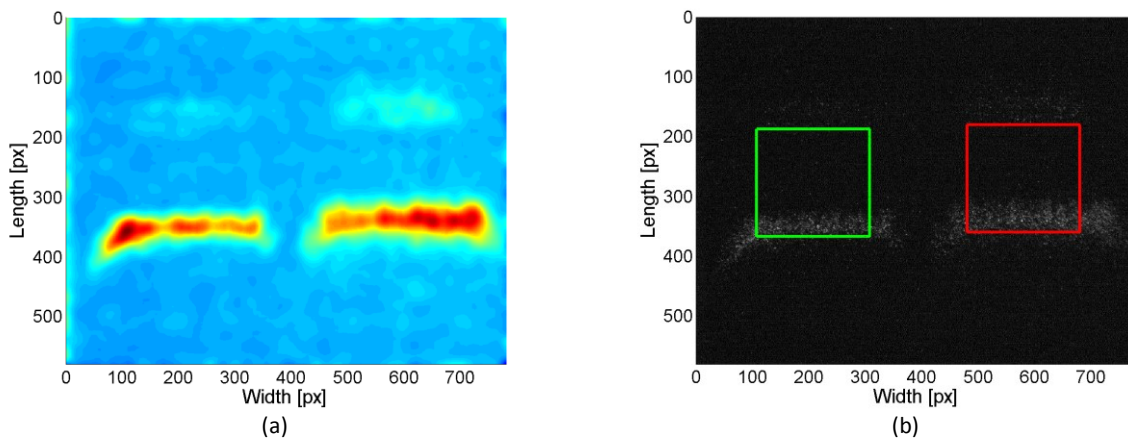


Figure 10-18. (a) Filtered surface plot of the discharge image. (b) Selected areas of the reference (green) and delayed (red) image.



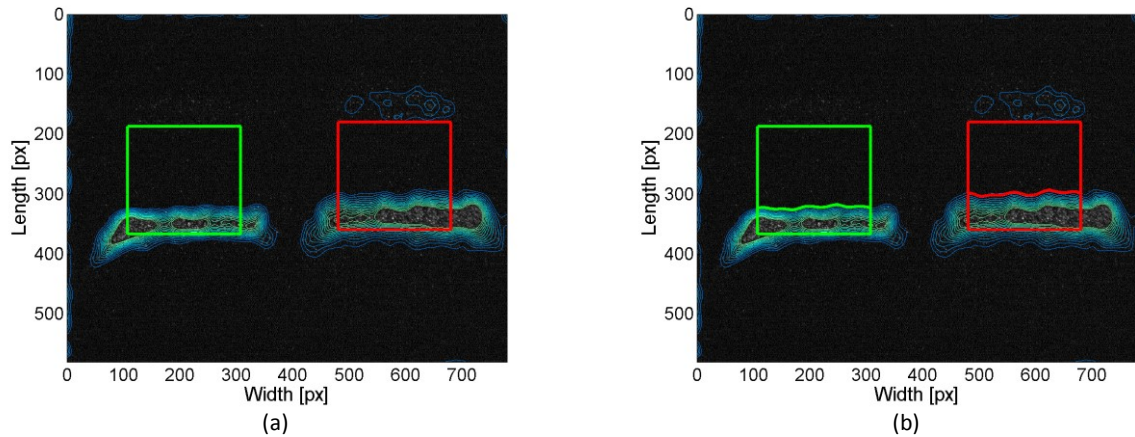


Figure 10-19. (a) From the filtered surface plot, Figure 10-18 (a), the equiv. intensity lines are obtained and are shown over the original discharge image. (b) the discharge front in both the reference and the delayed image are shown in green and red respectively.

Figure 10-17 (a) shows a standard discharge image. The time difference between the reference and delayed discharge image is 500 ps  $\pm$  17 ps. Due to the small amount of light, emitted during the first phase of the discharge, the images have a very noise character making filtering a bare necessity. After filtering a surface plot, Figure 10-18 (a), is obtained. This filtered image is used in the following steps to obtain contour lines and find the front of the discharge.

The bottom left corner of the discharge gap is used as a reference point. The gap is indicated with the green and red rectangle in the reference and delayed image respectively. These rectangles have their bottom left corner aligned with the bottom left corner of the gap and have the same width. For each vertical line in both these selection areas a sequence of steps is taken to identify the front of the discharge in both images and find the propagation velocity.

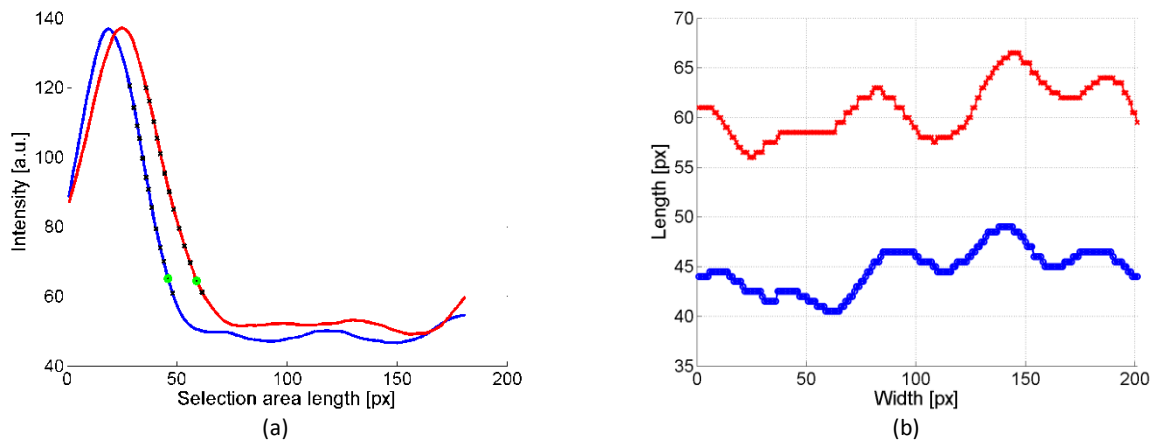


Figure 10-20. (a) The intensities in a single column of both the reference (blue) and delay (red) selection area. The black crosses indicate different intensity levels at which the velocity can be determined. The green circles indicate the selected intensity level used to determine the propagation velocity. (b) All the front positions found over the full width of the electrode for the reference (blue) and delayed (red) image.



Figure 10-20 shows the light intensity for one column of both the reference (blue) and delayed (red) image. For each vertical line the front of the discharge is identified in both images. The front is indicated with the black crosses. The lowest intensity value that is found on the front of both the reference and the delayed image and that also appears in all the vertical lines is used as the start and end position of the plasma front to determine the propagation velocity. Figure 10-20 (b) shows these two front lines. Here the blue line is the front as found in the reference image and the red line is the discharge front as found in the delayed image. The distance between each pair of points on the reference and delay line is used to determine a velocity. From this velocity a mean velocity is extracted and its standard deviation. This standard deviation is not a measure for the accuracy for this measurement but a measure for the variation in the discharge front velocity.

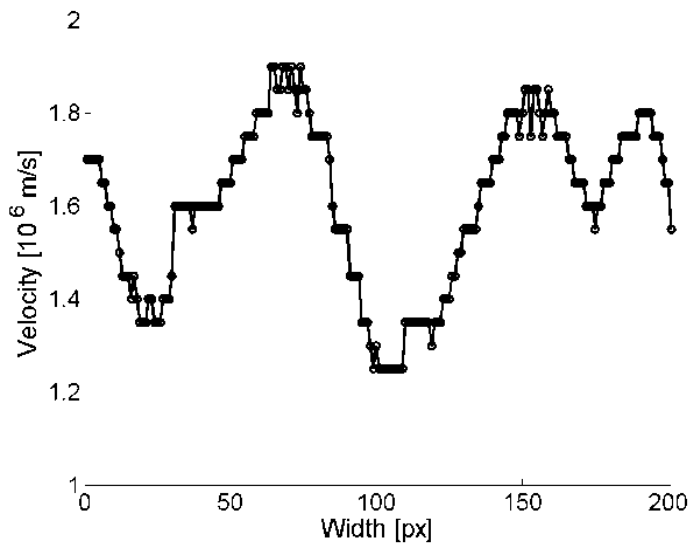


Figure 10-21. Propagation velocity of the plasma discharge front.

### 10.3.5 Limitations of the velocity measurement

The fastest velocity that can theoretically be measured is the full gap length of 8 mm in 500 ps, or,  $16 \cdot 10^6$  m/s. In this case the reference image would be without any discharge and the delayed image would have a discharge fully across the gap.

The fastest velocity that can be measured is a function of the position of the reference front

$$v_{max} = \frac{(l_g - x_t)}{\Delta t} \quad 10-9$$

Here  $v_{max}$  is the maximum velocity,  $l_g$  the length of the gap,  $x_t$  the position of the plasma front in the reference image and  $\Delta t$  the time difference between the images. For example, with a gap length of 8 mm, the plasma front at 3 mm from the source electrode in the reference image and a time difference between the images of 500 ps a maximum velocity of  $10^7$  m/s could be measured. The length needed to identify the plasma front in the images is not taken into account and will limit the maximum speed that can be measured in practice.

The smallest velocity that can be measured would be determined by the pixel size. As seen with the calibration, one pixel represents 50  $\mu\text{m}$ . So with a  $\Delta t$  of 500 ps, the minimum velocity would be  $10^5$  m/s. In this case a perfectly straight, 1 pixel long plasma front is assumed.

### 10.3.6 From $v(x)$ to $x(t)$ and $v(t)$

The velocity is easily related to position,  $v(x)$ . The  $v(x)$  data for a discharge in 1000 mBar air is shown in Figure 10-22.

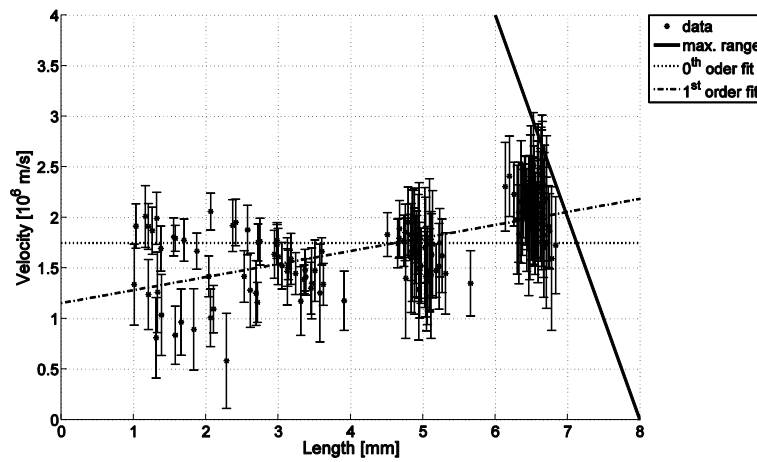


Figure 10-22. Measured avalanche propagation velocity.

To obtain the position and velocity as a function of time,  $x(t)$  and  $v(t)$ , a zero order and a first order fit are applied on the measured data. In this case the zero order fit has a standard deviation from the data of 0.38 and the first order fit has a standard deviation of 0.29. Using a zero order fit,  $x(t) = ct$  and  $v(t) = c$ . Using the first order fit, the velocity as a function of position can be described as

$$v(x) = ax + b \tag{10-10}$$

Now time can be obtained using  $v = x/t$

$$t(x) = \frac{x}{ax + b} \tag{10-11}$$

Finding for  $x(t)$

$$x(t) = \frac{bt}{1 - at} \tag{10-12}$$

And  $v(t)$  becomes

$$v(t) = \frac{dx(t)}{dt} = \frac{b}{(1 - at)^2} \tag{10-13}$$

Figure 10-23 and Figure 10-24 show the  $x(t)$  and  $v(t)$  obtained from the  $v(x)$  shown in Figure 10-22.

Coupling the  $v(t)$  to the change in capacitance,  $C(x)$ , we find an estimate for the capacitance as a function of time,  $C(t)$  as shown in Figure 10-25 and Figure 10-26.

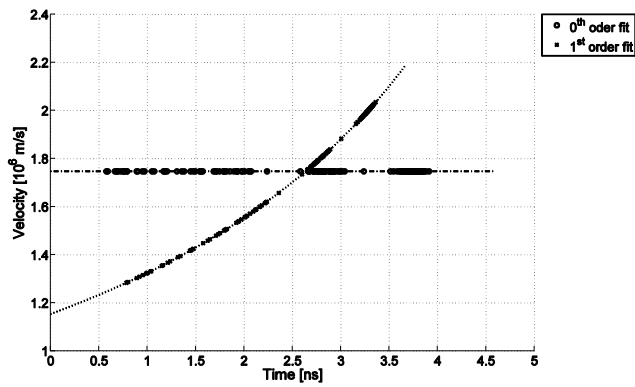


Figure 10-23. Avalanche front propagation velocity as function of time, 0<sup>th</sup> and 1<sup>st</sup> order fits.

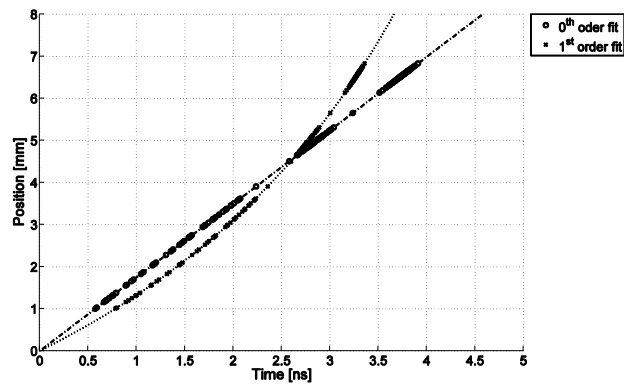


Figure 10-24. Avalanche front propagation position as function of time, 0<sup>th</sup> and 1<sup>st</sup> order fits.

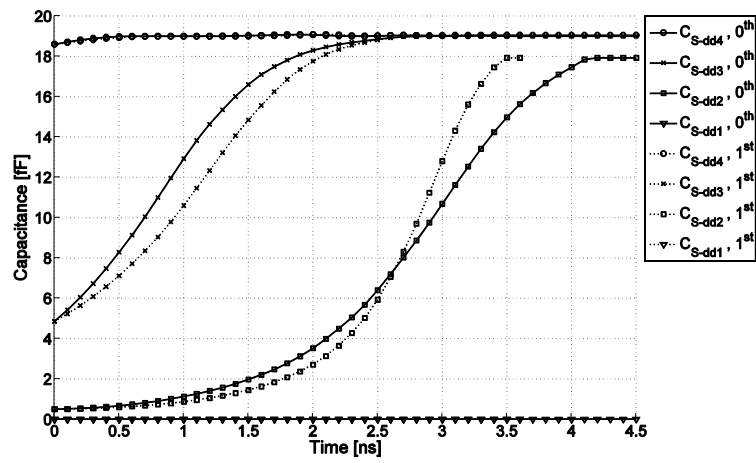


Figure 10-25. Time behavior of the capacitive coupling between the source electrode and the D-dot sensors, based on the capacitances obtained from numerical simulations and avalanche propagation velocities based on the optical images.

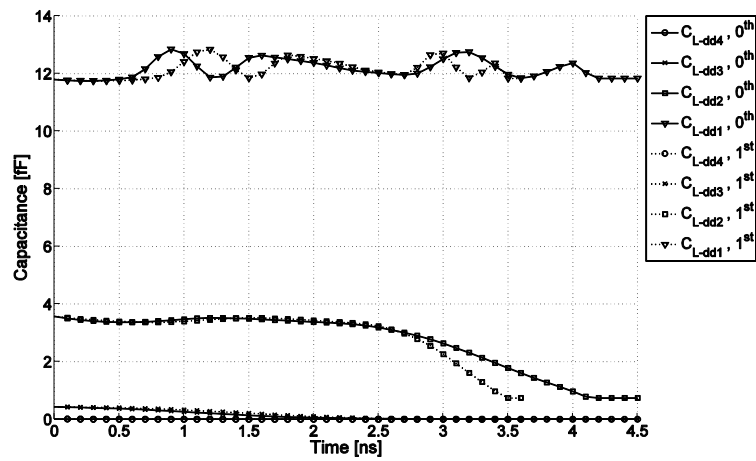


Figure 10-26. Time behavior of the capacitive coupling between the load electrode and the D-dot sensors, based on the capacitances obtained from numerical simulations and avalanche propagation velocities based on the optical images.

# 11 Bibliography

---

- [1] D. Wang, T. Matsumoto, T. Namihira, and H. Akiyama, "Development of Higher Yield Ozonizer Based on Nano-Seconds Pulsed Discharge," vol. 13, no. 1, pp. 71–78, 2010.
- [2] G. J. J. Winands, "Efficient Streamer Plasma Generation," Technische Universiteit Eindhoven, 2007.
- [3] K. Abe, K. Morotomi, K. Mitsutake, S. Katsuki, H. Akiyama, and S. Abe, "EFFECT OF PULSING SEQUENCE OF NANOSECOND PULSED ELECTRIC FIELDS ON HELA CELLS," *IEEE*, p. 1, 2010.
- [4] K. H. Schoenbach, S. Katsuki, R. H. Stark, E. S. Buescher, and S. J. Beebe, "Bioelectrics — New Applications for Pulsed Power Technology," *Scientist*, vol. 30, no. 1, pp. 293–300, 2002.
- [5] M. Yano, K. Abe, S. Katsuki, and H. Akiyama, "Gene expression analysis of apoptosis pathway in HeLa S3 cells subjected to nanosecond pulsed electric fields," *Pulsed Power Conference ...*, p. 5, 2011.
- [6] G. Taban, "A Cold Atom Electron Source," Technische Universiteit Eindhoven, 2009.
- [7] N. Debernardi, "UltraCold Ion Beam Source door," Technische Universiteit Eindhoven, 2012.
- [8] X. F. D. Stragier, "Towards external injection in laser wakefield acceleration," Technische Universiteit Eindhoven.
- [9] M. J. Van Der Wiel, O. J. Luiten, G. J. H. Brussaard, S. B. Van Der Geer, W. H. Urbanus, W. Van Dijk, and T. Van Oudheusden, "Laser wakefield acceleration: the injection issue. Overview and latest results.," *hilosophical Transactions of the Royal Society - Series A: Mathematical, Physical and Engineering Sciences*, vol. 364, no. 1840, pp. 679–687, 2006.
- [10] P. W. Smith, *Transient Electronics, Pulsed Circuit Technology*. Chichester: John Wiley & Sons, Inc., 2002, p. 288.
- [11] G. J. H. Brussaard and J. Hendriks, "Photoconductive switching of a high-voltage spark gap," *Applied Physics Letters*, vol. 86, no. 8, p. 081503, 2005.
- [12] C. E. Baum, W. L. Baker, W. D. Prather, S. Member, J. M. Lehr, J. P. O. Loughlin, L. Member, D. V. Giri, I. A. N. D. Smith, R. Altes, J. Fockler, D. M. C. Lemoire, M. D. Abdalla, and M. C. Skipper, "JOLT : A Highly Directive , Very Intensive , Impulse-Like Radiator," vol. 92, no. 7, 2004.
- [13] J. M. Lehr, C. E. Baum, W. D. Prather, and R. J. Torres, "FUNDAMENTAL PHYSICAL CONSIDERATIONS FOR ULTRAFast SPARK GAP SWITCHING," *Digest of Technical Papers 12th IEEE International Pulsed Power Conference*.

- [14] J. Hendriks and G. J. H. Brussaard, "Picosecond high voltage switching of a pressurized spark gap," *Digest of Technical Papers. PPC-2003. 14th IEEE International Pulsed Power Conference (IEEE Cat. No.03CH37472)*, vol. 1, pp. 587–590.
- [15] I. V Grekhov, A. F. Kardo-Sysoev, L. S. Kostina, and S. V Shenderoy, "HIGH POWER SUBNANOSECOND SWITCH," *IEEE*, pp. 662–663, 1980.
- [16] F. Davanloo, J. J. Coogan, T. S. Bowen, R. K. Krause, and C. B. Collins, "Flash x-ray source excited by stacked Blumlein generators," *Review of Scientific Instruments*, vol. 59, no. 10. p. 2260, 1988.
- [17] F. Davanloo, C. Collins, and F. Agee, "Ultra-fast flash X-ray pulses produced by Blumlein devices," *Nuclear Instruments and Methods in Physics Research Section B: Beam Interactions with Materials and Atoms*, vol. 241, no. 1–4, pp. 276–280, Dec. 2005.
- [18] D. B. Pawelek, P. a. a. F. Wouters, a. J. M. P. K. Yan, E. J. M. van Heesch, Z. Liu, G. J. J. Winands, G. J. H. Brussaard, N. Debernardi, and a. Kemper, "Design of Compact Transmission Line Transformer for High Voltage Nanosecond Pulses," *Conference Record of the 2006 Twenty-Seventh International Power Modulator Symposium*, pp. 522–525, May 2006.
- [19] L. Pang, F. Tao, B. Ren, and Q. Zhang, "Numerical Study for Obtaining the Optimum Conditions for Plasma Channel Formation in a Rail-Gap Closing Switch," *IEEE Transactions on Plasma Science*, pp. 1–6, 2012.
- [20] J. Hendriks, "The physics of photoconductive spark gap switching: Pushing the frontiers," Technische Universiteit Eindhoven, 2006.
- [21] J. Salge and U. Katschinski, "Fast Closing Switches for Low-Impedance Pulse Generators," *Pulsed Power Conference*, pp. 3–6, 1991.
- [22] G. Schaefer, M. Kristiansen, and A. Guenther, *Gas Discharge Closing Switches*. London: Plenum Press, 1990.
- [23] K. K. Trusov, "A model of multichannel mode formation," *Journal of Physics D: Applied Physics*, vol. 39, pp. 335–341, 2006.
- [24] J. M. Buzzi, H. J. Doucet, W. D. Jones, H. Lamain, and C. Rouillé, "A very-low-inductance triggered multichannel surface switch," *Review of Scientific Instruments*, vol. 61, no. 2, p. 852, 1990.
- [25] S. MacGregor, R. Fouracre, M. Given, and S. Turnbull, "The propagation of a 4 metre guided discharge across a dielectric surface," *Dielectric Materials, ...*, no. 4, pp. 23–26, 1996.
- [26] R. E. R. E. Reinovsky, J. H. J. H. Goforth, and J. Graham, "Surface-discharge switches for high-performance closing applications," *Plasma Science, IEEE Transactions on*, vol. 32, no. 5, pp. 1765–1777, 2004.
- [27] J. J. Mankowski, J. Dickens, and M. Kristiansen, "High voltage subnanosecond breakdown," *IEEE Transactions on Plasma Science*, vol. 26, no. 3, pp. 874–881, Jun. 1998.

- [28] R. D. Curry, M. Kristiansen, V. K. Agarwal, L. L. Hatfield, and G. R. Leiker, "Charging of insulators in a surface discharge switch," *Electrical Insulation, IEEE Transactions on*, vol. EI-21, no. 2, pp. 145–150, 1986.
- [29] L. Schachter, "Analytic expression for triple-point electron emission from an ideal edge," *Applied Physics Letters*, vol. 72, no. January, pp. 421–423, 1998.
- [30] M. D. Pozar, *Microwave Engineering*, Third edit. Hoboken: John Wiley & Sons, Inc., 2005.
- [31] J. A. Bittencourt, *Fundamentals of plasma physics*, Third Edit. New York: Springer-Verlag New York, Inc., 2004.
- [32] Y. Itikawa, "Cross Sections for Electron Collisions with Nitrogen Molecules," *Journal of Physical and Chemical Reference Data*, vol. 35, no. 1, p. 31, 2006.
- [33] A. Pemen, I. Grekhov, E. Heesch, K. Yan, S. Nair, and S. Korotkov, "Pulsed corona generation using a diode-based pulsed power generator," *Review of scientific ...*, vol. 74, no. 10, pp. 4361–4365, 2003.
- [34] G. M. Wilkinson, "TIME-DEPENDENT CAPACITANCE EFFECTS IN WATER DIELECTRIC SWITCHING," pp. 323–326.
- [35] H. M. Bergmann, "Triggered multichannel surface spark gaps," *Journal of Physics E: Scientific Instruments*, vol. 15, no. 6, p. 243, 1982.
- [36] J. C. Martin, *J. C. Martin on pulsed power*. New York: Plenum Press, 1996.
- [37] D. B. Pawelek, P. A. A. F. Wouters, A. J. M. Pemen, A. H. Kemper, and G. J. H. Brussaard, "Design of a Compact Transmission Line Transformer for High Voltage Nanosecond Pulses," *IEEE Transactions on Dielectrics and Electrical Insulation*, vol. 14, no. 4, pp. 900–906, Aug. 2007.
- [38] J. J. Coogan, F. Davanloo, and C. B. Collins, "Production of high-energy photons from flash x-ray sources powered by stacked Blumlein generators," *Review of Scientific Instruments*, vol. 61, no. 5, p. 1448, 1990.
- [39] W. Lane and P. W. Smith, "A REPETITIVE, THYRATRON SWITCHED, 200 kV, FAST RISE-TIME PULSE GENERATOR, BASED ON A STACKED TRANSMISSION LINE TRANSFORMER."
- [40] H. Heo, S. H. Kim, S. S. Park, and S. H. Nam, "DESIGN AND TEST OF A FAST CAPCITIVE HIGH VOLTAGE PROBE," *IEEE*, pp. 1345–1347, 2009.
- [41] A. Silve, L. M. Mir, and I. G. Roussy, "Implementation of a Broad Band , High Level Electric Field Sensor in Biological Exposure Device," *Exposure*, pp. 719–722, 2010.
- [42] I. A. Metwally, "Coaxial D-Dot Probe: Design and Testing," pp. 298–301.
- [43] Z. B. A. Malek, "Development of a non-inductive high voltage d- dot probe voltage transducer system," 2003.

- [44] A. Lorusso, V. Nassisi, and M. V. Siciliano, "Fast capacitive probe for electromagnetic pulse diagnostic," pp. 4–7, 2008.
- [45] D. Wang, T. Namihira, and H. Akiyama, "PULSED DISCHARGE PLASMA GENERATED BY NANO-SECONDS PULSED POWER IN ATMOSPHERIC AIR," pp. 1046–1049, 2009.
- [46] S. T. Pai and Q. Zhang, *Introduction to high power pulse technology*. Singapore: World Scientific, 1995.
- [47] T. Matsumoto, D. Wang, T. Namihira, and H. Akiyama, "IMPROVEMENT OF IMPEDANCE MATCHING BETWEEN NS PULSE GENERATOR AND DISCHARGE REACTOR," vol. 0.
- [48] T. Sakugawa, D. Wang, K. Shinozaki, T. Namihira, S. Katsuki, and H. Akiyama, "REPETITIVE SHORT-PULSED GENERATOR USING MPC AND BLUMLEIN LINE," *IEEE*, pp. 657–670, 2003.
- [49] D. Wang, T. Namihira, and H. Akiyama, "Recent Progress of Nano-Seconds Pulsed Discharge and its Applications," vol. 14, no. 1, pp. 131–137, 2011.
- [50] D. Wang, T. Namihira, and H. Akiyama, *Propagation of Streamer Heads During a 5-ns Pulsed Discharge*, vol. 39, no. 11. *IEEE*, 2011, pp. 2268–2269.
- [51] D. Wang, S. Okada, T. Matsumoto, T. Namihira, and H. Akiyama, "Pulsed Discharge Induced by Nanosecond Pulsed Power in Atmospheric Air," *IEEE Transactions on Plasma Science*, vol. 38, no. 10, pp. 2746–2751, Oct. 2010.
- [52] E. Husain and R. S. Nema, "TOWNSEND BREAKDOWN EQUATION," *IEEE Transactions on Electrical Insulation*, no. August, pp. 4–7, 1982.
- [53] "CST Microwave Studio." [Online]. Available: [www.cst.com](http://www.cst.com).
- [54] M. Kearney, A. Condie, and I. Dale, "GaAs planar doped barrier diodes for millimetre-wave detector applications," *Electronics Letters*, vol. 27, no. 9, pp. 721–722, 1991.
- [55] B. Szentpáli, V. Van Tuyen, G. Constantinidis, and M. Lagadas, "GaAs planar doped barrier diodes," *Materials Science and Engineering B*, vol. 80, pp. 257–261, 2001.
- [56] R. J. Malik, T. R. Aucoin, and R. L. Ross, "PLANAR-DOPED BARRIERS IN GaAs BY MOLECULAR BEAM EPITAXY," vol. 16, no. 22, pp. 836–838, 1980.
- [57] R. J. Malik and S. Dixon, "A subharmonic mixer using a planar doped barrier diode with symmetric conductance," *Electron Device Letters, IEEE*, no. 7, pp. 205–207, 1982.
- [58] Agilent, "Agilent 8474B / C / E Planar-Doped Barrier Diode Detectors," vol. 2. pp. 2–5.
- [59] T. Matsumoto, D. Wang, T. Namihira, and H. Akiyama, "Energy Efficiency Improvement of Nitric Oxide Treatment Using Nanosecond Pulsed Discharge," vol. 38, no. 10, pp. 2639–2643, 2010.





## 12 Dankwoord

---

Finally! After hours, days, weeks I finally get to write this part. I cannot express what 'doing my PhD' has done to me. It would be an understatement to say it was a ... 'road with a bump every once in a while'. I think that in a couple of years from now, when I am enjoying another great cup of coffee, I will think back to this period and ponder 'How did we do it?' Indeed, not in a million years could I have come this far if it weren't for the people around me. To all of you I say 'thank you!' from the bottom of my heart! To all whom I do not mention here; thank you all for the great time!

First I want to thank my parents. Thanks mom and dad! Your inexhaustible support, open minds, endless cheering, always willing to listen to all my stories, good or bad, day or night. Thanks for helping me grow and become the person I am today! I would have been nowhere without you. You're the best parents in the world! Wish you could see me today dad!

Thanks Joris, Marij, Martijn, Laura, Frank, Nicje, Jurian, Frans, Anny, Erik, Ronald and all my friends who have listened to the 'electron marble cannon' story and its progress more than once! Always more than enough other things to do besides a PhD with you guys. Activities to help forget the PhD every once in a while, especially when it knocked me down. The endless discussions we had kept me sharp and aware of the world outside of the magic bubble in which a PhD resides. All of you, each and everyone in their own special way, have inspired me to keep on going and not give up. Frank and Frans, thank you for each and every single smile.

Thank you Eddy! I still remember the moment you asked me 'What will be the ultimate experiment you want to do that represents the core of your PhD?' This one conversation has echoed through my mind ever since and ranks the top 3 list of 'Best guiding advises'. Our discussions on life and work were eye openers. Thank you for all your help, literally saving my PhD with your effort to help me build a setup that works (more than once) trust and your teaching!

Harry! Of course your name is here! Helping me out, arranging helium, argon, electronics, checking equipment time and time again! But not only that, also with you valuable discussion have helped me throughout my PhD. Not only a good technician but also an amazing musician.

Betty, I still remember how you confused me the first time we met. Now, I cannot imagine CQT (or the TU/e for that matter) without you! You're like the mom that makes sure that all goes smooth. For everybody else who reads this, ask yourself this question; how many secretaries can help you out when you call and say 'uhmmm ... I am at a conference right now but it still has to be paid ... uhhmmm can you help me out?' I know one, that's Betty! Many nice lunches enjoying just the last autumn sun. In the years of my PhD I think we have become friends, good friends.

Adam, Nicola and Thijs Meijer, I could write on and on about you guys and still not be able to express my gratitude. Countless nights of crashing at your places on beds and couches. Getting access to entire apartments for a week, coffee-chocolate-milk-in-a-huge-mug in the morning or real Italian espresso just before we go back to the TU/e. You guys have supported me throughout my PhD as more than colleagues, more than friends. I am grateful to have met you and if I could do it again, I would not have done it any other way (I would do the PhD-ing with you guys again, 100%! Of course I would try

not to make the same mistakes in the research again). May our paths cross many more times in the future!

Tom, good luck with your PhD! I am convinced you will shock the pulsed power community with something amazing. Be it a revolutionary new concept or great jokes! Call me when you need help on CST, but I think your CST qualities have surpassed mine a month or three ago, or if you want to discuss anything. I have had so much fun with our discussions!

Jom and Edgar, although you have not been directly involved in my PhD, both of you have been immensely inspiring. Jom you radiate so much energy and enthusiasm that ... you make physics fun! Edgar, not a single time have you not made time for me when I'd randomly pass by your office with a random question on any random subject. And your honest and clear answers have kept me on the right track in my PhD more than once. Thank you for that!

Prof. Namihira, Douyan Wang, Takao Matsumoto and everybody with whom I had the honor to work with, I can only say;

どうもありがとうございました！あなたは超素晴らしいです！

You have made Japan a home far from home! Not a day goes by without Japan passing through my mind! Thank you for the unforgettable and simply awesome time!

Guus and Seth. Thanks for your guidance. Each in your own way, and together in a, for me, perfect way, you have helped me through my PhD from beginning to end. 'But that is what we are here for, it's our job' I hear you say. But besides helping me with everything during my PhD, the both of you have given me the best support and all the room I needed when life showed its dark side. Not once, not twice but three times I could count on you. And for this I am forever grateful!

Raoul, Mariol, Erik, Sergio and the Reaction wheel team. I thank you all for the time you granted me to finish my PhD. While everybody gives all they have to get the job done, you allowed me to spend these valuable hours on my PhD. Well, this is the result, I hope you like it! Now let's go make the most awesome reaction wheels!

The most special thanks goes out to the love of my life, my girl, Marieke! Dear love, these last years have not been easy for us or for our beloved ones. The emptiness we deal with daily, hurts. And I think I will never be able to describe this emptiness to anyone. But every day I wake up, I wake up with a smile because I get to wake up next to you! And I am the luckiest guy in the universe that I can embark on a new exciting journey called 'today' together with you! With you by my side, I am convinced we can boldly go where no one has ever gone before!

---

## Curriculum Vitae

---

27 November 1980	Geboren in Nijmegen, Nederland
1993 - 1999	Atheneum <i>Dominicus College, Nijmegen</i>
1999-2001	Propedeuse Elektrotechniek <i>Technische Universiteit Eindhoven</i>
2004	Buitenland stage <i>Florida Institute of Technology, Florida, Verenigde Staten</i>
2001 - 2006	Ir. Elektrotechniek <i>Technische Universiteit Eindhoven</i> <i>Afstudeeronderzoek uitgevoerd by TNO</i>
2006 - 2007	Control Engineer <i>TNO</i>
2007 – 2012	Onderzoeker in opleiding <i>Technische Universiteit Eindhoven</i> <i>Faculteit Elektrotechniek</i> <i>Capaciteitsgroep Electrical Energy Systems (EES)</i> <i>Faculteit Technische Natuurkunde</i> <i>Capaciteitsgroep Coherence and Quantum Technology (CQT)</i>
2012 - heden	System engineer <i>Bradford Engineering, Heerle</i>